



# RESEARCH AND MODELLING IN CIVIL ENGINEERING 2018

EDITED BY JACEK KATZER  
KRZYSZTOF CICHOCKI  
AND JACEK DOMSKI

KOSZALIN UNIVERSITY OF TECHNOLOGY

KOSZALIN UNIVERSITY OF TECHNOLOGY

**RESEARCH AND MODELLING  
IN CIVIL ENGINEERING  
2018**

Edited by  
Jacek Katzer, Krzysztof Cichocki and Jacek Domski

KOSZALIN 2018

MONOGRAPH NO 355  
FACULTY OF CIVIL ENGINEERING,  
ENVIRONMENTAL AND GEODETIC SCIENCES

ISSN 0239-7129  
ISBN 978-83-7365-502-7

Chairman of the University Editorial Board  
*Zbigniew Danielewicz*

Editors  
*Jacek Katzer, Krzysztof Cichocki and Jacek Domski*  
*Koszalin University of Technology, Poland*

Reviewers  
*Jacek Gołaszewski – Silesian University of Technology, Poland*  
*Wojciech Sumelka – Poznań University of Technology, Poland*

Technical editor  
*Czesław Suchocki*

Website editor  
*Mariusz Ruchwa*

Linguistic consultations  
*Ewa Sokołowska-Katzer*

Typesetting  
*Czesław Suchocki*

Cover design  
*Tadeusz Walczak*

[www.cecem.eu](http://www.cecem.eu)

© Copyright by Koszalin University of Technology Publishing House  
Koszalin 2018

KOSZALIN UNIVERSITY OF TECHNOLOGY PUBLISHING HOUSE  
75-620 Koszalin, Raławicka 15-17, Poland

---

Koszalin 2018, 1<sup>st</sup> edition, publisher's sheet 13,42, circulation 120 copies  
Printing: INTRO-DRUK, Koszalin, Poland

## **Table of contents**

1. Relationship between mechanical properties and conductivity of SCC mixtures with steel fibres .....	7
2. Quantitative comparison between visual and UAV-based inspections for the assessment of the technical condition of building facades .....	19
3. Choice of optimal material solutions for the assessment of heat and humidity states of outer walls made using the technology of light steel framing .....	31
4. Behaviour of high performance concrete in mixed mode loadings: experiments and numerical simulation .....	45
5. Performance and optimization of prestressed beam with respect to shape dimensions.....	63
6. Plate strip in a stabilized temperature field and creep effect .....	87
7. Harnessing digital image correlation system for assessing flexural characteristics of SFRC based on waste ceramic aggregate.....	113
8. An experimental analysis of the determination of the elastic modulus of cementitious materials.....	129
9. X-ray investigation of steel fibres in high performance self-compacting concrete beams .....	149
10. Binary alkali-activated materials with brick powder.....	171
11. Numerical analysis of the temperature distribution in an office room .....	187
12. Generalized maximum tangential stress criterion in double cantilever beam specimens: choice of the proper critical distance .....	199
13. Comparison of pulse-echo-methods for testing of heat degradation concrete .....	213
14. Fundamental formulae for the calculation of shear flexible rod structures and some applications .....	237





## Preface

This monograph was created as the scientific outcome of the “3<sup>rd</sup> Central European Civil Engineering Meeting 2018” (CECEM 2018) which took place at Koszalin University of Technology (Faculty of Civil Engineering, Environmental and Geodetic Sciences) in Poland, 4 - 8 June 2018. Researchers representing five countries (Czech Republic, Slovakia, Spain, Vietnam and Poland) were attending the meeting. The meeting was organized as an ERASMUS+ event. CECEM 2018 had both staff training (STT) and teaching (STA) character and was a great opportunity to share knowledge and experience in the field of civil and structural engineering. The week-long programme included round table discussions, presentations, problem solving cases, lab visits, workshops and social events. The main objectives of CECEM 2018 included peer-learning, networking, transfer of knowledge and sharing research experiences and best practices. Participants brought into the discussion examples from their own institutions and present best practices and innovative approaches to the issues addressed.

The meeting was following the “1<sup>st</sup> Central European Civil Engineering Meeting 2016” (CECEM 2016) and the “2<sup>nd</sup> Central European Civil Engineering Meeting 2017” (CECEM 2017). Both meetings took place at Koszalin University of Technology (Faculty of Civil Engineering, Environmental and Geodetic Sciences) in Poland. The 1<sup>st</sup> CECEM 2016 (21 -23 June 2016) attracted researchers from Czech Republic and Ukraine. The 2<sup>nd</sup> CECEM 2017 (5 - 9 June 2017) attracted researchers from Czech Republic, Slovakia, Romania and Poland. The success of CECEM 2016 and CECEM 2017 encouraged organizers to organize the 3<sup>rd</sup> CECEM 2018.

During CECEM 2018 multiple scientific presentations were delivered and discussed. Organizers decided to prepare a monograph as the outcome of the meeting to prevent these high quality presentations from perishing. Willing authors prepared extended versions of their papers for publication. After very careful analyses and peer-review process 14 chapters were accepted for the final version of the monograph. The inclusion of a chapter in the monograph was free of charge for the authors. The peer-reviewing, editing and printing costs were covered by Faculty of Civil Engineering, Environmental and Geodetic Sciences at Koszalin University of Technology.

To embrace the scientific cooperation between attendees of all CECEM meetings an international scientific society “Research and Modelling in Civil Engineering” was established.

The 4<sup>th</sup> CECEM 2019 will take place in Koszalin (Poland), 3 - 7 June 2019. Colleagues from partner and non-partner institutions are encouraged to take part in the event. Contact person: prof. Jacek Katzer (cecem@cecem.eu). All details concerning the 4<sup>th</sup> CECEM 2019, previous meetings and an international scientific society “Research and Modelling in Civil Engineering” are available at the meeting website: **www.cecem.eu**. Free electronic versions of the current monograph and the monograph published after CECEM 2017 are also available there.

#### Editors

Jacek Katzer, Krzysztof Cichocki and Jacek Domski

# 1. Relationship between mechanical properties and conductivity of SCC mixtures with steel fibres

**Petr Konečný<sup>1a</sup>, Petr Lehner<sup>1b</sup>, Tomasz Ponikiewski<sup>2</sup>**

<sup>1</sup>*VSB-Technical University of Ostrava, Faculty of Civil Engineering, Department of Structural Mechanics, Ludvika Poděštlé 1875/17, 708 33 Ostrava-Poruba, Czech Republic,*

<sup>1a</sup>*orcid.org/0000-0001-6667-7522*

<sup>1b</sup>*orcid.org/0000-0002-1478-5027*

<sup>2</sup>*Silesian University of Technology, Faculty of Civil Engineering, Department of Building Materials and Processes Engineering, Akademicka 5, 44-100 Gliwice, Poland  
orcid.org/0000-0003-0535-2454*

## Abstract

Self-compacting concretes are more and more often combined with steel fibre reinforcement. In the paper the relationship between mechanical properties and conductivity of self-compacting concretes mixtures with steel fibres was studied. It was proven that there is a correlation between the amount of steel fibre and conductivity. However this relationship is not linear.

**Keywords:** conductivity, SCC, steel fibre, concrete

## 1.1. Introduction

The use of self-compacting concrete in combination with steel fibres increases its importance. With respect to some important properties such as the reduction of surface cracking, the improvement of some mechanical properties (e.g., bending strength), it is desirable to examine self-compacting concrete mixtures with steel fibers (Pajak and Ponikiewski, 2013). There are some disadvantages, of course. For fiber-concrete is limited design guidance (see e.g. FIB, 2011), there are different views of preparing mixtures themselves, and also there is some incompatibility in test methods. Since the durability of concrete exposed to aggressive agents is a significant issue. Thus, it is important to evaluate the ability of new concrete designs to resist harsh environment (Ghosh and Tran, 2015; Seddik Meddah, 2015; Ghosh *et al.*, 2017; Nguyen *et al.*, 2017). One of typical evaluation of quality of concrete against chloride ingress are based on evaluation of chloride profile (see e.g. Nordtest NTBuild 443, 1995; AASHTO T259, 2012). Those penetration test procedures require exposure of samples to chloride solution for several weeks, analysis of chloride profile using drilling or grinding, chemical analysis of chloride content in the profile with subsequent computation of steady-state diffusion coefficient. The electrochemical

procedures (AASHTO-TP95, 2011; ASTM C1202, 2012) are significantly faster. It is accepted that concrete ability against the penetration of aggressive agents is related to the passage of electrical current (electrical resistivity) (Feliu *et al.*, 1996; Morris, Moreno and Sagüés, 1996; Smith *et al.*, 2007; AASHTO-TP95, 2011). The evaluation via resistivity is nowadays rather standard in United States. The steel is much more conductive and that affects the reading. Since fibres of metallic nature have a significant influence on the measurement of the electrical resistance of concrete, which serves to determine the conductivity and consequently the coefficient of diffusion (Feliu *et al.*, 1996),

Evaluation of electrochemical properties on steel fibres reinforced concrete is not recommended (see e.g. Abad Zapico, 2015). The more advanced method such as Electrical Impedance spectroscopy shall be used if the steel is embedded in concrete (Martínez and Andrade, 2011; Jaśniok, 2013).

Since the knowledge of these electrochemical properties, may be related to the knowledge of diffusion of chloride ions (Lu, 1997; Konečný *et al.*, 2017) and relate the material property to the model of the concrete durability. Thus it would be interesting to be able to filter the effect of embedded steel fibres.

Thus, the evaluation of the effect of the amount of fibres on the concrete resistivity is conducted in this chapter. On the other hand, the partial task of measuring can be to prove whether the electrochemical methods used to determine the diffusive properties of concrete are at all appropriate in the use of wires or, conversely, totally inappropriate.

## 1.2. Laboratory experiments

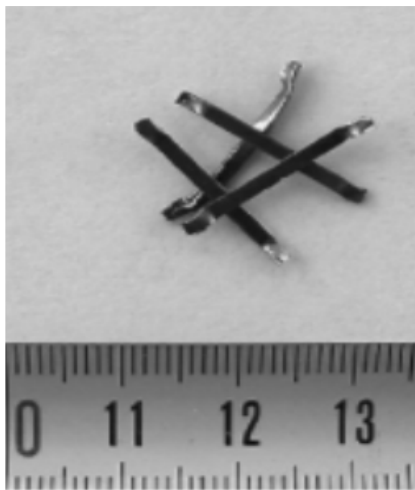


**Fig. 1.1.** Steel fibres KE20/1.7

Laboratory experiments were composed of several mechanical tests and electrical resistance measurements (AASHTO-TP95, 2011) on four concrete mixtures. The laboratory experiments were prepared at the laboratories of Silesian University of Gliwice and VŠB - Technical University of Ostrava.

The reference concrete was formed from Ordinary Portland Cement (OPC). The Self-Compacting Concrete (SCC) with several values of added steel fibres - 0 %, 1 % and 2 % of weight were casted in order to investigate the effect of fibres. The steel fibres were of type KE20/1.7 (Fig. 1.1). The composition of the mixtures is shown at Table 1.1 and it is based on earlier SCC research

at the SUT in Gliwice (Pająk and Ponikiewski, 2013; Sucharda *et al.*, 2017).

**Table 1.1.** Characteristics mixtures

Mixture No.	OPC	SCC 0%	SCC 1%	SCC 2%
Cement type I 42.5 R	313 kg/m <sup>3</sup>	490 kg/m <sup>3</sup>		
Water	164 kg/m <sup>3</sup>	201 kg/m <sup>3</sup>		
Sand	387 kg/m <sup>3</sup>	807 kg/m <sup>3</sup>		
River gravel	1546 kg/m <sup>3</sup>	807 kg/m <sup>3</sup>		
Superplasticizer	-	12.25 kg/m <sup>3</sup>		
Stabilizer	-	1.96 kg/m <sup>3</sup>		
Steel Fibres	-	-	80 kg/m <sup>3</sup>	160 kg/m <sup>3</sup>
Water/cement ratio (W/C)	0.52	0.41		

It should be noted that the cement applied in the mixture has been in laboratory storage for more than two years and partial hydration has been in progress. The concrete slump test was executed and all mixtures the similar value of workability. However, the data for slump were not properly recorded.

A complete range of tests including basic mechanical properties, fracture test and electrical resistance measurements in the (AASHTO-TP95, 2011), the Chloride Rapid Penetration Test (ASTM C1202, 2012) and accelerated penetration tests with chloride (Nordtest NTBuild 443, 1995) were performed.



**Fig. 1.2.** Example of preparation of laboratory samples for one set of mixtures

In Fig. 1.2 we can see a photograph of the set of laboratory samples consisted of seven large cylinders (diameter 150 mm, height 300 mm) six smaller cylinders (diameter 100 mm, height 250, 200 and 100 mm), four cubes (dimension 150 mm) and three beams (150 x 150 mm, length 450 mm). Each of the four mixtures contained such a set of samples. Three small cylinders and one large, with a different shape coefficient, were used for the tests described herein.

The evaluated experiment, calculations and results are part of the campaign discussed partly with respect to SCC without fibres in (Lehner, Konecny and Ponikiewski, 2018).

### 1.3. Mechanical properties

The basic measurements on each of the four sets were mechanical properties. Measurements of compressive strength were performed on standard cubes and cylinders samples (see Fig. 1.3). Further, a tensile splitting strength measurement was performed and a modulus of elasticity was determined (see Fig. 1.4).

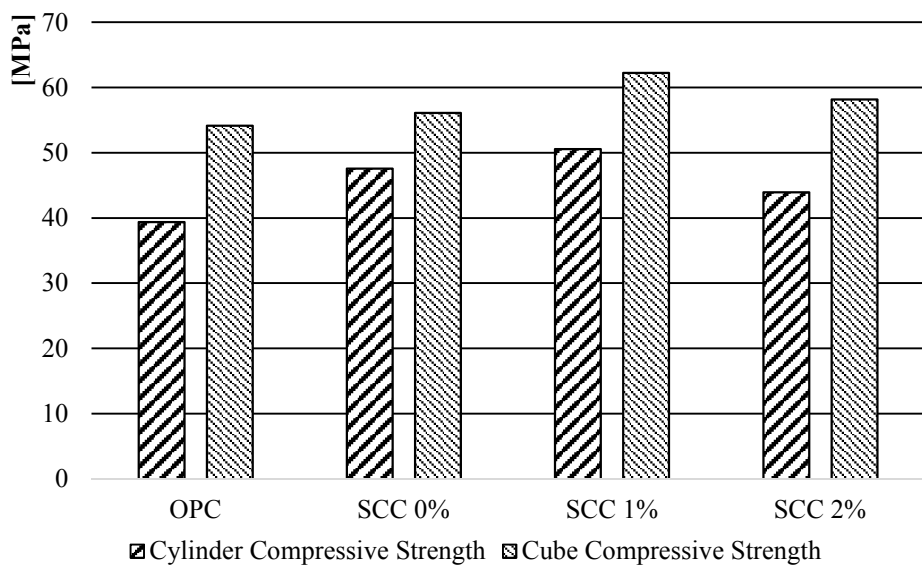


Fig. 1.3. Results of compressive strength for four mixtures sets

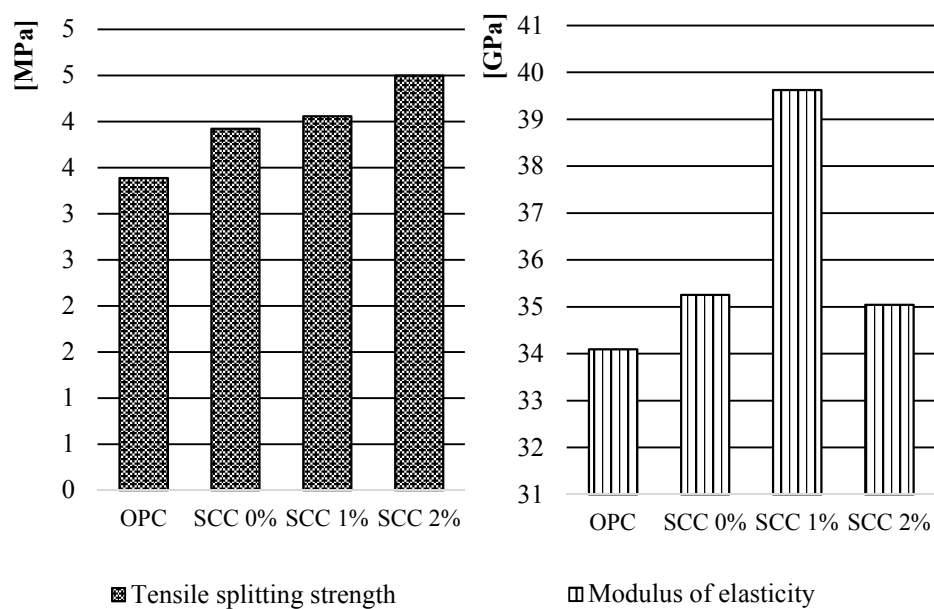


Fig. 1.4. Results of material characteristics for all mixtures



The results shown in the Fig. 1.3 and Fig. 1.4 can be interpreted from several aspects. Firstly, it is possible to compare the results between mixture from Ordinary Portland Cement and mixture from Self-Compacting Concrete. In all cases, SCC values are higher than OPC, but their difference is not as large as expected.

Another option is to look at the material properties compared to the number of steel fibres in the SCC mixture. It depicts that the higher is relative weight value of steel fibres, the higher is the tensile spitting strength.

On the other hand, other mechanical properties cannot be correlated like that. The greatest deviation can be seen in the modulus of elasticity, where the SCC 1%, i.e. 1% by weight of steel fibres per total weight, is almost twice the value of the other (SCC mixtures with 0% and 2% of steel fibres).

The modulus of elasticity is also interesting in view of the fact that for SCC 2% it is slightly smaller than for SCC 0%. The compressive strength view reveals that the SCC 2% is weaker than SCC 0% and SCC 1% in test at cylinder. But the in test at cube the value of SCC 2% is weaker than SCC 1% only. It is consistent with the typical limitation of the application of steel fibres up to 1.55 by mass of concrete. Further comparison and evaluation of results are contained at the end of the chapter.

#### **1.4. Electrochemical properties**

There are three procedures of detection of concrete diffusion coefficient. It can be evaluated using methods of rapid chloride penetration test (Nordtest NTBuild 443, 1995; AASHTO-T259, 2012), accelerated penetration tests with chloride (ASTM C1202, 2012) as well as surface measurement of electrical resistivity using Wenner probe (AASHTO-TP95, 2011), as mentioned above. For the purpose of the paper, the results from the electrical resistance measurement of Wenner's probe are selected.

The Wenner probe consists of four electrodes with a pitch of approx. 5 cm. The external electrodes use electrical current and the internal electrodes measure the electrical potential difference. The benefit of the method is rapid manipulation of instruments and samples. The method is non-destructive so the repeated measurement is possible in order to obtain to determine the time depending of diffusion.

Unfortunately, this measurement method may have a relatively large variation, partly due to the heterogeneity of the test material and also by the use of rather uncontrollable contact conditions. The contact between the electrodes and the concrete is maintained via a wet sponge where the electrical connection is

influenced by the contact pressure level and saturation of the sponge. After casting, the samples are cured in a water bath or lime water.

When using a lime bath, the container is filled with saturated lime solution to the edge and closed so that it is airtight. The samples are tested dry on a dry surface. The test of resistance for each of the cylinders is conducted four times around a diameter.

It should be noted, that surface resistivity can be converted to volume resistance using geometric correlation relationships (Morris, Moreno and Sagüés, 1996).

Knowledge of the electrical resistance of the concrete can be further used. The inverse parameter to the resistance is conductivity  $\sigma$  (S / m). Many factors have influenced these properties: relative humidity, type of cement used, w / c ratio, the presence of chloride ions or among others (Bertolini *et al.*, 2004). It is well-known, that electrical properties are influenced by conductive materials. Thus, it may be interesting to note the electrical conductivity values for self-compacting concrete with steel fibres admixtures.

As mentioned, it is a non-destructive test. Thus it is possible to measure electrical properties during maturing of concrete. In our case, it was tested at 7, 14, 28, 56, 91 and 161 days after concreting. The initial results of these tests is the evaluation of change in conductivity over time for all four mixtures under study (see Fig. 1.5.). Several interesting results can be seen in the Fig. 1.5. At the first measurement, 7 days after concreting, the OCP and SCC mixtures are different. Similarly, the weight ratio of steel fibres significantly influences the conductivity value, which was expected.

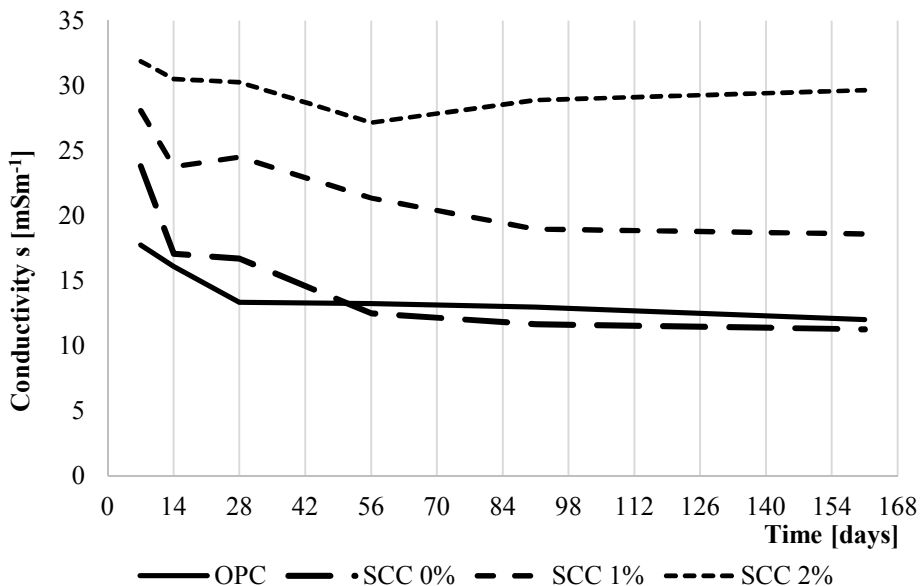


**Fig. 1.5.** The resulting of calculation conductivity over time for all the studied mixtures

Looking at the change in conductivity over the time for individual mixtures, we may derive following findings. First of all, the OPC mixture significantly reduces the conductivity between the seventh and the twenty-eighth day, but subsequently decreases its value less.

For SCC mixtures, pikes in graphs are observed. Although the relationships of pikes between 14 and 28 days are visible in all three mixtures, their absolute difference cannot be considered as constant or similar. Even with SCC 2%, the conductivity increases slightly from 56 days (see Fig. 1.6.).

Thus the absolute difference between the time-dependent conductivities of SCC with fibres is derived at Fig. 1.6., where the conductivity of SCC without fibres were subtracted from respective values of SCC with 1%, and SCC 2% of fibres, respectively.

It can be seen that if the influence of the conductivity based on the amount of added steel fibres would be proportional than we observe to horizontal lines in Fig. 1.6. This is not the case here. Thus there are also other influences that affect the readings such as start of corrosion of steel fibres.

Since mechanical properties have been measured at 28 days age only, the conductivity is compared with this data at this point in time. The Fig. 1.7. shows the conductivity results for all 4 mixtures under study at 28 days. These results are evaluated in the next chapter.

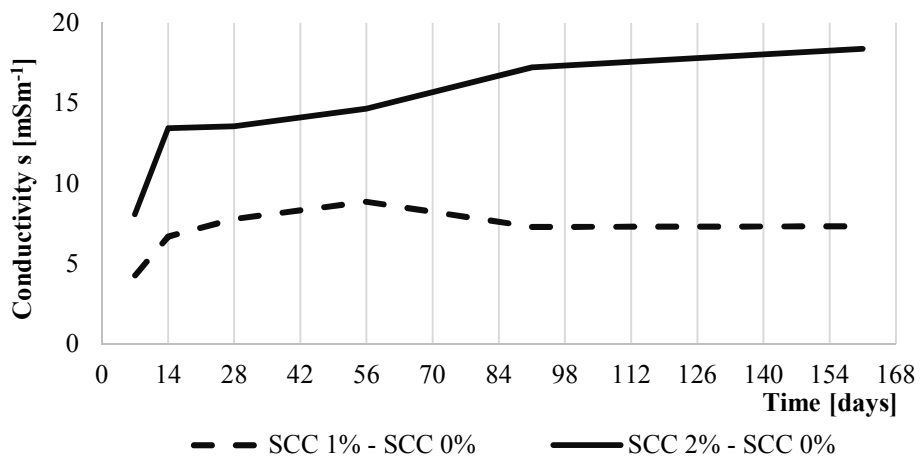


Fig. 1.6. Conductivity results for SCC 1% and SCC 2% after subtraction of SCC 0%

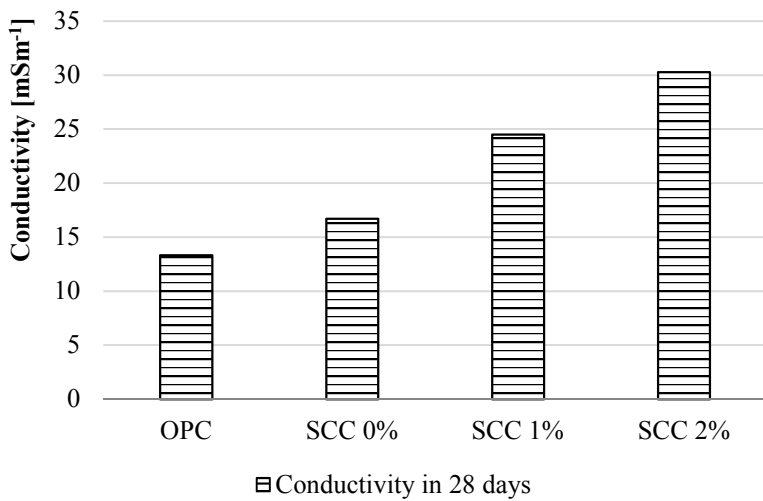
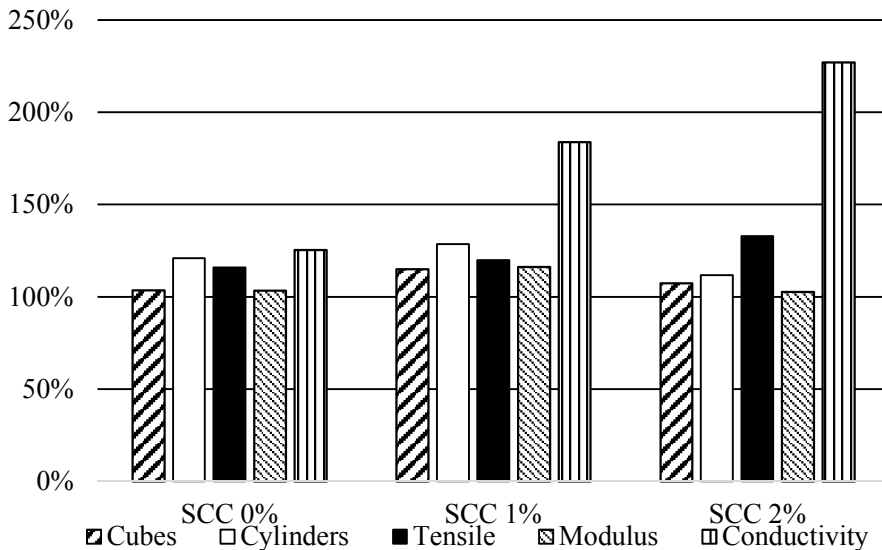


Fig. 1.7. The resulting of calculation conductivity all the studied mixtures at the age 28 days

## 1.5. Comparison of results

For the purpose of comparison, OPC mixture results were considered as the base values (100%), and the SCC mixtures difference are shown in the Fig. 1.8. There is relative values for cube and cylinder compression strength, tensile splitting strength, modulus of elasticity and electrical conductivity.



**Fig. 1.8.** Comparison of measured electrical conductivity values and material properties of SCC mixtures as a percentage of the OPC mixture values at the age 28 days

Looking at the percentage results, the conductivity is noticeably affected by the amount of steel fibres as expected. For mechanical properties such differences are not, and even there is not always, a gradual increase. For a SCC 2% mixture, values of cube and cylinder compression strength, modulus of elasticity are smaller. Only tensile splitting strength gradually increasing.

## 1.6. Conclusions

The comparison of relatively fast method for the evaluation of concrete ability to resist aggressive agents was conducted on the sample self-compacting concrete. There was correlation between the amount of steel fibres and conductivity as expected. However this relationship was not linear.

It should be noted that testing of mechanical properties over time could have contributed to the possibility of a subsequent correlation with the measurement of electrical conductivity. Since the conductivity measurement using Wenner's

probe is a non-destructive and simple test, if it finds certain correlation relationships, its use will be widely used. On the other hand, mechanical properties and electrochemical properties can influence different factors in a way that cannot always be determined in the same way. For example, in the case of a 2% SCC mixture, it is possible to estimate that there is excessive porosity. This causes some worse mechanical properties and, on the contrary, tends to increase the electrical conductivity of the saturated material. Also the cement applied in the mixture was in laboratory storage for more than two years and partial hydration has been in progress. Authors assumes that this affected the results.

From the point of view of the amount of fibres in the concrete, it would be advisable to prepare other mixtures, e.g., 1.2%, 1.4%, etc. That can leads to find the threshold at which the increasing properties change to decreasing.

The presented results are part of a campaign that includes another electrochemical tests, three-point bending fatigue test, calculation of the diffusion coefficient etc. However, the evaluation is still ongoing and the results will be published in a comprehensive work.

## References

- AASHTO-T259 (2012) *Standard method of test for resistance of concrete to chloride ion penetration*. Washington, D.C.: American Association of State Highway and Transportation Officials.
- AASHTO-TP95 (2011) 95-11 “*Standard Method of Test for Surface Resistivity Indication of Concrete’s Ability to Resist Chloride Ion Penetration.*”, *AASHTO Provisional Standards, 2011 Edition*. doi: 10.1520/C1202-12.2.
- Abad Zapico, L. (2015) *Experimental investigation on electrical resistivity of SFRC*.
- ASTM C1202 (2012) ‘Standard Test Method for Electrical Indication of Concrete’s Ability to Resist Chloride Ion Penetration’, *American Society for Testing and Materials*. doi: 10.1520/C1202-12.2.
- Bertolini, L. *et al.* (2004) ‘Effectiveness of a conductive cementitious mortar anode for cathodic protection of steel in concrete’, *Cement and Concrete Research*. doi: 10.1016/j.cemconres.2003.10.018.
- Feliu, S. *et al.* (1996) ‘A new method for in-situ measurement of electrical resistivity of reinforced concrete’, *Materials and Structures/Matériaux et Constructions*, 29(July), pp. 362–365. doi: 10.1007/BF02486344.
- FIB (2011) ‘Model Code 2010’, *fib Model Code for Concrete Structures 2010*. doi: 10.1002/9783433604090.ch6.
- Ghosh, P. *et al.* (2017) ‘Probabilistic time-dependent sensitivity analysis of

- HPC bridge deck exposed to chlorides', *Computers and Concrete*. doi: 10.12989/cac.2017.19.3.305.
- Ghosh, P. and Tran, Q. (2015) 'Correlation Between Bulk and Surface Resistivity of Concrete', *International Journal of Concrete Structures and Materials*. doi: 10.1007/s40069-014-0094-z.
- Jaśniok, M. (2013) 'Investigation and modelling of the impact of reinforcement diameter in concrete on shapes of impedance spectra', in *Procedia Engineering*. doi: 10.1016/j.proeng.2013.04.059.
- Konečný, P. *et al.* (2017) 'Comparison of Chloride Diffusion Coefficient Evaluation Based on Electrochemical Methods', in *Procedia Engineering*. doi: 10.1016/j.proeng.2017.05.326.
- Lehner, P., Konecny, P. and Ponikiewski, T. (2018) 'Experimental and Numerical Evaluation of SCC Concrete Durability Related to Ingress of Chlorides', in *AIP Conference Proceedings*.
- Lu, X. (1997) 'Application of the Nernst-Einstein equation to concrete', *Cement and Concrete Research*. doi: 10.1016/S0008-8846(96)00200-1.
- Martínez, I. and Andrade, C. (2011) 'Polarization resistance measurements of bars embedded in concrete with different chloride concentrations: EIS and DC comparison', *Materials and Corrosion*. doi: 10.1002/maco.200905596.
- Morris, W., Moreno, E. I. and Sagüés, A. A. (1996) 'Practical evaluation of resistivity of concrete in test cylinders using a Wenner array probe', *Cement and Concrete Research*. doi: 10.1016/S0008-8846(96)00175-5.
- Nguyen, P. T. *et al.* (2017) 'An Efficient Chloride Ingress Model for Long-Term Lifetime Assessment of Reinforced Concrete Structures Under Realistic Climate and Exposure Conditions', *International Journal of Concrete Structures and Materials*. doi: 10.1007/s40069-017-0185-8.
- Nordtest NTBuild 443 (1995) *Nordtest Method: Accelerated Chloride Penetration into Hardened Concrete, Nordtest method*. Esbo, Finland: Nordtest.
- Pajak, M. and Ponikiewski, T. (2013) 'Flexural behavior of self-compacting concrete reinforced with different types of steel fibers', *Construction and Building Materials*. doi: 10.1016/j.conbuildmat.2013.05.072.
- Seddik Meddah, M. (2015) 'Durability performance and engineering properties of shale and volcanic ashes concretes', *Construction and Building Materials*. doi: 10.1016/j.conbuildmat.2015.01.020.
- Smith, D. *et al.* (2007) *The Development of a Rapid Test for Determining the Transport Properties of Concrete*.
- Sucharda, O. *et al.* (2017) 'Identification of mechanical and fracture properties of self-compacting concrete beams with different types of steel fibres using inverse analysis', *Construction and Building Materials*. doi: 10.1016/j.conbuildmat.2017.01.077.

## 2. Quantitative comparison between visual and UAV-based inspections for the assessment of the technical condition of building facades

Carles Serrat<sup>1</sup>, Vicenç Gibert<sup>2</sup>, Anna Cellmer<sup>3</sup>, Anna Banaszek<sup>4</sup>

<sup>1</sup> *Dept of Mathematics, IEMAE-EPSEB, Universitat Politècnica de Catalunya-BarcelonaTECH, Barcelona, Spain, [orcid.org/0000-0002-1504-5354](https://orcid.org/0000-0002-1504-5354)*

<sup>2</sup> *Dept of Architectural Technology, LABEDI-EPSEB, Universitat Politècnica de Catalunya-BarcelonaTECH, Barcelona, Spain, [orcid.org/0000-0001-6341-5762](https://orcid.org/0000-0001-6341-5762)*

<sup>3</sup> *Dept of Geoinformatics, The Faculty of Civil Engineering, Environmental Engineering and Geodesy, Koszalin University of Technology, Koszalin, Poland, [orcid.org/0000-0002-7872-6325](https://orcid.org/0000-0002-7872-6325)*

<sup>4</sup> *Dept of Real Estate Resources, The Faculty of Geodesy, Geospatial and Civil Engineering, University of Warmia and Mazury, Olsztyn, Poland, [orcid.org/0000-0002-2744-2023](https://orcid.org/0000-0002-2744-2023)*

**Abstract:** In this chapter authors conduct a case study analysis in order to evaluate the potential benefits of using Unmanned Aerial Vehicles (UAVs) for the data collection involved in the failures diagnosis of facades. A quantitative approach is performed by testing for statistically significant differences between the proposed methodology and traditional visual inspections. Results allow to state that a highly significant global improvement for the data collection exists.

**Keywords:** UAV, building façade, quantitative comparison

### 2.1. Introduction

In recent years, a lot of research has been developed exploring the use of digital images acquired through Unmanned Aerial Vehicles (UAVs) monitoring the technical condition of real estate and inventories of technical infrastructure. Within this perspective, Banaszek *et al.* (2017) have proved the new opportunities that the use of UAVs offers in the area of technical inspection of buildings and constructions. In the civil engineering framework, large structures such as large-scale structures, bridges, chimneys, towers, dams, industrial power plants, power lines are often difficult to access for detailed technical inspection. New UAV data acquisition technologies offer new opportunities in this field. The data acquisition process is the most time-consuming, technically complex and therefore the most costly part of the audit (Eschmann *et al.*, 2012). UAV case studies to monitor the technical condition of objects of different sizes (residential building, dam, retaining wall at the runway) have shown that high resolution image quality enables visual identification of cracks of 0.3 mm at approx. 10 m from the recorded surface (Hallermann *et al.*, 2015).



Independently, BRAIN (Building Research Analysis and Information Network) has been introduced by Serrat *et al.* (2017a) as a platform for the predictive analysis of the technical condition of the urban canyon. The methodology was initially introduced by Serrat and Gibert (2011) and lately developed in Gibert (2016). BRAIN proposes, in a collaborative network of urban laboratories, a follow-up across time of the technical condition of the facades in a building stock. Supported by a GIS platform and a survival analysis-based methodology, BRAIN aims to infer on the time to the occurrence of potential failures or lesions in the existing facades. After modeling the time-to-event with the statistically significant variables, the predictive system allows strategic decision-making for the maintenance and the sustainability of the building stock (Serrat *et al.*, 2017b). One of the most relevant issues in the methodology is the data collection procedure. Conventional inspections are primarily based on visual research methods. However, the data collection must be as exhaustive and accurate as possible, in order to minimize the variability among inspectors. As well, a massive and periodic inspection should be efficient in terms of data quality versus time and cost resources.

In this Chapter authors conduct a quantitative analysis for checking the potential benefits of implementing the use of UAVs in the data collection within the BRAIN framework. The main aim of the contribution in this preliminary approach is to quantitatively assess the improvement with respect to visual inspections concerning the estimation of the technical condition of the facades by using this high graphic capture technology.

The Chapter presents and discusses the quantitative results of an experiment using UAV, equipped with a high-resolution digital camera (Serrat *et al.*, 2018a), for the failure diagnosis of facades in comparison to the visual assessment of the technical condition of the facades.

The Chapter is organized as follows. In Section 2.2 details on the BRAIN methodology and the previous UAV experiment and analysis will be introduced. Methodology used for the quantitative analysis will be described in Section 2.3. Results and discussion will compose Section 2.4. The Chapter ends with a summary of the main conclusions and a description of the ongoing research.

## **2.2. Previous work**

We introduce in this Section the fundamentals of the BRAIN inspection methodology as well as the preliminary experiment and contributions related with the use of UAVs for the technical condition assessment.

### **2.2.1. BRAIN methodology**

The BRAIN predictive system (Serrat *et al.*, 2017a) focuses on a massive prospecting campaign of the facades at a multiscale level. Indeed, it concentrates on the concept of the urban laboratory that collects the envelope of the buildings and constitutes the urban front. BRAIN protocol is integrated by four components. In short, a) a collaborative approach in order to joint and analyze the information coming from the nodes in the network of urban labs, b) an inspection methodology to be applied in each urban lab, c) a survival analysis methodology as a statistical technique for the durability and modeling estimation, and d) a GIS platform as a tool for managing the information and the analyses. Details of these components can be found in Gibert (2016).

The inspection protocol was designed in Gibert, Serrat and Casas (2014). It is based on a list of requirements in order to apply a population-based approach, that is to be applied in a massive manner in big cities. The final protocol was inspired in a previous datasheet developed by the Laboratory of Building (LABEDI) at the Barcelona School of Building Construction. That former datasheet evolved towards a weighted criterium that combines issues like identifiability of the facades, classification of the facades, methodological issues themselves, resources needed, data collection, and analytical skills for the decision-making and the methodology aims to be efficient in each of the requirements.

The protocol includes an inspection document that consists of two parts. Part a) allows the collection of field data, cartographic data, cadastral data as well as plot/building/facade data and architectural characteristics. Part b) covers the collecting of existing elements and materials and the state of any damage at the time of inspection. Fig. 2.1 shows part b) of the inspection document in detail. According to this second sheet the types of injuries analyzed in the inspected built environment are as follows:

- Mechanical injuries that appear from external or internal forces, having an effect on the mechanical integrity of the construction elements: detachment, crack, debonding, spalling and deformation.
- Chemical injuries as a result of chemical reactions between the materials that make up the construction elements and the atmospheric factors or other polluting products contained in the surrounding environment: material degradation and corrosion.
- Physical injuries caused by a process related to the physical laws, affecting the physical characteristics of the constructive elements and materials: moisture, as well as material degradation.

### 2.2.1. Preliminary UAV experiment and contributions

In order to explore the emerging possibilities derived from capturing the information on the technical condition of the facades through UAV devices, we conducted the following preliminary experiment.

A sample of six facades was selected in Poland, located in Warsaw (4 units) and Olsztyn (2 units). Facades were identified as units 1 to 6, respectively. The sample was chosen based on criteria of morphology and deterioration level. In Fig. 2.2 general views and characteristics of the sample under study are shown.

The experiment used the DJI Inspire One lightweight quadcopter with the following specifications: weight: 2,935g, vertical GPS accuracy: 0.5 m (accuracy determination), horizontal GPS accuracy: 2.5 m (accuracy of X, Y coordinates), climb speed: 5 m/s, max. drop speed: 4 m/s, max. cruising speed: 22 m/s (ATTI mode, no wind), max. flight height: 4,500 m ASL (Above Sea Level), max. wind force: 10 m/s, flight time: 18 minutes, operating temperature: -10°C to 40°C, size: 438x451x301 mm. To obtain digital images the UAV was equipped with a Digital camera (RGB sensor) with the following specifications: 12 Mpix resolution (4,000x3,000 pixels), physical size 6.170 mm x 4.628 mm, focal length: 3.55 mm. More details on the description of the flights can be found in Serrat *et al.* (2018a).

After the flights the images were processed and analyzed, facade by facade, by the technical inspector and the main advantages and possibilities were: a) UAV strengths include high mobility in data acquisition and the ability to fly at different heights, b) to observe any area of the facade with sufficiently precise approaches to detect any type of existing injury (in addition, the results of the images are sufficiently explicit as to enable an expert to identify the existing architectural elements and their construction techniques), c) sweeping of the camera from top to bottom allows making visible parts and elements of the facade which were not visible at that moment, d) zooming the images, when it is necessary, allows the inspector to detect the extent of the injuries, e) to accurately diagnose the injury and its severity, and f) the amount of information on the technical condition of the facade allows the inspector to perform accurate posterior measurements and analyses (Serrat *et al.*, 2018a).

Based on the conducted experiment authors stated that the use of UAVs for technical inspections of the facades in a building stock was an interesting alternative to the traditional visual inspections from the public way. The use of UAV provided new opportunities in the area of technical inspections due to the detail and accuracy of the data, low operating costs and fast data acquisition time.

FAÇADE CHARACTERISTICS			COATING			CON			DIS			MORPHOLOGY			FB			FT			OT		
ADDRESS		N°	FAC. No		T		C		N		P		D		M		R		S				
P		L	G	P	L	G	P	L	G	P	L	G	P	L	G	P	L	G	P	L	G		
<b>MAIN BODY</b>																							
WALL-ZB																							
WALL-ZM																							
HOLES																							
LINTEL-ZB																							
JAMB-ZB																							
LINTEL-ZM																							
JAMB-ZM																							
PARAPETS																							
<b>COATING</b>																							
DISCONTINUOUS																							
TILING-ZB																							
TILING-ZM																							
CONTINUOUS																							
PLASTERED MORTAR																							
STUCCO WORK																							
SCRATCH WORK																							
FINISHING																							
<b>DECK RAILING</b>																							
WALL-1																							
WALL-2																							
TILING																							
PLASTERED MORTAR																							
SERIF																							
<b>PROJECTING BODIES</b>																							
<b>BALCONIES</b>																							
SLAB-1																							
SLAB-2																							
EDGES																							
UNDER BALCONY																							
RAILING																							
WALL-1																							
WALL-2																							
TILING																							
PLASTERED MORTAR																							
SERIF																							
<b>TRIBUNES</b>																							
SLAB																							
EDGES																							
UNDER TRIBUNE																							
WALL-1																							
WALL-2																							
TILING																							
PLASTERED MORTAR																							
STUCCO WORK																							
SCRATCH WORK																							
FINISHING																							
HOLES																							
LINTELS																							
JAMBS																							
PARAPETS																							
<b>OTHER ELEMENTS</b>																							
PLINTH																							
BRACKETS																							
LEDGES																							
EAVES																							
DAVITS																							
OTHERS																							

ST. BUILDING ACCESS

TYPE OF DAMAGE			
T	DETACHMENT	D	DEFORMATION
C	CRACK	M	MAT. DEGRAD.
N	DEBONDING	R	CORROSION
P	SPALLING	S	MOISTURE

EXTENT	
P	PUNTUAL
L	LOCAL
G	GENERAL

SEVERITY			
1	SYMPTOM	5	VERY SEVERE
2	MILD	6	EXTREME
3	MODERATE		
4	SEVERE		

**Fig. 2.1.** Inspection sheet for the failures data in the BRAIN protocol



**Fig. 2.2.** General views of the facades in the sample. In parentheses (morphology, deterioration level)

Recently, Serrat *et al.* (2018b) conducted a qualitative study in order to analyse the goodness of fit to the fundamental requirements that support the BRAIN inspection methodology. Authors concluded that, based on the data from the abovementioned experiment, traditional inspections are nowadays slightly better scored than the UAV alternative. However, UAV scenario is quickly changing over time and the alternative is quite promising. On the one hand, the advantage in requirements as data quality and analysis are not questionable at all. On the other hand, authors noticed that technological progress will move this UAV resource to a more standard, better well-known and cheaper technology. Within this perspective UAV-based inspections can really improve their compliance with the standards of the requirements for a large-scale inspection protocol.

### 2.3. Materials and methods

Each of the injuries in Fig. 2.2 is evaluated according to its extent, by means of a visual approach: puntual (P) when less than 25% of the element is injured, local (L) when failures affect between 25% and 50% of the element, and general (G) when injuries exceed 50% of the element. Injuries are also evaluated in terms of severity by assigning, for each of the elements, a numerical value from 0 to 6 according to the severity of the injury observed in the element. This information allows to compute, numerically and graphically, the Weighted Severity Index (WSI) of the injuries as a weighted mean which allows the researcher to obtain a general image of the global condition of the damage in the facade.

If we denote by  $\mathcal{E}$  the set of existing elements in a facade, the WSI of the facade is given by the weighted mean of the injury severities, across the elements in  $\mathcal{E}$ , with weights 1, 2 and 3 for the extent variable, that is

$$WSI = \frac{\sum_{i \in \mathcal{E}} (P_i + 2L_i + 3G_i)}{18 \cdot \text{card}(\mathcal{E})} \cdot 100 \quad (2.1)$$

where  $P_i$ ,  $L_i$  and  $G_i$  denote the severities with puntual, local and general extent, respectively, being 18 ( $=3 \cdot 6$ ) the potential maximum contribution of an injury, and  $\text{card}(\mathcal{E})$  the cardinal of  $\mathcal{E}$ , i.e. the number of existing elements. The WSI represents the percentage of damage, in terms of severity and extent, of every facade and it is computed for each of the aforementioned injuries, as well as for the different parts of the facade (body, deck railing, balconies and tribunes).

For each facade, datasheet for the failure condition will be filled twice: firstly based on the visual inspection, and secondly based on the pictures obtained from the UAV flights. Let denote by  $WSI_{Vis}$  and  $WSI_{UAV}$  the WSI values derived from each of the methodologies, respectively.

Based on the previous works and the high graphic quality of the images reported by the UAV methodology, we can assume that estimated percentage of

damages in the facades will be higher with this methodology in comparison to the visual one, i.e.  $WSI_{UAV} \geq WSI_{Vis}$ .

Let denote by  $\Delta$  the potential improvement in the percentage of failures according to the expression

$$\Delta = WSI_{UAV} - WSI_{Vis}. \quad (2.2)$$

We are interested in the estimation of the expectation of  $\Delta$ ,  $\mu = E(\Delta)$ . The estimated value of this expectation corresponds to the difference between the respective means, that is

$$\hat{\mu} = \overline{WSI}_{UAV} - \overline{WSI}_{Vis}. \quad (2.3)$$

In order to decide on the significance of this improvement, we will apply a unilateral (right tail) paired  $t$ -test to the WSI pairs of data collected per façade. The aim is to test for the existence of statistically significant differences in favor of an alternative hypothesis that is proposing positive improvements. The formulation of the hypothesis test is as follows

$$\begin{cases} H_0: \mu = 0 \\ H_1: \mu > 0 \end{cases} \quad (2.4)$$

and, under normality distribution conditions and controlling by the dependency between the measurements in a façade, the  $t$ -value statistic follows a  $t$ -Student distribution with  $n-1$  degrees of freedom, where  $n$  is the sample size.

## 2.4. Results and discussion

The results of the twelve hypothesis tests are shown in Table 2.1. Per each of the injuries and each of the parts of the facade, the sample size ( $n$ ), the estimation of the expected improvement ( $\hat{\mu}$ ), the standard error of the mean (s.e.), the  $p$ -value and the significance of the test are reported.

From the results in Table 2.1 the following remarks can be derived:

- In the case of the deformation injury test could not be applied because in every unit (facade) values for extent and severity of the injuries both for the UAV-based and visual-based inspection coincide.
- For crack, spalling, material degradation, and moisture injuries differences are almost significant. This fact suggests that under a larger sample size, the statistical power of the test would be higher and significant differences could be found.
- For the WSI computations for the body of the facade, differences are really significant. This global benefit of the UAV methodology supports the evidences in favor of using this technology for the data collection.

**Table 2.1.** Results of the hypothesis test per each of the injuries (8) and each part of the facade (4). ( $n$ : sample size,  $\hat{\mu}$ : estimation of the expected improvement, s.e.: standard error of the mean, n.a.: not available, -:  $p \geq 0.05$  non significative, \*:  $p < 0.05$ , significative, \*\*:  $p < 0.01$ , very significative, \*\*\*:  $p < 0.001$ , highly significative)

	$n$	$\hat{\mu}$	s.e.	$p$ -value	Significance
Injury					
Detachmet	6	0.133	0.102	0.124	-
Crack	6	1.067	0.669	0.086	-
Debonding	6	0.133	0.133	0.182	-
Spalling	6	0.750	0.379	0.052	-
Deformation	6	0.000	0.000	n.a.	n.a.
Material Degradation	6	0.783	0.408	0.056	-
Corrosion	6	0.417	0.288	0.104	-
Moisture	6	3.470	1.960	0.069	-
Part of the facade					
Body	6	0.617	0.130	0.003	**
Deck Railing	3	0.833	0.463	0.107	-
Balconies	3	0.733	0.433	0.116	-
Tribunes	3	0.450	0.071	0.035	*

- d) For the case of assessing the technical condition of tribunes, UAV-based strategy also improve significantly the estimation of the percentage of damage in this part of the facade.

## 2.5. Conclusions and ongoing research

Concerning the comparative analysis aimed to assess the improvement of using UAV inspections versus visual ones in measuring the technical condition of facades, the experiment and posterior analyses allows to draw the following conclusions:

- Potential quantitative benefits of the UAV-based methodology have been shown.
- Despite at the injury level there are only some cases in which differences are significative, at the part-of-the-facade level there is a highly significative global improvement.
- The possibility of collecting images at different heights drives to a significative improved diagnosis at the level of tribunes.

After these preliminaries studies, authors' ongoing research on the topic addresses, in an holistic manner, issues like a) to review the list and weights of the general and specific requirements for the BRAIN protocol of inspections, in



order to take into account the use of high graphic capture technologies, b) to extend the source of images management to ortophoto, photogrammetry, 3D point-cloud, termographic camera as a potential alternative or complement to the traditional inspection methodology, c) to incorporate the urban canyon perspective in the approach of the massive inspection methodology instead of the isolated building case considered in this experiment, d) to increase the sample size of the study for a better sampling of variables like morphology and level of damage, and e) to explore adaptative and smart flying plans in order to get a more efficient data collection.

## Acknowledgements

This research has been partially supported by grants MTM2015-64465-C2-1-R (MINECO/FEDER) from the Ministerio de Economía y Competitividad (Spain) and 2017 SGR 622 from the Departament d'Economia i Coneixement de la Generalitat de Catalunya. Authors are grateful to the Laboratory of Photogrammetry and Remote Sensing (LFiT) Dron House S.A., Warsaw (Poland) its contribution in the technical part of using UAV technologies, as well as, to members of the IEMAE, LABEDI and GRASS-GRBIO groups their valuable comments and suggestions in the development of the work.

## References

- Banaszek, A. *et al.* (2017) 'Possibilities of Use of UAVS for Technical Inspection of Buildings and Constructions', *IOP Conference Series: Earth and Environment Science*, 95, 032001, pp. 1–6.
- Eschmann, C. *et al.* (2012) 'Unmanned Aircraft Systems for Remote Building Inspection and Monitoring', in *Proceedings of the 6th European Workshop on Structural Health Monitoring*, Th.2.B.1, pp. 1–8.
- Gibert, V. (2016) 'A multiscale predictive system for the degradation of the built urban front, *PhD Thesis, Universitat Politècnica de Catalunya-BarcelonaTECH*, Barcelona, Spain, (in Spanish).
- Gibert, V., Serrat, C. and Casas, J.R. (2014) 'Determination of criteria for the exploration and for obtaining indicators in evolutionary analysis of degradation in urban facades', in *Proceedings of the 13th International Conference on Durability of Building Materials and Components*, Sao Paulo, Brasil, pp. 656–663.
- Hallermann, N. *et al.* (2015) 'Unmanned Aerial Systems (UAS) – Case Studies of Vision Based Monitoring of Ageing Structures', in *Proceedings of the International Symposium Non-Destructive Testing in Civil Engineering*

- (NDT-CE), Berlin, Germany.
- Serrat, C. *et al.* (2017a) 'BRAIN: Building Research Analysis and Information Network', in *Proceedings of the XIV International Conference on Durability of Building Materials and Components*, Ghent, Belgium, 325, pp. 1–11.
- Serrat, C. *et al.* (2017b) 'On the selection of significant variables in a model for the deteriorating process of facades', *IOP Conference Series: Materials Science and Engineering*, 251, 012071, pp. 1–8.
- Serrat, C. *et al.* (2018a) 'Use of UAVs for Technical Inspection of Buildings Within the BRAIN Massive Inspection Platform', *IOP Conference Series: Materials Science and Engineering*, to be published.
- Serrat, C. *et al.* (2018b) 'Exploring Conditions and Usefulness of UAVs in the BRAIN Massive Inspections Protocol', Submitted to *Open Engineering*.
- Serrat, C. and Gibert, V. (2011) 'Survival analysis methodology for service live prediction and building maintenance', in *Proceedings of the 12th International Conference on Durability of Building Materials and Components*, Porto, Portugal, vol. II, pp. 599–606.



### 3. Choice of optimal material solutions for the assessment of heat and humidity states of outer walls made using the technology of light steel framing

**Maciej Major<sup>1</sup>, Izabela Major<sup>2</sup>, Mariusz Kosiński<sup>3</sup>**

<sup>1</sup> *Czestochowa University of Technology, Faculty of Civil Engineering, Częstochowa, Poland, [orcid.org/0000-0001-5114-7932](https://orcid.org/0000-0001-5114-7932)*

<sup>2</sup> *Czestochowa University of Technology, Faculty of Civil Engineering, Częstochowa, Poland, [orcid.org/0000-0003-1234-9317](https://orcid.org/0000-0003-1234-9317)*

<sup>3</sup> *Czestochowa University of Technology, Faculty of Civil Engineering, Częstochowa, Poland, [orcid.org/0000-0003-2683-7784](https://orcid.org/0000-0003-2683-7784)*

**Abstract:** The subject of the article is the evaluation of thermal and humidity conditions of external partitions made in the light steel skeleton technology in terms of building physics requirements.

**Keywords:** heat, humidity, wall, steel framing

#### 3.1. Introduction

A substantial part of investments is financed from mortgages. Therefore, investors search for optimal materials and designs. One of the solutions is offered by technology of light steel framing. Compared to conventional solutions, this technology can meet investors' expectations. With light structure, quick construction, the use of recycled material while meeting the requirements concerning heat and humidity in detached houses, light steel framing can be competitive with other technologies.

Temperature distribution in outer walls whose layers are homogeneous in individual cross-sections of the wall does not represent a computational problem. The use of steel framing structures for building a wall leads to the disturbance in temperature distribution and needs to be analysed in detail. It is justified to use numerical software to determine heat and humidity parameters in such a wall. This paper presents the examples of numerical analyses for external walls built using the modern technology of light steel framing and emphasizes the differences in physical parameters of the analysed design and material solutions resulting from the specific design. For numerical analysis of the heat flow the commonly known Ansys software was used (ANSYS 2013),

(Flodr et al. 2015) and (Vican & Sykora 2013). Furthermore, to determine the humidity state of the wall WUFI software was employed (Kunzel 1995).

### **3.2. Heat and humidity protection of wall in the technology of light steel framing**

In the outer walls of the light steel framing, the insulation layer is located between the load-bearing pillars. Therefore, this space has to be entirely filled with the insulating material to avoid thermal bridges. Reduction of the thermal bridge that is present in steel pillars can be achieved by using an additional layer of insulation or perforated sections.

From the standpoint of heat transfer, distances between steel sections and the thickness of the section itself are also very important. Therefore, the best solution is to use maximal distances between the pillars and relatively thin walls of the sections.

Maximal permissible values of thermal transmittance for outer walls up to the year 2017 were  $U = 0.23 \text{ W/m}^2\text{K}$ , and, for 2021 this value will be  $U = 0.20 \text{ W/m}^2\text{K}$  (Rozporządzenie w sprawie warunków technicznych, Dz.U. 2013). With light steel framing, and assuming adequate approach at the stage of design and construction, these levels can be already achieved.

Calculations of the material parameters are usually adopted for dry conditions. If the wall is insufficiently protected from humidity, its thermal insulation properties are lower and it is exposed at risk of corrosion of steel components (Urbańska-Galewska & Kowalski 2018).

Humidity of the walls depends on the effect of climate factors and their material and design properties. One of the major sources of humidity that gets to external walls is vapour contained in air.

One of the basic criteria for designing the wall and its joints is humidity criterion, obtained based on the condition of prevention from surface condensation of humidity. Examination of the risk of development of condensation and growth of mould in the interior is conducted by means of the comparison of the temperature factor  $f_{Rsi(obl.)}$  with the threshold value of  $f_{Rsi,(kryt)}$ , which, according to (Rozporządzenie w sprawie warunków technicznych, Dz.U. 2013), is 0.72.

### **3.3. Computational assumptions**

In the case of walls composed of non-homogeneous layers, thermal resistance of the wall should be computed according to the guidelines contained in PN-EN ISO 6946:2008. The method described in the standard is a simplified version.

More detailed results are obtained from the computations made using computer software based on the finite element methods (Pawłowski 2016), (Major & Kosiń 2016).

Further part of the study presents the results of heat and humidity analysis of the adopted material and design solutions of the walls using the technology of light steel framing.

Numerical analysis concerning the flow of heat was made using the Ansys software based on the finite element method. The analysis was performed for the assumption of homogeneity and isotropy of materials of individual layers. Furthermore, WUFI software was employed to determine the humidity state of the wall.

In the thermals analysis, the internal temperature was adopted as  $t_i = +20^\circ\text{C}$  based on (ANSYS 2013), whereas the external temperature was adopted as  $t_e = -20^\circ\text{C}$  according to PN-EN 12831:2006. Thermal transfer coefficients for the FEM analysis were adopted on the internal side for the horizontal flow as  $h_i = 7.69 \text{ W}/(\text{m}^2\cdot\text{K})$ , for the vertical flow downwards as  $h_i = 5.88 \text{ W}/(\text{m}^2\cdot\text{K})$ , for the vertical flow upwards as  $h_i = 10 \text{ W}/(\text{m}^2\cdot\text{K})$  and on the external side as  $h_e = 25 \text{ W}/(\text{m}^2\cdot\text{K})$ . They represent the reverse value of the resistances  $R_{si}$ ,  $R_{se}$  ( $\text{m}^2\cdot\text{K})/\text{W}$  (Pawłowski 2016) and (Pawłowski & Kosiń 2017). The boundary conditions for calculations of minimal temperature on the internal side of the wall  $t_{\min}$   $^\circ\text{C}$  and the temperature factor  $f_{Rsi}$  are used according to PN-EN ISO 13788:2003, which is  $R_{si} = 0.13 (\text{m}^2\cdot\text{K})/\text{W}$  for frames and windows, whereas in other cases, this value is  $R_{si} = 0.25 (\text{m}^2\cdot\text{K})/\text{W}$ . In the case of humidity analysis, the material data and the data concerning the external climate were defined by the choice of the geographical location of the wall. The external climate conditions took into consideration the changes in temperature and relative air humidity according to the standard PN-EN ISO 13788:2003.

### 3.4. Thermal analysis of external wall corner

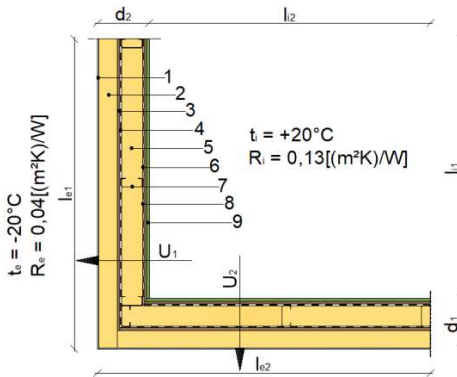
Six-layer walls were adopted for the analysis (Fig. 3.1), with their load-bearing components differing from each other (Fig. 3.2).

The C-shaped section was assumed in the analysed cases (Fig. 3.2c) with cross dimensions of  $h = 140 \text{ mm}$ ,  $b = 38 \text{ mm}$ ,  $c = 18 \text{ mm}$ ,  $t = 1.5 \text{ mm}$  and internal radius of  $r = 3 \text{ mm}$ .

Table 3.1 presents heat and humidity parameters of the analysed walls. Using the algorithm below through computer simulation, the thermal transmittance  $U [\text{W}/(\text{m}^2\cdot\text{K})]$  was evaluated for the individual parts of the joint (Gołaś at al. 2011):

- calculation of the value of the mean horizontal component of heat flux density for the part of joint  $q_1$  W/m<sup>2</sup>,
- calculation of the thermal transmittance for individual parts of the joint based on:

$$U_i = q_i / (t_i - t_e) \text{ [W/(m}^2\cdot\text{K)]} \quad (3.1)$$



- 1 – thin-coat plaster, thickness 0.5cm -  $\lambda = 0.7$  W/(m·K),
- 2 – mineral wool, thickness 16cm -  $\lambda = 0.035$  W/(m·K),
- 3 – cement bound particle-board, thickness 1.2cm -  $\lambda = 0.215$  W/(m·K),
- 4 – vapour-permeable membrane,
- 5 – mineral wool 140cm -  $\lambda = 0.215$  W/(m·K),
- 6 – steel pillar C140, thickness 0.15cm -  $\lambda = 50$  W/(m·K),

- 7 – vapour-barrier membrane,
- 8 – cement bound particle-board, thickness 1.2cm -  $\lambda = 215$  W/(m·K),
- 9 – drywall, thickness 1.25cm -  $\lambda = 25$  W/(m·K),

**Fig. 3.1.** Computational model and material characteristics for the analysed wall made using the technology of light steel framing

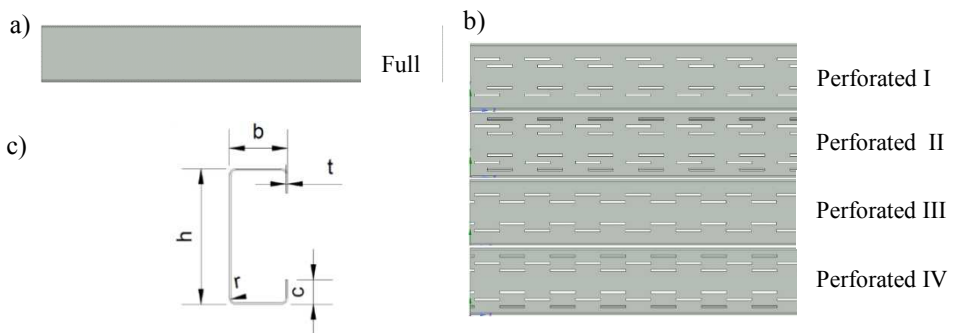


**Fig. 3.2.** Thin-wall C sections: a) solid section, b) perforated section, c) dimensions of the cross section

Thermal transmittance for the wall made of solid sections is  $U=0.137 \text{ W/m}^2\text{K}$ . Furthermore, for the design based on perforated components, this value is  $U=0.144 \text{ W/m}^2\text{K}$ . In light of the holes with small surface in a perforated section and the simplified grid of finite components in the numerical model, it can be presumed that building a more complex grid would reduce this difference.

Quite different situation is observed for the heat flux  $\Phi$  [W] where energy loss through the joint in the form of the wall corner is smaller for the perforated sections, as shown in Table 3.1. The same pattern is observed for the linear thermal transmittance  $\Psi_e$  [ $\text{W}/(\text{m}\cdot\text{K})$ ] (Tab. 3.1). A significant difference between the wall made of solid sections compared to perforated sections is observed (60%). This difference is insignificant between the design based on perforated components, with these sections differing in their arrangement and insignificant number of holes (Tab. 3.1).

**Table 3.1.** Heat and humidity parameters of the analysed external walls

		Profiles				
		Full	Perforated I	Perforated II	Perforated III	Perforated IV
Total heat flow through the wall [W] <sup>1)</sup>		15.348	15.050	14.991	15.052	14.980
Temperature [°C] <sup>2)</sup>	min	-20	-19.991	-19.991	-19.991	-19.991
	max	+19.743	+19.524	+19.521	+19.524	+19.520
Risk of condensation on the inside $f_{\text{Rsi,calculative}}$ ( $f_{\text{Rsi,critical}}=0.72$ ) <sup>3)</sup>		0.833	0.836	0.835	0.837	0.836
Linear heat transfer coefficient (the external dimensions) $\Psi_e$ [ $\text{W}/(\text{m}\cdot\text{K})$ ] <sup>4)</sup>		-0.030	-0.070	-0.071	-0.069	-0.071
<sup>1), 2)</sup> Calculated using ANSYS; <sup>3)</sup> Calculated on the basis of PN-EN ISO 13788:2003; <sup>4)</sup> Calculated on the basis of PN-EN ISO 10211:2008						

Fig. 3.3 presents temperature distributions for the variants of wall corner. Disturbances in temperature distributions can be observed in the location of structural pillars. Comparison of the solid section with perforated section reveals the difference in temperature distribution only for greater magnification. However, no changes are observed for the comparison of perforated sections.



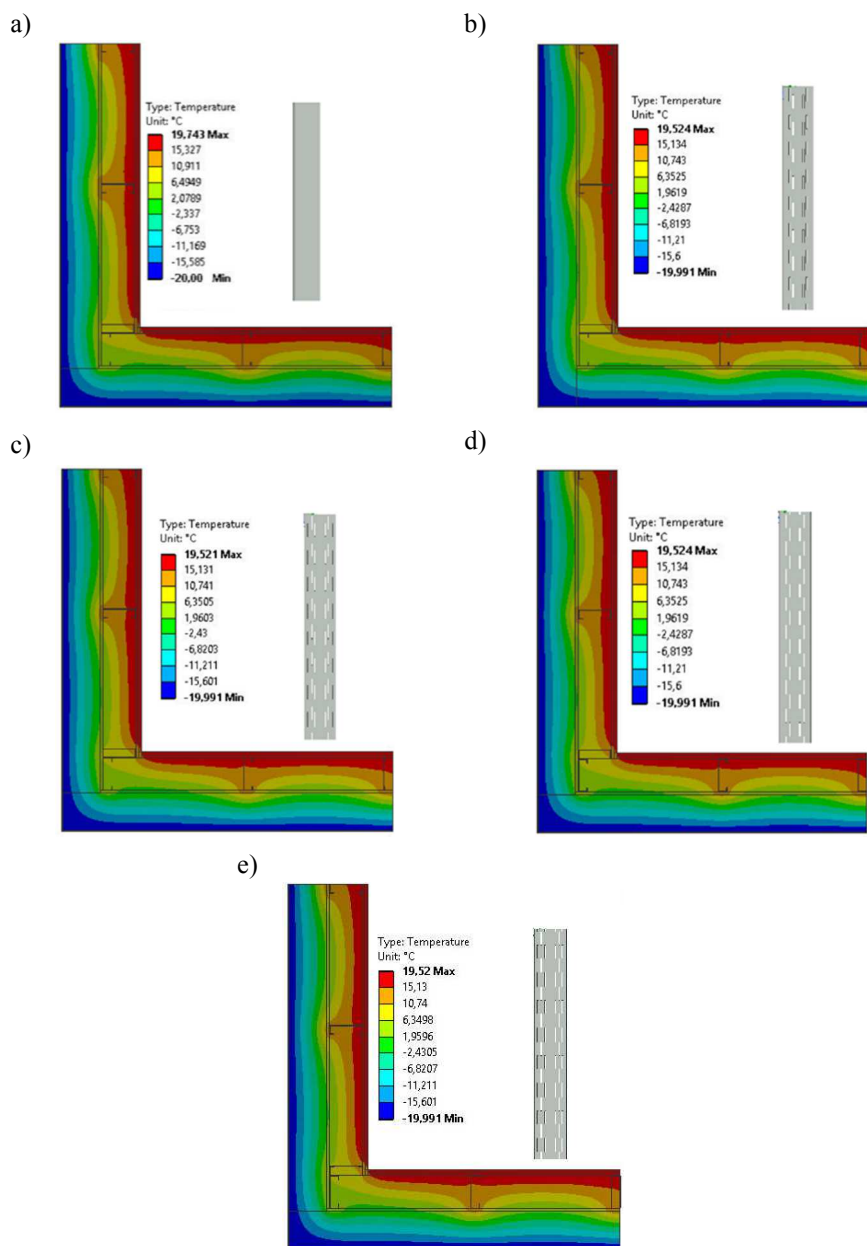


**Fig. 3.3.** Results of computer simulation for the adopted sections: a) solid section, b)-c) perforated sections with different number and arrangement of holes (see Fig. 3.2b)

### 3.5. Analysis of humidity states

Fig. 3.4 and 3.5 presents various design and material solutions subjected to humidity analysis based on the finite element method. A 4-year period was analysed for the wall located on the western façade. The external climate was defined for the city of Kraków, Poland, whereas the internal climate takes into consideration the changes in temperature and relative air humidity according to the standard PN-EN ISO 13788:2003.

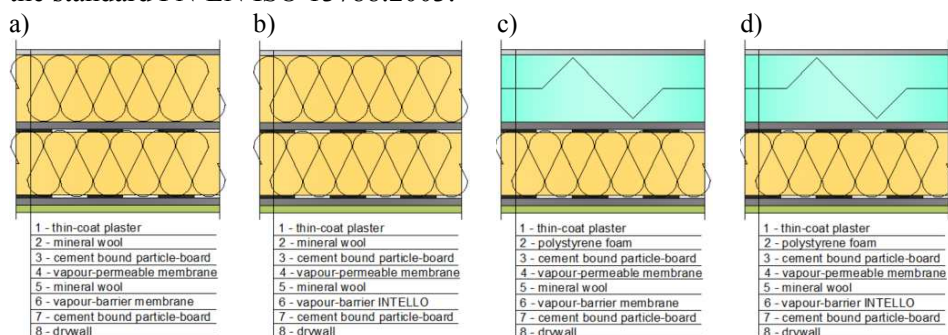


**Fig. 3.4.** Designs of the walls using the technology of light steel framing with sheathing made of cement board adopted for the humidity analysis: a) Wool - PE variant, b) Wool - Intello variant, c) Polystyrene - PE variant, d) Polystyrene – Intello variant

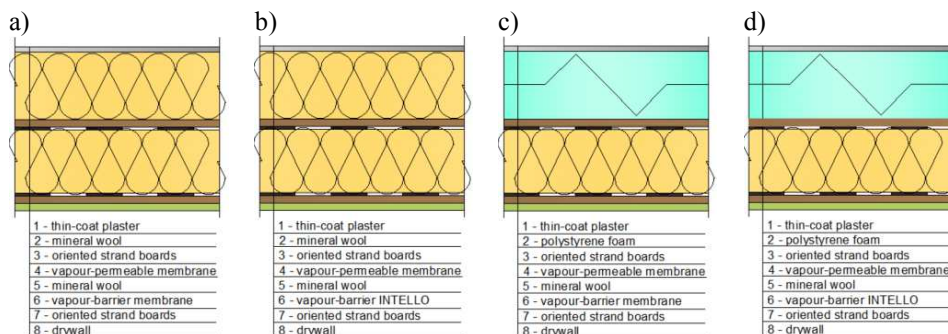


**Fig. 3.5.** Designs of the walls using the technology of light steel framing with sheathing made of OSB boards adopted for the humidity analysis: a) Wool - PE variant, b) Wool - Intello variant, c) Polystyrene - PE variant, d) Polystyrene – Intello variant

The results of computations of total water content are presented in Figs. 3.6 and 3.7, whereas for individual materials - in Figs. 3.8 and 3.9. As shown in Fig. 3.7, with the use of cement boards and a layer of external insulation made of polystyrene foam, humidity is substantially lower than in other solutions. The most favourable option with the OSB board is the wall with external insulation in the form of polystyrene foam and Intello vapour-barrier membrane (Fig. 3.6a). In all analysed cases, the use of Intello membrane was in initial period characterized by lower content of water compared to PE vapour-barrier membrane (Figs. 3.6 and 3.7).

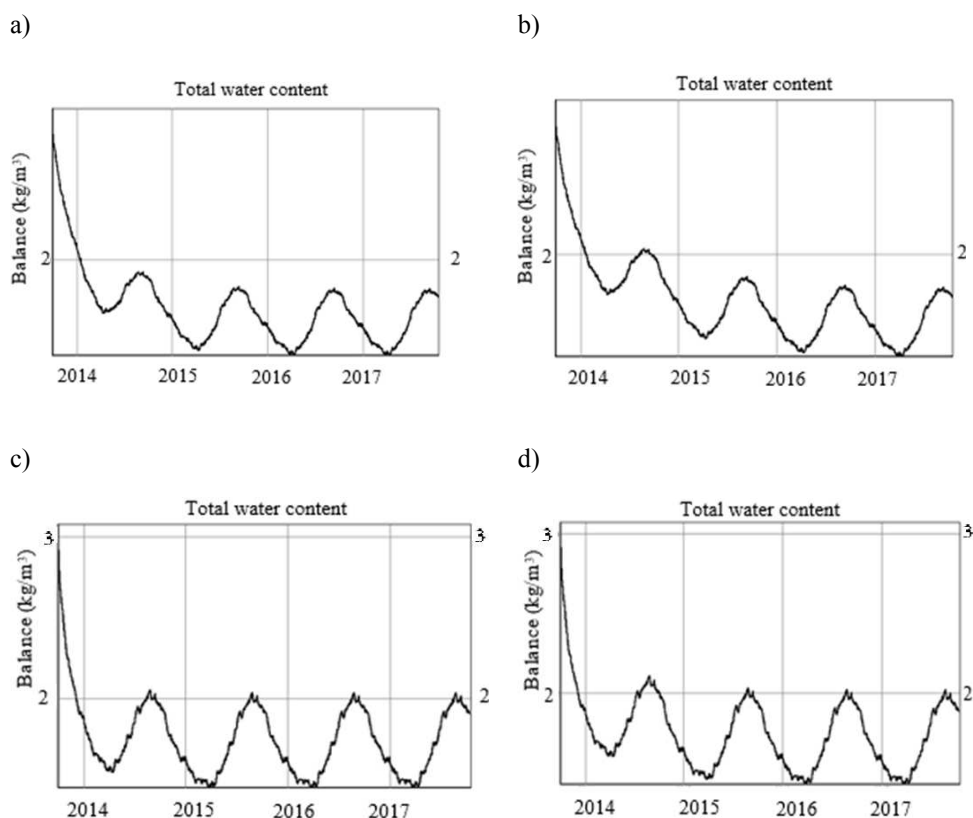


**Fig. 3.6.** Total water content [kg/m<sup>3</sup>] in the analysed wall made using the technology of light steel framing with OSB boards: a) Polystyrene – Intello variant, b) Polystyrene - PE variant, c) Wool - Intello variant, d) Wool – PE variant

Analysis of the individual layers of material (Figs. 3.8 and 3.9) reveals a substantial difference in water content for the boards of sheathing made of OSB boards. For the functional life adopted in the analysis, water content for the OSB design on the internal side ranges from 60 to 75 kg/m<sup>3</sup>. For the same arrangement but using the cement boards, the water content is 15 ÷ 25 kg/m<sup>3</sup>. The disappearing humidity from the initial period is observed for all layers of the material, which confirms the rightness of the adopted solutions (Figs. 3.8 and 3.9).

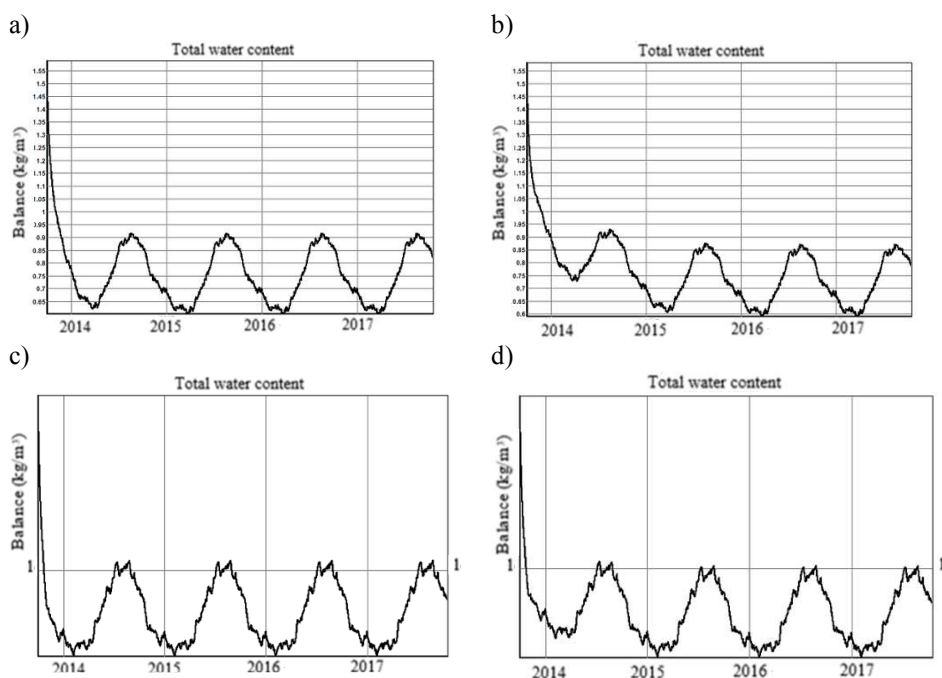


**Fig. 3.7.** Total water content [kg/m<sup>3</sup>] in the analysed wall made using the technology of light steel framing with cement boards: a) Polystyrene – Intello variant, b) Polystyrene - PE variant, c) Wool - Intello variant, d) Wool – PE variant

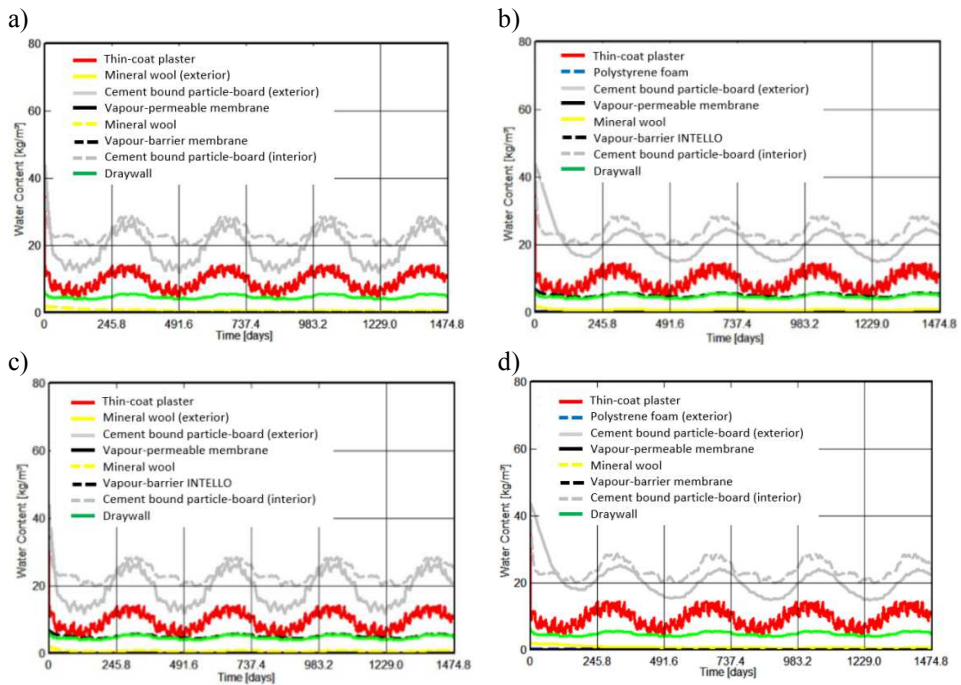


**Fig. 3.8.** Total water content [kg/m<sup>3</sup>] for individual materials in the analysed wall made using the technology of light steel framing with cement boards: a) Wall – PE variant, b) Polystyrene - Intello variant, c) Wool - Intello variant, d) Polystyrene – PE variant

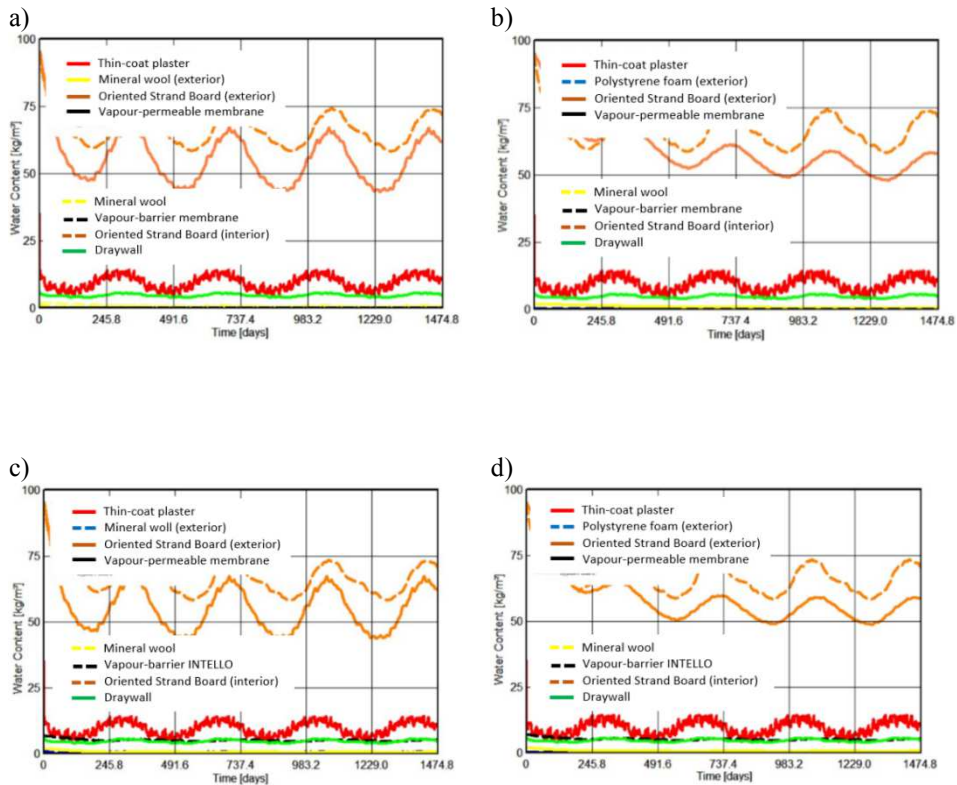


**Fig. 3.9.** Total water content [ $\text{kg/m}^3$ ] for individual materials in the analysed wall made using the technology of light steel framing with OSB boards: a) Wall – PE variant, b) Polystyrene - PE variant, c) Wool - Intello variant, d) Polystyrene – Intello variant

### 3.6 Conclusions

The findings of the study lead to the following conclusions:

- Structures based on the technology of light steel framing made of perforated sections are characterized by improved thermal parameters compared to solid sections. This eventually leads to lower energy consumption and lower heating costs for the building.
- The effect of arrangement and number of holes in the perforated sections on thermal parameters is insignificant

- All the walls analysed in terms of humidity collect greater amount of water in the winter season which is evaporated in summer
- The state of wall humidity is affected by both the type of the material and its arrangement
- Numerical computations provide information about the physical parameters and they allow for a graphical representation of the distribution of these parameters in the wall. With the numerical computation, it is possible to identify, at the design stage, the weak points with highest heat loss, which consequently opens up opportunities for the improvement in the adopted design and material solutions.

## References

- ANSYS Mechanical APDL Thermal Analysis Guide. ANSYS, Inc. Canonsburg, 2013.
- Flodr J., Krejsa M., Mikolasek D., Brozovsky J., Parenica P., Numerical modeling of a thin-walled profile with respect to the redistribution of bending moments, In: Proceedings of the Fifteenth International Conference on Civil, Structural and Environmental Engineering Computing, ed. J. Kruis, Y. Tsompanakis, B.H.V. Topping, Civil-Comp Press, Stirlingshire, UK, 2015 Paper 37.
- Gołaś A., Ryś M., Gajda R., Badanie własności termoizolacyjnych okien z wykorzystaniem metody elementów skończonych, „Modelowanie Inżynierskie” 2011, Vol. 10, no 41, p. 91-98 (in polish).
- Kunzel M. H., Simultaneous heat and moisture transport in Building components, Fraunhofer IRB Verlag Stuttgart 1995.
- Major M., Kosiń M., Modelowanie rozkładu temperatur w przegrodach zewnętrznych wykonanych z użyciem lekkich konstrukcji stalowych, „Budownictwo o zoptymalizowanym potencjale energetycznym” 2016, No 2(18), p. 55-60, (in polish).
- Pawłowski K., Projektowanie przegród zewnętrznych w świetle aktualnych warunków technicznych dotyczących budynków, Grupa Medium, Warszawa 2016, (in polish).
- Pawłowski K., Kosiń M., Numeryczna analiza złącza przegrody zewnętrznej wykonanej w technologii szkieletowej drewnianej i stalowej, „Budownictwo o zoptymalizowanym potencjale energetycznym” 2017, No 1(19), p. 111-120 (in polish).
- PN-EN 12831:2006, Instalacje ogrzewcze w budynkach – Metoda obliczania projektowego obciążenia cieplnego, (in polish).
- PN-EN ISO 13788:2003, Ciepłno – wilgotnościowe właściwości komponentów budowlanych i elementów budynku. Temperatura powierzchni wewnętrznej

- umożliwiająca uniknięcie krytycznej wilgotności powierzchni wewnętrznej kondensacji. Metody obliczania, (in polish).
- PN-EN ISO 6946:2008, Komponenty budowlane i elementy budynku–Opor cieplny i współczynnik przenikania ciepła–Metoda obliczania, (in polish).
- Rozporządzenie w sprawie warunków technicznych jakim powinny odpowiadać budynki i ich usytuowanie, Dz.U. z 2013, poz. 926, (in polish).
- Urbańska-Galewska E., Kowalski D. Zastosowanie lekkich konstrukcji stalowych do renowacji, rozbudowy i remontów obiektów budowlanych, XXIII Ogólnopolska Konferencja, Szczyrk 2008, (in polish).
- Vican J., Sykora M., Numerical analysis of the bridge orthotropic deck time dependent resistance, "Komunikacie" 2013, Vol. 15, Issue 3, p. 112-117.





## 4. Behaviour of high performance concrete in mixed mode loadings: experiments and numerical simulation

**Stanislav Seitl<sup>1</sup>, Petr Miarka<sup>1</sup>, Vlastimil Bílek<sup>2</sup>, Wouter De Corte<sup>3</sup>**

<sup>1</sup> *Brno University of Technology, Faculty of Civil Engineering, Brno, Czech Republic,  
orcid.org/0000-0002-4953-4324, orcid.org/0000-0002-4103-8617*

<sup>2</sup> *VŠB-Technical University of Ostrava, Faculty of Civil Engineering, Ostrava, Czech Republic,  
orcid.org/0000-0001-6433-4892*

<sup>3</sup> *Ghent University, Faculty of Engineering and Architecture  
Department of Structural engineering, Ghent, Belgium*

**Abstract:** The paper presents experimental and numerical results of HP concrete. Brazilian disc test is used in the evaluation of the fracture mechanical parameters.

**Keywords:** high performance concrete, numerical simulation, Brazilian disc

### 4.1. Introduction

The design of concrete structural elements used in civil engineering is optimized to reduce material consumption and to improve structural behavior. Concrete structures such as highway bridges, power plant cooling towers, shell roofs and especially prestressed concrete precast elements constitute important infrastructure and therefore receive increased attention in both design and subsequent maintenance. If well-organized, the use of precast concrete structural elements decreases construction time by two to three times in comparison to the traditional cast-in-place approach (Tomek R. 2017). The main requirement of investors in civil engineering is to extend the structural service life time by repair instead of complete replacement of the structure. The need for repair works is mainly caused by chemical actions of the environment or the long-term actions of load (i.e. creep). The other important global requirement is that the repair and construction must be environmentally friendly. This demand drives the development and use of new and advanced materials with reduced CO<sub>2</sub> consumption. This is also applicable to structures currently under construction and planned for the near future. (de Freitas V.P. 2013).

The prior renovation durability and sustainability of structures made from cementitious materials are often investigated in order to prevent accidents, unnecessary expenses and to get a basic understanding of the material used. To obtain a material sample from renovated structure, a core-drill is used to remove a cylindrical sample from the structure. The concrete samples are submitted for laboratory tests to identify the material's characteristics. The common material characteristics determined through testing the cylindrical specimen are: bulk density, the Young's modulus, the compressive strength, the flexural strength, etc. The design and structural behaviour of the abovementioned structures are, in the most cases, advanced and complex. These structures are not only subject to uniaxial load (tensile load), but very often to a combination of bending and tensile load (mixed mode I/II) conditions. To perform a modern advanced analysis of structural behaviour, knowledge of the material's fracture mechanical parameters is essential.

The advanced structural analysis uses fracture mechanical properties as an input parameter to predict total structural service life time and fracture resistance. The fracture parameters used in the advanced design are fracture toughness  $K_{IC}$  and fracture energy  $G_f$ . The structural elements after certain time can show minor surface damage or shrinkage can create micro-cracks. These defects are zones of weakness, where the crack can initiate. (Karihaloo B.L. 1995).

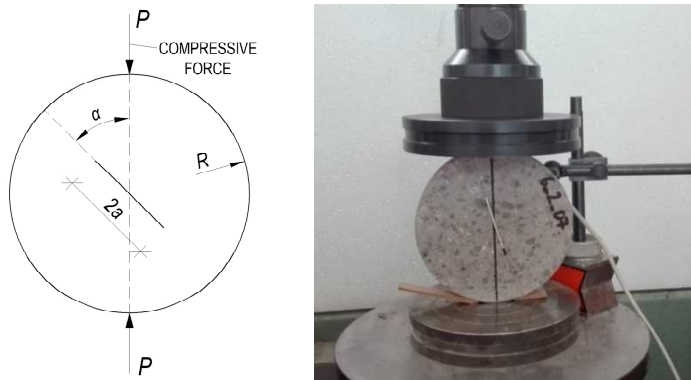


**Fig. 4.1.** Brazilian disc with central notch (left) and experimental setup (right).

The load presence on the structural element can be characterized by tensile mode I and shear mode II. In reality, some cracks are loaded by a combination of tension and shear - mixed mode I/II load. Hence, it is necessary to test material under the mixed mode loading conditions with circular cross section. The Brazilian disc test with a central notch (BDCN) suggests such application.

This contribution evaluates the fracture mechanical parameters of C 50/60 concrete material by the BDCN test specimen and investigates the failure and crack propagation process by employing the concrete damaged plasticity (CDP) material model. The fracture resistance curves were evaluated based on the maximum tangential stress (MTS) criterion (Erdogan F. and Sih G.C. 1963) and generalised maximum tangential stress (GMTS) criterion (Smith D. J. 2001). The MTS and GMTS criteria are commonly used for prediction of onset of fracture under the mode I, mixed mode I/II and mode II load conditions.

## 4.2. Material C 50/60

In this study, the investigated material was a C 50/60 concrete according to EN 206–1 (2005). In order to assess fracture mechanical properties and the FE numerical model, a C 50/60 was chosen because it is a typical material used for the pre-stressed precast elements, which are produced nowadays. C 50/60 shows variety in structural applications because of its high compressive and tensile strength. Usually, concrete with a compressive strength higher than 60 MPa and water to cement ratio lower than 0.42 can be considered as a high-performance concrete (HPC) (Nawy, E.G. 2001).

The mixture contains crushed high-quality granite 4/8 mm and 8/16 mm coarse aggregates and natural sand as a fine aggregate 0/4 mm. The water to cement ratio w/c was 0.4 and a polycarboxylates-based superplasticizer was used to reach good workability. The concrete was mixed in a volume of 1 m<sup>3</sup>, poured into moulds and tested at 28 days. Cone flow was measured 540 mm in accordance with (EN 12350-5 2009) and can be classified as class F4. Table 4.1 gives an overview of the material's mechanical properties.

**Table 4.1.** Overview of the mechanical properties of C 50/60 concrete at 28 days from Seitzl et al. (2018) (mean values and standard deviation)

Young's Modulus $E$ [GPa]	Bulk density $\rho$ [kg/m <sup>3</sup> ]	Compressive cube strength $f_{c\_cube}$ [MPa]	Compressive cylindrical strength $f_{c\_cyl}$ [MPa]	Indirect tensile strength $f_t$ [MPa]
$38.3 \pm 0.3$	$2390 \pm 27.32$	$85.8 \pm 2.9$	$72.8 \pm 2.5$	$5.515 \pm 0.31$

To simulate proper material behaviour a nonlinear material model was used. The input parameters are based on the material stress-strain relation from CEB-FIP (Model Code 2010), which were evaluated from the experiments. To obtain a post peak behaviour (softening branch), damage parameters  $d_c$  for compression and  $d_t$  for tension were used. The maximum value of the tension damage parameter  $d_t$  was 0.99.

The recommendation provides a post peak behaviour in compression as well as in tension. It assumes a linear compressive behaviour up to 40% of the mean compressive strength  $f_{cm}$ , and after this point a quadratic function is used, which can be characterized by eq. 4.1.

$$\frac{\sigma_c}{f_{cm}} = - \left( \frac{k \cdot \eta - \eta^2}{1 + (k-2) \cdot \eta} \right) \text{ for } |\varepsilon_c| < |\varepsilon_{c,lim}| \quad (4.1)$$

where:

- $f_{cm}$  — mean compressive strength,
- $\varepsilon_{c1}$  — compressive strain at maximum compressive stress,
- $\varepsilon_{c,lim}$  — ultimate compressive strain,
- $k$  — the plasticity number,
- $\eta$  —  $\eta = \varepsilon_c / \varepsilon_{c1}$

For a cracked section under tension, a bilinear stress-crack opening relation approach is used. The bilinear response can be characterized by eq. 4.2 and 4.3.

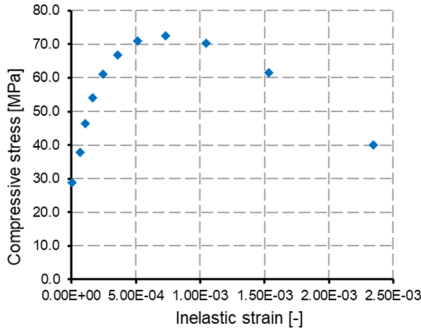
$$\sigma_{ct} = f_{cm} \left( 1 - 0.8 \frac{w}{w_1} \right) \text{ for } w \leq w_1 \quad (4.2)$$

$$\sigma_{ct} = f_{cm} \left( 0.25 - 0.05 \frac{w}{w_1} \right) \text{ for } w_1 < w \leq w_c \quad (4.3)$$

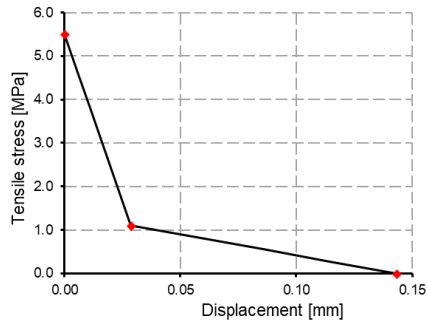
$$w_1 = \frac{G_f}{f_{ctm}} \text{ when } \sigma_t = 0.2 \cdot f_{ctm} ; w_c = \frac{5G_f}{f_{ctm}} \text{ when } \sigma_t = 0 \quad (4.4)$$

where:

- $f_{ctm}$  — tensile strength,
- $w$  — crack opening,
- $\varepsilon_{c,lim}$  — ultimate compressive strain,
- $G_f$  — fracture energy  $G_f = 73 \cdot f_{cm}^{0.18}$ .
- $w_1, w_c$  — limit points by eq. 4.4



(a)



(b)

**Fig. 4.2.** Input parameters for CDP material model - compression (a) and tension (b).

A material with similar mechanical and fracture mechanical properties was tested earlier by Zimmermann, T. and Lehký, D. (2015)

### 4.3. Theoretical Background

This contribution is based on a linear elastic fracture mechanics (LEFM). The LEFM uses for description of the stress field in the vicinity of a crack tip infinite power series, often called as a Williams expansion (Williams, M.L. 1956). The stress field description can be then described by a eq. 4.5.

$$\sigma_{i,j} = \frac{K_I}{\sqrt{2\pi r}} f_{i,j}^I(\theta) + \frac{K_{II}}{\sqrt{2\pi r}} f_{i,j}^{II}(\theta) + T + O_{i,j}(r, \theta), \quad (4.5)$$

where:

- $\sigma_{i,j}$  – stress tensor components,
- $K_I$  – stress intensity factor for mode I,
- $K_{II}$  – stress intensity factor for mode II,
- $f_{i,j}^I(\theta)$  – shape functions for mode I,
- $f_{i,j}^{II}(\theta)$  – shape functions for mode II,
- $T$  – the second independent term on  $r$ ,
- $O_{ij}$  – higher order terms
- $r, \theta$  – polar coordinates (with origin at the crack tip; crack faces lie along the  $x$ -axis)

According to the GMTS criterion (Smith, D.J. *et. al* 2001) the brittle fracture takes place radially from the crack tip and perpendicular to the direction of maximum tangential stress  $\sigma_{\theta\theta}$ . Crack growth initiates, when the  $\sigma_{\theta\theta}$  reaches its maximum (critical value)  $\sigma_{\theta\theta C}$ . The  $\sigma_{\theta\theta C}$  is reached under the crack initiation angle  $\theta_0$  and a critical distance from the crack tip  $r_C$ . Both  $\theta_0$  and  $r_C$  are material constants. The tangential stress  $\sigma_{\theta\theta}$  around the crack tip can be expressed as:

$$\sigma_{\theta\theta} = \frac{1}{\sqrt{2\pi r}} \cos \frac{\theta}{2} \left[ K_I \cos^2 \frac{\theta}{2} - \frac{3}{2} K_{II} \sin \frac{\theta}{2} \right] + T \sin^2 \theta + O(r^{1/2}) \quad (4.6)$$

While the MTS criterion uses only first terms (SIFs), the GMTS uses two terms of Williams expansion (SIFs and  $T$ -stress) in the series for  $\sigma_{\theta\theta}$ . The higher order terms  $O(r^{1/2})$  are often negligible near the crack tip. Singular terms  $K_I$ ,  $K_{II}$  and the  $T$ -stress are considered in the further analysis. According to the first hypothesis of the GMTS criterion, the angle of maximum tangential stress  $\theta_0$  is determined from:

$$\frac{\partial \sigma_{\theta\theta}}{\partial \theta} \big|_{\theta=\theta_0} = 0 \text{ and } \frac{\partial^2 \sigma_{\theta\theta}}{\partial^2 \theta} < 0 \quad (4.7)$$

This assumption leads into the following equation:

$$[K_I \sin \theta_0 + K_{II} (3 \cos \theta_0 - 1)] - \frac{16T}{3} \sqrt{2\pi r_C} \cos \theta_0 \sin \frac{\theta_0}{2} = 0 \quad (4.8)$$

Eq. 4.8 shows that the angle  $\theta_0$  of maximum tangential stress for any combination of modes I and II depends on  $K_I$ ,  $K_{II}$ ,  $T$  and  $r_c$ . The angle  $\theta_0$  determined from eq. 4.8 is then used to predict beginning of the mixed mode fracture. According to GMTS criterion, the brittle fracture occurs when:

$$\sigma_{\theta\theta}(r_c, \theta_0) = \sigma_{\theta\theta,c} \quad (4.9)$$

By substituting the initiation angle  $\theta_0$  from eq. 4.7, one can derive:

$$\sqrt{2\pi r_c} \sigma_{\theta\theta,c} = \cos \frac{\theta_0}{2} \left[ K_I \cos^2 \frac{\theta_0}{2} - \frac{3}{2} K_{II} \sin \theta_0 \right] + \sqrt{2\pi r_c} T \sin^2 \theta_0 \quad (4.10)$$

Eq. 4.6 can be used for calculation of fracture initiation for pure mode I, pure mode II and mixed mode I/II. Pure mode I fracture initiation appears when  $K_I = K_{IC}$ ,

$K_{II} = 0$ . and  $\theta_0 = 0^\circ$ , this assumption simplifies eq. 4.10 to:

$$\sqrt{2\pi r_c} \sigma_{\theta\theta,c} = K_{IC} \quad (4.11)$$

where  $K_{IC}$  is the fracture toughness for mode I. By substituting eq. 4.11 into eq. 4.10 a general equation for mixed mode fracture is obtained.

$$K_{IC} = \cos \frac{\theta_0}{2} \left[ K_I \cos^2 \frac{\theta_0}{2} - \frac{3}{2} K_{II} \sin \theta_0 \right] + \sqrt{2\pi r_c} T \sin^2 \theta_0 \quad (4.12)$$

#### 4.3.1. Application of the GMTS Criterion to BDCN Geometry

Fracture resistance for both modes is expressed by ratio  $K_I/K_{IC}$  and  $K_{II}/K_{IC}$ . This ratio is obtained from eq. 4.12 by dividing whole expression by  $K_I$ ,  $K_{II}$  respectively. Fracture resistance for mode I can be expressed as:

$$\frac{K_{IC}}{K_I} = \cos \frac{\theta_0}{2} \left[ \cos^2 \frac{\theta_0}{2} - \frac{3}{2} \frac{K_{II}}{K_I} \sin \theta_0 \right] + \sqrt{2\pi r_c} \frac{T}{K_I} \sin^2 \theta_0 \quad (4.13)$$

and for mode II:

$$\frac{K_{IC}}{K_{II}} = \cos \frac{\theta_0}{2} \left[ \frac{K_I}{K_{II}} \cos^2 \frac{\theta_0}{2} - \frac{3}{2} \sin \theta_0 \right] + \sqrt{2\pi r_c} \frac{T}{K_{II}} \sin^2 \theta_0 \quad (4.14)$$

From both eq. 4.13 and eq. 4.14 it is noticeable, that the fracture resistance depends not only on the first and second terms of Williams expansion, but also on the critical distance  $r_c$ . Literature shows two different options for the calculation of the  $r_c$  considering various boundary conditions. For plane stress and plane strain boundary condition (Anderson, T.L. 2017) the critical distance can be calculated by eq. 4.15 and eq. 4.12, respectively.

$$r_c = \frac{1}{2\pi} \left( \frac{K_{IC}}{\sigma_t} \right)^2 - \text{plane stress}, \quad (4.15)$$

$$r_c = \frac{1}{6\pi} \left( \frac{K_{IC}}{\sigma_t} \right)^2 - \text{plane strain}. \quad (4.16)$$

The values of the SIFs for a finite specimen with a shape of BDCN and the polar angle  $\theta = 0^\circ$  can be expressed in the following form by eqs. 17 and 18 (Fett, T 2001, Ayatollahi, M.R. and Aliha, M.R.M. 2008, Seitzl et al 2018):

$$K_I = \frac{P\sqrt{a}}{RB\sqrt{\pi}} \frac{1}{\sqrt{1-\frac{a}{R}}} Y_I(a/R, \alpha) \quad (4.17)$$

$$K_{II} = \frac{P\sqrt{a}}{RB\sqrt{\pi}} \frac{1}{\sqrt{1-\frac{a}{R}}} Y_{II}(a/R, \alpha), \quad (4.18)$$

where:

- $P$  – compressive load,
- $a$  – crack length,
- $R$  – radius of the disc ( $D/2$ ),
- $B$  – disc thickness,
- $\alpha$  – initial notch inclination angle,
- $Y_I(a/R, \alpha)$ , – dimensionless shape function for mode I,
- $Y_{II}(a/R, \alpha)$  – dimensionless shape function for mode II.

#### 4.3.2. Numerical Model - Geometry

A numerical simulation was performed using the FE software Abaqus (Abaqus 2016). For this, a two-dimensional (2D) plane stress model was created, and meshed with a 4-node linear element (type CPS4). The basic element size was 1 mm with refinements around the notch tip of 0.25 mm.

The simulated BDC specimen had a radius of  $R = 75$  mm, initial notch lengths  $2a = 40$  mm and  $2a = 60$  mm (the relative crack length  $a/R = 0.26$  and  $0.4$ ), and inclination notch angles  $\alpha$  of  $0^\circ$ ,  $5^\circ$ ,  $10^\circ$ ,  $15^\circ$ ,  $20^\circ$ ,  $25^\circ$  and  $27^\circ$ . The numerical analysis was performed with a displacement controlled loading at the top point of the BDCN specimen. The total induced vertical displacement was  $u_y = -0.1$  mm ( $u_x = 0$  mm) over the pseudo time step. Adequate boundary conditions were added to prevent rigid body translations (See Fig. 4.3).

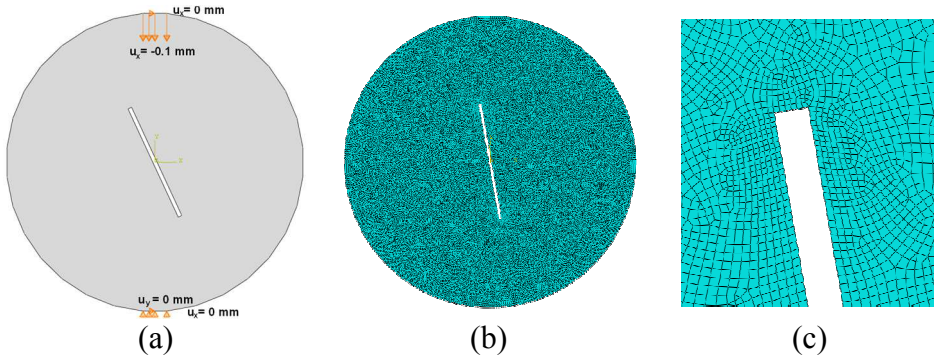


**Fig. 4.3.** Boundary conditions (left) and meshed BDC specimen with detail on the notch tip (right)



#### 4.4.3. Material Model – Concrete Damaged Plasticity

The Concrete Damaged Plasticity (CDP) model was used similar like in Miarka, P. *et. al* (2018a). A brief introduction of the concrete damaged plasticity (CDP) material model, as implemented in (Abaqus 2016), is presented below. The model's yield function was proposed by Lubliner, J. *et. al* (1989) and later modified by Lee and Fenves Lee, J. and Fenves Gregory. L. (1998) to account for the different strength evolution in tension and compression. The yield function in terms of effective stresses has the following form:

$$F = \frac{1}{1-\alpha} (\bar{q} - 3\alpha\bar{p} + \beta(\bar{\varepsilon}^{pl})(\bar{\sigma}_{max}) - \gamma(-\bar{\sigma}_{max})), \quad (4.19)$$

where:

- $\bar{p}$  – hydrostatic pressure,
- $\bar{q}$  – von Misses equivalent effective stress,
- $\bar{\sigma}_{max}$  – maximum principal effective stress,
- $\alpha, \beta$  – constitutive parameters describing the flow of the yield function,
- $\gamma$  – parameter related to the shape of the yield function,
- $Y_I(a/R, \alpha)$  – dimensionless shape function for mode I,
- $Y_{II}(a/R, \alpha)$  – dimensionless shape function for mode II,

Parameters  $\alpha$ ,  $\beta$ , and  $\gamma$  are expressed by eqs. 4.20 to 4.22.

$$\alpha = \frac{(\sigma_{b0}/\sigma_{c0})-1}{2(\sigma_{b0}/\sigma_{c0})-1}; 0 \leq \alpha \leq 0.5, \quad (4.20)$$

$$\beta = \frac{\sigma_c(\varepsilon_c^{pl})}{\sigma_t(\varepsilon_t^{pl})} (1 - \alpha) - (1 + \alpha), \quad (4.21)$$

where:

- $\sigma_{b0}$  – biaxial compressive strength,
- $\sigma_{c0}$  – uniaxial compressive strength,
- $\sigma_c(\varepsilon_c^{pl})$  – effective cohesion stresses for compression,
- $\sigma_t(\varepsilon_t^{pl})$  – the effective cohesion stresses for tension,

The shape of the yield surface is expressed as:

$$\gamma = \frac{3(1-K_c)}{2K_c-1}. \quad (4.22)$$

In this,  $K_c$  is the ratio of the tensile to the compressive meridian and defines the shape of the yield surface in the deviatoric plane in Fig. 4.4 (a). In biaxial compression, where  $\bar{\sigma}_{max} = 0$ , the parameter  $\beta$  is not active, and only the parameter  $\alpha$  is being used. Parameter  $\gamma$  is active when the  $\bar{\sigma}_{max} < 0$ , which occurs in triaxial compression. The concrete damaged plasticity model uses the flow potential function  $G(\sigma)$ , which is a non-associated Drucker–Prager hyperbolic function and is defined by eq. 4.23.

$$G(\sigma) = \sqrt{(\varepsilon\sigma_{t0} \tan \psi)^2 + \bar{q}^2} - \bar{p} \tan \psi, \quad (4.33)$$

where:

- $\varepsilon$  — eccentricity,  
 $\psi$  — dilation angle.

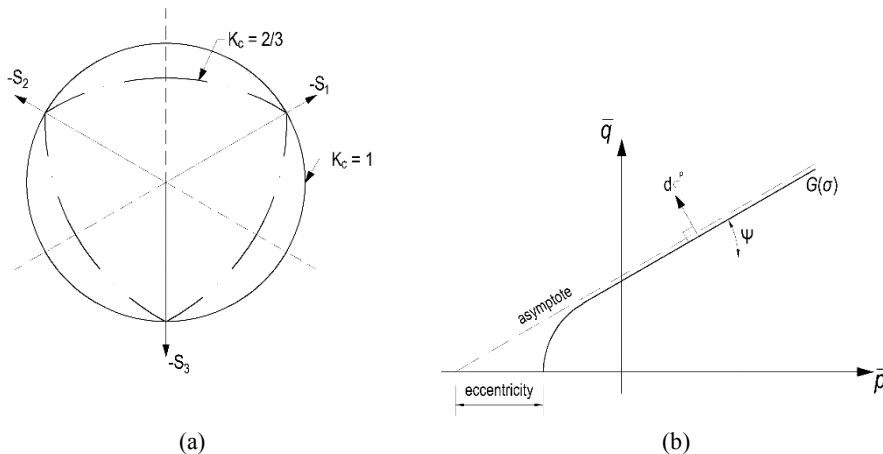


**Fig. 4.4.** Yield surfaces in the deviatory plane ( $K_c = 2/3$  corresponds to the Rankine formulation and 1 to the Drucker–Prager criterion) (a) and schematic of the plastic flow potential with dilation angle  $\psi$  and eccentricity in the meridian plane (b).

The CDP constitutive input parameters, which define the plasticity are shown in Table 4.2. These plasticity parameters were comprehensively studied by Kmiecik, P. And Kamiński, M. (2011) and showed accurate results.

**Table 4.2.** Input constitutive material parameters for CDP model.

Dilatation angle $\psi [^\circ]$	Eccentricity $\varepsilon$ [-]	$\sigma_{b0}/\sigma_{c0}$ [-]	$K_c$ [-]	Viscosity parameter [-]
36	0.1	1.16	0.666	0

The CDP material model assumes that the uniaxial tensile and compressive response of concrete is characterized by damaged plasticity, which is defined by the damage parameter  $d$  and is used in the model according to Eq. (4.6).

$$\sigma = (1 - d)\bar{\sigma} = (1 - d)E_0(\varepsilon - \varepsilon^{pl}), \quad (4.24)$$

The damage parameter  $d$  is defined in terms of compression and tension  $d_c$  and  $d_t$ , respectively by:

$$(1 - d) = (1 - s_t d_c)(1 - s_c d_t), \quad (4.25)$$

where:

- $s_t$  — tensile stiffness recovery,
- $s_c$  — compressive stiffness recovery,

The damage parameters for compression  $d_c$  and tension  $d_t$  can be calculated according to Eq.(4.8) and Eq.(4.9), respectively

$$d_c = 1 - \frac{\sigma_c}{E_o(\varepsilon_c - \varepsilon_c^{pl})}, \quad (4.26)$$

$$d_t = 1 - \frac{\sigma_t}{E_o(\varepsilon_t - \varepsilon_t^{pl})}, \quad (4.27)$$

where:

- $E_o$  — tensile stiffness recovery,
- $\sigma_c$  — compressive stress,
- $\sigma_t$  — tensile stress,
- $\varepsilon_c$  — compressive strain,
- $\varepsilon_t$  — tensile strain,
- $\varepsilon_c^{pl}$  — compressive plastic strain,
- $\varepsilon_t^{pl}$  — tensile plastic strain,

### 3.4. Results and Discussion

An overview of fracture mechanical parameters of C 50/60 material and the numerical results from the FE simulations is given in next sections.

#### 3.4.1. Mechanical - Fracture Properties

In total a series of 19 BDCN specimens were tested with a different  $a/R$  ratios and initial notch inclination angles  $\alpha$ . The machine for tests has a maximum loading capacity 200 kN. The speed of the induced displacement of the upper support was equal to 0.025 mm/s.

A fracture toughness for mode I  $K_{IC}$  was evaluated from the test specimen with  $\alpha = 0^\circ$  for both  $a/R$  ratios. The fracture toughness for mode II  $K_{IIC}$  were measured under the  $\alpha = 27.7^\circ$  and  $\alpha = 25.2^\circ$  for  $a/R = 0.267$  and  $a/R = 0.4$ , respectively. The measured maximum forces for each inclination angle  $\alpha$  and with evaluated stress intensity factors for both modes are presented in table 4.3.

**Table 4.3.** Overview of measured mean values of fracture loads  $P_c$  ( $B=30$  mm), stress intensity factor for mode I  $K_I$  and mode II  $K_{II}$  for relative crack length  $a/R = 0.267$  and  $0.4$ .

$\alpha$ [°]	$a/R$ [-]	Load $P_c$ [kN]	$K_I$ [MPa $m^{1/2}$ ]	$K_{II}$ [MPa $m^{1/2}$ ]
0	0.267	24.34	0.90	-
5		24.92	0.89	0.34
10		24.49	0.78	0.69
15		21.79	0.55	0.94
20		21.13	0.35	1.11
27.7		21.54	-	1.31
0	0.4	18.50	0.97	-
5		16.31	0.81	0.35
10		16.93	0.72	0.70
15		15.98	0.49	0.91
25.2		16.05	-	1.33

Fracture mechanical parameters evaluated from the BDCN test specimens are the fracture toughness for mode I  $K_{IC}$  and  $T$ -stress.

**Table 4.4.** Overview of measured fracture mechanical properties of C 50/60 material for  $a/R = 0.267$  and  $0.4$  (Mean values and standard deviation).

Fracture toughness for mode I - $K_{IC}$ [MPa $m^{1/2}$ ]		$T$ - stress [MPa]	
BDCN ( $a/R = 0.267$ )	BDCN ( $a/R = 0.4$ )	BDCN ( $a/R = 0.267$ )	BDCN ( $a/R = 0.4$ )
$0.903 \pm 0.09$	$0.973 \pm 0.10$	$-13.92 \pm 1.72$	$-12.13 \pm 1.26$

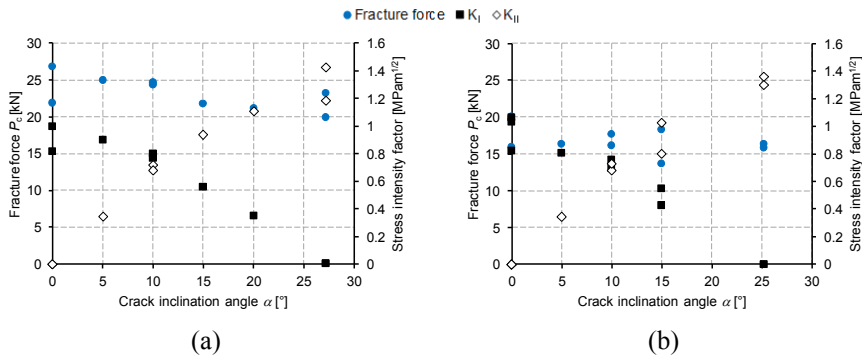


**Fig. 4.5.** Fracture forces and value of SIFs for selected angle  $\alpha$  in case of relative notch length  $a/R=0.267$  (a) and  $a/R=0.4$  (b), respectively

From the knowledge of material fracture toughness and employing the MTS or the GMTS fracture criteria a material's fracture resistance curves can be evaluated. The fracture resistance curve curves evaluated for the C 50/60 concrete are show in Fig. 4.6.

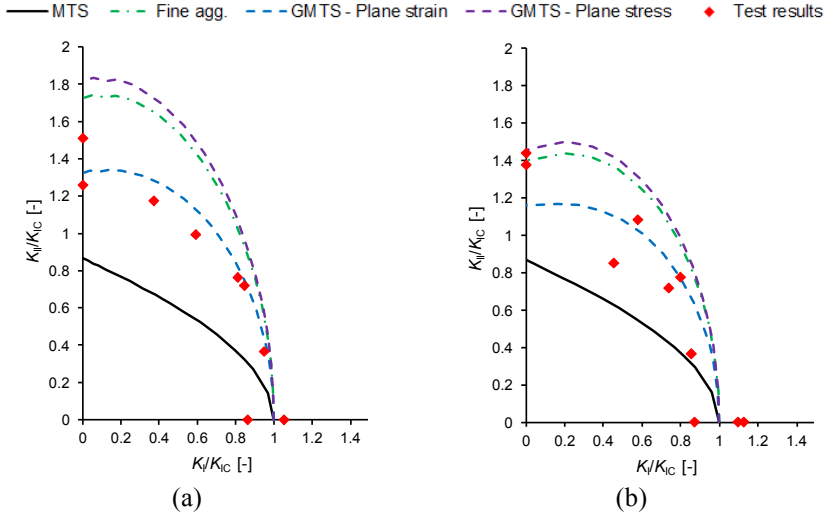


**Fig. 4.6.** Mixed mode I/II fracture resistance curves for C 50/60 for  $a/R = 0.267$  (a) and  $a/R=0.4$  (b).

The comparison of experimental results is done by fracture resistance curve. For each relative crack length,  $a/R$  and critical distance  $r_c$  were calculated resistance curves using eqs. 4.13 and 4.14. From Fig. 4.6, it can be noted, that the MTS criterion is very conservative (Seitl et. al 2018, Miarka et. al 2018). The GMTS criterion predict fracture resistance curves for both cases of  $a/R$  with good agreement especially for plane strain boundary condition for which the value of critical distance is  $r_c = 1.559$  mm. For concrete the value of fracture process zone or ( $r_c$ ) is relatively large in comparison with other engineering materials like polymers and metals, the effect of second term ( $T$ -stress) might not be ignored. For C 50/60 material, the critical distance  $r_c$  is 1.559 mm.

### 3.4.2. Numerical Results

Numerical software Abaqus generates a typical stress and inelastic strain fields for the studied geometry of the BDCN specimen. The inelastic strain represents smeared crack in the studied geometry. Stress and strain fields generated by numerical model give Figs 4.7-4.10 for each point of interest.

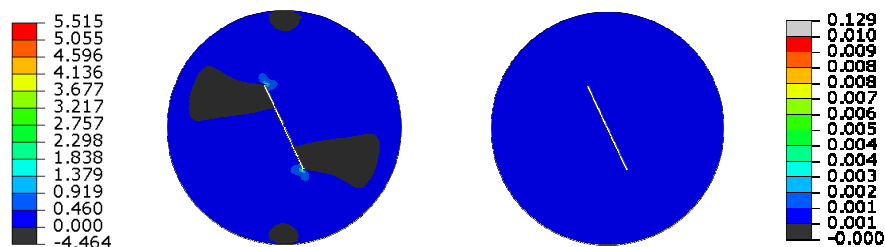


**Fig. 4.7.** Calculated maximum principal stress [MPa] and inelastic strain [-] fields with equivalent vertical compressive load for  $a/R = 0.4$  and  $\alpha = 25^\circ$ ,  $P = 36.2$  N

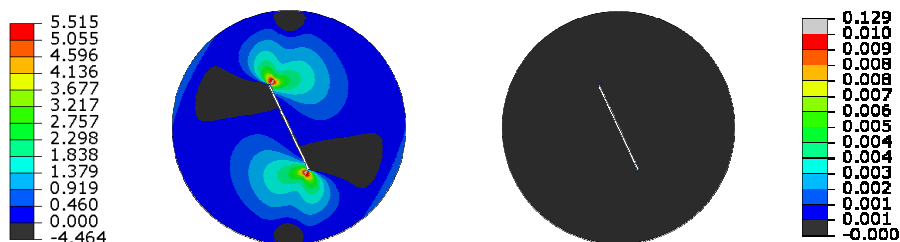


**Fig. 4.8.** Calculated maximum principal stress [MPa] and inelastic strain [-] fields with equivalent vertical compressive load for  $a/R = 0.4$  and  $\alpha = 25^\circ$ ,  $P = 36.2$  N.

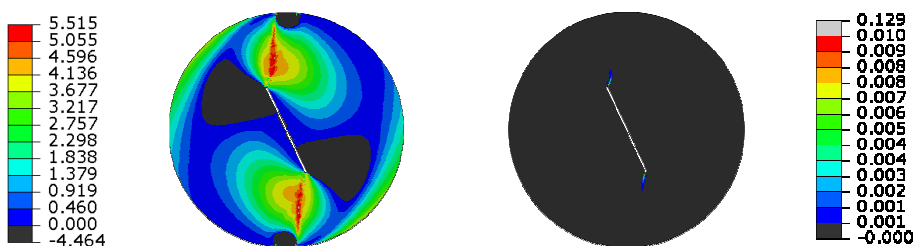


**Fig. 4.9.** Calculated maximum principal stress [MPa] and inelastic strain [-] fields with equivalent vertical compressive load for  $a/R = 0.4$  and  $\alpha = 25^\circ$ ,  $P = 36.2$  N.

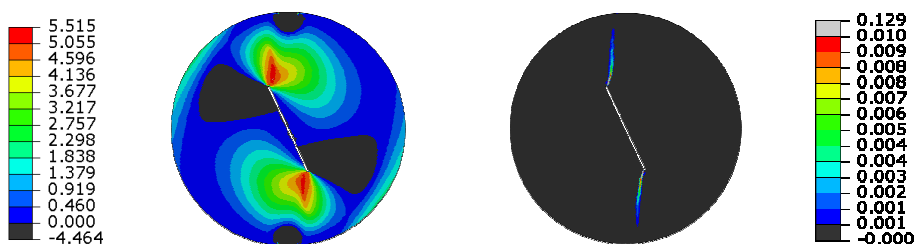


**Fig. 4.10.** Calculated maximum principal stress [MPa] and inelastic strain [-] fields with equivalent vertical compressive load for  $a/R = 0.4$  and  $\alpha = 25^\circ$ ,  $P = 36.2$  N.

**Table 4.5.** Overview of measured and calculated fracture forces for  $a/R = 0.4$ .

$\alpha [^\circ]$	0	5	10	15	25.2
Calculated force [N/mm]	562.85	543.72	540.90	522.54	505.40
Thickness $B$ [mm]	30.92	31.44	30.77	30.97	31.17
Force – Calculated FEA [kN]	17.40	17.10	16.70	16.18	15.80
Force $P_C$ – Experiment [kN]	15.80	19.60	20.00	13.70	15.80

From Table 4.5 it can be noted, that the numerical analysis showed a reasonable agreement (difference up to 20%) for the  $a/R = 0.267$  specimens and a good agreement (difference limited to 7%) for the  $a/R = 0.4$  specimens.

A comparison of measured and calculated maximum forces for various notch inclination angles  $\alpha$  can be found in **Fig. 4.11**.

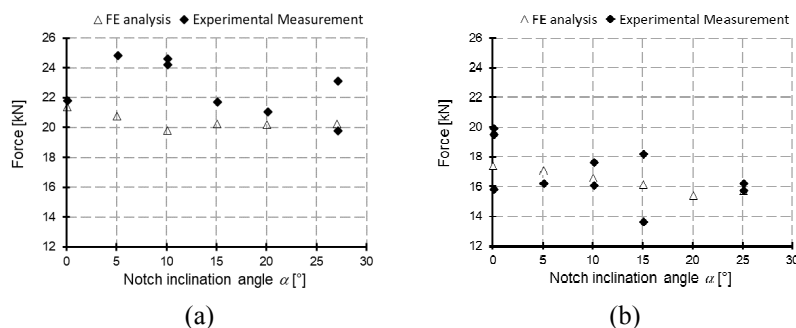


**Fig. 4.11.** A comparison of measured and calculated maximum forces for BDNC made from C 50/60 with thickness  $B \approx 30$  mm: (a)  $a/R = 0.267$  and (b)  $a/R = 0.4$ .

A typical numerical result from the simulation is a Load-displacement diagram, where a reaction load (N per unit width) is plotted against the total vertical displacement.

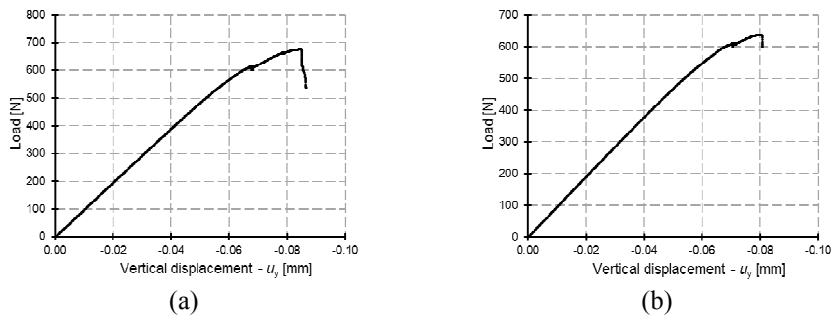


**Fig. 4.12.** Load-displacement diagram for BDNC made from C 50/60 with thickness  $B \approx 30$  mm:  $a/R = 0.267$  and for angle  $\alpha = 0^\circ$  (a) and  $\alpha = 25^\circ$  (b).

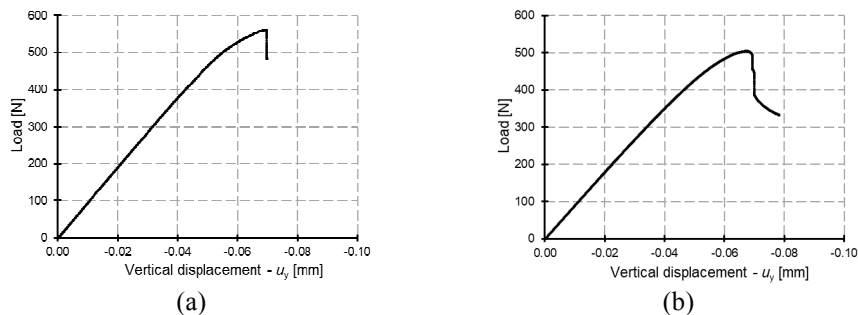


**Fig. 4.13.** Load-displacement diagram for BDNC made from C 50/60 with thickness  $B \approx 30$  mm:  $a/R = 0.4$  and for angle  $\alpha = 0^\circ$  (a) and  $\alpha = 25^\circ$  (b).

### 3.5 Conclusions

The C 50/60 concrete material was analysed in combination of experimental and numerical studies. From experimental campaign the fracture mechanical parameters of C 50/60 were evaluated by using Brazilian disc test specimen with a central notch. Numerical model of the BDCN provides information about failure behaviour of such a test. From the presented results above a following conclusion can be done:

- Fracture resistance curves for mixed mode I/II provide information about onset of fracture and help to predict failure.
- Fit of resistance curves depends on the  $T$ -stress and on critical distance  $r_C$ , which was in C 50/60 calculated for plane strain  $r_C = 1.559$  mm and should not be neglected in the evaluation of the mixed mode fracture resistance.



- The numerical model provides accurate results of the crack pattern in studied BDCN geometry.
- The numerical results of maximum reaction loads give accurate results for used concrete damaged plasticity material model with an error limited to 4% for  $a/R = 0.4$  and 20% for  $a/R = 0.267$ .

## Acknowledgment

This paper has been written with financial support from the projects: FAST-J-18-5164, FAST-S-18-5614 and “National Sustainability Programme I” project “AdMaS UP – Advanced Materials, Structures and Technologies” (No. LO1408) supported by the Ministry of Education, Youth and Sports of the Czech Republic and Brno University of Technology.

The second author is Brno Ph.D. Talent Scholarship Holder – Funded by the Brno City Municipality.

## References

- Abaqus, (2016), ‘Analysis User’s Manual 6.14’, *Dassault Systemes Simulia Corp., Providence*.
- Anderson, T.L. (2017) ‘Fracture mechanics: fundamentals and applications’, *CRC press*.
- Ayatollahi, M.R. and Aliha, M.R.M. (2008) ‘On the use of Brazilian disc specimen for calculating mixed mode I-II fracture toughness of rock materials’, *Engineering Fracture Mechanics*, 75 pp. 4631-4641, doi: 10.1016/j.engfracmech.2008.06.01.
- de Freitas, V. P. *et. al* (2013) ‘Durability of Building Materials and Components’, Springer Berlin Heidelberg.
- Erdogan, F. And Sih, G.C.(1963) ‘On the Crack Extension in Plates Under Plane Loading and Transverse Shear’, *Journal of Basic Engineering*, 85 pp. 519-525, doi: 10.1115/1.3656897.
- Fett, T (2001) ‘Stress intensity factors and T-stress for internally cracked circular disks under various boundary conditions’, *Engineering Fracture Mechanics*, 68 (2001) 1119-1136, doi: 10.1016/S0013-7944(01)00025-X
- Flager, F.L. (2003) ‘The design of building structures for improved life-cycle performance’.
- International Federation for Structural Concrete, (2010), ‘Model Code 2010, First complete draft’, Lausanne, Switzerland.
- Karihaloo, B.L. (1995) ‘Fracture Mechanics and Structural Concrete (Concrete Design and Construction Series)’, *Ed. Longman Scientific & Technical*. United States.

- Kmiecik, P. And Kamiński, M. (2011) 'Modelling of reinforced concrete structures and composite structures with concrete strength degradation taken into consideration', *Archives of Civil and Mechanical Engineering*, 11 pp. 623-636. doi: 10.1016/S1644-9665(12)60105-8.
- Lee, J. and Fenves Gregory. L. (1998) 'Plastic-Damage Model for Cyclic Loading of Concrete Structures', *Journal of Engineering Mechanics*, 124 pp. 892-900. doi: 10.1061/(ASCE)0733-9399(1998)124:8(892)
- Lubliner, J. et. al (1989) 'A plastic-damage model for concrete', *International Journal of Solids and Structures*, 25 pp. 299-326. Doi: 0.1016/0020-7683(89)90050-4.
- Miarka, P. et. al (2018) 'Comparison of Fracture Resistance of the Normal and High Strength Concrete Evaluated by Brazilian Disc Test', *Proceedings* (2), p. 399; doi:10.3390/ICEM18-05236.
- Miarka, P. et. al (2018a) 'Numerical Analysis of the Failure Behavior of a C50/60 Brazilian Disc Test Specimen with a Central Notch'. *Advances in Fracture and Damage Mechanics XVII. Key Engineering Materials*, 774, pp. 570-575. ISBN: 978-3-0357-1350-3. ISSN: 1662-9795, doi: 10.4028/www.scientific.net/KEM.774.570.
- Nawy, E.G. (2001) 'Fundamentals of High-Performance Concrete', Wiley, 2001.
- EN 12350-5 (2009), 'Testing fresh concrete, in: Part 5: Flow table test', *European Committee for Standardization*.
- Seitl, S. et al. (2018) 'The mixed-mode fracture resistance of C 50/60 and its suitability for use in precast elements as determined by the Brazilian disc test and three-point bending specimens', *Theoretical and Applied Fracture mechanics*, 97(3), pp. 108-119, doi: 10.1016/j.tafmec.2018.08.003.
- Tomek, R. (2017) 'Advantages of Precast Concrete in Highway Infrastructure Construction', *Procedia Engineering*, 196, pp. 176–180, doi: 10.1016/j.proeng.2017.07.188.
- Zimmermann, T. and Lehký, D. (2015) 'Fracture parameters of concrete C40/50 and C50/60 determined by experimental testing and numerical simulation via inverse analysis', *International Journal of Fracture*, (192), pp. 179–189, doi: 10.1007/s10704-015-9998-0.
- Williams, M.L. (1956) 'On the Stress Distribution at the Base of a Stationary Crack', *Journal of Applied Mechanics*, 24.
- Smith, D.J. et. al (2001), 'The role of T-stress in brittle fracture for linear elastic materials under mixed-mode loading', *Fatigue & Fracture of Engineering Materials & Structures*, 24 pp. 137-150. doi: 10.1046/j.1460-2695.2001.00377.x.



## 5. Performance and optimization of prestressed beam with respect to shape dimensions

**Tuan Duc Le<sup>1</sup>, Pavlína Matečková<sup>2</sup> and Petr Konečný<sup>3</sup>**

<sup>1</sup> Faculty of Civil Engineering, Saigon Technology University, 180 Cao Lo Str., Ward 4, Dist. 8, HCMC 70000, Vietnam, [orcid.org/0000-0003-3188-6759](https://orcid.org/0000-0003-3188-6759)

<sup>2</sup> Faculty of Civil Engineering, VSB – Technical University of Ostrava, Department of Structural Mechanics, L. Podeste 1875, 708 33 Ostrava-Poruba, Czech Republic, [orcid.org/0000-0002-8049-3153](https://orcid.org/0000-0002-8049-3153)

<sup>3</sup> Faculty of Civil Engineering, VSB – Technical University of Ostrava, Department of Structural Mechanics, L. Podeste 1875, 708 33 Ostrava-Poruba, Czech Republic, [orcid.org/0000-0001-6667-7522](https://orcid.org/0000-0001-6667-7522)

**Abstract:** The chapter deals with the performance and optimization of prestressed concrete beam. A simple probabilistic model aiming at the determination of bending resistance and vertical deflection of a simply supported prestressed concrete T-beam is built. Time dependent behavior of basic properties of concrete such as modulus of elasticity and compressive strength are approximated by suitable curves through data obtained from experiment. Monte Carlo simulation technique is used to take into account of the variation of input parameters. Normal distributions are assumed for random variability of elastic modulus and compressive strength of concrete as well as the change in position of tendons in the beam section. Relaxation loss of tendons is also considered. All procedures for analysis and simulation are composed using Matlab/Octave compatible environment. Bending moment resistance and vertical deflection of the beam are comparatively analyzed via numerical examples. Section of the prestressed concrete T-beam is then optimized with respect to its dimensions.

**Keywords:** beam, bending resistance, deflection, Monte Carlo simulation, prestressed concrete, probabilistic model, random, T-section, variation.

### 5.1. Introduction

Due to its conveniences in comparison with reinforced concrete and other building materials, prestressed concrete has become a popular material in construction for ages. Concept of prestressed concrete structures arose from the need of a concentric or eccentric force imposed in the longitudinal direction of the structural element to prevent crack development at early stages of loading (Nawy, 2009). In addition, the current trend is the improvement of concrete performance and reduction of the cement usage through using progressive high performance materials (Aitcin, 1998, Konecny *et al.*, 2017, Ghosh *et al.*, 2017,

Cajka *et al.*, 2017, Keulenl *et al.*, 2017). The more application of prestressed concrete in construction take place, the more research and study of advanced design methods for this type of structure is expected.

The rapid development of design methods for prestressed concrete structures has taken place during past decades (Nawy, 2009) and the trend is now focusing on the evaluation of capacities of advanced non-linear modelling (Králík and Klabník, 2016, Sucharda *et al.*, 2017). Deterministic and probabilistic theories have been both integrated in current codes and design standards (EN 1992-1-1, 2004, Matthews *et al.*, 2016) even though the first one is usually referencing and following by many engineers. In fact, input parameters governing resistances of prestressed concrete elements often show high variation and fluctuation. As a result, probability-based design approaches (Marek *et al.*, 2003, Melchers, 1999, Stewart and Rosowsky, 1998) for reinforced concrete and prestressed concrete structures are increasingly used nowadays.

Resistance of prestressed concrete beams based on probabilistic method has been recently studied for various purposes. Such a work e.g. (Le *et al.*, 2018) has been carried out to serve for the designing the full scale samples for the laboratory experiments of a simply supported beam with rectangular section. Results from (Le *et al.*, 2018) confirmed experience and expectations that rectangular high performance concrete (HPC) prestressed shape is not effective with respect to concrete utilization. The T-section or I-section beams are more effective comparing to rectangular one and they should be employed to fully utilize the potential of HPC. The calculation of the flexural strength of concrete T-beams was also discussed in many issues of the PCI (Precast Concrete Institute) Journal (Seguirant *et al.*, 2005). The work in (Seguirant *et al.*, 2005) examined the fundamentals of T-beam behavior at nominal flexural strength via a strain compatibility approach using non-linear concrete compressive stress distributions.

In this chapter, the preparation of a simple probability-based model for the bending resistance computation of a simply supported prestressed concrete T-beam is presented. The goal of this development is to prepare numerical codes for evaluation of bending resistance and deflection of the T-beam with respect to section optimization. Available time dependent behavior of basic properties such as compressive strength and elastic modulus of concrete is exploited. Scatter of input parameters is taken into account by using Monte Carlo simulation technique (Anderson, 1999). Random variability of elastic modulus and compressive strength of concrete as well as the change of position of tendons in the beam section is set up with the assumption of normal distributions. The approximation of relaxation loss of tendons is considered. Matlab/Octave compatible environment ([www.mathworks.com](http://www.mathworks.com),

www.octave.org) is adopted to compose procedures for facilitating all the simulations in this research.

## 5.2. Material properties

Time dependent modulus of elasticity and compressive strength are substantial properties governing behavior of prestressed concrete beams. The magnitudes of two properties may be approximated using Eurocode 2 (EN 1992-1-1, 2004), as follows:

$$E_{cm}(t) = (f_{cm}(t)/f_{cm})^{0.3} E_{cm} \quad (5.1)$$

and

$$f_{cm}(t) = \beta_{cc}(t) \cdot f_{cm} \quad (5.2)$$

where:

- $E_{cm}(t)$  – average modulus of elasticity (GPa) of concrete at age  $t$  (days)
- $f_{cm}(t)$  – average strength (MPa) of concrete in compression at age  $t$  (days)
- $E_{cm}$  – mean modulus of elasticity (GPa) of concrete at 28 days
- $f_{cm}$  – mean compressive strength at 28 days
- $\beta_{cc}(t)$  – coefficient depends on the age of the concrete

In this study, however, modulus of elasticity and compressive strength are approximated by suitable curves through data obtained from aging process of concrete sample with strength class of C50/60 from precast concrete production facility. Fig. 5.1 depicts the approximation of elastic modulus of such a sample case on which the magnitude of modulus of elasticity is approximated in a time by regression function, eq. 5.3.

$$E_{c,cyl}(t) = 4.3067 \ln(t) + 23.537 \quad (5.3)$$

where:

- $E_{c,cyl}(t)$  – elastic modulus (GPa) of a reinforced concrete tested sample at age  $t$  (days).

Similarly, approximation of the cylinder compressive strength is carried out based on the same laboratory sample. In this case, content from (Le *et al.*, 2018) is adopted, as shown in Fig. 5.2 and eq. 5.4.

$$f_{c,cyl}(t) = 12.845 \ln(t) + 33.627 \quad (5.4)$$

where:

- $f_{c,cyl}(t)$  – cylindrical strength (MPa) of a reinforced concrete tested sample at age  $t$  (days)

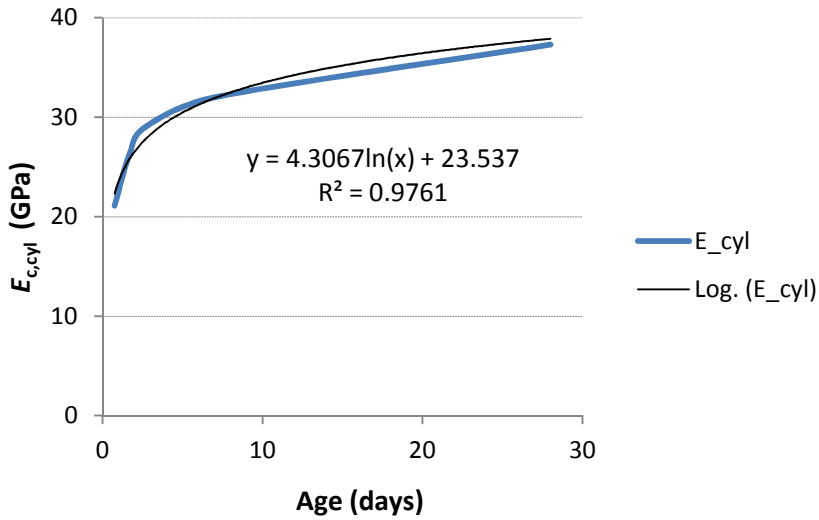


**Fig. 5.1.** Approximation of considered elastic modulus time dependent behavior

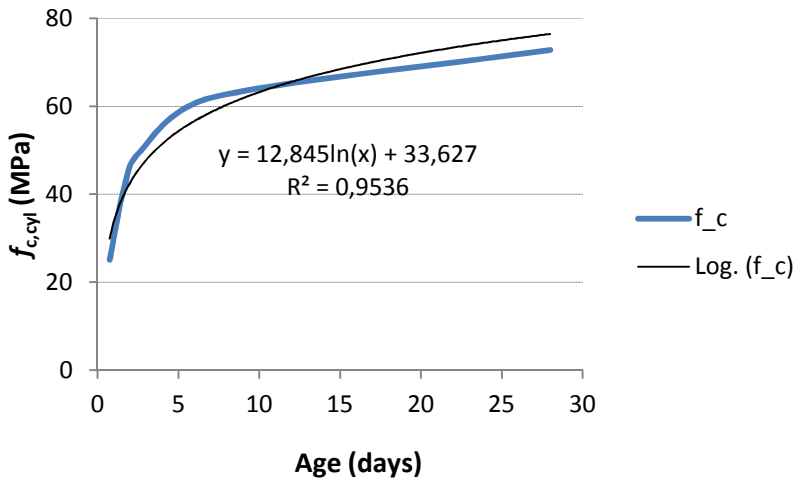


**Fig. 5.2.** Approximation of considered cylinder strength time dependent behavior (Le *et al.*, 2018)

It can be observed from Fig. 5.1 and Fig. 5.2 that the coefficients of determination in both cases are very good,  $R^2 = 0.9761$  and  $R^2 = 0.9536$ , respectively. Therefore, the approximation in eq. 5.3 and eq. 5.4 has good fit.

As above mentioned that a simple probabilistic model is aimed at in this study, the statistic characteristics of probability density functions shall be studied and the variation of elastic modulus is described as follows:

$$E_{c,cyl}(t) = \mu(E_{c,cyl}(t)) + cov(E_{c,cube}(28)) \cdot \mu(E_{c,cyl}(t)) \quad (5.5)$$

where:

$E_{c,cyl}(t)$	–	elastic modulus (GPa) of sample at age $t$ (days)
$\mu(E_{c,cyl}(t))$	–	mean value of elastic modulus of sample at age $t$
$cov(E_{c,cube}(28))$	–	coefficient of variation of elastic modulus of sample, $t = 28$ days

And then variation of concrete strength is:

$$f_{c,cyl}(t) = \mu(f_{c,cyl}(t)) + cov(f_{c,cube}(28)) \cdot \mu(f_{c,cyl}(t)) \quad (5.6)$$

where:

$f_{c,cyl}(t)$	–	cylindrical strength (MPa) of sample at age $t$ (days)
$\mu(f_{c,cyl}(t))$	–	mean value of cylindrical strength of sample at age $t$
$cov(f_{c,cube}(28))$	–	coefficient of variation of cubic strength of sample, $t = 28$ days

### 5.3. Probabilistic modelling of T-beam resistance

#### 5.3.1. Computational model for T-beam.

Without taking into account of reinforcement, ultimate bending moment resistance ( $M_r$ ) of a critical T-section and prestressing tendons of a beam is computed according to 2 cases as follows:

\* Case 1: Height of compression zone is larger than the flange thickness (Fig. 5.3):

$$M_r = F_{c1}(d - 0.4x) + F_{c2}(d - 0.5h_f), \quad (5.7)$$

where:

$F_{c1}$  – compressive forces (kN) in concrete due to the contribution of web,

$F_{c2}$  – compressive forces (kN) in concrete due to the contribution of flange.

They are determined as:

$$F_{c1} = 0.8f_{c,cyl}b_w x, \quad (5.8)$$

$$F_{c2} = 0.8f_{c,cyl}(b - b_w)h_f, \quad (5.9)$$



where:

$d$	–	effective height (m) of considering cross section of the beam
$x$	–	height of compression zone (m), calculated based on the limit strain approach (strain compatibility), as follows:

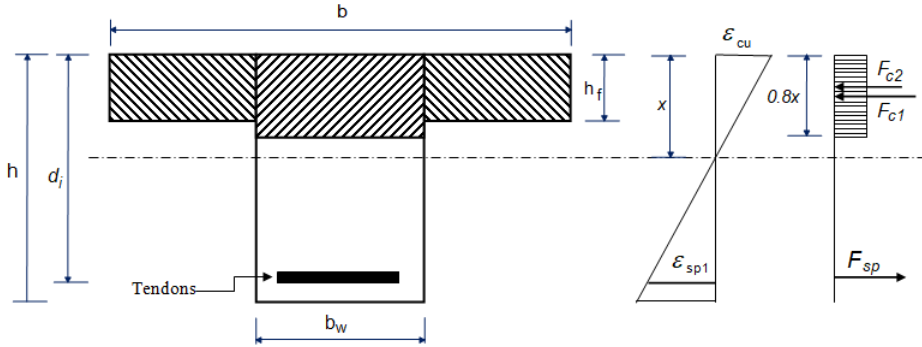


**Fig. 5.3.** Sketch of a cross-sectional T-beam in the computation model

$$x = \frac{F_{sp} - F_{c2}}{0.8 f_{c,cyl} b_w} \quad (5.10)$$

- $b_w$  – thickness (m) of the web of T-beam  
 $b$  – width (m) of the flange of T-beam  
 $h_f$  – thickness (m) of flange of T-beam,  
 $f_{c,cyl}$  – cylinder compressive strength (kPa) of concrete  
 $F_{sp}$  – total prestressing force (kN) in all layers of tendons after relaxation losses, computed as:

$$F_{sp} = \sum N_{xi} A_p \sigma_{pst}, \quad (5.11)$$

where:

- $N_{xi}$  – number of tendons horizontally in layer  $i$   
 $A_p$  – cross-sectional area (m<sup>2</sup>) of prestressing tendon  
 $\sigma_{pst}$  – prestressing stress (kPa) after relaxation losses, determined as:

$$\sigma_{pst} = \sigma_{pmax} \text{ if } t < 72 \text{ hours} \quad (5.12a)$$

$$\sigma_{pst} = \sigma_{pmax} \times 0.85 \text{ if } 72 \text{ hours} \leq t < 500,000 \text{ hours}, \quad (5.12b)$$

$$\sigma_{pst} = \sigma_{pmax} \times 0.85 \times 0.85 \text{ if } t \geq 500,000 \text{ hours}, \quad (5.12c)$$

where:

$\sigma_{pmax}$  – maximum prestressing stress (kPa) of tendons.

\* Case 2: Height of compression zone is smaller than the flange thickness (behaves as rectangular section):

$$M_r = F_c(d - 0.4x), \quad (5.13)$$

where:

$F_c$  – compressive forces (kN) in concrete, calculated as:

$$F_c = 0.8f_{c,cyl}bx \quad (5.14)$$

$x$  – height of compression zone (m), calculated as:

$$x = \frac{F_{sp}}{0.8f_{c,cyl}b} \quad (5.15)$$

Instant deflection at middle of this simply supported beam in the time when the test of ultimate carrying capacity is conducted:

$$w = w_g + w_p + w_F \quad (5.16)$$

where:

$w$  – total deflection (m) at the middle of the beam

$w_g$  – deflection (m) at the middle of the beam due to dead load:

$$w_g = \frac{5}{384} g \frac{l^4}{EI} \quad (5.17)$$

$g$  – dead load (kN/m) due to self weight of the beam,

$$g = 9.81 \times A \times \rho / 1000 \quad (5.18)$$

$A$  – cross-sectional area of T-beam

$\rho$  – unit weight (kg/m<sup>3</sup>) of concrete

$E$  – elastic modulus (kPa) of concrete

$I$  – inertia moment (m<sup>4</sup>) of T-section

$L$  – loading span (m) of the beam

$w_p$  – deflection (m) at the middle of the beam due to prestressing force:

$$w_p = \frac{1}{8} M_p \frac{l^2}{EI}, \quad (5.19)$$

$M_p$  – bending moment (kNm) due to eccentricity of prestressing forces:

$$M_p = -F_{sp} e, \quad (5.20)$$

$E$  – eccentricity (m) of prestressing forces

$w_F$  – deflection (m) at the middle of the beam due to induced moment without prestressing:

$$w_F = \frac{1}{48} F \frac{l^3}{EI}, \quad (5.21)$$

$F$  – ultimate force for bending of the T-beam:

$$F = \frac{4M_r}{l} \quad (5.22)$$

$M_r$  – ultimate bending moment resistance (kNm) given in eq. 5.7 or eq. 5.13.

### 5.3.2. Monte Carlo simulation technique.

Monte Carlo approach is one of the popular simulation techniques allowing obtaining numerical results through a process of repeated random sampling. It uses random sampling and statistical modelling to estimate mathematical functions and mimic the operations of complex systems (Harrison, 2010). It can be considered as the art of approximating an expectation by the sample mean of a function of simulated random variables (Anderson, 1999). It was used in (Le *et al.*, 2018) to consider time dependent variation of carrying capacity of prestressed rectangular beam. Creating the sample, running the model and analyzing the data are the three main steps of this method.

### 5.3.3. Transformation and generation of random variables.

A desired distribution of a parameter can be modeled using the following formula (Fegan and Gustar, 2003):

$$N(\mu, \sigma) = \mu + \sigma \times N(0, 1), \quad (5.23)$$

where:

- $\mu$  – specified mean value
- $\sigma$  – specified standard deviation
- $N(0, 1)$  – represents random numbers from the normalized normal distribution
- $N(\mu, \sigma)$  – represents random numbers from the generated normal distribution

For time dependent parameters, their distribution can be written as:

$$N(\mu, \sigma, t) = \mu(t) + \sigma(t) \times N(0, 1), \quad (5.24)$$

where:

- $N(\mu, \sigma, t)$  – represents time dependent normal distribution from the normalized one at age  $t$ ,
- $\mu(t)$  – specified time dependent mean value at age  $t$  (days)
- $\sigma(t)$  – specified time dependent standard deviation at age  $t$

In addition, desired uniform distribution of a parameter can also be modeled using available commands in Matlab/Octave.

## 5.4. Numerical examples

For illustrative purpose, examples of calculation of resistance and vertical deflection of a prestressed concrete T-beam is presented in this part. Bending resistance and deflection of the beam will also be analyzed with respect to section optimization.

It is a simply supported prestressed concrete T-beam with dimensions of cross section as depicted in Fig. 5.4.

In order to compare results of this analysis with those of (Le *et al.*, 2018), a width of 0.9 m is assigned for the flange and the height of 0.56 m of the beam is selected. The length of the beam is 7 m. There are 3 layers of bottom tendons with 4 wires each. Area of one-wire prestressing tendon is  $A_p = 150 \times 10^{-6} \text{ m}^2$ . Distance between the two layers of tendons is 0.05 m and a 0.08 m concrete cover is assumed. Effect of conventional reinforcement is neglected in this study. Its effect in case of ultimate carrying capacity is limited comparing to prestressing tendons. The cross-sectional bending resistance of the beam will be investigated by implementation of the above set up model in combination with Monte Carlo simulation technique.

To verify the prepared procedure, however, this example is solved by both deterministic and probabilistic methods.

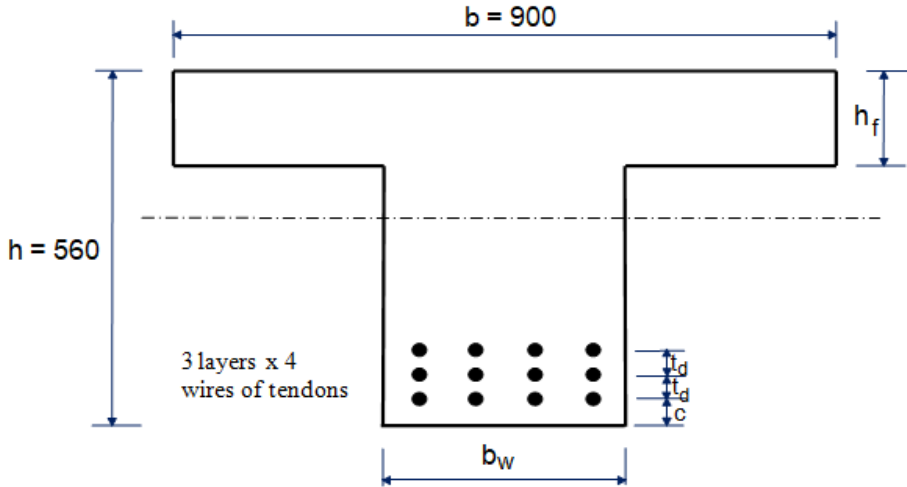


Fig. 5.4. Cross section of considered T-beam

#### 5.4.1. Deterministic solution.

Input parameters for deterministic problem are as follows:

- Geometry:  $h = 0.56 \text{ m}$ ,  $b = 0.9 \text{ m}$ ,  $h_f = 0.18 \text{ m}$ ,  $b_w = 0.31 \text{ m}$ ,  $c = 0.08 \text{ m}$ ,  $t_d = 0.05 \text{ m}$ ,  $d = 0.52 \text{ m}$ ,  $l = 7 \text{ m}$ .

→ Cross-sectional area  $A = 0.2798 \text{ m}^2$  and inertia moment:  $I = 0.0072 \text{ m}^4$ .

- Concrete properties:

- + Unit weight:  $\rho = 2390 \text{ kg/m}^3$ ,
- + Elastic modulus:  $E_c = 26.522 \text{ kPa}$ ,

- + Compressive strength:  $f_{c,cyl} = 42.531$  kPa.
- Prestressing tendons:
  - + Cross-sectional area of one wire of tendon:  $A_p = 150 \times 10^{-6} \text{ m}^2$ ,
  - + 0.1% proof-stress of prestressing steel:  $f_{p01} = 1687 \times 10^3$  kPa,
  - + Maximum prestressing stress of tendon:  $\sigma_{pmax} = 1400 \times 10^3$  kPa.
- Limit strain of concrete and steel:
  - + Maximum strain at the compression fiber of concrete at strength limit state (BS 8110-1, 1997 and EN 1992-1-1, 2004):  $\varepsilon_{cu} = 0.0035$ ,
  - + Limit deformation in steel of prestressed reinforced concrete elements at ULS (EN 1994-1-1, 2004):  $\varepsilon_{ud} = 0.02$ .

Results of the problem with deterministic computation are summarized in Table 5.1. The deflections represent values related to the time of the carrying capacity with the load imposed in the day of testing.

It is important to note that the cross-sectional area ( $A$ ) of T-beam used in the computation is only  $0.2798 \text{ m}^2$ , about 55.52 % of cross-sectional of rectangular beam ( $0.504 \text{ m}^2$ ) studied in (Le *et al.*, 2018).

**Table 5.1.** Results from deterministic analysis of considered T-beam ( $A = 0.2798 \text{ m}^2$ )

Deterministic analysis results with $A = 0.2798 \text{ m}^2$	$t < 3$ days = 72 hours (at $t = 2$ days)	72 hours $\leq t < 500.000$ hours (at $t = 14$ days)	$t \geq 500.000$ hours (at $t = 28$ days)
Bending moment resistance, $M_r$ (kNm)	1,227.4	1,076.1	1,080.5
Vertical deflection, $w$ , at middle of the beam under the ultimate loading (m)	0.0200	0.0135	0.0125

In order to observe the effectiveness of prestressed concrete section type under bending, another cross-sectional T-beam with area of  $0.5018 \text{ m}^2$  ( $h = 1.2 \text{ m}$ ,  $h_f = 0.22 \text{ m}$ ,  $d = 1.12 \text{ m}$ , other dimensions are keep unchanged) is analyzed, i. e. cross-sectional area of T-beam in this study and that of rectangular one in (Le *et al.*, 2018) are almost the same. The results are shown in Table 5.2.

**Table 5.2.** Results from deterministic analysis of considered T-beam ( $A = 0.5018 \text{ m}^2$ )

Deterministic analysis results with $A = 0.5018 \text{ m}^2$	$t < 3$ days = 72 hours (at $t = 2$ days)	72 hours $\leq t < 500.000$ hours (at $t = 14$ days)	$t \geq 500.000$ hours (at $t = 28$ days)
Bending moment resistance, $M_r$ (kNm)	2,739.4	2,361.3	2,365.7
Vertical deflection, $w$ , at middle of the beam under the ultimate loading (m)	0.0047	0.0031	0.0029

Here, we make a comparison of bending moment resistance between T-section in this research and rectangular section in (Le *et al.*, 2018).

Since results of work in (Le *et al.*, 2018) are probabilistic, only mean values of those results will be used to compare as described in Table 5.3. In addition, case of  $t = 14$  days was not studied in (Le *et al.*, 2018). Therefore, case  $t = 2$  days and  $t = 28$  days are compared.

**Table 5.3.** Bending resistance of considered T-section in this study versus bending resistance of rectangular section investigated in (Le *et al.*, 2018)

Age of concrete (days)	Bending moment resistance, $M_r$ (kNm)			Increase (+) / Decrease (-) of $M_r$	
	T-section, $A = 0.2798 \text{ m}^2$ (a)	T-section, $A = 0.5018 \text{ m}^2$ (b)	Rectangular section, $A = 0.504 \text{ m}^2$ (Le <i>et al.</i> , 2018) (c)	(a) vs. (c)	(b) vs. (c)
$t = 2$	1,227.4	2,739.4	1,458.4	- 15.8 %	+ 87.8 %
$t = 28$	1,080.5	2,365.7	1,511.8	- 28.5%	+ 56.5%

It is worth noticing from Table 5.3 that at almost the same cross-sectional area (b and c), bending resistance of the beam can be increased to 87.8 % (at  $t = 2$  days) and 56.5 % (at  $t = 28$  days) if T-section is used instead of rectangular one. It is important to mention that in case of rectangular section (Le *et al.*, 2018), the relaxation losses were not considered. Thus the bending resistance increases due to the increase of concrete strength over the time. Furthermore, even though the cross-sectional area is reduced 44.48 % in comparison with rectangular section, the bending moment resistance of the T-beam decreases only 15.8 % and 28.5 % at  $t = 2$  days and  $t = 28$  days, respectively. It is likely that the

reduction in bending resistance of T-beam in this study is partly caused by relaxation losses (15 % since 3 days and 22.5 % after 500,000 hours). Therefore, it is confirmed that T-section is a better choice than rectangular section for prestressed precast concrete beam with respect to bending. Resulted maximum deflection at the middle of the beam under ultimate loading via deterministic method is 0.020 m, equals to allowable deflection of the beam,  $w_{lim} = 1/350$  of beam span = 7 m/350 = 0.020 m (ACI 318-08, 2008).

#### 5.4.2. Probabilistic solution.

**Table 5.4.** Information on input parameters employed in the probabilistic study

Parameter	Notation	Mean	Coefficient of variation	Transformation
Elastic modulus of concrete (kPa)	$E_{c,cyl}(t)$	eq. 5.1	0.0388	$\mu(E_{c,cyl}(t)) + 0.0388 \times N(0,1)$
Concrete strength (kPa)	$f_{c,cyl}(t)$	eq. 5.2	0.0388	$\mu(f_{c,cyl}(t)) + 0.0388 \times N(0,1)^{(*)}$
Effective height of the beam (m)	$d$	0.52	0.0096	$d = 0.52 + 0.005 \times N(0,1)$
Thickness of the web (m)	$b_w$	0.31	-	-
Thickness of the flange (m)	$h_f$	0.18	-	-
Loading span (m)	$l$	6.85	-	-
Width of flange of the considered beam (m)	$b$	0.9	-	-
Height of cross section of the beam (m)	$h$	0.56	-	-
Cross-sectional area of prestressing tendons (m <sup>2</sup> )	$A_p$	$150 \times 10^{-6}$	-	-
0.1% proof-stress of prestressing steel (kPa)	$f_{p01}$	$1687 \times 10^3$	-	-
Thickness of concrete covered layer (m)	$c$	0.08	-	-

(\*): Please be noted that  $E_{c,cyl}(t)$  and  $f_{c,cyl}(t)$  are considered as uncorrelated parameters here.

Input parameters for probability-based analysis are presented in Table 5.4. Eq. 5.23 is used to build up histograms of elastic modulus, cylinder compressive strength of concrete and effective height of considered cross section of the T-beam. Ultimate bending moment resistance of the critical T-section is computed by eq. 5.7 or eq. 5.13.

In this study, effect of conventional reinforcement is neglected as mentioned above. So, the resistance is provided by concrete and prestressed tendons. Fig.

5.5 displays the distribution of bending moment resistance of the cross section of the T-beam at different ages of concrete.

It is remarkable from the figure that bending moment resistance of the cross section at different ages of concrete follow normal distributions and these distributions are not the same with concrete aging. This result is quite similar to that of (Le *et al.*, 2018).

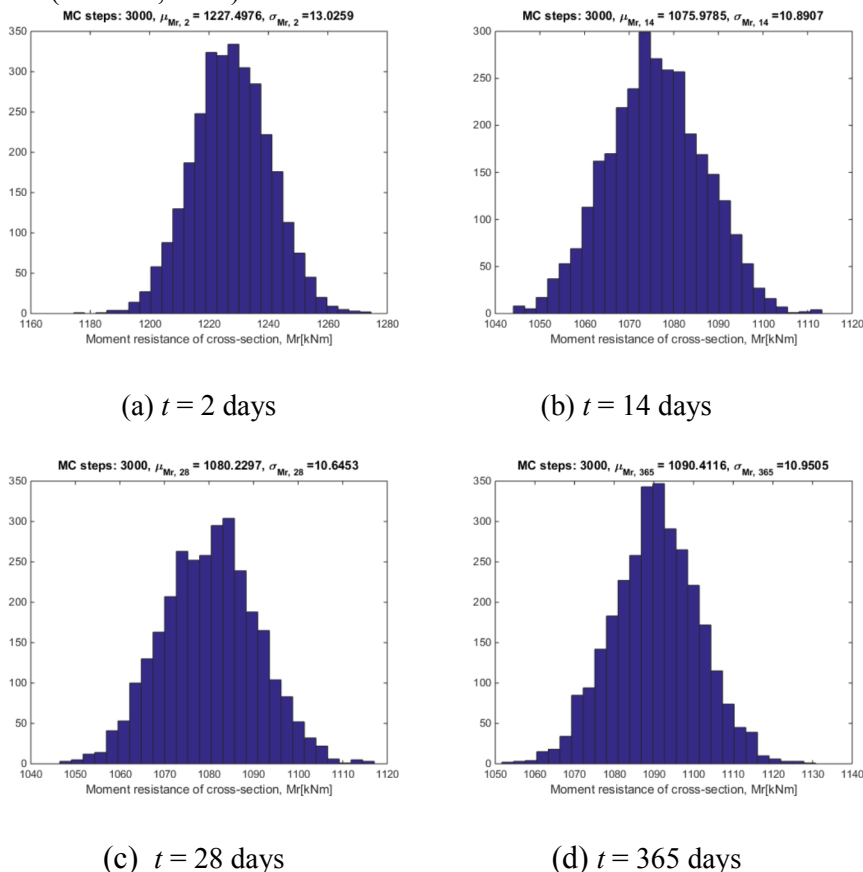


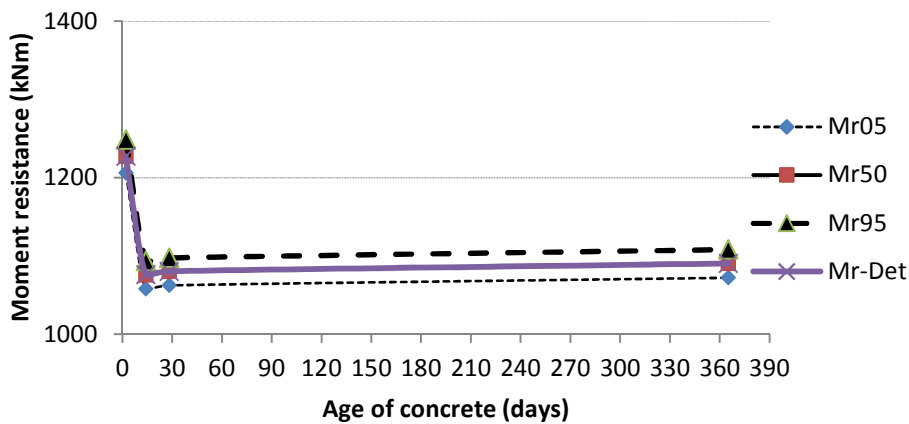
**Fig. 5.5.** Distribution of bending moment resistance of the cross section of the T-beam

Simulation results on bending moment resistance of cross section of the T-beam and their confidence bounds are summarized in Table 5.5 and illustrated in Fig. 5.6 together with results from deterministic solution, marked as  $Mr_{\text{Det}}$  in the figure.



**Table 5.5.** Simulation results on bending moment resistance of cross section of the T-beam

Age of concrete $t$ (days)	Bending moment resistance of the cross section of the T-beam (kNm)			
	$M_{r05}$ (5%)	$M_{r50}$ (50%)	$M_{r95}$ (95%)	Deterministic analysis
2	1,206.072	1,227.498	1,248.923	1,227.4
14	1,058.065	1,075.979	1,093.892	1,076.1
28	1,062.720	1,080.230	1,097.740	1,080.5
365	1,072.400	1,090.412	1,108.424	1,090.5

**Fig. 5.6.** Bending moment resistance of the cross section of the T-beam

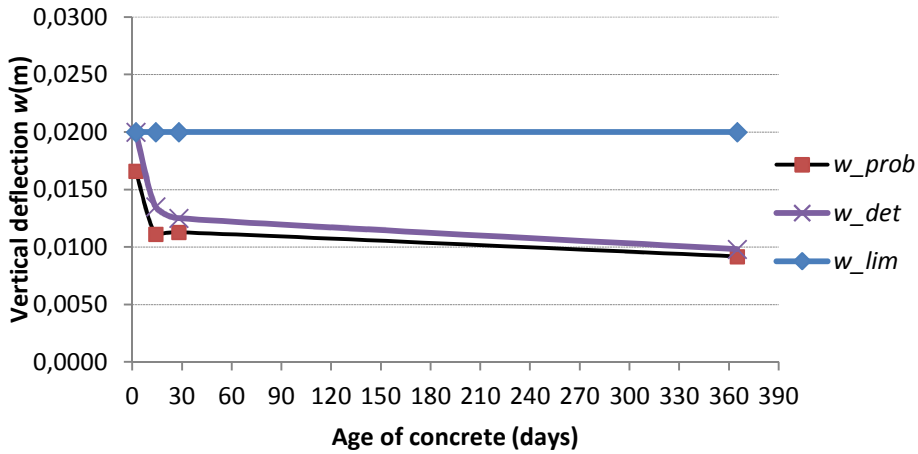
It can be seen from Table 5.5 and Fig. 5.6 that values of bending resistance from deterministic calculation are almost the same with mean values resulted from probabilistic simulations. This means that the built up probabilistic model works well.

Fig. 5.6 also displays that moment resistance of the T-section sharply decreases in the first two weeks before gradually increasing from the 3<sup>rd</sup> week onwards. The drop trend in this duration is inversed in compare with that of (Le *et al.*, 2018). This can be explained by the fact that relaxation losses were not taken into account in (Le *et al.*, 2018). In addition, it can be observed from Fig. 5.6 that the variation of bending resistance is insignificant, around of  $\pm 2$  percent.

In the mean time, results on vertical deflection ( $w_{prob}$ ) at middle of the beam are shown in Table 5.6 and Fig. 5.7 together with those of deterministic computation and maximum allowable vertical deflection specified by design code ( $w_{lim}$ ).

**Table 5.6.** Results on vertical deflection of the T-beam

Age of concrete $t$ (days)	Vertical deflection (m) at the middle of the T-beam	
	Probabilistic solution (maximum value)	Deterministic solution
2	0.0166	0.0200
14	0.0111	0.0135
28	0.0113	0.0125
365	0.0092	0.0098

**Fig. 5.7.** Vertical deflection at middle of the T-beam

It can be observed from Table 5.6 and Fig. 5.7 that deterministic calculation produces higher values of deflection than probabilistic analysis does. It needs to be underlined also that the differences in values of deflection resulted from between the two methods are small and these are almost negligible. Fig. 5.7 also showed that vertical deflection of considered T-beam is still in allowable limit because the two curves  $w_{prob}$  and  $w_{det}$  locate beneath the curve  $w_{lim}$ .

### 5.4.3. Section optimization.

Through above deterministic computation and probabilistic simulations of considering T-beam, the set up probability-based model has been verified. It can be developed more in order to apply for section optimization.

Continuing this numerical example, resistance of the cross section will be investigated on the basis of variation of flange thickness ( $h_f$ ) and web thickness ( $b_w$ ). Uniform distribution of these two parameters is given in range for the

optimization. However, to have practical dimensions of cross section of the T-beam, minor revision of these two parameters' range of variation was made to generate values from the uniform distribution on the reasonable intervals. Thickness of the web is allowed to vary from 0.286 m to 0.610 m to meet requirement of minimum clear spacing between pre-tensioned tendons (EN 1992-1-1, 2004) while thickness of the flange fluctuates from 0.14 m to 0.36 m. Width of the flange and height of the beam are kept unchanged. Partial results on section optimization are summarized in Tables 5.7, 5.8 and 5.9.

**Table 5.7.** Partial simulation results on section optimization of considered T-beam at  $t = 2$  days

Age of concrete, $t$ (days)	Maximum resistance, $max\_Mr = 1271.0$ kNm		Minimum vertical deflection, $min\_w = 1.095 \times 10^{-7}$ m		Maximum vertical deflection, $max\_w = 0.127$ m	
	$b_w$ (m)	$h_f$ (m)	$b_w$ (m)	$h_f$ (m)	$b_w$ (m)	$h_f$ (m)
2	0.408	0.242	0.406	0.257	0.334	0.243

**Table 5.8.** Partial simulation results on section optimization of considered T-beam at  $t = 14$  days

Age of concrete, $t$ (days)	Maximum resistance, $max\_Mr = 1113.1$ kNm		Minimum vertical deflection, $min\_w = 6.653 \times 10^{-8}$ m		Maximum vertical deflection, $max\_w = 0.096$ m	
	$b_w$ (m)	$h_f$ (m)	$b_w$ (m)	$h_f$ (m)	$b_w$ (m)	$h_f$ (m)
14	0.582	0.228	0.561	0.164	0.452	0.296

**Table 5.9.** Partial simulation results on section optimization of considered T-beam at  $t = 28$  days

Age of concrete, $t$ (days)	Maximum resistance, $max\_Mr = 1122.3$ kNm		Minimum vertical deflection, $min\_w = 6.641 \times 10^{-8}$ m		Maximum vertical deflection, $max\_w = 0.080$ m	
	$b_w$ (m)	$h_f$ (m)	$b_w$ (m)	$h_f$ (m)	$b_w$ (m)	$h_f$ (m)
28	0.396	0.220	0.501	0.358	0.415	0.326

In order to observe how the geometry of the T-section is at maximum bending resistance, their visual relations could be captured in figures. For instance, Fig. 5.8 describes relation between geometry of the section and its bending moment resistance in case of time  $t = 28$  days.

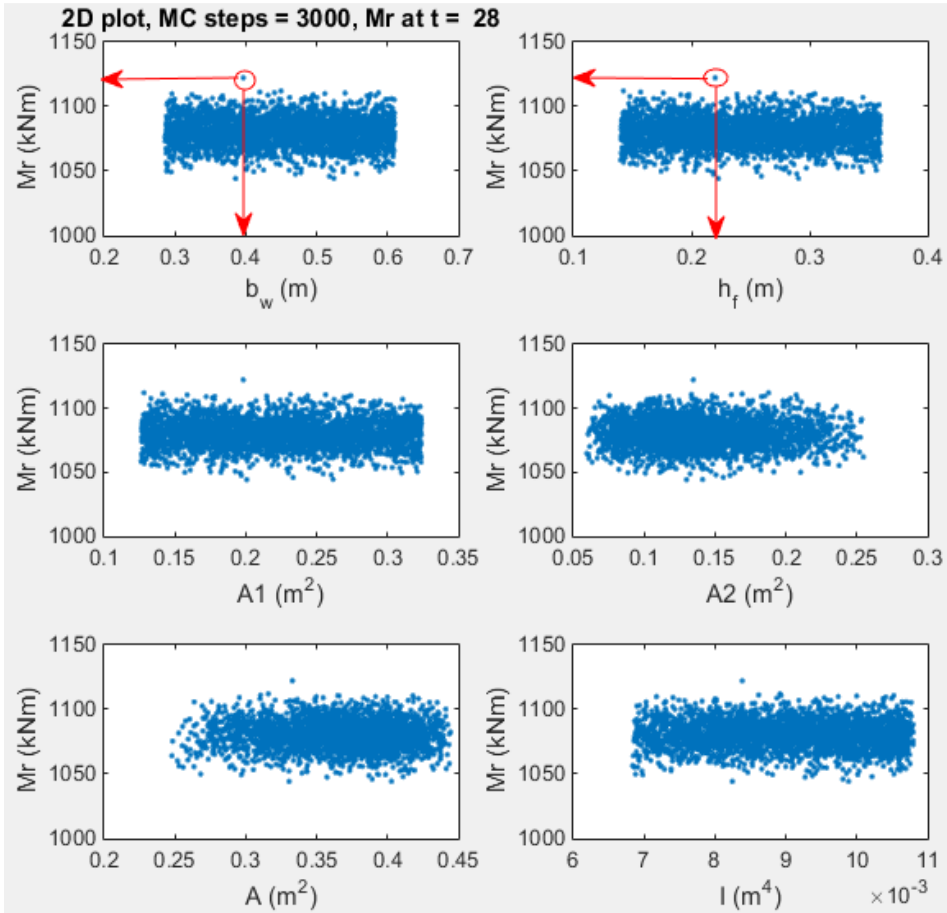


**Fig. 5.8.** Relations between bending resistance and geometry of the T-section at  $t = 28$  days

From Fig. 5.8, it is possible to find out web thickness and flange thickness in accordance with maximum bending resistance of the T-section at specific age of concrete of 28 days. Red ellipses and arrows on this figure illustrate the way to pick up specific dimensions of optimal section with respect to maximum bending resistance of the T-beam. Other parameters of section such as area of the flange ( $A_1$ ), area of the web ( $A_2$ ), total cross sectional area ( $A$ ) and inertia moment ( $I$ ) when bending resistance reaches maximum value can also be picked up in the same way. Similarly, relations between vertical deflections and geometry of the T-section can be intuitively depicted in figures. Fig. 5.9, for example, displays the relation between geometry of the section and its vertical deflections in case of time  $t = 28$  days.

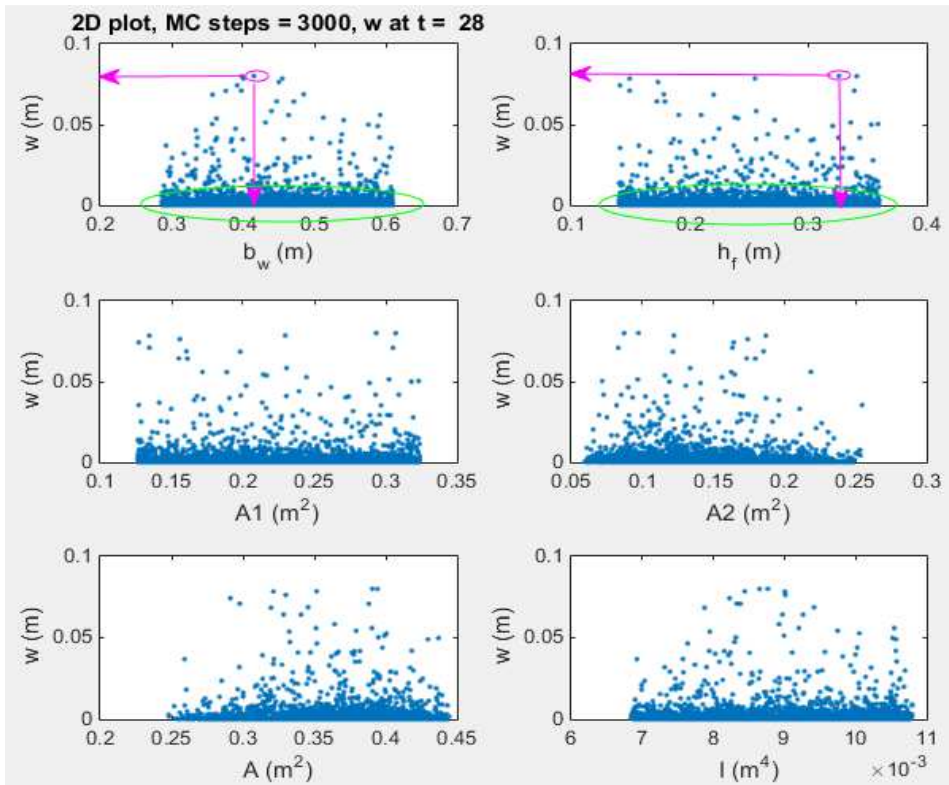


**Fig. 5.9.** Relations between vertical deflections and geometry of the T-section at  $t = 28$  days

In the case of maximum vertical deflection is targeted, intuitive observation of accordingly geometry dimensions of the section is quite easy based on Fig. 5.9 (marked pink ellipses and arrows).

However, if minimum of vertical deflection of the T-section is aimed, visual identification of accordingly geometry dimensions becomes difficult. As marked by large green ellipses in Fig. 5.9, there are a wide range of web thickness and flange thickness values at very low vertical deflections. In these situations, picking up specific values of these dimensions should be done directly with results in numerals from the built up code as summarized in above Tables 5.7, 5.8 and 5.9. Identification of other geometry parameters of the T-section could also be carried out in the same ways.

Meanwhile, general interaction between bending resistances of the T-section and its vertical deflections are displayed in Fig. 5.10 in case of time  $t = 28$  days, as illustrative purpose.

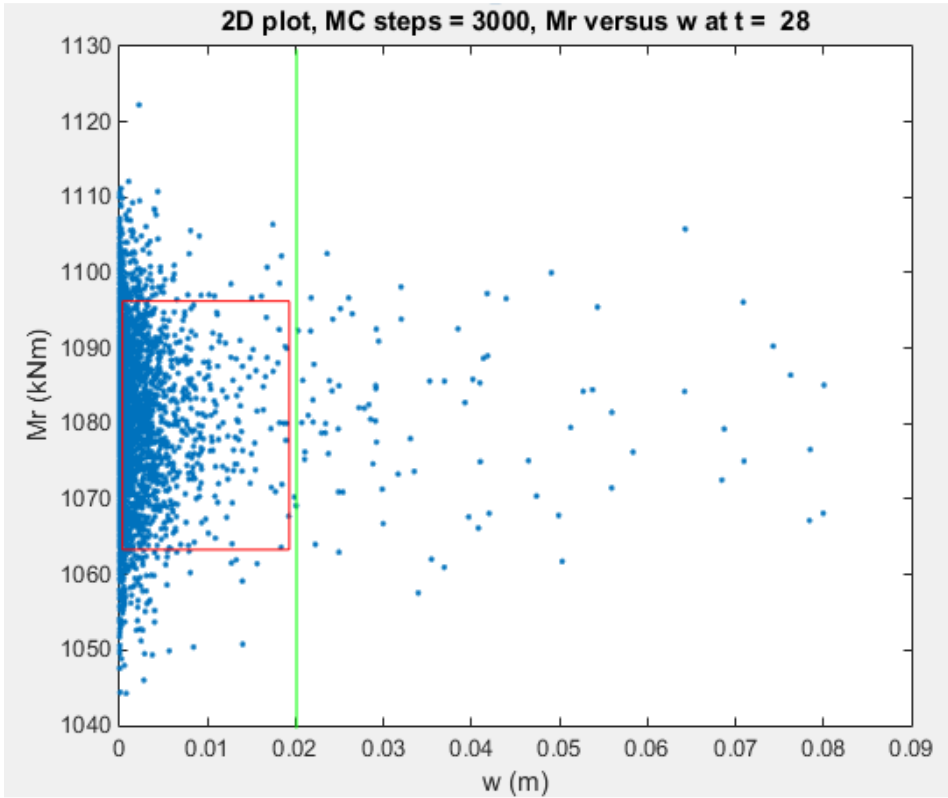


**Fig. 5.10.** Interaction between resistance and vertical deflections of the T-section at  $t = 28$  days

It is remarkable from Fig. 5.10 that the bending resistance of considering T-section has normal distribution. This is consistent with results described in Fig. 5.5. In the relationship with vertical deflection of the section, the zone of mean value spectrum of bending resistance (marked by red rectangle in Fig. 5.10) locates on the left hand side of the limit line of allowable maximum vertical deflection in this example (marked as green line).

To obtain overall results of section optimization, another procedure is composed with 2 conditions: (i) vertical deflection ( $w$ ) of the cross section is always smaller than maximum allowable vertical deflection ( $w_{lim}$ ); (ii) bending moment resistance of the cross-sectional T-beam ( $M_r$ ) is larger than minimum value of bending moment resistance of the beam at concrete age of 28 days.

**Table 5.10.** Overall simulation results on section optimization of considered T-beam at  $t = 28$  days (10 options of best scores)

Option No.	Vertical deflection			Bending resistance			Area of cross section			Score (%)
	$w$ (m)	Percentage of the best (%)	weight	$M_r$ (kNm)	Percentage of the best (%)	weight	$A$ (m <sup>2</sup> )	Percentage of the best (%)	weight	
1	$7.6 \times 10^{-6}$	93	0.3	1098.8	95	0.2	0.2743	97	0.5	95.4
2	$1.3 \times 10^{-6}$	97	0.3	1100.9	96	0.2	0.2897	94	0.5	95.3
3	$1.2 \times 10^{-7}$	99	0.3	1101.5	97	0.2	0.3016	90	0.5	94.1
4	$7.8 \times 10^{-7}$	98	0.3	1095.3	90	0.2	0.2940	93	0.5	93.9
5	$2.9 \times 10^{-6}$	96	0.3	1090.6	81	0.2	0.2877	95	0.5	92.5
6	$8.1 \times 10^{-6}$	93	0.3	1086.9	71	0.2	0.2593	99	0.5	91.6
7	$8.6 \times 10^{-6}$	93	0.3	1092.6	85	0.2	0.2933	93	0.5	91.4
8	$6.4 \times 10^{-5}$	81	0.3	1092.8	86	0.2	0.2532	99	0.5	91.0
9	$6.3 \times 10^{-5}$	81	0.3	1100.1	96	0.2	0.2810	95	0.5	91.0
10	$1.1 \times 10^{-6}$	97	0.3	1098.4	94	0.2	0.3110	86	0.5	90.9

However, the considered problem has many parameters changing with geometry such as deflection and resistance. In addition, results of optimization process strongly depend on its target. Therefore, determination of target for the optimization problem is significantly important. In this example, weight function has been used to make decision of optimal geometry. An example of results presented in Table 5.10 on which weights of deflection, bending moment resistance and cross-sectional area of the T-beam are 30%, 20% and 50%, respectively. The weight factor of 50% reveals that reducing volume of concrete is aimed at in this study.

Table 5.10 is considered as a tool to suggest the best option for section optimization of the T-beam based on the best overall score with specified weight function. Only 10 best options (descendent order) were shown for

illustrative purpose. In case of option number 1 (the best score among 10 options in Table 5.10) is selected, for instance, the corresponding dimensions of T-beam are  $b_w = 0.3079$  m,  $h_f = 0.1721$  m.

If weight function is changed to meet new targets of optimal problem, values in the last column of Table 5.10 would be changed and hence new decision would be made.

## **5.5. Conclusions**

The model used for the analysis of behavior of prestressed precast beam may be used for preliminary analysis of bending resistance with respect to preparation of full scale testing at laboratory conditions. Also important part is shape parameters' optimization capability via application of simple Monte Carlo based technique and weight function.

Computation of bending resistance and vertical deflection over the time of a prestressed precast concrete T-beam was done through a new built simple probabilistic model. Randomness of input parameters such as elastic modulus and compressive strength of concrete as well as position of tendons in the section was taken into account with assumption of normal distributions. The performance of the T-beam under prestressing was studied via numerical examples by application of Monte Carlo simulation technique. Dimensions of T-section of the beam in the example were also optimized targeted at minimum cross-sectional area, maximum bending resistance and best performance of vertical deflections.

As expected, results of the study confirmed that T-section is a better choice in comparison with rectangular one for prestressed precast concrete beam in bending resistance. In this study, for example, with almost the same cross-sectional area, bending resistance of the T-beam was about 187.8 % (at  $t = 2$  days) and 156.5 % (at  $t = 28$  days) of that of the rectangular one.

Investigation of vertical deflection of the considered T-beam shown that under conditions in the example, vertical deflection of the beam is still in allowable limit. Therefore, selected dimensions of the section are suitable enough for performance of the beam in such a case.

Optimization results proved their consistence and coherence with those of bending resistance computation part. So, the built procedure for section optimization seems to be applicable for prestressed precast concrete T-beam.

The current study deals only with prestressing tendons from bottom part of the section. In addition, influences of conventional reinforcement to performance of the T-beam were not considered. Furthermore, shear resistance and cracking



were not also been studied yet. This work, therefore, should be further developed with taking into account of tendons in the top part of the section and longitudinal reinforcement. Impacts of shear resistance and cracking would be expected expansion of the topic.

## References

- ACI 318-08 (2008) 'Building Code Requirements for Structural Concrete and Commentary', *American Concrete Institute*, 38800 Country Club Drive Farmington Hills, MI 48331, ISBN 978-0-87031-264-9.
- Aitcin, P. C. (1998) 'High performance concrete', *Taylor & Francis*, ISBN-10: 0419192700, ISBN-13: 978-0419192701.
- Anderson, E. C. (1999) 'Monte Carlo methods and importance sampling - Lecture notes for Stat 578C', *Statistical Genetics*.
- BS 8110-1 (1997) 'Structural use of concrete. Code of practice for design and construction', *British Standards Institution*, ISBN 978 0 580 59893 7.
- Cajka, R., *et al.* (2017) 'Stress and strain of fiber reinforced concrete composites', *Proc. 6<sup>th</sup> Int. Conf. Non-traditional Cement & Concrete*, June 19-22-2017, Brno.
- EN 1992-1-1 (2004) 'Eurocode 2: Design of concrete structures - Part 1-1: General rules and rules for buildings', *The European Union Per Regulation* 305/2011.
- EN 1994-1-1 (2004) 'Eurocode 4: Design of composite steel and concrete structures – Part 1-1: General rules and rules for buildings', *The European Union Per Regulation* 305/2011.
- Fegan, G. and Gustar, M. (2003) 'Chapter 2 – Monte Carlo Simulation' in: Marek, P. *et al.* (2003) 'Probabilistic Assessment of Structures using Monte Carlo Simulation - Background, Exercises and Software', TeReCo 2nd edition, *Institute of Theoretical and Applied Mechanics*, Academy of Sciences of Czech Republic, Praha.
- Ghosh, P. *et al.* (2017) 'Probabilistic time-dependent sensitivity analysis of HPC bridge deck exposed to chlorides', *J. Computers and Concrete*, 19(3), pp. 305-313. DOI: <https://doi.org/10.12989/cac.2017.19.3.305>.
- GNU Octave Scientific programming language on-line: [www.octave.org](http://www.octave.org).
- Harrison, L. R. (2010) 'Introduction to Monte Carlo simulation', *AIP Conference Proceedings* 1204, 17(2010), doi: 10.1063/1.3295638.
- Keulenl, A. *et al.* (2017) 'Durability evaluation of aam using a plasticizing additive, enhancing fresh concrete rheology', *Proc. 6<sup>th</sup> Int. Conf. Non-traditional Cement & Concrete*, June 19-22-2017, Brno.
- Konecny, P. *et al.* (2017) 'Variation of diffusion coefficient for selected binary and ternary concrete mixtures considering concrete aging effect', *Proc. 6<sup>th</sup>*

- Int. Conf. Non-traditional Cement & Concrete*, June 19-22-2017, Brno.
- Králík, J. and Klabník, M. (2016) 'Nonlinear analysis of the failure of nuclear hermetic reinforced concrete structure due to extreme pressure and temperature', *Transactions of the VŠB – Technical University of Ostrava Civil Engineering Series*, 16(2), paper#17.
- Le, D. T. *et al.* (2018) 'Time dependent variation of carrying capacity of prestressed precast beam', *IOP Conference Series: Earth and Environmental Science*, 143(2018) 012013, IOP Publishing, doi:10.1088/1755-1315/143/1/012013.
- Marek, P. *et al.* (2003) 'Probabilistic Assessment of Structures using Monte Carlo Simulation - Background, Exercises and Software', TeReCo 2<sup>nd</sup> edition, *Institute of Theoretical and Applied Mechanics*, Academy of Sciences of Czech Republic.
- MatLab: The language of technical computing *MathWorks* - on-line: [www.mathworks.com](http://www.mathworks.com).
- Matthews, *et al.* (2016) 'Fib model code 2020 – A new development in structural codes: Towards a general code for both new and existing concrete structures', edited by Beushausen, H. (2016) 'Proc. fib Symp', *Performance-based approaches for concrete structures*, Cape Town, pp. 22-31.
- Melchers, R. (1999) 'Structural reliability analysis and prediction (Civil Engineering)', *Wiley*, West Sussex.
- Nawy, E. G. (2009) 'Prestressed concrete - a fundamental approach, 5<sup>th</sup> edition update', *Prentice Hall*, Upper Saddle River, New Jersey 07458, ISBN-10: 0-13-608150-9, ISBN-13: 978-0-13-608150-0.
- Seguirant, S. J. *et al.* (2005) 'Flexural strength of reinforced and prestressed concrete T-beams', *PCI Journal*, January-February 2005, pp. 44-73.
- Stewart, M. G. and Rosowsky, D. V. (1998) 'Time-dependent reliability of deteriorating reinforced concrete bridge decks', *Structural Safety*, 20(1), pp. 91-109.
- Sucharda, O. *et al.* (2017) *Periodica Polytechnica Civil Engineering*, 61(4), pp. 972-986.



## 6. Plate strip in a stabilized temperature field and creep effect

Katarína Tvrdá<sup>1</sup>

<sup>1</sup> *Slovak University of Technology, Faculty of Civil Engineering, Bratislava, Slovakia,*

**Abstract:** Deflection and stress states of a plate strip with variable stiffness and Boussinesq half-space subjected to actions of discontinuous temperature field under assumption of plane deformation are investigated. The hereditary creep of the plate and of the subgrade materials according to different constitutive equations is applied. The formulation and the solution of the basic integro-differential equation system are performed in Laplace's transforms using an undirect way. The time dependent solution is constructed by means of modified Erdélyi Schapery algorithm. The numerical method with a detailed analysis of the obtained results is demonstrated on a numerical example.

**Keywords:** plate strip, stress states, temperature, creep

### 6.1. Introduction

The temperature stresses and deformations can play significant, sometimes even prevailing part in the design of foundation plates and structures. It is concerned the road and airdrome plates, the foundation plates in metallurgical and chemical plants, foundation plates and blocks of dams etc. The magnitude of the temperature stresses and deformations can depend on the thermo-physical properties of concrete, on the temperature of fresh concrete, on the exothermic reaction of cement, on the temperature of ambient environment, i.e. on that of air, water, and subgrade, and on the interaction mode of the foundation structure and the subgrade. In evolution of temperature stresses and deformations, the relaxation properties of material of the foundation structures and of the subgrade play a non negligible part. As will be shown further, while e.g. the deflections of the plates are getting larger, the bending moments and the shear forces are getting smaller. These findings can have a great importance from the viewpoint of the life time of the foundation structures. Only a sporadic attention has been paid in literature to the time dependent problems of temperature and deformations in massive concrete blocks and plates. Among the former sources the works of the Armenian School represented by N. Ch. Arutjunjan and his collaborators (Arutjunjan, 1955), (Zadajan, 1957), and those of the Polish

school headed by W. Nowacki (Nowacki, 1963) are to be mentioned. Nowadays, particular attention is paid to contact problems (Moravkova, 2017), (Farhatnia, 2017), (Korotchenko, 2017) but time-dependent deformations less (Mistrikova, 2007), (Mistrikova, 2012), (Sumeć, 2010). This chapter deals with the temperature stresses and deformations of the plate strip with the rigid borders, which is freely supported on the half-space, due to temperature actions of the ambient environment. By means of stiff borders is simulated in solution the lateral concrete walls the stiffness of which can be considered as infinitely large with regard to the finite thickness of plate. For example, craft locks, sludge-digestion tanks, blocks of dams, and other. It is assumed that the ambient temperature is stabilized. The investigations is limited to the temperatures for which the thermal and material characteristics of the plate can be consider as the permanent magnitudes independent on the temperature. It is further contemplated that the materials of the plate and of the subgrade undergo the creep with time and that they fulfil the basic equations of the theory of hereditary creep proposed by L. Boltzmann & V. Volterra (Boltzmann, 1970), (Volterra, 1913). That theory is based on the assumption of linear relationship between stresses and strains for which the law of superposition is valid. Experimental measurements show that the both assumptions are very well fulfilled till to the 40 percent of strength of materials. Constitutive equations of the hereditary creep are the most satisfying for the rheological properties of concrete structures and of the real subgrades in the time of their exploitation.

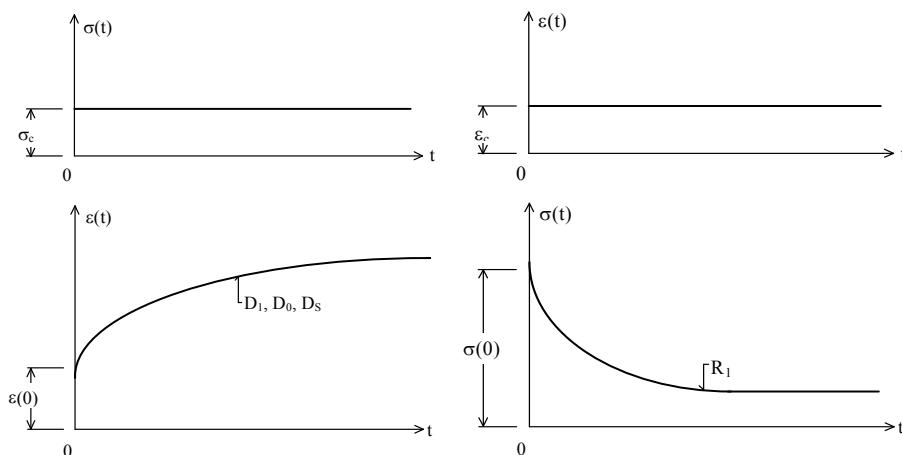


**Fig. 6.1.** Transient functions of creep D1 and those of relaxation R1 at uniaxial deformation

As the phenomena of creep and relaxation, i.e. the transient functions of creep and those of relaxation (Fig. 6.1) represent discontinuous functions of time, these physical variables are interpreted as so called Schwartz distributions (some type of the generalized functions with the carrier on the time half-axis  $<0, \infty$ ). Such an interpretation permits to write down the constitutive equations in terms of the time invariant linear theory of the hereditary creep in a very compact form, as the equations with convolutions. Constructing the solution starting from the long term measurements for concrete (Loom and Base, 1990), (Neville, 1970) and for subgrade (Mesčjan, 1967), (Zareckij, 1993) it is assumed that concrete (subscript d) and subgrade (subscript z) are represented by quasielastic bodies having the instantaneous and the time variables values of Poisson's ratio practically constant:

$$\mu_d(0) = \mu_d(t) = \text{const}, \mu_z(0) = \mu_z(t) = \text{const}.$$

The basic equations are solved in Laplace's transforms. The time dependent solution is constructed using Erdélyi – Scahapery method of inverse transformation modified by B. Novotný (Novotný, 1980). The formulation of the basic equations and their solution is represented using the dimensionless variable  $\xi$  given by the quocient of the real ordinate  $x$  and of a half of the foundation joint  $\ell/2$ , i.e.  $\xi = 2x/\ell$  and then  $\alpha = 2a/\ell, \beta = 2b/\ell$ .

## 6.2 Basic equations and their solution

Assume that a plate strip with variable thickness is freely placed on a viscoelastic half-space and has a constant thickness  $h$  within the interval  $<-\beta, +\beta>$ , and that its stiffness is infinite within the extreme intervals  $<-1, -\beta>$  and  $<+\beta, +1>$ . It is assumed that the plate strip on a finite area  $<-\alpha, \alpha>$  is subjected to a constant temperature  $T(z)H(t)$ , where  $H(t)$  is Heaviside's function, and that  $T(z) = 0$  except this area. The thermal gradient is assumed to be variable along the thickness of the plate (Fig. 6.2).

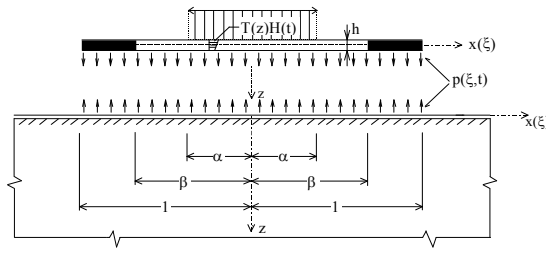


**Fig. 6.2.** Geometric scheme of the plate strip interacting with the half-space in a discontinuous temperature field  $T(z)H(t)$ .

The plate strip will be deformed due to influence of temperature. The stresses  $p(\xi, t)$  will arise on the contact of the strip with the half-space. The problem is to determine the magnitude and the distribution way of these stresses within the time  $t \in (0, \infty)$ . The stresses  $p(\xi, t)$  is determined from the equilibrium equations of the plate strip as a stiff entity

$$\int_{-1}^{+1} p(\xi, t) d\xi = 0, \quad \int_{-1}^{+1} \xi p(\xi, t) d\xi = 0 \quad (6.1)$$

and from the deformation condition

$$w(\xi, t) = -v_z(\xi, t) \quad (6.2)$$

expressing the equality of the plate strip deflections  $w(\xi, t)$  and of the vertical displacements of the border ( $z = 0$ ) of the half-space  $v_z(\xi, t)$  in each point  $\xi$  of the interval  $< -1, +1 >$  of the foundation joint. Deriving the equations for the deflections of the plate strip and for its internal forces is started from the constitutive equations in which the deformations of each element of plate are composed of the temperature deformation and of the viscoelastic deformation caused by temperature stresses.

$$\begin{aligned} \sigma_x(\xi, t) &= \frac{1}{1 - \mu_d^2} R_{d1}^{[1]} * [\varepsilon_x(\xi, t) - (1 + \mu_d) \alpha_T T(z) H(t)] \\ \sigma_y(\xi, t) &= \frac{1}{1 - \mu_d^2} R_{d1}^{[1]} * [\mu_d \varepsilon_x(\xi, t) - (1 + \mu_d) \alpha_T T(z) H(t)] \\ \tau_{xy}(\xi, t) &= 0 \end{aligned} \quad (6.3)$$

The relationships (6.3) are obtained from the following adjoint equations of Duhamel – Neumann (Duhamel, 1838)

$$\begin{aligned} \sigma_x(\xi) &= \frac{E_d}{1 - \mu_d^2} [\varepsilon_x(\xi) - (1 + \mu_d) \alpha_T T(z)] \\ \sigma_y(\xi) &= \frac{E_d}{1 - \mu_d^2} [\mu_d \varepsilon_x(\xi) - (1 + \mu_d) \alpha_T T(z)] \\ \tau_{xy}(\xi) &= 0 \end{aligned} \quad (6.4)$$

by assignment of the correspondent viscoelastic equivalent (Kovařík, 1987). In equations (6.3) the strain  $\varepsilon_x(\xi, t)$  be means of the deflections  $w(\xi, t)$  of the middle plane of the plate strip is expressed as follows:

$$\varepsilon_x(\xi, t) = -\frac{z}{\left(\frac{\ell}{2}\right)^2} \frac{\partial^2 w(\xi, t)}{\partial \xi^2} \quad (6.5)$$

Then the stress resultants can be expressed, i.e. the bending moment and the shear forces in the following form (Fig. 6.3).

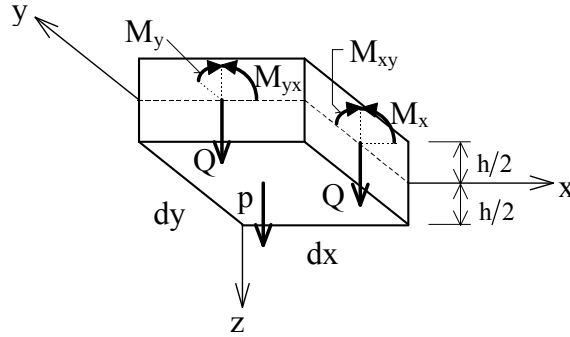


**Fig. 6.3.** Differential element of the plate strip placed on the half-space with a volume of  $dV = dx dy h$  under the actions of contact stresses  $p$  and the section quantities  $M_x$ ,  $M_y$ ,  $M_{xy}$ ,  $Q_x$ ,  $Q_y$ .

$$\begin{aligned} M_{xy}(\xi, t) &= 0 \\ Q_x(\xi, t) &= -U(t) * \frac{1}{\left(\frac{\ell}{2}\right)^3} \frac{\partial^3 w(\xi, t)}{\partial \xi^3} \\ Q_y(\xi, t) &= 0. \end{aligned} \quad (6.6)$$



$$M_x(\xi, t) = -U(t) * \left[ \frac{1}{\left(\frac{\ell}{2}\right)^2} \frac{\partial^2 w(\xi, t)}{\partial \xi^2} + (1 + \mu_d) \alpha_T \chi_T H(t) \right]$$

$$M_y(\xi, t) = -U(t) * \left[ \mu_d \frac{1}{\left(\frac{\ell}{2}\right)^2} \frac{\partial^2 w(\xi, t)}{\partial \xi^2} + (1 + \mu_d) \alpha_T \chi_T H(t) \right]$$

For the deflection of the plate strip the following equation is valid

$$\frac{\partial^2}{\partial \xi^2} \left[ U(t) * \frac{1}{\left(\frac{\ell}{2}\right)^2} \frac{\partial^2 w(\xi, t)}{\partial \xi^2} \right] = \left(\frac{\ell}{2}\right)^2 p(\xi, t) \quad (6.7)$$

Where

$$U = \frac{h^3}{12(1 - \mu_d^2)} R_{d1}^{[1]}(t) \quad (6.8)$$

represents the time function of the flexural stiffness of the strip which is obtained from the flexural stiffness for the elastic problem

$$U = \frac{E_d h^3}{12(1 - \mu_d^2)} \quad (6.9)$$

The vertical displacements of the border of the viscoelastic half-space are determined by assuming its planar deformations due to stresses  $p(\xi, t)$  from the following integral equation

$$v_z(\xi, t) = \frac{(1 + \mu_z) \frac{\ell}{2}}{\pi} D_{z1}^{[1]}(t) *$$

$$\int_{-1}^{+1} p(\bar{\xi}, t) \left[ 2(1 - \mu_z) \ln \left( \xi - \bar{\xi} + \delta(t) \right) \right] d\bar{\xi} + C(t) \quad (6.10)$$

the elastic adjoint equivalent of which is the well-known Flamant's equation

$$v_z(\xi) = - \frac{(1 + \mu_z) \frac{\ell}{2}}{\pi E_z} \cdot \int_{-1}^{+1} p(\bar{\xi}) \left[ 2(1 - \mu_z) \ln \left( \xi - \bar{\xi} \left( +1 \right) \right) d\bar{\xi} + C \right] \quad (6.11)$$

In Equation (6.10)  $C(t)$  represents an arbitrary function of time and in Equation (6.11) an arbitrary constant. Abbreviations in the above equations is given:

$$\chi_T = \frac{12}{h^3} \int_{-h/2}^{h/2} z T(z) dz \quad (6.12)$$

Approach to the solution of the integro-differential system of basic equations (6.1), (6.7), (6.10), and (6.2) is used indirectly. As the temperature field is symmetric with regard to the plane  $\xi = 0$ , also the distribution of the contact stresses  $p(\xi, t)$  in foundation joint is symmetric. Therefore, let us chose the functions of the contact stresses in the form as follows

- $\alpha_T$  — the coefficient of thermal dilatation,
- $E_d, E_z$  — Young moduli of the plate and of the subgrade materials,
- $R_{dl}, R_{zl}$  — the transient relaxation functions,
- $D_{dl}, D_{zl}$  — the transient creep functions of the plate and of the subgrade materials at the uniaxial stress state,
- $*$  — symbol that denotes the convolution product,
- $^{[1]}$  — symbol that denotes the derivation according to the theory of generalized functions (distributive derivation) defined over the time half-axis  $t \geq 0$ ,
- $\delta(t)$  — Dirac's delta function (distribution),
- $\chi_T$  — the curvature of the middle plane of the strip due to temperature change only.

$$p(\xi, t) = \frac{A(t)}{\sqrt{1 - \xi^2}} + \sum_{n=0}^{\infty} a_{2n}(t) P_{2n}(\xi) \quad (n = 0, 1, 2, \dots) \quad (6.13)$$

where  $A(t)$  and  $a_{2n}(t)$  are the time functions, unknown for the present, and  $P_{2n}(\xi)$  are Legendre polynomials of the first order. The  $n$ -th Legendre polynomial of the first order is defined as follows

$$P_n(\xi) = \sum_{r=0}^{\left[\frac{n}{2}\right]} \frac{(-1)^r (2n-2r)!}{2^n r! (n-r)! (n-2r)!} \xi^{n-2r} \quad (6.14)$$

$$(n = 0, 1, 2, \dots) \quad -1 \leq \xi \leq +1$$

where  $[n/2]$  means the integer of the number  $n/2$ .

The first equilibrium condition (6.1) leads to the following Equation

$$\pi A(t) + 2a_0(t) = 0 \quad (6.15)$$

The second condition (6.1) is fulfilled identically. As it can be seen from Equation (6.15), the resultant of the contact stresses equals zero and the stresses  $p(\xi, t)$  represent a self-loading system. The following relationships between the time functions  $A(t)$  and  $a_{2n}(t)$  are derived from the deformation condition (6.2). The deflections of the plate strip  $w(\xi, t)$  are composed from two parts: from the deflections  $w_p(\xi, t)$  due to contact stresses  $p(\xi, t)$  and from the deflections  $w_T(\xi, t)$  due to temperature  $T(z)H(t)$ , i.e.

$$w(\xi, t) = w_p(\xi, t) + w_T(\xi, t) \quad (6.16)$$

It is dealt with the deflections due to contact stresses (6.13). For the plate strip with absolutely stiff borders is given then in the following form

$$w_p(\xi, t) = \left(\frac{\ell}{2}\right)^4 U^{*-1}(t) * \left\{ A(t) \left\{ w_A(\xi) [H(\xi) - H(\xi - \beta)] + \right. \right. \\ \left. \left. + [w_A(\beta) + (\xi - \beta) w'_A(\beta)] [H(\xi - \beta) - H(\xi - 1)] \right\} + \right. \\ \left. + \sum_{n=0}^{\infty} a_{2n}(t) \left\{ w_{2n}(\xi) [H(\xi) - H(\xi - \beta)] + \right. \right. \\ \left. \left. + [w_{2n}(\beta) + (\xi - \beta) w'_{2n}(\beta)] [H(\xi - \beta) - H(\xi - 1)] \right\} \right\}, \quad (6.17)$$

where

$$U^{*-1}(t) = \frac{12(1 - \mu_d^2)}{h^3} D_{d1}^{[1]}(t) \quad (6.18)$$

$(\ell/2)^2$  was the inverse element of the flexural stiffness of the strip plate (6.8), and

$$\begin{aligned}
w_A(\xi) &= \frac{1}{36} \left[ \xi (6\xi^2 + 9) \arcsin \xi + (11\xi^2 + 4) \sqrt{1 - \xi^2} - 4 \right] \\
w_0(\xi) &= \frac{1}{24} (\xi^4 + 6\xi^2) \\
w_2(\xi) &= \frac{1}{240} (\xi^6 - 5\xi^4 + 15\xi^2) \\
w_4(\xi) &= \frac{1}{384} (\xi^8 - 4\xi^6 + 6\xi^4 - 4\xi^2) \\
w_6(\xi) &= \frac{1}{3840} (11\xi^{10} - 45\xi^8 + 70\xi^6 - 50\xi^4 + 15\xi^2) \\
w_8(\xi) &= \frac{1}{15360} (65\xi^{12} - 286\xi^{10} + 495\xi^8 - 420\xi^6 + 175\xi^4 - 30\xi^2) \\
&\vdots
\end{aligned} \tag{6.19}$$

were the deflection functions of the strip plate due to particular terms of the approximation function (6.13).

The deflections due to temperature have to fulfil the following differential equation

$$\frac{1}{\left(\frac{\ell}{2}\right)^2} \frac{\partial^2}{\partial \xi^2} \left[ U(t) * \frac{1}{\left(\frac{\ell}{2}\right)^2} \frac{\partial^2 w_T(\xi, t)}{\partial \xi^2} \right] = 0 \tag{6.20}$$

as well as the following conditions:

In the middle ( $\xi = 0$ )

$$w_T^I(\xi, t) \Big|_{\xi=0} = 0 \quad \frac{\partial w_T^I(\xi, t)}{\partial \xi} \Big|_{\xi=0} = 0 \quad Q_{xT}^I(\xi, t) \Big|_{\xi=0} = 0 \tag{6.21}$$

in the discontinuity point of the temperature field ( $\xi = \alpha$ )

$$\begin{aligned}
w_T^I(\xi, t) \Big|_{\xi=\alpha} &= w_T^{II}(\xi, t) \Big|_{\xi=\alpha} \quad \frac{\partial w_T^I(\xi, t)}{\partial \xi} \Big|_{\xi=\alpha} = \frac{\partial w_T^{II}(\xi, t)}{\partial \xi} \Big|_{\xi=\alpha} \\
M_{xT}^I(\xi, t) \Big|_{\xi=\alpha} &= M_{xT}^{II}(\xi, t) \Big|_{\xi=\alpha}
\end{aligned} \tag{6.22}$$

in the abrupt change of stiffness ( $\xi = \beta$ )

$$M_{xT}^{II}(\xi, t) \Big|_{\xi=\beta} = M_{xT}^{III}(\xi, t) \Big|_{\xi=\beta} \quad Q_{xT}^{II}(\xi, t) \Big|_{\xi=\beta} = Q_{xT}^{III}(\xi, t) \Big|_{\xi=\beta},$$

and on the border ( $\xi = 1$ ) of the plate strip

$$M_{xT}^{III}(\xi, t) \Big|_{\xi=1} = 0 \quad Q_{xT}^{III}(\xi, t) \Big|_{\xi=1} = 0 \quad (6.23)$$

The equation (6.20) and the conditions (6.21) ÷ (6.23) is fulfilled by the following function

$$w_T(\xi, t) = \left(\frac{\ell}{2}\right)^2 KH(t) \bar{w}_T(\xi) \quad (6.24)$$

where

$$K = (1 + \mu_d) \alpha_T \chi_T \quad (6.25)$$

and

$$\begin{aligned} \bar{w}_T(\xi) = & -\frac{1}{2} \xi^2 [H(\xi) - H(\xi - \alpha)] + \frac{1}{2} (\alpha^2 - 2\alpha\xi) \cdot \\ & \cdot [H(\xi - \alpha) - H(\xi - \beta)] + \left[ \frac{1}{2} (\alpha^2 - 2\alpha\beta) - \alpha(\xi - \beta) \right] \cdot \\ & \cdot [H(\xi - \beta) - H(\xi - 1)]. \end{aligned} \quad (6.26)$$

As it can be seen from Equations (6.24) and (6.25), the deflections due to temperature do not depend on the relaxation properties of the plate material, but on the character of the temperature field only. The influence of the temperature field is expressed by the curvature  $\chi_T$ . It is given by the formulae (6.12). It depends on the character of the temperature gradient through the plate thickness. The temperature gradient can be linear, but also non linear. In both cases is calculated the curvature  $\chi_T$  from the formula (6.12). In the case of the linear temperature gradient (Fig. 6.4)

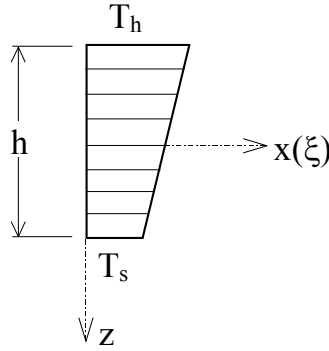


**Fig. 6.4.** Linear temperature gradient along the plate thickness  $h$

$$T(z) = \frac{\Delta T}{h} z + T_0 \quad (6.27)$$

where  $\Delta T = T_s - T_h$  and  $T_0 = (T_s + T_h)/2$  is obtained

$$\chi_T = \frac{\Delta T}{h} \quad (6.28)$$

In the case of non linear temperature gradient (Fig. 6.5) is approximated with a sufficient accuracy the temperature change in an arbitrary point of the plate thickness using the following expression

$$T(z) = az^3 + bz^2 + cz + d \quad (6.29)$$

where

$$\begin{aligned} a &= \frac{9}{2h^3} [T_4 - T_1 + 3(T_2 - T_3)] & b &= \frac{9}{4h^2} [T_1 - T_2 - T_3 + T_4] \\ c &= \frac{1}{8h} [T_1 - T_4 + 27(T_3 - T_2)] & d &= \frac{1}{16} [9(T_2 + T_3) - (T_1 + T_4)] \end{aligned}$$

and  $T_1, T_2, T_3, T_4$  are the discrete temperature values in the planes  $z = -h/2, -h/6, +h/6, +h/2$ . The curvature  $\chi_T$  after substitution of (6.29) into (6.12), and after integration is as follows:

$$\chi_T = \frac{1}{20h} [11(T_4 - T_1) + 27(T_3 - T_2)] \quad (6.30)$$

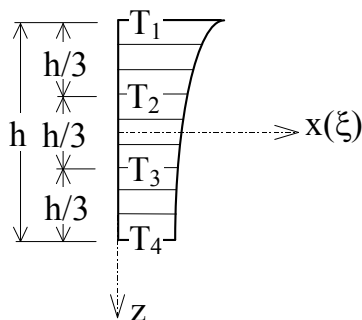


**Fig. 6.5.** Non linear temperature gradient along the plate thickness  $h$

Let us return again to the deformation condition (6.2). The vertical displacements of the half-space border ( $z=0$ ) are caused only by contact stresses  $p(\xi, t)$ . They determined them from the integral equation (6.10). If is assumed that the stresses (6.13) have a form (6.13), then the displacements  $v_z(\xi, t)$  can be represented in the form as follows

$$v_z(\xi, t) = \frac{(1 - \mu_z^2) \ell}{\pi} D_{z1}^{[1]}(t) * \left[ \sum_{n=0}^{\infty} a_{2n}(t) v_{2n}(\xi) \right] [H(\xi) - H(\xi - 1)] \quad (6.31)$$

$$(n = 0, 1, 2, \dots)$$

where

$$v_0(\xi) = (\xi - 1) \ln |\xi - 1| - (\xi + 1) \ln |\xi + 1|$$

$$v_2(\xi) = \frac{1}{2} \left[ (\xi^3 - \xi) \ln \frac{|\xi - 1|}{|\xi + 1|} + 2\xi^2 \right]$$

$$v_4(\xi) = \frac{1}{8} \left[ (7\xi^5 - 10\xi^3 + 3\xi) \ln \frac{|\xi - 1|}{|\xi + 1|} + \frac{1}{3} (42\xi^4 - 46\xi^2) \right]$$

$$v_6(\xi) = \frac{1}{16} \left[ (33\xi^7 - 63\xi^5 + 35\xi^3 - 5\xi) \ln \frac{|\xi - 1|}{|\xi + 1|} + \frac{1}{5} (330\xi^6 - 520\xi^4 + 206\xi^2) \right]$$

$$\begin{aligned}
v_8(\xi) &= \frac{1}{128} \left[ (715\xi^9 - 1716\xi^7 + 1386\xi^5 - 420\xi^3 + 35\xi) \ln \frac{\|\xi-1\|}{\|\xi+1\|} + \right. \\
&\quad \left. + \frac{2}{105} (75075\xi^8 - 155155\xi^6 + 100485\xi^4 - 20901\xi^2) \right] \\
&\vdots
\end{aligned}$$

are the veritcal displacements of the half-space border due to particular terms of the approximation function (6.13). After expressing the deflections  $w(\xi, t)$  and  $v_z(\xi, t)$  according to (6.16), (6.27), (6.24), and (6.31), respectively, and after modification, the deformation condition leads to the functional equation for the infinite sequence of the time functions  $A(t)$  and  $a_{2n}(t)$ , as follows:

$$\begin{aligned}
&k(t) * A(t) \left\{ w_A(\xi) (H(\xi) - H(\xi - \beta)) + \right. \\
&\quad \left. + (w_A(\beta) + (\xi - \beta)w'_A(\beta)) (H(\xi - \beta) - H(\xi - 1)) \right\} + \\
&\quad + \sum_{n=0}^{\infty} a_{2n}(t) * \left\{ \delta(t) v_{2n}(\xi) (H(\xi) - H(\xi - 1)) + k(t) \cdot \right. \\
&\quad \cdot [w_{2n}(\xi) (H(\xi) - H(\xi - \beta)) + (w_{2n}(\beta) + (\xi - \beta)w'_{2n}(\beta)) \\
&\quad \cdot (H(\xi - \beta) - H(\xi - 1))] \left. \right\} = \frac{1}{\left(\frac{\ell}{2}\right)^2} k(t) * U(t) * KH(t) \bar{w}_T(\xi)
\end{aligned} \tag{6.32}$$

This equation is to be fulfilled identically for all points of the interval  $-1 \leq \xi \leq +1$  ( $n = 0, 1, 2, \dots$ ) and in the each instant  $t \in (-\infty, \infty)$ . The time function of the relative flexural stiffness of the plate strip is defined by the convolution relationship

$$k(t) = 2 \frac{3 \left(\frac{\ell}{2}\right)^3 (1 - \mu_d^2)}{h^3 (1 - \mu_z^2)} D_{d1}^{[1]}(t) * R_{z1}^{[1]}(t) \tag{6.33}$$

The equations (6.15) and (6.32) are solved using collocation method in the space of Laplace's transforms. Applying collocation method are not fulfilled the deformation condition for each  $\xi$  of the interval  $< -1, +1 >$  of the foundation joint, but in a finite number of the discrete points  $\xi = 0,2; 0,4; 0,6; 0,8$ , and  $1,0$  only. (Equation (6.32) is satisfied for negative arguments  $\xi$  because of symmetry. In the middle of the plate strip the equation is satisfied in advance



because of the first condition (6.21)). In such a way, are obtained together with the equilibrium equation (6.15) a finite system of six functional equations for six unknown time functions  $A(t)$  and  $a_{2n}(t)$  ( $n = 0, 1, 2, 3, 4$ ). The time unknown  $t$  from in such a way obtained equation system are eliminated by means of the following Laplace integral transformation

$$\mathbb{L}\{f(\xi, t)\} = \tilde{f}(\xi, \lambda) = \int_0^{\infty} f(\xi, t) e^{-\lambda t} dt \quad (6.34)$$

where  $\lambda$  is the parameter of the Laplace transformation. Consequently, is started from the following equations

$$\pi \tilde{A}(\lambda) + 2 \tilde{a}_0(\lambda) = 0 \quad (6.35)$$

$$\begin{aligned} & \tilde{k}(\lambda) \tilde{A}(\lambda) \left[ w_A(\xi) (H(\xi) - H(\xi - \beta)) + (w_A(\beta) + (\xi - \beta) w'_A(\beta)) \cdot \right. \\ & \left. \cdot (H(\xi - \beta) - H(\xi - 1)) \right] + \sum_{n=0}^{\infty} \tilde{a}_{2n}(\lambda) \left\{ v_{2n}(\xi) (H(\xi) - H(\xi - 1)) \right. \\ & \left. + \tilde{k}(\lambda) \left[ w_{2n}(\xi) (H(\xi) - H(\xi - \beta)) + (w_{2n}(\beta) + (\xi - \beta) w'_{2n}(\beta)) \cdot \right. \right. \\ & \left. \left. \cdot (H(\xi - \beta) - H(\xi - 1)) \right] \right\} = \frac{1}{\left(\frac{\ell}{2}\right)^2} \tilde{k}(\lambda) \tilde{U}(\lambda) K \bar{w}_T(\xi) \frac{1}{\lambda} \end{aligned} \quad (6.36)$$

The Laplace's transforms of the holomorphic functions of the relative flexural stiffness of the plate strip and its flexural stiffness (6.8) with regard to the transformant

$$\lambda \tilde{R}(\lambda) = \frac{1}{\lambda D(\lambda)}$$

resulting from (Kovářík, 1987) results in the following relations

$$\begin{aligned} \tilde{k}(\lambda) &= 2 \frac{3 \left(\frac{\ell}{2}\right)^3 (1 - \mu_d^2) \tilde{D}_{d1}(\lambda)}{h^3 (1 - \mu_z^2) \tilde{D}_{z1}(\lambda)} \\ \tilde{U}(\lambda) &= \frac{h^3}{12(1 - \mu_d^2)} \frac{1}{\lambda \tilde{D}_{d1}(\lambda)} \end{aligned} \quad (6.37)$$

The originals  $A(t)$  and  $a_{2n}(t)$  of the holomorphic functions  $\tilde{A}(t)$  and  $\tilde{a}(t)$  are constructed applying numerical inverse transformation modified by

Erdélyi – Schapery method. The knowledge of the originals of time functions  $A(t)$  and  $a_{2n}(t)$  permits to determine the stresses in the foundation joint of the plate strip, its deflections and its internal forces for different instants  $t$ . For the contact stress the approximation relationship (6.13) is valid. At the determination of the resultant deformations of the plate strip the following two cases should be distinguished:

- when the material of the strip plate is not subjected to creep, then determining deflections are determined from the following relationship

$$\begin{aligned}
 w(\xi, t) = & \left( \frac{\ell}{2} \right)^4 U^{-1} \left\{ A(t) \left[ w_A(\xi) (H(\xi) - H(\xi - \beta)) + \right. \right. \\
 & + \left( w_A(\beta) + (\xi - \beta) w'_A(\beta) \right) \cdot (H(\xi - \beta) - H(\xi - 1)) \Big] + \\
 & + \sum_{n=0}^{\infty} a_{2n}(t) \left[ w_{2n}(\xi) (H(\xi) - H(\xi - \beta)) + (w_{2n}(\beta) + \right. \\
 & + (\xi - \beta) w'_{2n}(\beta)) (H(\xi - \beta) - H(\xi - 1)) \Big] + \\
 & \left. + \frac{1}{\left( \frac{\ell}{2} \right)^2} UK \bar{w}_T(\xi) \right\}, \tag{6.38}
 \end{aligned}$$

where  $U$  and  $K$  are the relationships (6.9) and (6.25) valid for an ideally elastic plate.

- when the material of the plate strip is subjected to creep, then for the determination of the time function of deflections are determined using the inverse transformation of its Laplace's transforms according to the Erdélyi Schapery method

$$\begin{aligned}
\tilde{w}(\xi, \lambda) = & \left( \frac{\ell}{2} \right)^4 \tilde{U}^{*-1}(\lambda) \left\{ \tilde{A}(\lambda) \left[ w_A(\xi) (H(\xi) - H(\xi - \beta)) + \right. \right. \\
& + \left. \left( w_A(\beta) + (\xi - \beta) w'_A(\beta) \right) \right] \cdot (H(\xi - \beta) - H(\xi - 1)) \Big] + \\
& + \sum_{n=0}^{\infty} \tilde{a}_{2n}(\lambda) \left[ w_{2n}(\xi) (H(\xi) - H(\xi - \beta)) + \left( w_{2n}(\beta) + \right. \right. \\
& + \left. \left. (\xi - \beta) w'_{2n}(\beta) \right) (H(\xi - \beta) - H(\xi - 1)) \right] + \\
& + \left. \frac{1}{\left( \frac{\ell}{2} \right)^2} \tilde{U}(\lambda) \tilde{K} \frac{1}{\lambda} \bar{w}_T(\xi) \right\}.
\end{aligned} \tag{6.39}$$

At the determination of internal forces the following common relationships are valid in both cases:

$$\begin{aligned}
M_X(\xi, t) = & - \left( \frac{\ell}{2} \right)^2 \left[ A(t) w''_A(\xi) + \sum_{n=0}^{\infty} a_{2n}(t) w''_{2n}(\xi) \right] \cdot [H(\xi) - H(\xi - \beta)] \\
Q_X(\xi, t) = & - \left( \frac{\ell}{2} \right)^3 \left[ A(t) w'''_A(\xi) + \sum_{n=0}^{\infty} a_{2n}(t) w'''_{2n}(\xi) \right] \cdot [H(\xi) - H(\xi - \beta)].
\end{aligned} \tag{6.40}$$

It is demonstrated the general procedure of the solution on the thermoviscoelastic analysis of the plate strip in metallurgical operation which is placed in a stabilised temperature field of ambient environment.

### 2.3. Examples and analysis of the obtained results

Let us consider the plate strip having a constant stiffness ( $\beta = 1$ ) subjected to a high temperature  $T(z)H(t)$  on the whole range  $-\ell/2, +\ell/2$  of its surface (Fig. 6.6).

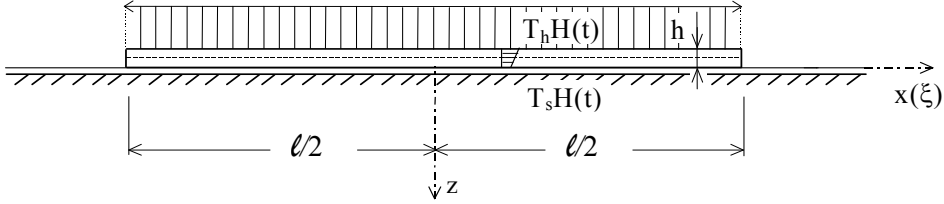


**Fig. 6.6.** A road plate strip in a stabilized temperature field along the whole strip width  $\ell$

Stress and deformation states of such a strip are described by Equations (6.38), (6.39), and (6.40) where are determined the time functions  $A(t)$  and  $a_{2n}(t)$  by inverse Laplace's transformation of Equations (6.35) and (6.36). In Equation (6.36) the following function corresponds on the basis of (6.26) for  $\alpha = 1$  and  $\beta = 1$  to the temperature field given in Fig. 6.6:

$$\bar{w}_T(\xi) = \frac{1}{2} \xi^2 [H(\xi) - H(\xi - 1)] \quad (6.41)$$

and the curvature  $K$  is given by the relationship (6.25). As the holomorphic functions  $\tilde{k}(\lambda)$  and the functions of the flexural stiffness of the strip  $\tilde{U}(\lambda)$ , as it can be seen from (6.37), depend on the Laplace's transforms of the transient creep functions of the materials of the plate strip and of the subgrade, are introduced them for the plate material (concrete) according to J. E. Prokopovič – V. A. Zedgenidze (Prokopovič and Zedgenidze, 1980)

$$D_{d1}(t) = \frac{1}{E_d} + C_0 (1 - B_1 e^{-\gamma_1 t} - B_2 e^{-\gamma_2 t}) \quad (6.42)$$

and for the material of subgrade according to (Mesčjan, 1967)

$$D_{z1}(t) = \frac{1}{E_z} \left[ 1 - \frac{\delta_1}{\delta_2} (1 - e^{-\delta_2 t}) \right] \quad (6.43)$$

where

$E_d, E_z$  (Mpa),  $C_0$  (MPa<sup>-1</sup>),  $B_1, B_2, \gamma_1$  (1/day),  $\gamma_2$  (1/day),  $\delta_1$  (1/day),  $\delta_2$  (1/day), are free parameters among which  $B_1$  and  $B_2$  vary within the limits  $0 \leq B_1 \leq 1, 0 \leq B_2 \leq 1$  and their sum equals  $B_1 + B_2 = 1$ . Laplace's transforms of the functions (6.42) and (6.43) are the following holomorphic function

$$\begin{aligned}\tilde{D}_{d1}(\lambda) &= \frac{1}{E_d} \frac{1}{\lambda} \left[ 1 + E_d C_0 \left( 1 - B_1 - B_2 + \frac{B_1 \gamma_1}{\gamma_1 + \lambda} + \frac{B_2 \gamma_2}{\gamma_2 + \lambda} \right) \right] \\ \tilde{D}_{z1}(\lambda) &= \frac{1}{E_z} \frac{1}{\lambda} \left( 1 + \frac{\delta_1}{\delta_2 + \lambda} \right).\end{aligned}\quad (6.44)$$

On the basis (6.44) the transformants  $\tilde{k}(\lambda)$  and  $\tilde{U}(\lambda)$  can be represented in the following final form

$$\tilde{k}(\lambda) = k \frac{1 + E_d C_0 \left( 1 - B_1 - B_2 + \frac{B_1 \gamma_1}{\gamma_1 + \lambda} + \frac{B_2 \gamma_2}{\gamma_2 + \lambda} \right)}{1 + \frac{\delta_1}{\delta_2 + \lambda}} \quad (6.45)$$

$$\tilde{U}(\lambda) = U \frac{1}{\left[ 1 + E_d C_0 \left( 1 - B_1 - B_2 + \frac{B_1 \gamma_1}{\gamma_1 + \lambda} + \frac{B_2 \gamma_2}{\gamma_2 + \lambda} \right) \right]}, \quad (6.45)$$

where

- $k$  – the coefficient of the relative flexural stiffness,
- $U$  – the flexural stiffness of the plate strip for the elastic problem given by the relation (6.9),

$$k = 2 \frac{3\pi(1-\mu_d^2)E_z \left(\frac{l}{2}\right)^3}{(1-\mu_z^2)E_d h^3}$$

When is satisfied Equation (6.36) only in points  $\xi = 0,2; 0,4; 0,6; 0,8$ , and  $1,0$  at the relative flexural stiffnesss  $k = 20$  and at the free parameters  $E_d = 2,9 \cdot 10^4$  MPa;  $E_z = 4,374 \cdot 10^2$  MPa;  $C_0 = 0,28 \cdot 10^{-4}$  MPa<sup>-1</sup>;  $B_1 = 0,43$ ;  $B_2 = 0,57$ ;  $\gamma_1 = 0,0018 \cdot 1/\text{day}$ ;  $\gamma_2 = 0,01 \cdot 1/\text{day}$ ;  $\delta_1 = 0,15 \cdot 1/\text{day}$ ,  $\delta_2 = 0,02 \cdot 1/\text{day}$ , the following inverted values of the roots correspond at instants  $t = 0, 5, 15$ , and  $\infty$  days in Table 6.1.

**Table 6.1.** Inverted values of the roots

The instant	$t = 0$	$t = 5$ days	$t = 15$ days	$t = \infty$
$A$	1,992058 L	1,295969 L	0,722833 L	0,606914 L
$a_0$	-3,129118 L	-2,035704 L	-1,135424 L	-0,953339 L
$a_2$	1,240038 L	1,006344 L	0,644525 L	0,506457 L
$a_4$	0,595200 L	0,285634 L	0,115315 L	0,114697 L
$a_6$	0,100727 L	0,054153 L	0,026399 L	0,024023 L
$a_8$	0,014467 L	0,008272 L	0,004147 L	0,003678 L

where

$$L = \frac{UK}{\left(\frac{l}{2}\right)^2}$$

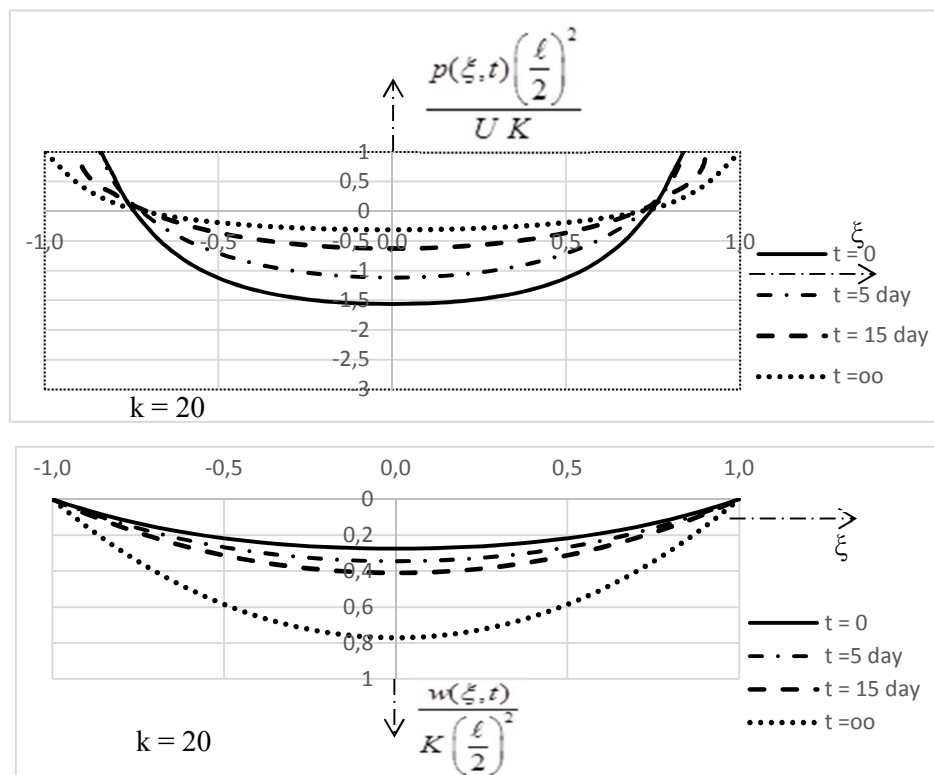


**Fig. 6.7.** Graphs of contact stresses  $p(\xi, t)$  and of deflections  $w(\xi, t)$  corresponding to the different instances  $t$  due to continuous temperature field according to Fig. 6.6, when the simultaneous creep of plate and of half-space occurs.

The graphs of the corresponding contact stresses, deflections, bending moments, and shear forces are given in Fig. 6.7 and Fig. 6.8. As it can be seen on Fig. 6.7 and Fig. 6.8, while the deflections increase with time, the stresses in the foundation joint, the bending moments and the shear forces decrease rapidly.

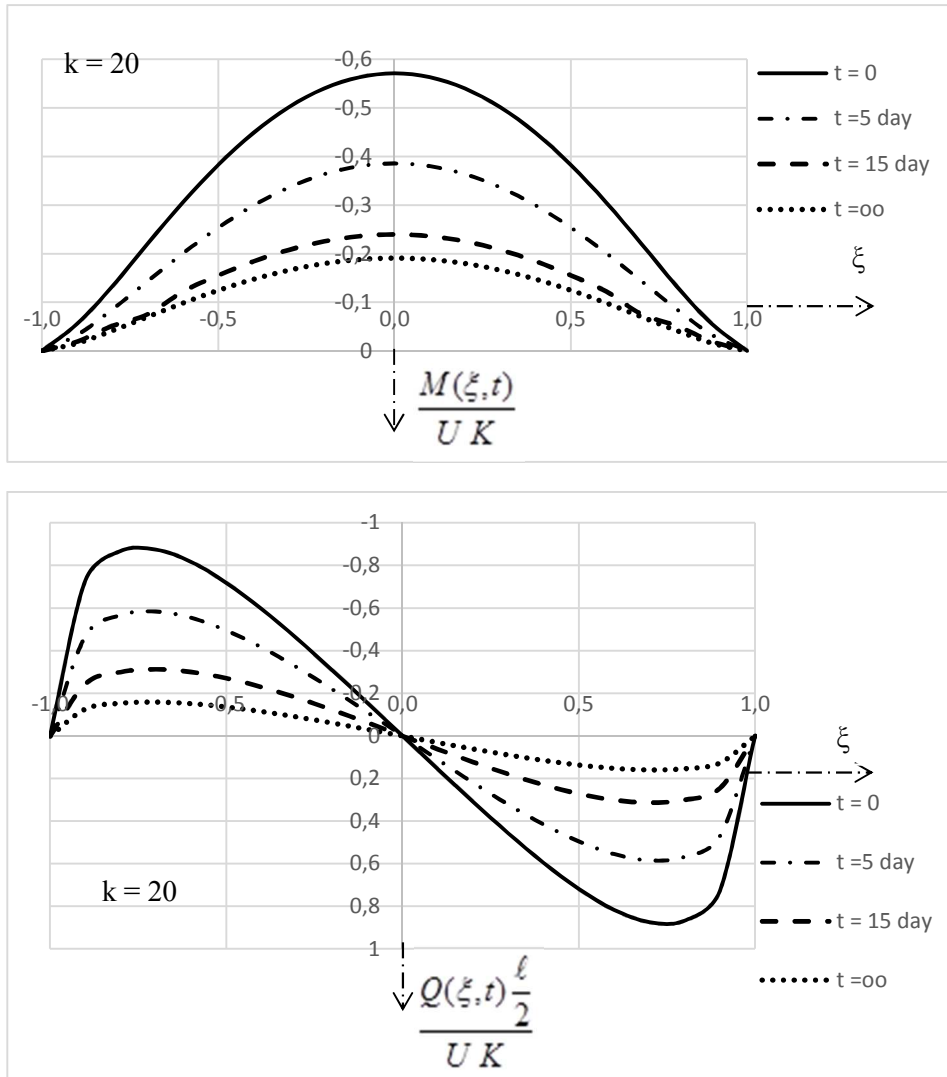


**Fig. 6.8.** Graphs of bending moments  $M(\xi, t)$  and of shear forces  $Q(\xi, t)$  in different instances  $t$  due to temperature field according to Fig. 6.6, when creep of material both of the plate and that of the subgrade occur simultaneously.

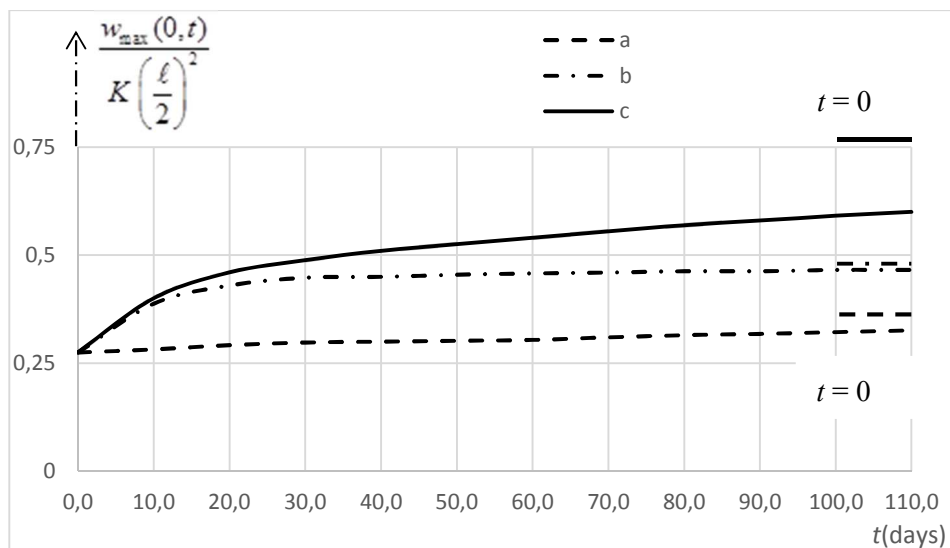


**Fig. 6.9.** Time dependent change of deflections in the middle of the plate strip, when creep occurs only in the material of plate (curve *a*), when creep occurs only in the material of subgrade (curve *b*), and when creep occurs in the material of plate, as well in that of subgrade simultaneously (curve *c*).

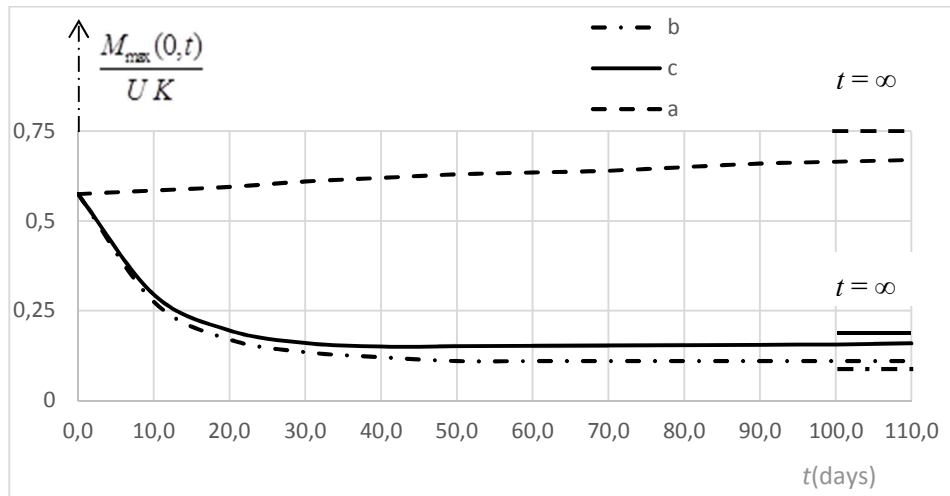


**Fig. 6.10.** Time dependent change of bending moments in the middle of the plate strip, when creep occurs only in the material of plate (curve *a*), when creep occurs only in the material of subgrade (curve *b*), and when creep occurs in the material of plate, as well as in that of subgrade simultaneously (curve *c*).



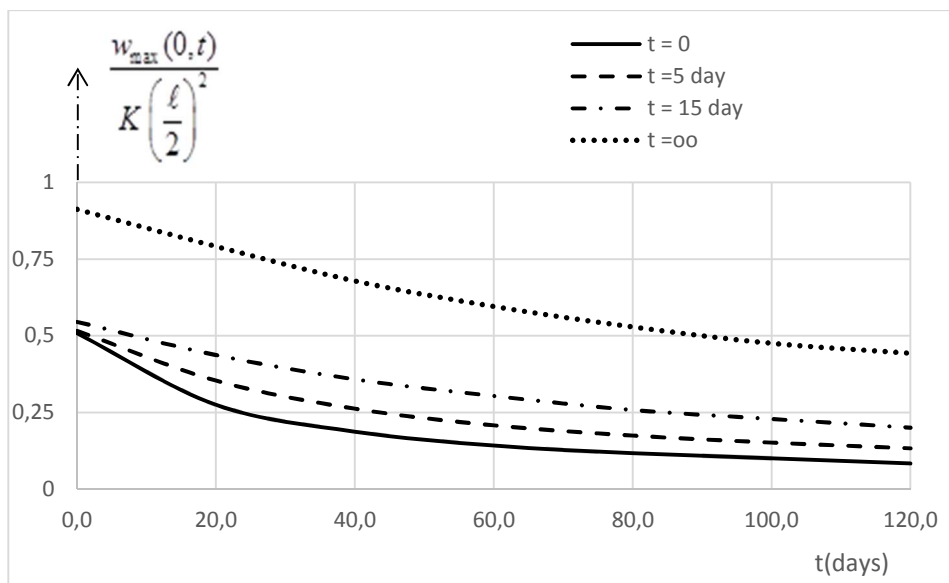


**Fig. 6.11.** Change of maximum deflections of the plate strip in time  $t$  at simultaneous creep of plate and of subgrade, when flexibility of the strip is gradually obtaining the following values:  $k = 0, 20, 40, \dots, 120$ .

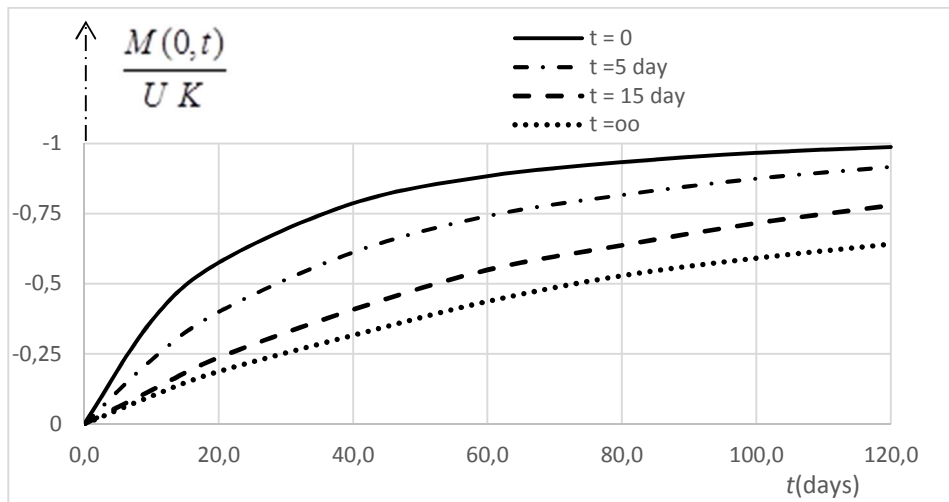


**Fig. 6.12.** Change of maximum bending moments of the plate strip in time  $t$  at simultaneous creep of plate and of subgrade, when flexibility of the strip is gradually obtaining the following values:  $k = 0, 20, 40, \dots, 120$ .

The maximum deflection in the middle of the plate ( $\xi = 0$ ) at instant  $t = \infty$  increased 2,8-times, while the bending moment decreased 2,98-times at the same instant in comparison with the state of its instantaneous warming ( $t = 0$ ). As to shear forces, this decrease represent in the cross section  $\xi = 0,7$  a multiplier of 3,03. Further, in Fig. 6.9 and Fig. 6.10 the change of the maximum moments and that of bending moments in the middle of the plate strip ( $\xi = 0$ ) on the whole time half-axis  $t \in <0, \infty$ ) can be monitored at a constant relative flexural stiffness of 20, for three possible cases of creep of the plate and subgrade materials. In Figures is denoted by the letter **a** the solution, when only the material of plate was subjected to creep and then is substituted  $\delta_1 = 0$  and  $\delta_2 = 0$  in the relationships (6.45), further by the letter **b** the solution when material of the subgrade showed relaxation abilities and the plate material was elastic ( $B_1 = 0$ ,  $B_2 = 0$ ,  $\gamma_1 = 0$ , and  $\gamma_2 = 0$ ), and finally by the letter **c** the solution when both materials of the plate and of the subgrade was subjected to the creep at the same time with the input data as they was given above. As it can be seen in Fig. 6.9 and Fig. 6.10, while the deflections in all three cases increase gradually, the variation of the bending moments is directly surprising. The change of the maximum deflections and of the bending moments in the middle of the plate is given in Fig. 6.11 and Fig. 6.12 in dependence on the relative flexural stiffness at the simultaneous creep of the materials of the plate and of the subgrade. The area of the change of the mentioned calculation magnitudes is limited by the lines  $t = 0$  and  $t = \infty$ . That area, as it can be seen, is very broad owing to the relaxation properties of plate and subgrade and leads to the contradictory results. While the deflection at time  $t = \infty$ , at the relative flexural stiffness  $k = 120$  increased 5,08-times, the bending moment decreased 1,54-times at the same relative flexural stiffness in comparison with the state of instantaneous warming.

## 2.4 Conclusions

Stress and deformation states of a plate strip with variable stiffness and Boussinesq half-space subjected to actions of discontinuous temperature field under assumption of plane deformation are investigated, the hereditary creep of the plate and of the subgrade materials according to different constitutive equations is applied. The formulation and the solution of the basic integro-differential equation system are performed in Laplace's transforms using an undirect way. The time dependent solution is constructed by means of modified Erdélyi - Schapery algorithm. The numerical method with a detailed analysis of the obtained results is demonstrated on a numerical example in the chapter 6.3.

This contribution is the result of the research supported by the grant from VEGA Slovak Grant Agency Project No. 1/0412/18.

## References

- Arutjunjan N.CH., Abramjan B.L. (1955) 'O temperaturnych naprjaženijach v prijamougol'nych betonnych blokach', *Izvestija AN Arm. SSR, Serija fiz.-mat. nauk*, T. VIII, vyp. 4.
- Boltzmann L.(1970) *Zur Theorie der elastischen Nachwirkung, Sitzungsberichte der Kaiserlichen Akademie der Wissenschaften*, Bd. 70, H. 6-10.
- Duhamel J.M.C.(1838) 'Mémoires sur le calcul des actions moléculaires développées par le changements de température dans les corps solides', *Mémoires présentés.par divers savants*, 5, 440.
- Farhatnia, F. et al. (2017) Thermal buckling analysis of functionally graded circular plate resting on the Pasternak elastic foundation via the differential transform method. *Facta Universitatis – Series Mechanical Engineering*. Volume: 15, Issue: 3, Pages: 545-563, WOS:000424114700015.
- Korotchenko, I. A. et al.(2017) Deformation of concrete creep in the thermal stress state calculation of massive concrete and reinforced concrete structures. *Magazine of Civil Engineering*, Volume: 69 Issue: 1 pp: 56-63, WOS:000405372100004 .
- Kovářík V. (1987) 'Problémy vazkopružnosti v teorii plošných konstrukcí', *Studie ČSAV*, Praha.
- Loom Y.M., Base G.D. (1990) 'Variation of creep Poisson's ratio with stress in concrete under short term uniaxial compression', *Magazine of Concrete Research*, 42. No. 151.
- Mesčjan S.R. (1967) *Polzučest' glinistych gruntov*, 1. izd., Erevan, Izd. AN ASSR.
- Mistrikova, Z. (2007) Creep of the louvre plate on the viscoelastic subgrade. In: *International Conference VSU 2007*, Sofia, Bulgaria, Vol. I. pp. I- 104-110.
- Mistrikova, Z. and Jendzelovsky, N. (2012) Static analysis of the cylindrical tank resting on various types of subsoil. *Journal of Civil Engineering and Management*, Volume: 18, Issue: 5, Pages: 744-751, DOI: 10.3846/13923730.2012.723346 .
- Moravkova, Z. et al. (2017) Beam rested on unilateral elastic foundation – (theory, experiments and finite element approach), Book Series: *Engineering Mechanics*, pp: 670-673, WOS:000411657600157
- Neville A.M. (1970) *Creep of concrete: Plain, reinforced and prestressed*, Amsterdam.
- Novotný B. (1980) 'An approximate Laplace transform inversion using

- exponential series representation', *Int. J. Num. Math. Engng.*, 15, č. 2.
- Nowacki W. (1963) *Thermoelasticity*, Warszawa, PWN - Pergamon Press
- Prokopovič J.E., Zedgenidze V.A. (1980) 'Prikadnaja teorija polzučesti, Moskva', *Strojizdat*.
- Sumec, J., et all (2010) Application of some linear viscoelastic mathematical models in continuum mechanics. In: *Book of Proceedings Structural and Physical Aspects of Civil Engineering*, Štrbské Pleso.
- Tvrda, K. (2010) Contact problem between the plate strip and the subgrade considering the creep effects, In: *Book of Proceedings Mechanical structures and foundation engineering 2010, International scientific conference MSFE 2010*, Ostrava.
- Volterra V. (1913) *Leçons sur les fonctions de lignes*, Paris.
- Zadojan M.A. (1957) 'Termonaprjažennoje sostojanije v blokach s učetom polzučesti materialov', *Izvestija AN Arn. SSR, Serija fiz.-mat. nauk*, T. X., vyp. 5.
- Zareckij Yu.K. (1993) *Soil viscoelasticity and design of structures*, A.A. Balkema, Rotterdam/Brookfield.



## 7. Harnessing digital image correlation system for assessing flexural characteristics of SFRC based on waste ceramic aggregate

**Jacek Katzer<sup>1</sup>, Jacek Domski<sup>2</sup>**

<sup>1</sup> Koszalin University of Technology, Faculty of Civil Engineering Environmental and Geodetic Sciences, Koszalin, Poland, [orcid.org/0000-0002-4049-5330](https://orcid.org/0000-0002-4049-5330)

<sup>2</sup> Koszalin University of Technology, Faculty of Civil Engineering Environmental and Geodetic Sciences, Koszalin, Poland, [orcid.org/0000-0002-5112-1035](https://orcid.org/0000-0002-5112-1035)

**Abstract:** The paper presents a research programme focused on steel fibre reinforced concrete based on waste ceramic aggregate. The matrix was reinforced by commercially available engineered steel fibre. Flexural tests were performed using a limit of proportionality method and values of crack mouth opening displacement were followed. The measurements were conducted simultaneously using two independent procedures: a traditional procedure described in the standard and a procedure based on optical measurements with the help of Digital Image Correlation System.

**Keywords:** aggregate, waste, ceramic, fibre, concrete

### 7.1. Introduction

Red waste ceramic is one of the key elements of the worldwide volume (particularly in Europe) of construction and demolition waste (Correia, De Brito and Pereira, 2006). It is increasingly recycled and in a form of waste ceramic aggregate (WCA) used for concrete production. So far, successful applications of WCA for concrete production is limited to elements characterized by lesser mechanical performance. Pavement slabs are the most common application of such concretes (Hendriks and Janssen, 2003; De Brito, Pereira and Correia, 2005). Multiple technological problems are associated with using WCA to substitute natural aggregate. There are issues associated both with properties of a fresh mix (workability and stability of a mix) and hardened concrete (small homogeneity of main mechanical properties and limited mechanical characteristics). Red ceramics is porous and thus characterized by very high water absorptivity. Designing methods commonly used for the creation of ordinary concrete mixes are not suitable for WCA based mixes. To overcome these technological and performance issues one can harness internal curing process (Bentur, Igarashi and Kovler, 2001; Suzuki, Seddik Meddah and Sato,

2009) and fibre reinforcement (Domski, 2015; Ponikiewski and Gołaszewski, 2015). Internal curing process which is associated with pre-saturation of porous aggregate guarantees stable and uniform properties of fresh concrete mix during all stages of mixing, handling and casting (Bentur, Igarashi and Kovler, 2001; Suzuki, Seddik Meddah and Sato, 2009). On the other hand, engineered steel fibre proved to be very effective in enhancing limited mechanical characteristics of concretes based on different types of waste aggregates (Katzer, 2008; Łapko, A., Grygo, 2014; Domski, 2015) and thus promising achieving similar improvement in case of WCA concrete (Domski, Katzer and Fajto, 2012). Using fibre reinforcement and WCA simultaneously may prove to be demanding due to irregularities in shape and size of WCA particles which often look like small blades rather than sphere-like grains. Size and shape of an aggregate particles directly influences fibre spacing in hardened concrete (Maidl, 1995; Johnston, 2000). Fibre agglomeration and non-uniform fibre distribution is much more likely to happen in WCA based concrete than in an ordinary mix affecting mechanical performance of the cast elements. Successful merging WCA based concrete and engineered fibre reinforcement would create new opportunities for sustainable development of construction and civil engineering industry. The first objective of the planned study was to evade technological problems with WCA and fibre reinforcement used simultaneously. The second objective was to test cast elements using two methods: traditional limit of proportionality (LOP) method (EN 14651, 2005) and a method based on optical measurements with the help of Digital Image Correlation (DIC) System. DIC is a validated and well-established method for determining displacements in the domain of experimental mechanics and vision-based optical metrology (Malesa and Kujawinska, 2012, 2013). It is being increasingly used to monitor civil engineering structures (Piekarczyk *et al.*, 2012). Nevertheless, feasibility of using DIC systems for testing SFRC is still unknown and needs to be studied. A comparison of results achieved by popular standard LOP method and DIC method bring a clear answer to this question.

## 7.2. Materials

Raw ceramic waste consisting of different types of broken and crushed ceramic elements (wall blocks, hollow bricks and wire-cut bricks) was used for the “production” of WCA in question. Debris was contaminated by cement mortar and represented the most common type of debris available in Europe (De Brito, Pereira and Correia, 2005). The WCA was created through grinding the debris using an electric industrial grinder. The grinder and grinding procedure were

thoroughly described in a previous publication (Cichocki *et al.*, 2014). As a result of grinding all-in-aggregate was achieved (see **Fig. 7.1**). Aggregate fractions characterized by a diameter larger than 32.0 mm and smaller than 1.0 mm were removed. The grading characteristics of prepared WCA was tested using rectangular sieve set (EN 933-1, 2012). Median diameter (Katzner, 2012) and fineness moduli characterizing the WCA were calculated. Loose and compacted bulk densities of the WCA were also tested (. The last tested property of WCA, which is crucial for mix designing and internal curing process, was water absorptivity by weight. All tested properties of WCA are presented in Table 7.1 (Cichocki *et al.*, 2014).

**Table 7.1.** Properties of WCA

Loose bulk density	Compacted bulk density	Water absorptivity by weight	Median diameter	Fineness modulus by		
				Hummel	Abrams	Kuczynski
[kg/m <sup>3</sup> ]	[kg/m <sup>3</sup> ]	[%]	[mm]	$m_H$	$m_A$	$m_K$
$\rho_{lbd}$	$\rho_{cbd}$	$A_w$	$d_m$	213.4	7.1	8.2
948	1170	22	7.4			




**Fig. 7.1.** Waste ceramic all-in-aggregate

Currently there is a dozen of large global producers of engineered steel fibre. Altogether they offer hundreds of steel fibre types differentiated by geometric



shape, size, diameter and finishing of surface (Maidl, 1995; Johnston, 2000; Naaman, 2003; Bentur and Mindess, 2007). Over 90% of the steel fibre available on the market is engineered steel fibre with deformed ends, treated surface, twisted, crimped or hooked. A hooked type of engineered steel fibre is the most popular on the global civil and structural engineering market (Domski, 2016). Properties of SFRC based on ordinary aggregates and reinforced by hooked engineered steel fibre are thoroughly tested and described in literature giving the best reference point for comparison and discussion (Zollo, 1997; Katzer and Domski, 2012). The chosen fibre was made of cold drawn wire (Group I with compliance to (EN 14889-1, 2006)) and was characterized by a circular cross-section. Mechanical and geometrical characteristics of the fibre are presented in Table 7.2.

**Table 7.2.** Mechanical and geometrical characteristics of the engineered steel fibre

Length	Diameter	Aspect ratio	FIER	Hook	Tensile strength	Ductility
$L$	$d$	$L/d$	$(\Psi \cdot L)/A^*$	$l + (a^2 + h^2)^{0.5} **$	$R_m$ ***	****
(mm)	(mm)	(-)	(-)	(mm)	(MPa)	(No bends)
60	0.75	80	135.88	5.75	1040	9
						
* - (Naaman, 2003); ** - (Katzer and Domski, 2012); *** - ISO 6892-1:2009; **** - EN 10218-1:2012						

Natural sand washed from all-in-aggregate of post-glacial origin during hydro-classification process was used as fine aggregate. The sand consists of quartz and crystalline rock, dominated by granite. It was thoroughly tested and described in a previous publication (Cichocki *et al.*, 2014). Portland cement CEM I 42.5 meeting the requirements of (EN 197-1, 2011) was utilized as a binder. Tap water in compliance with (EN 1008, 2002) was the last major ingredient. Mixes were modified by 1% of admixture to keep the required consistency. Silica fume modified superplasticizer of type FM and characterized by density of 1.45 g/cm<sup>3</sup> was harnessed as the admixture.

### 3.3. Procedures

WCA was fully saturated before the use. Mix composition computed for dry aggregates was adjusted to take into account water absorbed by WCA. Due to the fact that proportions of water absorbed by WCA influencing consistency and internal curing were unknown authors were forced to use the traditional “trial and error method”. The amount of needed tap water was established on the basis of a required consistency C2 (degree of compactability according to (EN 12350-4, 2009)). The final mix proportions of one cubic meter were as follows: fully saturated WCA – 830kg (the amount of trapped water – 182.6kg), natural sand – 652kg, cement – 307kg, tap water – 92kg, admixture – 3.1kg, giving together the total mass of 1884.1kg. Fibre reinforcement was added in volumes of 0.0%, 0.5%, 1.0% and 1.5%.

Cast specimens were in a form of cubes (150 mm · 150 mm · 150 mm) and prisms (150 mm · 150 mm · 550 mm). All specimens were compacted in two layers using a vibrating table. Curing was divided into two phases. Phase one lasted 24 hours and specimens were kept in moulds covered with polyethylene sheets. Phase two lasted 27 days and specimens were placed in a water tank (temp:  $+21^{\circ}\text{C} \pm 1^{\circ}\text{C}$ ).

Compressive strength and tensile splitting test were both tested on cube specimens. The tests were conducted according to (EN 12390-3, 2009) and (EN 12390-6, 2009) respectively. Flexural tensile strength was tested according to the limit of proportionality (LOP) method (EN 14651, 2005). The three-point flexural test was chosen as the most reliable one in comparison to four-point tests. In case of three-point test, a beam is formed with a notch and the first crack always appears in the vicinity of the mid-span. The crack mouth opening displacement (CMOD) was measured for all tested beams. The residual tensile strength  $f_R$  and the responses of SFRC prisms for CMOD equal to 0.5mm, 1.5mm, 2.5mm and 3.5mm were of special interest. The loading rate was equal to 0.2mm/min and load-CMOD curves were registered. The examination results were statistically processed, and values bearing the gross error were assessed on the basis of Grabb's criterion (Bayramov, Taşdemir and Taşdemir, 2004). This testing procedure was thoroughly described in a previous publication (Cichocki *et al.*, 2014). Flexural toughness was assessed for all tested concretes. Flexural toughness is very useful to evaluate the resistance of the fibre composites under dynamic loadings (impact, harmonic, fatigue) (Maidl, 1995; Johnston, 2000; Bentur and Mindess, 2007). During the research programme flexural toughness was understood as total energy absorbed in breaking a specimen in flexure. On the basis of force – deflection relationships achieved during the research programme there were calculated two values of toughness. The first was based on the area up to maximum load, the second was based on the area up to

a specified end-point deflection equal to 3.44 mm. Shear strength was tested according to (JCI-SF6, 1984). There were used prism specimens (half-beams leftovers after flexural tests) which were loaded using shear apparatus. During the test, load acts perpendicularly on the specimen at all times. Loading was applied to the specimen continuously without impact. The rate of loading was such that the increase in shear stress was from 0.06 MPa to 0.1 MPa. The objectivity of all conducted experiments was assured by the choice of the sequence of the realization using a table of random numbers.

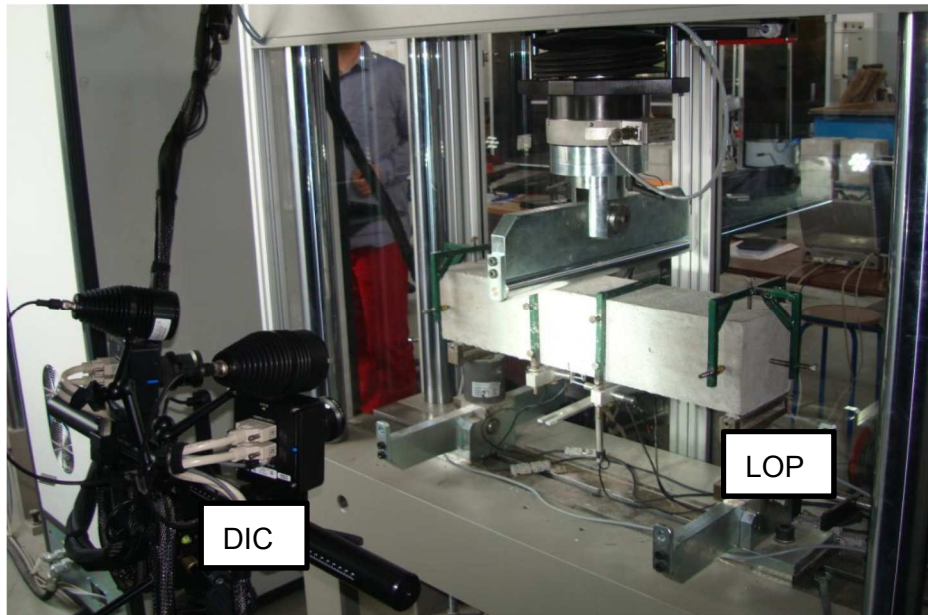


**Fig. 7.2.** Laboratory set-up used for flexural tests.

The whole process of flexural LOP test was simultaneously followed by DIC procedure. In **Figure 7.2** one can see the set-up of both apparatuses (LOP and DIC) during the flexural test of a prism specimen. DIC apparatus was focused on central (notched) part of a prism. During the research programme commercially available DIC apparatus of German origin was utilized. The apparatus was in a standard configuration offered by the producer. Two cameras were equipped with lenses characterized by the focal length of 2.8/50mm. Pictures were taken with the speed of 1 per second. The cameras' angle setting was equal to 25°. Cameras were located 334 mm away from each other. The distance to an observed beam was equal to 820mm. The adopted facet size was 19 pixels and facet step was 15 pixels. Two halogen spotlights (20W each)

provided by the producer of the apparatus were used to light the tested part of a beam.

DIC is a well-established method for estimation of displacements in experimental mechanics and optical metrology (Malesa and Kujawinska, 2012, 2013). The method was introduced in the early 1980s. Since then the quality of digital images has improved enormously and harnessed algorithms have gone through multiple mayor modifications. The technological development of DIC enabled new areas of its application. DIC technique entered civil and structural engineering and are being more and more often utilized for testing specimens and most recently whole structures (Piekarczyk *et al.*, 2012). The main advantage of using DIC technique in comparison to traditional gauges and sensors techniques is the ability to observe thousands of points simultaneously in 3-D. Using such technique in case of SFRC elements seems to be very promising.

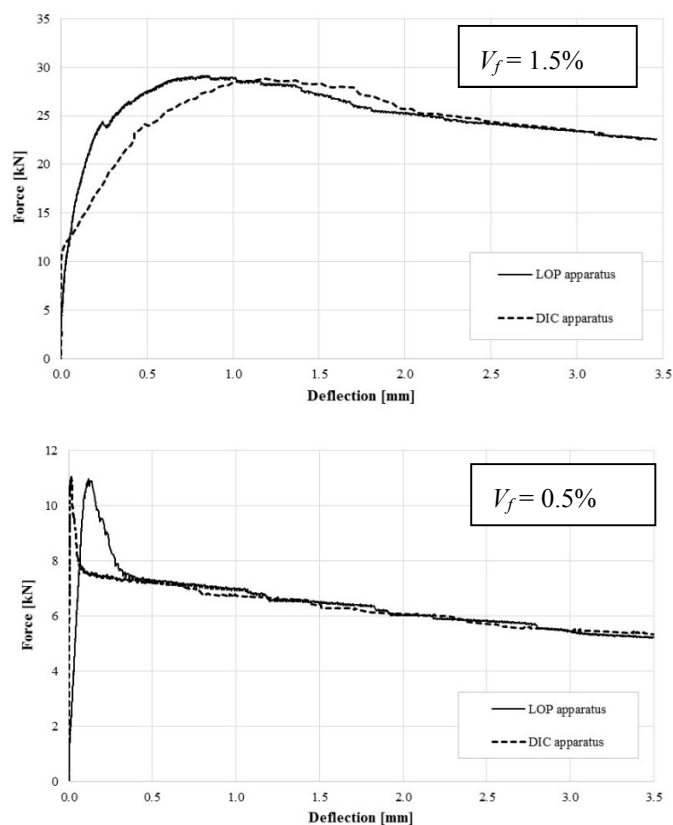


Fig. 7.3. Flexural characteristics of tested SFRC.

SFRC is much more demanding in testing than ordinary concrete or even traditionally reinforced concrete elements. Comparison of results achieved by means of standardized LOP method and by DIC method would give a preliminary answer to the question if LOP method could be substituted by DIC method. There is also very large potential space for developing brand new testing methodology of SFRC based solely on DIC method. Such a new testing procedure would be very useful in case of SFRC based on waste aggregate which is even more difficult for testing than ordinary SFRC while using traditional standardized methods. During the research programme commercially available DIC apparatus with dedicated computer and software was used.

## 7.4. Results and discussion

Results of density, compressive strength, splitting tensile strength and shear strength are presented in **Table 7.3**. In case of all tested strengths fibre reinforcement significantly improves the mechanical characteristics of WCA concrete. Changes in values of splitting tensile strength and shear strength mirror the behaviour of ordinary concrete reinforced by engineered steel fibre (Maidl, 1995; Johnston, 2000; Bentur and Mindess, 2007). Compressive strength was improved by 11.8% and 29.4% for fibre volume of 0.5% and 1.5% respectively. These values are much higher in comparison to ordinary concrete reinforced by the same volume of hooked steel fibre (Zollo, 1997; Domski, 2016).

**Table 7.3.** Mechanical properties of tested SFRC

Properties			Fibre $V_f$ [%]		
			0.0	0.5	1.5
Density of hardened concretes [kg/m <sup>3</sup> ]			2001	2006	2096
Strength [MPa]	Compressive		39.1	43.7	50.6
	Splitting tensile		3.1	3.4	5.4
	Shear		5.0	7.3	11.6
Flexural toughness [kN·mm]	LOP	Maximum loading force	0.0	0.8	20.4
		Deflection 3.44mm	0.0	22.2	86.6
	DIC	Maximum loading force	0.0	0.6	27.6
		Deflection 3.44mm	0.0	22.7	83.2

In Figure 7.3 flexural characteristics of tested SFRC are presented in a form of force-deflection relations. Two sets of force-deflection relation are available for each SFRC: prepared on the basis of LOP apparatus and DIC apparatus. DIC based relation was created using multiple strain images. One can follow the whole process of crack forming, crack opening and destruction of a specimen in

these images. DIC strain images for the start of the flexural test, crack forming and ultimate destruction of the specimens are presented in Figure 7.4 and Figure 7.5 for prism with  $V_f = 0.5\%$  and  $1.5\%$  respectively. The images are prepared in artificial colours mirroring strain values from 0% to 100%. Both sets of relations (obtained from LOP and DIC procedures) enabled calculations of flexural toughness (see Table 7.3) and residual strengths (see Table 7.4). Flexural toughness representing the amount of energy needed to ultimately destroy a SFRC specimen is almost the same for LOP and DIC results in case of low ( $V_f = 0.5\%$ ) volume of added fibre. For the large volume of fibre ( $V_f = 1.5\%$ ) results differ significantly. DIC gives the value of flexural toughness larger than LOP for maximum loading (by 35.3%) but smaller for deflection of 3.44mm (by 3.9%). The residual strengths  $f_{R1}$ ,  $f_{R2}$ ,  $f_{R3}$ ,  $f_{R4}$  were calculated according to (EN 14651, 2005) and they correspond to values of Crack Mouth Opening Displacement (CMOD) of 0.5 mm, 1.5 mm, 2.5 mm and 3.5 mm respectively. Strength classes were assigned to tested SFRC using value of  $f_{R1}$  (representing the strength interval) and the  $f_{R3}/f_{R1}$  ratio (codified by letters  $a$ ,  $b$ ,  $c$  and  $d$  - *fib* Model Code 2010). This classification represents the most common cases of hardening and softening of SFRC (where  $a$  stands for “pure” softening and  $d$  stands for “pure” hardening). Traditional rebar and stirrup reinforcement substitution was assessed using the  $f_{R3}/f_{R1}$  and  $f_{R1}/f_{LOP}$  ratios. According to the *fib* Code  $f_{R1}$  and  $f_{R3}$  are significant for service limit states (SLS) and ultimate limit states (ULS) respectively. The traditional reinforcement substitution is enabled if the  $f_{R3}/f_{R1}$  and  $f_{R1}/f_{LOP}$  ratios are larger than 0.5 and 0.4 respectively.

**Table 7.4.** Residual strengths, strength class and traditional reinforcement substitution

Residual strengths (MPa)	$V_f = 0.5\%$		$V_f = 1.5\%$	
	LOP	DIC	LOP	DIC
$f_{LOP}$	4.3	4.6	6.7	5.4
$f_{R1}$	3.1	3.0	11.3	9.8
$f_{R2}$	2.9	2.8	12.0	11.9
$f_{R3}$	2.7	2.5	10.4	10.5
$f_{R4}$	2.5	2.3	9.8	9.7
Strength class classification and traditional reinforcement substitution				
$f_{R3}/f_{R1} > 0.5$	0.87	0.83	0.92	1.07
$f_{R1}/f_{LOP} > 0.4$	0.72	0.65	1.69	1.81
Class	3b	3b	11c	9c
Substitution	enabled	enabled	enabled	enabled

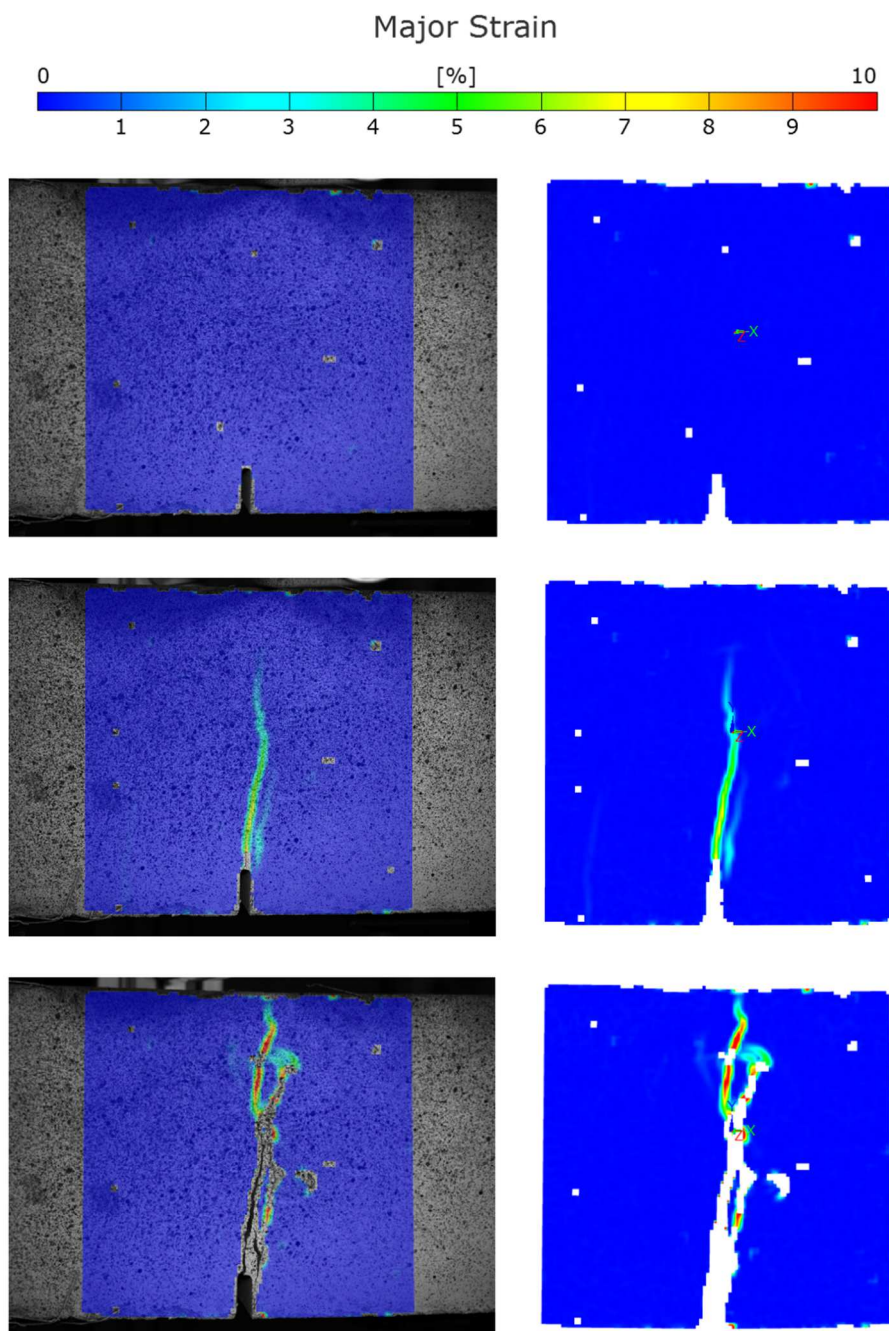


**Fig. 7.4.** Crack opening – prism with  $V_f = 0.5\%$  – DIC strain image



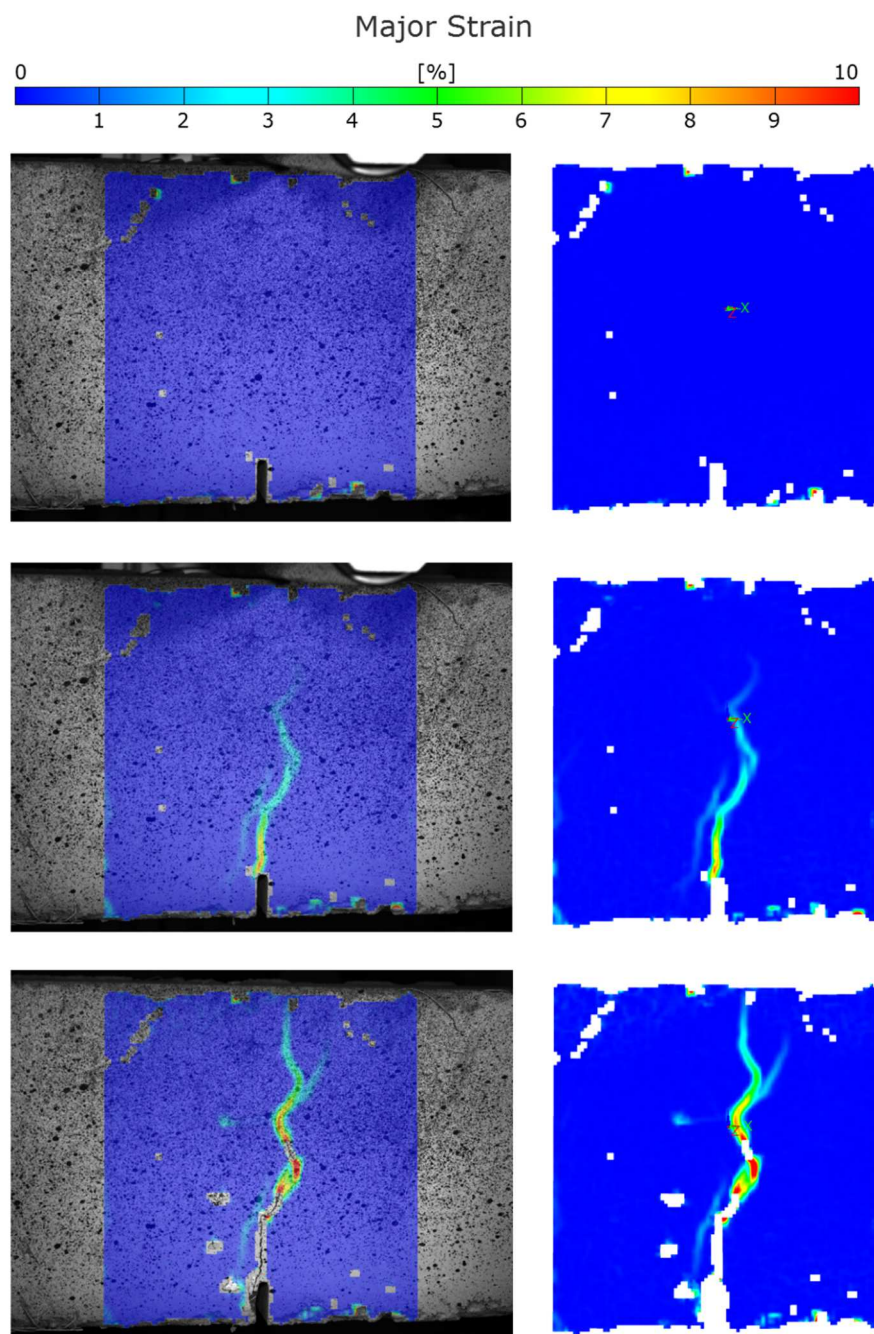


**Fig. 7.5.** Crack opening – prism with  $V_f = 1.5\%$  – DIC strain image



Both tested SFRC achieved results by LOP and DIC methods enabling a traditional reinforcement substitution. All residual strengths calculated for SFRC with  $V_f$  equal to 0.5% are very similar for both methods. In case of SFRC reinforced by 1.5% of fibre DIC method gave lower values of  $f_{LOP}$  (by 18.4%) and  $f_{RI}$  (by 13.3%) and thus significantly influencing strength class and assessment of traditional reinforcement substitution. Differences in values of other residual strengths are less than 1%. Following the force-deflection relations in Figure 7.3 one can notice that the elastic part of the curves is much steeper for DIC method and influencing the initial part of the plastic part of the curves. For large deflections both methods gave the same relations. This phenomenon is probably associated with accuracy of the DIC method which was originally developed for testing steel and other metals. SFRC, as quasi-plastic material behaves in a very specific way which is challenging for DIC.

## 7.5 Conclusions

The conducted research programme allows to draw the following conclusions:

- Flexural characteristics of SFRC based on WCA enables traditional reinforcement substitution.
- Force-deflection characteristics achieved by LOP and DIC methods are similar, but differences (especially in case of elastic part of the relations) are noticeable.
- Flexural toughness calculated for LOP and DIC results is very similar in case of low volume of added fibre ( $V_f = 0.5\%$ ).
- There are differences in calculated values of flexural toughness for LOP and DIC results for large volume of added fibre ( $V_f = 1.5\%$ ) ranging from -3.9% to +35.3%.
- LOP and DIC method give very similar results in case of low volume of added fibre ( $V_f = 0.5\%$ ) resulting in assignment of the same strength class.
- LOP and DIC methods give significantly different results in case of large volume of added fibre ( $V_f = 1.5\%$ ) resulting in assignment of a different strength class.
- DIC method can be used for testing SFRC, but caution and awareness of DIC accuracy should be maintained.
- Research programmes should be conducted focusing on different SFRC, steel fibre volumes and fibre types utilizing LOP and DIC testing methods.

## Acknowledgements

The first version of this paper was presented at international conference CONCRETE 2017 “Advances in Concrete Materials and Structures” which took place in Adelaide (South Australia) between 22<sup>nd</sup> and 25<sup>th</sup> October 2017. This is the amended and extended version of this paper.

## References

- Bayramov, F., Taşdemir, C. and Taşdemir, M. A. (2004) ‘Optimisation of steel fibre reinforced concretes by means of statistical response surface method’, *Cement and Concrete Composites*, 26(6), pp. 665–675. doi: 10.1016/S0958-9465(03)00161-6.
- Bentur, A., Igarashi, S. I. and Kovler, K. (2001) ‘Prevention of autogenous shrinkage in high-strength concrete by internal curing using wet lightweight aggregates’, *Cement and Concrete Research*, 31(11), pp. 1587–1591. doi: 10.1016/S0008-8846(01)00608-1.
- Bentur, A. and Mindess, S. (2007) *Fibre Reinforced Cementitious Composites, Modern Concrete Technology Series*.
- De Brito, J., Pereira, A. S. and Correia, J. R. (2005) ‘Mechanical behaviour of non-structural concrete made with recycled ceramic aggregates’, *Cement and Concrete Composites*, 27(4), pp. 429–433. doi: 10.1016/j.cemconcomp.2004.07.005.
- Cichocki, K. *et al.* (2014) ‘Impact resistant concrete elements with nonconventional reinforcement’, *Rocznik Ochrona Środowiska*, 16(2), p. 136.
- Correia, J. R., De Brito, J. and Pereira, A. S. (2006) ‘Effects on concrete durability of using recycled ceramic aggregates’, *Materials and Structures/Materiaux et Constructions*, 39(2), pp. 169–177. doi: 10.1617/s11527-005-9014-7.
- Domski, J. (2015) ‘Long-term study on Fibre reinforced fine aggregate concrete beams based on waste sand’, *Rocznik Ochrona Srodowiska*, 17(1), pp. 188–199.
- Domski, J. (2016) ‘A blurred border between ordinary concrete and SFRC’, *Construction and Building Materials*, 112, pp. 247–252. doi: 10.1016/j.conbuildmat.2016.02.205.
- Domski, J., Katzer, J. and Fajto, D. (2012) ‘Load-CMOD characteristics of fibre reinforced cementitious composites based on waste ceramic aggregate’, *Rocznik Ochrona Srodowiska*, 14(1), pp. 69–80.
- EN 1008 (2002) ‘Mixing water for concrete: Specification for sampling, testing and assessing the suitability of water, including water recovered from processes in the concrete industry, as mixing water for concrete.’, *European*

- Committee for Standardization*, p. 22.
- EN 12350-4 (2009) 'Testing fresh concrete. Degree of compactability.', *European Committee for Standardization*, p. 8.
- EN 12390-3 (2009) 'Testing hardened concrete. Compressive strength of test specimens.', *European Committee for Standardization*, p. 22.
- EN 12390-6 (2009) 'Testing hardened concrete. Tensile splitting strength of test specimens', *European Committee for Standardization*, p. 14.
- EN 14651 (2005) 'Test method for metallic fibre concrete - Measuring the flexural tensile strength (limit of proportionality (LOP), residual)', *European Committee for Standardization*, p. 20.
- EN 14889-1 (2006) 'Fibres for concrete. Steel fibres - Definitions, specifications and conformity', *European Committee for Standardization*, p. 30.
- EN 197-1 (2011) 'Cement. Composition, specifications and conformity criteria for common cements', *European Committee for Standardization*, p. 48.
- EN 933-1 (2012) 'Tests for geometrical properties of aggregates. Determination of particle size distribution. Sieving method', *European Committee for Standardization*, p. 20.
- Hendriks, C. F. and Janssen, G. M. T. (2003) 'Use of recycled materials in constructions', *Materials and Structures*, 36(9), pp. 604–608. doi: 10.1007/bf02483280.
- JCI-SF6 (1984) 'Method of test for shear strength of fibre reinforced concrete', *JCI Standards for test methods of fiber reinforced concrete*, p. 4.
- Johnston, C. D. (2000) *Fiber-reinforced cements and concretes*. Gordon & Breach.
- Katzer, J. (2008) 'Properties of Precast SFRCC Beams under Harmonic Load', *Science and Engineering of Composite Materials*, 15(2), pp. 107–120. doi: 10.1515/SECM.2008.15.2.107.
- Katzer, J. (2012) 'Median diameter as a grading characteristic for fine aggregate cement composite designing', *Construction and Building Materials*, 35, pp. 884–887. doi: 10.1016/j.conbuildmat.2012.04.050.
- Katzer, J. and Domski, J. (2012) 'Quality and mechanical properties of engineered steel fibres used as reinforcement for concrete', *Construction and Building Materials*, 34, pp. 243–248. doi: 10.1016/j.conbuildmat.2012.02.058.
- Łapko, A., Grygo, R. (2014) 'Effectiveness of the Use of Recycling Aggregate Concrete for Sustainable Building Structures', *Rocznik Ochrona Środowiska*, 16(1), pp. 627–638.
- Maidl, B. R. (1995) *Steel fibre reinforced concrete*. Ernst & Sohn.
- Malesa, M. and Kujawska, M. (2012) 'Modified two-dimensional digital image correlation method with capability of merging of data distributed in

- time', *Applied Optics*. Optical Society of America, 51(36), pp. 8641–8655. doi: 10.1364/AO.51.008641.
- Malesa, M. and Kujawinska, M. (2013) 'Deformation measurements by digital image correlation with automatic merging of data distributed in time', *Applied Optics*. Optical Society of America, 52(19), pp. 4681–4692. doi: 10.1364/AO.52.004681.
- Naaman, A. E. (2003) 'Engineered Steel Fibers with Optimal Properties for Reinforcement of Cement Composites', *Journal of Advanced Concrete Technology*, 1(3), pp. 241–252. doi: 10.3151/jact.1.241.
- Piekarczyk, A. *et al.* (2012) 'Application of Hybrid FEM-DIC Method for Assessment of Low Cost Building Structures', *Experimental Mechanics*. Springer US, 52(9), pp. 1297–1311. doi: 10.1007/s11340-012-9616-2.
- Ponikiewski, T. and Gołaszewski, J. (2015) 'X-Ray Investigation And Modelling Of Steel Fibres In Self-Compacting Concrete', *Transactions of the VŠB – Technical University of Ostrava, Civil Engineering Series.*, 15(2), p. #20. doi: 10.1515/tvsb-2015-0020.
- Suzuki, M., Seddik Meddah, M. and Sato, R. (2009) 'Use of porous ceramic waste aggregates for internal curing of high-performance concrete', *Cement and Concrete Research*, 39(5), pp. 373–381. doi: 10.1016/j.cemconres.2009.01.007.
- Zollo, R. F. (1997) 'Fiber-reinforced concrete: an overview after 30 years of development', *Cement & Concrete Composites*, 19(2), pp. 107–122. doi: 10.1016/S0958-9465(96)00046-7.



## 8. An experimental analysis of the determination of the elastic modulus of cementitious materials

**Dalibor Kocáb<sup>1</sup>, Barbara Kucharczyková<sup>2</sup>, Romana Halamová<sup>3</sup>**

<sup>1</sup> *Brno University of Technology, Faculty of Civil Engineering, Brno, Czech Republic, [orcid.org/0000-0002-8273-4571](https://orcid.org/0000-0002-8273-4571)*

<sup>2</sup> *Brno University of Technology, Faculty of Civil Engineering, Brno, Czech Republic, [orcid.org/0000-0002-7123-5099](https://orcid.org/0000-0002-7123-5099)*

<sup>3</sup> *Brno University of Technology, Faculty of Civil Engineering, Brno, Czech Republic, [orcid.org/0000-0001-9399-3694](https://orcid.org/0000-0001-9399-3694)*

**Abstract:** The paper is focused on experimental analysis of cementitious materials. The determination of the elastic modulus is of special interest. The experiment results showed the elastic modulus of cementitious materials can be determined during initial stages when the internal microstructure is still beginning to form.

**Keywords:** elastic modulus, cementitious materials, experimental analysis

### 8.1. Introduction

Over its fairly short existence, concrete has become one of the most commonly used building materials (Abdelgader *et al.*, 2014, Aïtcin 1998). The rapid development in this area had the effect that the concrete of today must meet far stricter requirements than the concrete of several decades ago (Tsai and Hsu, 2002). Unlike the past, compressive strength is no longer the only important property (Cikrle and Bilek, 2010); other characteristics have been the subject of attention of engineers and researchers and have been extensively measured and discussed. Aside from the commonly examined parameters, such as durability, shrinkage, or sustainability and environmental impact, these are mainly deformation properties, the most notable of which is the modulus of elasticity (Tang *et al.* 2015, Collepardi, 2010). Development of new types of concrete, e.g., self-compacting (SCC), high-strength (HSC), ultra-high-performance (UHPC), or freshly compressed concrete (FCC) (Nematzadeh and Naghipour 2012), has been shifting the boundaries of material characteristics and concrete properties (Dehestani *et al.* 2014, Ma *et al.* 2016, Procházka *et al.* 2011, Parra *et al.* 2011). The use of various modern admixtures and additives can significantly improve the compressive strength of concrete (often exceeding 200 N/mm<sup>2</sup>),

however, their effect may not be as strong in terms of increasing the modulus of elasticity (Gu *et al.* 2015).

The modulus of elasticity is one of the most important physical properties that characterise a material. Concrete is undoubtedly one such material, especially when it comes to structural calculations. The elastic modulus is an important parameter for calculating deflections and creep especially in long-span elements and in pre-stressed or post-tensioned structures (Navrátil 2008, Neville and Brooks 2010, CEB-FIP Model Code 1990, 1993). Besides deformation calculations, in structurally uncertain buildings it also enters the calculation of internal forces; it thus affects the determination of the limit states of the load-bearing capacity. The elastic modulus is indicative of the deformation behaviour of concrete structures, such as deflections, shifts, shrinkage, or elevation in pre-stressed elements (Ma *et al.* 2016). This is why it has recently seen extensive investigation by a rising number of experts, companies, and institutions (Křížová *et al.* 2013, Huňka and Kolísko 2011).

## 8.2. Theoretical background

In order to properly explain the concept of the elastic modulus, it is necessary to start in broader terms, i.e. the theory of elasticity and plasticity. The two main points of examination in the theory of elasticity are stress and strain. The theories of elasticity and plasticity draw on fields that focus on studying the strength of materials, which is the ability of a material to resist external forces without sustaining damage. In civil engineering, elasticity and plasticity constitute the foundation for the theory of structures.

In elastic materials there is a clear dependence between stress and strain caused by stress, which applies in all stages of its action, i.e. during loading, unloading, loading in the opposite direction, etc. In an elementary body stressed along the  $x$  axis there is a linear relationship between strain  $\varepsilon_x$  and normal stress  $\sigma_x$  expressed by Hooke's law as:

$$\sigma_x = E \cdot \varepsilon_x \quad (8.1)$$

Where:

- $\sigma_x$  – stress in N/mm<sup>2</sup>,
- $E$  – modulus of elasticity (also Young's modulus) in N/mm<sup>2</sup>,
- $\varepsilon_x$  – strain in [-].

A precise relationship between changes in the shape and dimensions of bodies and the loading of a real material by external forces can never be precisely determined in advance, because it depends on many factors, mainly the properties of the material. It cannot even be derived from the physical nature of

the material being tested. However, when designing building structures or elements, and especially when determining their deformation, the knowledge of the calculation characteristics corresponding to this dependence is necessary. The relationship between the deformation of solid bodies caused by external forces can be plotted as an idealised  $F-d$  curve, or, after conversion, as a  $\sigma-\varepsilon$  curve, see e.g. (Neville 2011). In real materials, the curves are substantially more complicated. However, the records of their real progress can usually be approximated and replaced part by part by the ideal curves (Navrátil 2008, Neville 2011).

The real behaviour concrete is more complex. Several types of the compressive modulus of elasticity can be identified depending on which part of the stress-strain curve is considered and what type of line (tangent or secant) is fitted (Newman and Choo 2003, Neville 2011, Navrátil 2008). The initial modulus of elasticity is identified by the standard (EN 1992-1-1 2004 and Navrátil 2008) as  $E_c$ , the other standard (EN 12390-13 2013)  $E_{c,0}$  and in (Huňka 2014) it is  $E_0$ . This is a modulus of elasticity that concrete should exhibit at very low stress. According to the standard (EN 1992-1-1 2004) its value can be considered 1.05 times of the secant modulus of elasticity  $E_{cm}$ . The value of the static modulus of elasticity commonly considered for ordinary concrete ranges between 20 and 40 GPa (Neville 2011). On the other hand, the dynamic modulus of elasticity reaches higher values, ranging from 30 to 50 GPa for ordinary concrete. The determination of the dynamic value operates with the very beginning of the stress-strain curve, because the specimen suffers virtually no strain. The dynamic modulus can thus be considered tangent (Neville 2011). However, it is different from the initial (also tangent) modulus of elasticity given the way it is defined in (EN 1992-1-1 2004, EN 12390-13 2013). The ratio between the static and dynamic values of the elastic modulus is substantially higher than 1.05 as written therein.



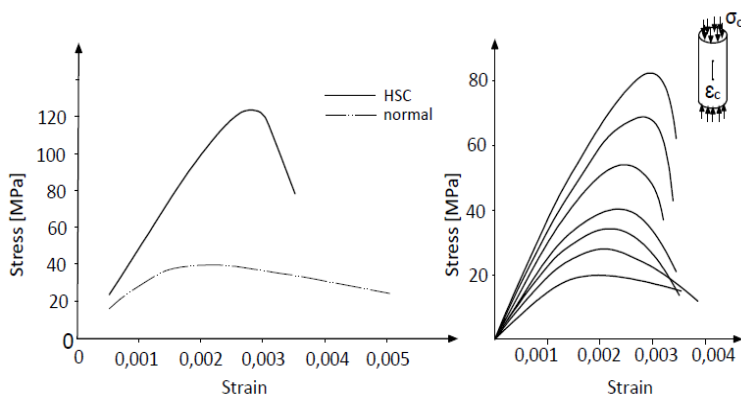


**Fig. 8.1.** Idealised comparison of stress-strain curves for high-strength and ordinary concrete in compression (Newman and Choo 2009) (left) and real stress-strain curves for concrete in compression (Nilson and Winter 1991) (right)

It must be understood that, unlike e.g. steel, the elastic modulus of concrete is not one specific number, but can vary due to a number of reasons, and in some situations this variation may be rather significant. It is also given by the way the stress-strain curves are plotted (the slope of the first part of the diagram) for concretes of varying strength. Fig. 8.1 compares stress-strain curves from different authors.

The elastic modulus of concrete in compression (tension) depends mainly on its composition, which affects all of its properties (CEB-FIP Model Code 1990, 1993, Yildirim and Sengul 2010, Hela and Křížová 2011). Still, it would be wrong to say that composition is the only factor. There are a great number of factors that affect the final value of the elastic modulus (Lydon and Iacovou 1995). These can be divided into technological and testing-related ones (Huňka *et al.* 2013). Composition is undoubtedly a technological factor. The elastic modulus will be affected mainly by the type of aggregate (Mitrenga 2011, Aïtcin 1998), but also by the content of admixtures, especially air-entraining (Vymazal *et al.* 2011), various other additives and their amount (Křížová *et al.* 2013), or the w/c ratio (Newman and Choo 2003, Neville and Brooks 2010). Another one of these factors can also be the curing conditions present during early stages of setting and hardening. The ambient temperature is the most decisive factor in that respect. Curing especially in difficult conditions – in winter (concrete must be heated during construction at temperatures below freezing), or in summertime (concrete must be protected from desiccation at high temperatures) – is an important factor that influences the elastic modulus in

no small way (Kocáb *et al.* 2017). Fig. 8.2 – 8.5 display examples of the technological factors influencing the value of the elastic modulus.

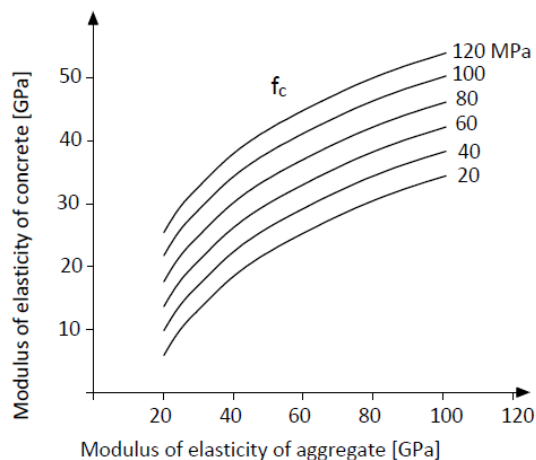


**Fig. 8.2.** Nomogram of the dependence of the elastic modulus of concrete on the elastic modulus of aggregate and compressive strength (Aïtcin 1998)

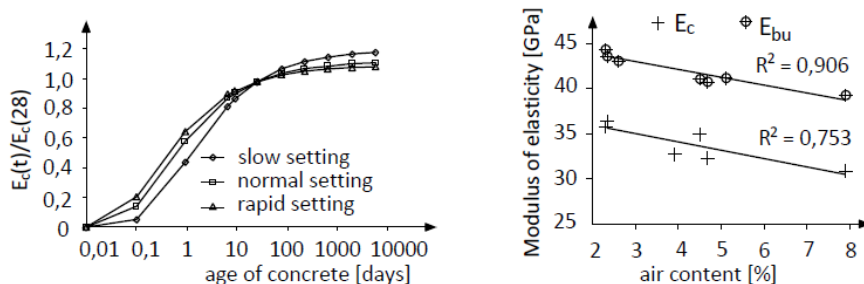


**Fig. 8.3.** Development of the modulus of elasticity (CEB-FIP Model Code 1990, 1993); the x axis has a logarithmic scale (Navrátil 2008) (left); plot of the dependence of the static ( $E_c$ ) and dynamic modulus of elasticity ( $E_{bu}$ ) on air content (Vymazal *et al.* 2011) (right)

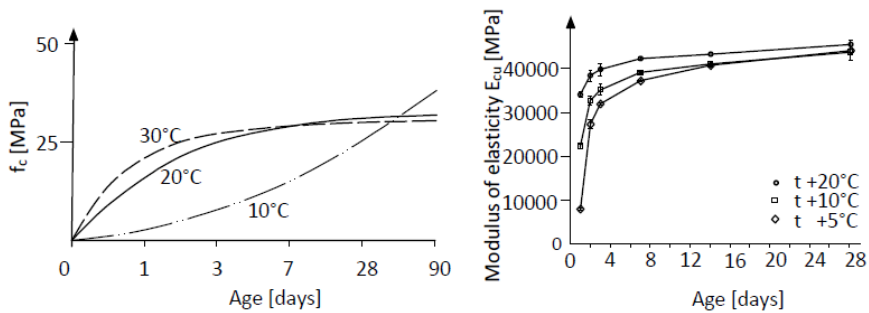


**Fig. 8.4.** Influence of the ambient temperature on the development of compressive strength (Collepari 2010) (left) and on the development of the dynamic modulus of elasticity (Kocáb *et al.* 2017) (right)

Another category of factors influencing the value of the elastic modulus are testing-related factors. This category includes, e.g., the choice of method to determine the elastic modulus, what specimens are used, or how the ends of the specimens are finished (Huňka 2014). Technological factors can be seen as real factors, because, for instance, using a different aggregate results in a real change in the value of the modulus of elasticity. On the other hand, the testing-related factors can be seen as largely “apparent”. While a measurement of the modulus of elasticity performed on a cylinder will return a different value than measurement made on a prism, the real value of the modulus of elasticity for that particular concrete remains the same.

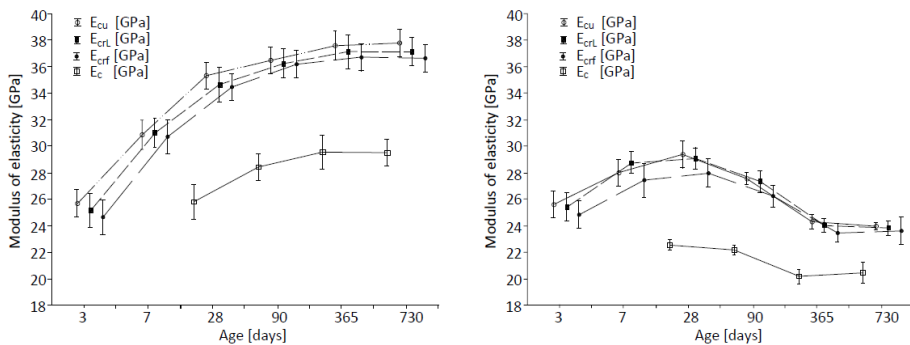


**Fig. 8.5.** Diagram of the progress of the average values of elastic moduli for concrete; a) set of cured specimens and b) set of uncured specimens (Kocáb *et al.* 2017)

If we do try to categorise testing factors, we can establish two basic groups - those that can be influenced (e.g., specimen preparation, loading rate, etc.) and those that cannot (method for determining the dynamic modulus vs. the static modulus of elasticity). One must also realise that the modulus of elasticity measured on a specimen will never quite correspond to the real modulus of concrete used in a structure – the concrete in the specimens ages differently than concrete in a structure. If the modulus of elasticity is measured on a structure, one is faced with limitations of the testing methods or equations for calculation.

There are multiple methods that can be used to determine the value of the elastic modulus of concrete. A basic division can be the method of measuring the elastic modulus; static methods make use of introducing load to the specimen while measuring strain, while dynamic methods usually operate on non-destructive electroacoustic principles and use the physical law for flexural wave propagation in solids (Huňka 2014). In general, the value of the dynamic modulus of elasticity tends to be higher than the value of the static modulus. The difference between the static and dynamic value depends mostly on the quality and age of the concrete. A general rule is that the lower the quality of the concrete (or the younger the concrete), the smaller the ratio between the static and dynamic modulus (can be as low 0.6). On the other hand, in very high-quality concretes this ratio can be relatively high (approx. 0.9). It is thus clear that measurements e.g. by the resonance method, which returns the dynamic (tangent) modulus of elasticity, the result will be a different number than using, e.g., the compressive strength test, which returns the static (secant) modulus of elasticity. Moreover, neither static methods (mostly compression and flexural load) nor dynamic methods (ultrasonic pulse velocity, resonance, or the impact-echo test) give the same result. Another factor is the shape and size of specimens and also the quality and a flatness of the surfaces which are in direct contact with the plates of testing machine.

The testing of the modulus of elasticity carries with it a multitude of other factors that influence the modulus of elasticity, although mostly only in a small way – e.g. the material and dimensional accuracy of the moulds used to make the specimens, the type of instrument used (e.g. ultrasonic tester or strain gauge), or the loading rate during the compressive strength test when determining the static modulus of elasticity (Huňka *et al.* 2013).

In recent years, interest in the trend of the elastic modulus value development during the early hardening increased. This is related to the shrinkage strain, especially to the determination of the critical stress inducing the cracks initiation.

Such analysis focused on the determination of the early elastic modulus value was also performed by authors of this chapter. The description of the experiment, results and main conclusions are given in the next paragraphs.

## **8.5. Materials and methods**

Most of the above-described testing methods are designed to determine the modulus of elasticity by making measurements on hardened cement materials. However, in many cases (a need to remove formwork early, installing tensioning cables at ages of less than 4 hours) it is necessary to know the development of the modulus of elasticity of a concrete during the setting and early hardening. The main goal of the experiment described herein was thus to explore the possibilities of determining the modulus of elasticity of cement-based materials during the first 3 days of age. The experiment has several stages, but only the first stage (when cement pastes were tested) is described here. The subsequent stages used cement mortars and later also concretes. However, first, it is good to verify the possibilities of determining the modulus of elasticity using basic materials – in this case cement pastes.

Six cement pastes were made using cement CEM I 52.5 R (Mokrá, Czech Republic), a half of which contained plasticiser Sika ViscoCrete 4035 at an amount of 1 % of cement mass. Pastes without plasticiser had the w/c ratio equal to 0.50, 0.40 and 0.33. The lowest w/c ratio corresponds to the lowest theoretical amount of water required for the cement to fully hydrate. These pastes were identified as 050, 040, and 033. Pastes with plasticiser had the same w/c ratio as the pastes without plasticiser and were named P050, P040, and P033. Each cement paste was made into nine prism-shaped specimens with the nominal dimensions of  $40 \times 40 \times 160$  mm and one specimen in the shape of Vicat's ring, see Fig. 8.6. The ring specimen was used for continuous measurement of the dynamic modulus of elasticity during the first 24 hours using an ultrasonic device. The apparatus consists of measurement cell/chamber equipped with the ultrasonic probes and datataker, where the data are stored in the interval of 60 sec. The strength of the signal was set to 2000 V for the purpose of early measurement. The prisms were used for measuring the dynamic and static modulus of elasticity at an age of 24 through 72 hours. Over the first 24 hours the prisms were left in plastic moulds under standard laboratory conditions at an ambient temperature of  $(22 \pm 2)$  °C and relative humidity of  $(55 \pm 5)$  %, covered with a PE sheet. At the age of 24 hours they were demoulded, four were non-destructively and later destructively tested and the remaining four were wrapped in the PE sheet and left to age in the same

conditions. These other four specimens were used for determining the modulus of elasticity at the age of 48 and 72 hours.



**Fig. 8.6.** Specimens – 9 prisms of  $40 \times 40 \times 160$  mm and 1 Vicat's ring

Once the cement paste was mixed, the next step was filling the Vicat's ring and placing it in the measurement chamber of the ultrasonic measurement device. The apparatus is pictured in Fig. 8.7, refer to (<http://www.schleibinger.com>) for more details. The ring with the setting cement paste is positioned between two transducers running at 54 kHz, one of which is a transmitter and the other a receiver of the ultrasonic pulse. The instrument continuously records the transit time of ultrasonic waves travelling through the material, which is primarily designed to measure the setting time. Given the fact that the instrument's design ensures a constant distance from the measurement base (40 mm), it is possible to calculate the ultrasonic pulse transit velocity and subsequently also values of the dynamic modulus of elasticity over the observed time period using the following formula (included in the manual to the instrument):

$$E = \rho \cdot v^2 \quad (8.2)$$

Where:

- $E$  – dynamic modulus of elasticity in  $\text{N/mm}^2$ ,
- $\rho$  – bulk density in  $\text{kg/m}^3$ ,
- $v$  – ultrasonic pulse velocity in  $\text{km/s}$ .

A slight disadvantage of this measurement and subsequent calculation of the dynamic modulus of elasticity is the fact that the equation (eq. 8.2) does not take into account Poisson's ratio, which typically enters the calculation when using the ultrasonic pulse velocity test.

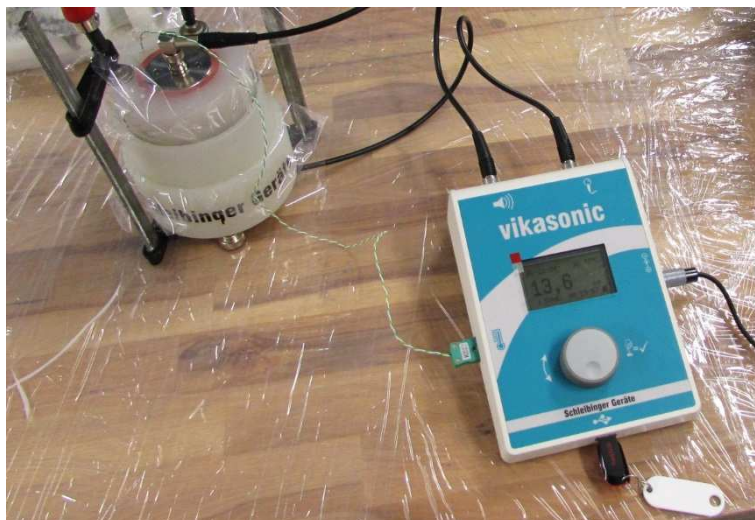


**Fig. 8.7.** Measurement using the ultrasonic device during setting and early hardening

During the first 24 hours of ageing the modulus of elasticity was thus observed using the ultrasonic apparatus. At ages 24 through 72 hours, other test methods were applied using the prisms as specimens for measurement. As mentioned earlier, the first four specimens were tested for the modulus of elasticity at an age of 24 hours. The dynamic modulus of elasticity was measured again using the ultrasonic pulse velocity test, however, using an ultrasonic device (<https://www.proceq.com>) as well as using the resonance method. The natural frequencies of longitudinal, flexural, and torsional vibration of the specimens were measured using an oscilloscope with an acoustic emission sensor. The vibration was produced by a mechanical impulse delivered by an impact hammer. Fig. 8.8 shows the measurement of the dynamic moduli of elasticity using the prisms.

The dynamic modulus of elasticity determined by the ultrasonic pulse velocity test was calculated using the following equation:

$$E_{cu} = \rho \cdot v_L^2 \cdot \frac{(1+\mu) \cdot (1-2\mu)}{1-\mu} \quad (8.3)$$

Where:

- $E_{cu}$  – dynamic modulus of elasticity in  $\text{N/mm}^2$ ,
- $\rho$  – bulk density in  $\text{kg/m}^3$ ,
- $v_L$  – ultrasonic pulse velocity in  $\text{km/s}$ ,
- $\mu$  – dynamic Poisson's ratio [-].

The dynamic modulus of elasticity was calculated from the natural frequency of longitudinal vibration using the equation:

$$E_{crL} = 4 \cdot L^2 \cdot f_L^2 \cdot \rho \quad (8.4)$$

Where:

- $E_{crL}$  – dynamic modulus of elasticity in N/mm<sup>2</sup>,
- $L$  – specimen length in m,
- $f_L$  – natural frequency of longitudinal vibration in kHz,
- $\rho$  – bulk density in kg/m<sup>3</sup>.

The dynamic modulus of elasticity was calculated from the natural frequency of flexural vibration using the equation:

$$E_{crf} = 0,0789 \cdot c_1 \cdot L^4 \cdot f_f^2 \cdot \rho \cdot \frac{1}{i^2} \quad (8.5)$$

Where:

- $E_{crf}$  – dynamic modulus of elasticity in N/mm<sup>2</sup>,
- $c_1$  – correction coefficient [-],
- $L$  – specimen length in m,
- $f_f$  – natural frequency of flexural vibration in kHz,
- $\rho$  – bulk density in kg/m<sup>3</sup>,
- $i$  – cross-sectional radius of gyration of a specimen in m.

An advantage of the resonance method is the fact that it can be used to determine the dynamic Poisson's ratio, which enters the calculation of the dynamic modulus of elasticity  $E_{cu}$  using equation (eq. 8.3). A slight disadvantage is that the resonance method can only be applied when testing solid materials, cement materials can thus only be measured once they have hardened.



**Fig. 8.8.** Measurement using the resonance method (left) and the ultrasonic pulse velocity test (right)



After non-destructive measurements the prisms were tested for the static modulus of elasticity at the age of 24 hours. The static test was performed according to standard (ISO 1920-10, 2010) by applying a compressive load onto a specimen while measuring longitudinal strain. The test itself is designed as cyclic, alternating between two loading levels – the basic load is  $0.5 \text{ N/mm}^2$  and the top load is equal to  $1/3$  of the expected compressive strength. For this reason, one specimen was always used to determine compressive strength and the remaining three were then tested for the modulus of elasticity  $E_c$ . The specimens were loaded using a hydraulic testing press. Their longitudinal strain was measured along an 80-mm base using strain transducers connected to a data logger (Fig. 8.9). The  $E_c$  test was completed by measuring the compressive strength of the specimens.



**Fig. 8.9.** Measurement of the static modulus of elasticity (left) and a detailed view of the strain transducers (right)

At the age of 48 hours the cement pastes were tested only for the dynamic modulus of elasticity following the above-described methods using the remaining four specimens (the ninth prism was used for the measurement of internal temperature during ageing). Immediately after the end of measurement at the age of 48 hours, the specimens were again wrapped in a PE sheet and left until the age of 72 hours, when they were once again tested for both the dynamic and static modulus of elasticity.

## 8.6. Results and discussion

The results of measurements of the dynamic modulus of elasticity over the first 24 hours of age using the ultrasonic device with a measurement chamber are shown in Fig. 8.10. The average values of the dynamic moduli of elasticity  $E_{cu}$ ,  $E_{crL}$ , and  $E_{crf}$  as well as the static modulus of elasticity  $E_c$  are plotted as bar charts in Fig. 8.11 through 8.14, with the error bars representing a sample standard deviation.

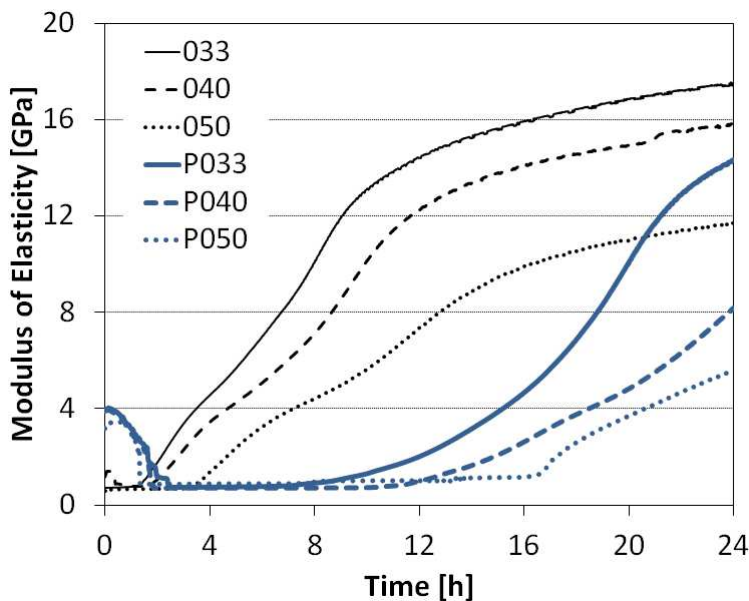


**Fig. 8.10.** Development of the dynamic modulus of elasticity determined over the first 24 hours, measured using the ultrasonic device with a measurement chamber

The continuous measurement (see Fig. 8.10) captured a very early stage of hydration period (end of the first hydration peak) when the viscosity of the material was changing from the fluid to thixotropic state. This process was very well visible in the case of cement pastes with the plasticizer, when the initial value (at the start of measurement) of the modulus of elasticity corresponded to the ultrasonic pulse velocity of approx. 1420 m/s which was close to the value of the ultrasonic pulse velocity of water. The subsequent changes in viscosity and formation of material's microstructure caused damping of the ultrasonic waves which was reflected in the decrease in the elastic modulus value. During the dormant period there were no changes in the value of elastic modulus. The subsequent growth of the elastic modulus started with the growth of the internal temperature measured inside the test specimens.

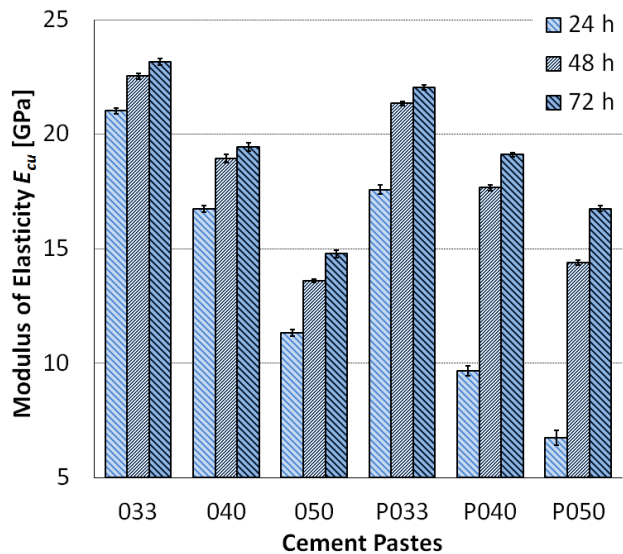


**Fig. 8.11.** Results of the dynamic modulus of elasticity  $E_{cu}$  at the age of 24, 48, and 72 hours

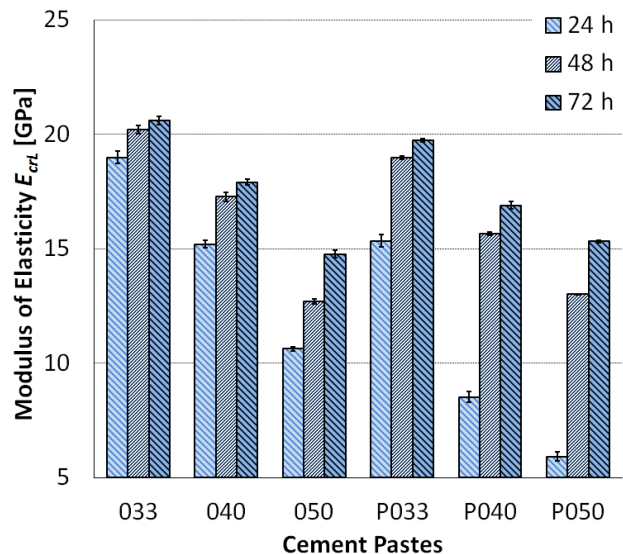


**Fig. 8.12.** Results of the dynamic modulus of elasticity  $E_{crL}$  at the age of 24, 48, and 72 hours

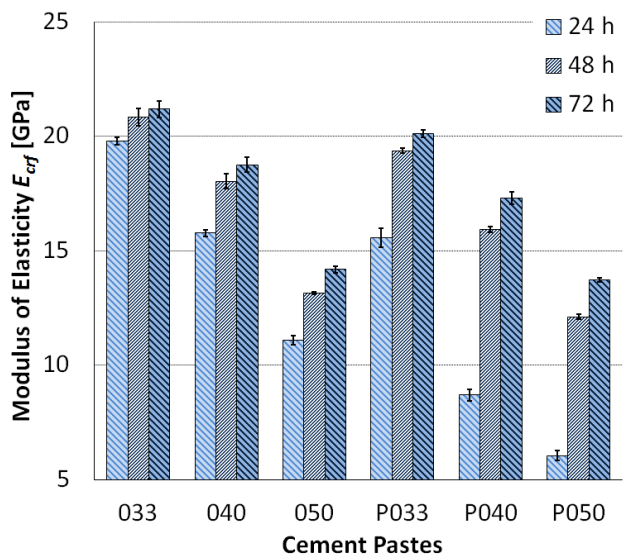


**Fig. 8.13.** Results of the dynamic modulus of elasticity  $E_{crf}$  at the age of 24, 48, and 72 hours

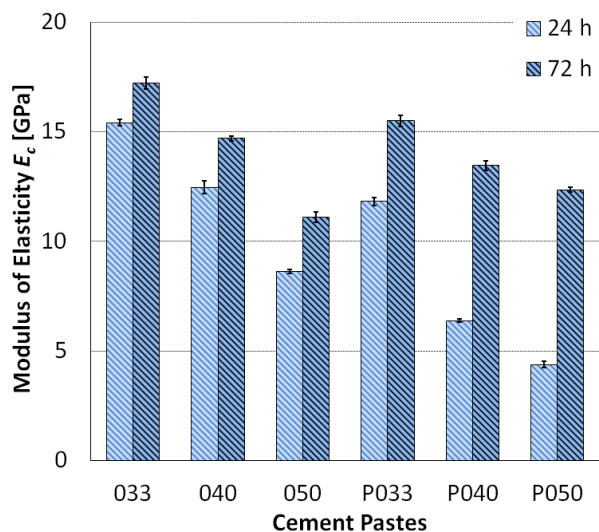


**Fig. 8.14.** Results of the static modulus of elasticity  $E_c$  at the age of 24 and 72 hours

The diagrams above show that the modulus of elasticity in pastes with plasticiser began to increase later than in pastes without plasticiser. This is most clearly visible in the first 24 hours of ageing. The results of the elastic modulus measurements also showed an influence of the w/c ratio, specifically, where the w/c ratio decreased, the modulus of elasticity increased. Aside from technological factors, the experiment also confirmed the influence of testing factors. It was demonstrated that the static modulus of elasticity reaches lower values than the dynamic modulus. In pastes with no plasticiser the ratio between the static and dynamic modulus, measured by the ultrasonic pulse velocity test, was within 0.73 and 0.76; in pastes with plasticiser it was 0.65 to 0.74. The same ratio, only in the dynamic modulus of elasticity measured by the resonance method, was 0.75 to 0.83 in pastes without plasticiser and 0.72 to 0.90 in pastes with plasticiser. Differences between the measured values of the elastic modulus were registered also in the dynamic values – the ratio between the modulus of elasticity determined by the ultrasonic pulse velocity test and the resonance method was approx. 1.05 – 1.10 in pastes without plasticiser and approx. 1.10 – 1.20 in pastes with plasticiser.

The ultrasonic pulse velocity test appears to be a suitable method for determining the development of the elastic modulus, however, it may have problems giving the precise value of the dynamic modulus of elasticity at a certain time. Measurements made by the ultrasonic pulse velocity test are influenced by many factors, e.g., the frequency of the transducers used, measuring base length (i.e. the distance between the transducers), measuring instrument, the material's moisture content, etc., which makes it difficult to obtain an "accurate" value. The results of the experiment showed this fact in the comparison of the values measured by different types of ultrasonic devices (Fig. 8.7 and Fig. 8.8) at an age of 24 hours – the results differed by up to 20 %. Moreover, if the calculation of the dynamic modulus of elasticity determined by the apparatus (see Fig. 8.7) included Poisson's ratio, the difference may have been even greater. In fact, the standard (ASTM C597-16, 2016) does not even recommend the calculation of the elastic modulus using data obtained by the ultrasonic pulse velocity test.

## **8.7 Conclusions**

The experiment results showed the elastic modulus of cementitious materials can be determined not only in the hardened state, but also during initial stages when the internal microstructure is still beginning to form. They also confirmed the fact that technological and testing factors have an influence on the value of the modulus of elasticity in cement pastes. Both the w/c ratio and plasticiser

content have been proved to have an effect on the development of the elastic modulus in young cement pastes. Pastes, which contained plasticisers, showed significant delays in the development of the modulus of elasticity, especially during the first 24 hours. The fact that the choice of testing method affects the value was also confirmed. Tests made with the prism specimens have shown that the highest values were reached by dynamic moduli of elasticity measured by the ultrasonic pulse velocity test, whereas the lowest values were, as expected, the static moduli. The influence of the specimens (and probably also the testing apparatus) was apparent in the values of the dynamic modulus of elasticity at the age of 24 hours measured by the ultrasonic instrument using Vicat's rings and the another one using prism specimens – the modulus of elasticity measured for the rings reached, depending on the type of paste, approx. 80 to 95 % of the value of the elastic modulus measured on prisms.

In conclusion, the ultrasonic apparatus with a measurement chamber appears to be a suitable tool for determining the dynamic modulus of elasticity during the setting of cement composites. The question remains, however, how to ascertain Poisson's ratio in a setting material, as it also affects the value of the dynamic modulus of elasticity, see equation (eq. 8.3). This would probably require an instrument capable of measuring compressive and shear wave velocity, see e.g. (Carette *et al.*, 2012).

## Acknowledgement

The presented results were obtained within the implementation of the project No. GA17-14302S "Experimental analysis of the early-age volume changes in cement-based composites", supported by the GA0 - Czech Science Foundation.

## References

- Abdelgader, H. et al. (2014). 'Concreting method that produce high modulus of elasticity', *MATEC Web of concretes*: 10.1051/mateconf/20141103012, 11(03012), pp.1-7.
- Aïtcin, P. (1998) '*High-performance concrete*', New York: E&FN Spon, ed. Stern, B.
- ASTM C597-16 (2016) '*Standard Test Method for Pulse Velocity Through Concrete*', ASTM International, West Conshohocken, PA.
- Carette, J. *et al.* (2012) 'Monitoring of the E-modulus in early age concrete since setting time with embedded piezoelectric transducers', In *Structural Faults & Repair - 2012*. Edinburgh.
- CEB-FIP Model Code 1990 (1993), '*CEB-FIP Model Code 1990: Design Code*', U.K.: Thomas Thelford.

- Cikrle, P. and Bílek, V. (2010) 'Modul pružnosti vysokopevných betonů různého složení', *Časopis Beton TKS*, 10(5), pp.40-44 (in Czech).
- Colleparadi, M. (2010) 'The new concrete', 2 ed., Villorba, Italy: Grafiche Tintoretto.
- Dehestani, M. *et al.* (2014) 'Effect of specimen shape and size on the compressive strength of self-consolidating concrete (SCC)', *Construction and building materials*, (66), pp.685-691.
- EN 12390-13 (2013) 'Testing hardened concrete. Determination of secant modulus of elasticity in compression', Brussels, CEN.
- EN 1992-1-1 (2004) 'Eurocode 2: Design of concrete structures - Part 1-1 : General rules and rules for buildings'. Brussels, CEN.
- Gu, C. *et al.* (2015), 'Ultrahigh performance concrete-properties, applications and perspectives', *Science China Technological Sciences*, 58(4), pp.587-599.
- Hela, R. and Křížová, K. (2011), 'Comparison of static elasticity modulus of Conventional and Self-compacting Concrete', pp.1-8.
- [http://www.schleibinger.com/cmsimple/en/?Setting\\_and\\_Maturity:Ultrasonic\\_Setting\\_Measurement](http://www.schleibinger.com/cmsimple/en/?Setting_and_Maturity:Ultrasonic_Setting_Measurement).
- <https://www.proceq.com/compare/pundit-ultrasonic-pulse-velocity-and-pulse-echo-testing/>
- Huňka, P. (2014), *Modul pružnosti betonu - možnosti stanovení, technologické a zkušební vlivy*, Doctoral thesis. Prague. (in Czech).
- Huňka, P. *et al.* (2013), 'Test and Technological Influences on Modulus of Elasticity of Concrete – Recapitulation', *Concrete and Concrete Structures*. pp.266-272.
- Huňka, P. and Kolísko, J. (2011) 'Studium vlivu tvaru, velikosti a způsobu přípravy zkušebního tělesa na výsledek zkoušky statického modulu pružnosti betonu v tlaku', *Časopis Beton TKS*, 11(1), pp. 69–71 (in Czech).
- ISO 1920-10 (2010), 'Determination of static modulus of elasticity in compression', Geneva, ISO.
- Kocáb, D. *et al.* (2017) 'Experimental Analysis of the Development of Elastic Properties and Strength under Different Ambient Temperature during the Hardening of Concrete', In *Procedia Engineering: 18th International Conference on Rehabilitation and Reconstruction of Buildings 2016*. pp. 102-107.
- Kocáb, D. *et al.* (2017) 'Experimental analysis of the influence of concrete curing on the development of its elastic modulus over time', *Materiali in Tehnologije*, 51(4) pp. 657-665.
- Křížová, K. *et al.* (2013), 'Long term monitoring of the modulus of elasticity depending on the composition of the concrete', In *Recenzovaný sborník příspěvků vědecké interdisciplinární mezinárodní vědecké konference*

- doktorandů a odborných asistentů QUAERE 2013*. Hradec Králové, pp. 2523-2527.
- Lydon, F. and Iacovou, M. (1995), 'Some factors affecting dynamic modulus of elasticity of high strength concrete', *Construction and Buildings Materials*, 25(4), pp.1645-1652.
- Ma, C. *et al.* (2016), 'Flexural ductility design of confined high-strength concrete columns: Theoretical modeling', *Measurement*, (78), pp.42-48.
- Mitrenga, P. (2011), '*Vliv kameniva na hodnoty modulu pružnosti betonu*', doctoral thesis, Brno (in Czech).
- Navrátil, J. (2008), '*Předpjaté betonové konstrukce*', Brno: CERM (in Czech).
- Nematzadeh, M. and Naghipour, M. (2012), 'Compressive strength and modulus of elasticity of freshly compressed concrete'. *Construction and Building Materials*, 34, pp.476-485.
- Neville, A. (2011) '*Properties of concrete*', 5th., London: Pearson.
- Neville, A. and Brooks, J. (2010), '*Concrete technology*', 2nd ed., Harlow, England: Prentice Hall.
- Newman, J. and Choo, B. (2003), '*Advanced Concrete Technology - Concrete Properties*', GB: Elsevier Ltd.
- Newman, J. and Choo, B. (2009) '*Advanced Concrete Technology – Processes*', G.B.: Elsevier Ltd.
- Nilson, A. and Winter, G. (1991), '*Design of Concrete Structures*', 11th edition., Singapore: McGraw-Hill.
- Parra, C. *et al.* (2011), 'Splitting tensile strength and modulus of elasticity of self-compacting concrete', *Construction and building materials*, 1(25), pp.201-207.
- Procházka, D. *et al.* (2011), 'High-strength modulus of elasticity evaluation', In *New approaches in numerical analysis in civil engineering*. Academic society Matei Teiu Botez, pp. 5-16.
- Tang, S. *et al.* (2015), 'Recent durability studies on concrete structure', *Cement and Concrete Research*, 78(10.1016/j.cemconres.2015.05.021), pp.143-154.
- Tsai, C. and Hsu, D. (2002), 'Diagnosis of Reinforced Concrete Structural Damage Base on Displacement Time History using the Back-Propagation Neural Network Technique', *Journal of Computing in Civil Engineering*, 16(1), pp.49-58.
- Vymazal, T. *et al.* (2011), 'Vliv obsahu vzduchu ve ztvrdlém provzdušněném betonu na hodnotu statického modulu pružnosti a pevnosti v tlaku stanovenou NDT metodami', *Beton TKS*, 11(4), pp.73-75 (in Czech).
- Yildirim, H. and Sengul, O. (2010), 'Modulus of elasticity of substandard and normal concrete', *Construction and Building materials*, 25(4), pp.1645-1652.





## 9. X-ray investigation of steel fibres in high performance self-compacting concrete beams

**Tomasz Ponikiewski<sup>1</sup>**

<sup>1</sup> *Silesian University of Technology, Faculty of Civil Engineering, Gliwice, Poland,  
<https://orcid.org/0000-0003-0535-2454>*

**Abstract:** The paper is focused on harnessing x-ray for non-destructive testing of self compacting concrete. It has been observed that there were fewer steel fibres in the immediate proximity of the form walls.

**Keywords:** x-ray, steel fibre, SCC, concrete

### 9.1. Introduction

The effect of steel fibres content on the self-compatibility of concrete mixture as well as on the mechanical properties of hardened concrete has already been investigated. Previous studies on SFRHPSCC have not provided systematic, validated experimental data to enable their design for their assumed mechanical parameters as well as the distribution and orientation of the dispersed reinforcement (Ding *et al.*, 2004), (Sirijaroonchai *et al.*, 2009), (Ding *et al.*, 2012). This causes the discrepancy between the projected and obtained mechanical parameters of the modified concretes (Ding *et al.*, 2008), (Kang *et al.*, 2011). It is important to determine the degree of variation of the assumed mechanical properties of SFRHPSCC due to the location and orientation of the dispersed reinforcement (Kang *et al.*, 2011), (Tanikella *et al.*, 2008). These research results should form the basis for development of the design method for SFRHPSCC applied to selected molded components.

The presented research is a basis for identifying the behavior of fibres with different geometrical parameters in the matrix of self-compacting concrete, taking into account the assumed differentiated states of stress. In view of the diversity of the currently used steel fibres and high impact the formation methods have on the homogeneity of the mixture, forming SFRHPSCC of the assumed mechanical properties is difficult, which creates the desire for additional research (Torrijos *et al.*, 2008), (Vandewalle *et al.*, 2008), (Brandt, 2009), (Ponikiewski and Cygan, 2011), (Pająk and Ponikiewski, 2013). Results of previous studies of self-compacting fiber concrete indicate that their self-thickening and physical-mechanical properties are mainly determined by the

geometric parameters of fibres and their volume ratio in concrete mix. However, in previous publications, there has been no assessment of the impact on methods of forming SFRHPSCC have on their physical-mechanical properties, which in the case of these concretes is a substantial problem. Currently, fibre reinforcement is treated as an additive to concrete which improves its properties, but not as structural reinforcement (there are already examples of completed construction). In this approach, a uniform distribution of reinforcement can be considered safe, but not optimal (Yardimci *et al.*, 2008), (Stroeve and Shah, 1978), (Ponikiewski and Gołaszewski, 2012). In the future I expect development of concrete structures reinforced only by fibres. The formation effect on the orientation and uniformity of distribution of fibres must be considered in designing of such structures. This study provides the first systematic data that can be used for this purpose.

## 9.2. Research significance

The main aim of this study was to determine the distribution and orientation of reinforcement in SFRHPSCC. This will allow the design of concrete structures with anticipated deployment of the dispersed reinforcement, specific to the structural elements and method of its formation. The core of the problem is to determine how in various structures the deployment of the dispersed reinforcement is dependent on the laying of the mixture, taking into account its rheological properties, the volume ratio and geometric parameters of the steel fibres. The research results can be used to improve the accuracy of modeling the mechanical properties of selected elements of structures with dispersed reinforcement. This will allow better optimization of the use of fibres in a matrix of concrete, which in some cases is a good alternative to traditional reinforcement, identifying and reducing the technological limitations. This research project results may be the starting point for further, more advanced research, including complex concrete structural elements, or leading to proposals for fibre directionality factors to be applied in procedures and standards.

Laboratory studies have shown and it has commonly accepted that rheological behavior of concrete may be sufficiently described by the Bingham model according to equation:

$$\tau = \tau_o + \eta_{pl} \cdot \dot{\gamma} \quad (9.1)$$

where:  $\tau$  (Pa) is the shear stress at shear rate  $\dot{\gamma}$  (1/s) and  $\tau_o$  (Pa) and  $\eta_{pl}$  (Pas) are the yield stress and plastic viscosity, respectively. Yield stress determines the value of shear stress necessary for initiating flow. When the shear stress ( $\tau$ )

surpasses the yield stress, the flow of the mixture occurs and the resistance of the flow depends on plastic viscosity; the bigger the plastic viscosity of the mixture, the slower it can flow.

Rheological parameters of fresh concrete, can be measured using Two Point Workability Test (TPWT), by applying a given shear rate and measuring the resulting shear stress (Tattarsall and Banfill, 1983). In the TPWT the rheological parameters of fresh concrete are measured by applying a given shear rate and measuring the resulting shear stress (Fig. 9.1).

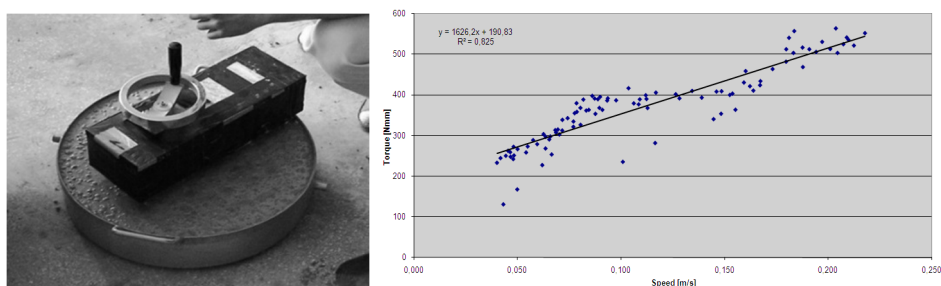


**Fig. 9.1.** BT-2 concrete rheometer and procedure to determine  $g$  and  $h$  values

The rheological parameters are determined by regression analysis according to the relation:

$$T = g + N \quad (9.2)$$

where:  $T$  is the shear resistance of a sample measured at rotation rate  $N$  and  $g$  (Nmm) and  $h$  (Nmms) are constants corresponding respectively to yield value  $\tau_0$  and plastic viscosity  $\eta_{pl}$ . By suitable calibration of the rheometer, it is possible to express  $g$  and  $h$  in fundamental units.

### 9.3. Specimens

The uniformity of distribution of steel fibers has been studied in SFRHPSCC formed into beams with dimensions of 600x150x150 mm (Fig. 9.2). Tests of concretes were made by digital image analysis (destructive method - Fig. 9.3) and computed tomography (non-destructive method - Fig. 9.4).



**Fig. 9.2.** Slump-flow test and forming SFRHPSCC beam C4 600x150x150 mm

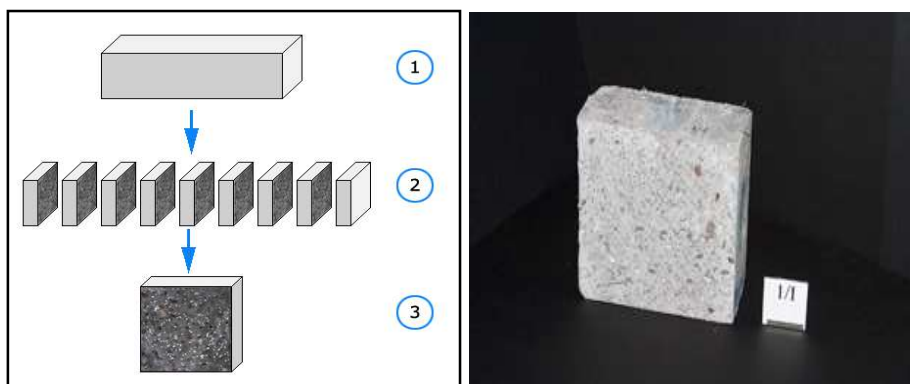


**Fig. 9.3.** Phases of micro-section preparation and a specimen prepared for analysis



**Fig. 9.4.** The CT scanner applied for this research was equipped with 64 rows of detectors, and the thickness of a series of reconstructed native CT scan was 0.625 mm

In order to smooth the image analysis of concrete with distributed steel fibres, my crew developed a program whose mission is to find the cut fibers and to describe their position in the sample. This developed program was used to evaluate the homogeneity of distribution of steel fibers in self-thickening concrete. The paper also presents the results of the computer tomography. The CT scanner applied for this research was equipped with 64 rows of detectors, and the thickness of a series of reconstructed native CT scan was 0.625 mm, i.e. the width of a single detector. The penetration factor in the study was an X-ray beam. The dimension of the surface of each layer of concrete was 150x150 mm. For each beam the result consisted of a native series written in DICOM format with at least 950 images, and reconstructed series with at least 1500 images taking into account the interval in the range 50 ÷ 80% of the thickness of the native layer. Parameters of acquisition were not less than: 140kVp lamp voltage, 400 mAs.

## 9.4 Materials



The composition of the investigated compounds of HPSCC is shown in Table 9.1.

**Table 9.1.** Composition of SFRHPSCC mixture kg/m<sup>3</sup>

Component	Symbol	Content
CEM I 42,5 R	C	490
Sand 0–2 mm	S	756
Basalt 2–8 mm	B	944,4
Silica fume	SF	49
Water	W	226,4
Steel fibres – kg/m <sup>3</sup> (% by volume)	F	98 – 177 (1.25 – 2.25)
Superplasticizer Glenium ACE 48 (3.5 % m.c.)	SP	17
Stabilizer RheoMatrix (0.4 % m.c.)	ST	1,6
W/(C+SF)	-	0,42
Slump-flow (SF)	-	SF3

They were considered in the study two types of steel fibres (Table 9.2) for different volume ratios (Table 9.3).

**Table 9.2.** Characteristics of steel fibres using in research

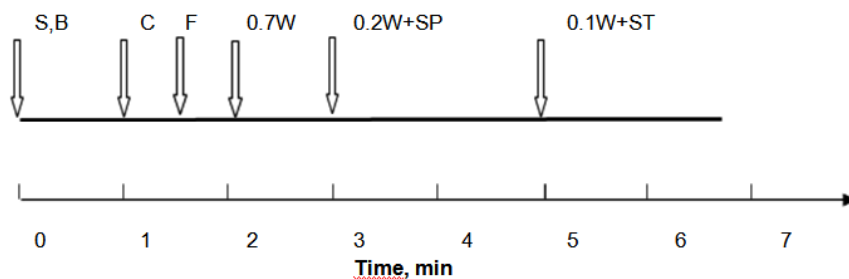
Name	Length	Diameter	Cross-section	Shape	Tensile strength (N/mm <sup>2</sup> )
	(mm)	(mm)			
KE 20/1.7	20±10%	1,70±10%	rectangular <sup>1)</sup>		770±15%
SW 35/1.0	35±10%	2.30±2.95 <sub>2)</sub>	part of circle		800±15%

Designations: <sup>1)</sup> thickness 0.50±10%; <sup>2)</sup> width (mm);

**Table 9.3.** The characteristics of steel fibres and their percentage in the mixture

Mixture	Content of fibres, % by volume	
	KE 20/1,7	SW 35/1.0
C0	-	-
C1	1.25	-
C2	2.25	-
C3	-	1.25
C4	-	2.25

The self-compacting criterion (repeatability of workability) was met by all tested concretes, according to prepared mixing procedure (Fig. 9.5).

**Fig. 9.5.** Mixing procedure for SFRHPSCC (SF added with C)

The detailed results are presented for compounds with the fiber content 1.25 and 2.25% (98 and 177 kg/m<sup>3</sup>). In Table 9.4 the results for investigated SFRHPSCC mixtures are presented. The ability of self-compaction was verified by

measurements of time and flow diameter using the Abrams cone as well as basing on the values of rheological parameters by rheological procedure. The compressive strength was measured after the 28 day storage.

**Table 9.4.** The properties of fresh and hardened SFRHPSCC mixtures

Mixture	Workability				$f_{c,cube\ 28}$ [MPa]
	Slump-flow		Rheological parameters		
	T <sub>500</sub> [s]	SF [mm]	g [Nmm]	h [Nmmmin]	
C0	3	750	88	1 457	90
C1	4	700	105	3 008	105
C2	5	650	362	3 146	110
C3	2	740	160	2 802	95
C4	3	690	421	1 596	100

## 9.5. Methods of X-ray analysis

For effective analysis of scattered fibres reinforced concrete the computer program has been used; the accuracy of results depends only upon the resolution of analyzed image. The program finds the intersections of fibres on the surface and their orientation. Some steps can be distinguished when the program operates. At first, the area of analyzed part of the image is delineated. In this stage the virtual table of colors is created in which the contents of particular meshes correspond with the colors. The next step of image recognition consists in elimination of those meshes which represent the values under the assumed limit. After this operation the table of colors transforms into the logic table which contains only the values 0 or 1; it means that in the mesh there is a part of analyzed fibers or there is no fibers. Because the transfer from the real color scale to the grey color scale leads always to the loss of some information, the next step consists in filling and rounding the contours of fibers. The new table, determining the number of fibres and some other data is formed. In the next step the program eliminates too small or too large areas which could be positively identified as fibre cross sections. Finally the results of image analysis are highlighted. The values determining the amount of fibres present in every square area are generated.

Image processing was implemented using open-source medical image processing C++ libraries The Insight Toolkit (ITK) (Ibáñez *et al.*, 2005).



Statistical data analysis was performed using STATISTICA and MATLAB software.

### 9.5.1. Image Processing

Let  $I_0$  denote the acquired volumetric CT intensity image (Rudzki *et al.*, 2013), (Ponikiewski *et al.*, 2014). First stage of the image processing was responsible for automatic determination of the volume of interest (VOI) in order to perform subsequent analyses only on the concrete beam and consists of the following:

1. initial binarization above 500 Hounsfield Units (HU),
2. binary image labeling,
3. selection of the largest object,
4. VOI coordinates retrieval from the smallest rectangular cuboid circumscribed over the object selected in step 3.

Further processing was performed only within the VOI (done by image cropping, Fig. 9.6 (a)) and consisted of the following steps:

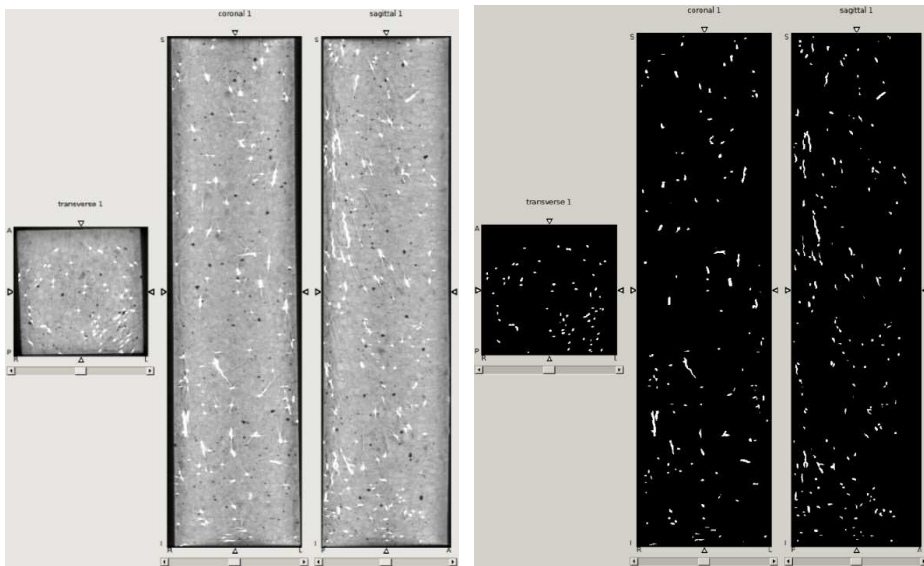


**Fig. 9.6.** Cross sections of an exemplary beam: (a) image after VOI selection, (b) after steel fibers segmentation (Rudzki *et al.*, 2013),

1. image framing  $I_0$  to beam area
2. binarization of the image  $I_0$  above 3000HU,
3. binary median filtering,
4. separation of objects similar to (Stroeven and Shah, 1978),

5. binary image labeling with rejection of objects smaller than 100 [mm<sup>3</sup>] and larger than 300 [mm<sup>3</sup>],
6. for each object within the label image its geometrical center and orientation was found. Orientation was defined with the eigenvector corresponding to the smallest eigenvalue of the object's rotation matrix.

Fibers segmentation results are shown in Figure 6(b).

### 9.5.2. Statistical Analysis

For each fiber in the analyzed beam the data retrieved during the image analysis was as follows (Rudzki *et al.*, 2013):

- label defining each fiber,
- coordinates of the fiber center in 3D,
- eigenvector of the fibers's rotation matrix corresponding to the smallest eigenvalue,
- volume of the fiber.

Having the above mentioned values, spherical histograms can be generated following the presented steps. The total number of fibers is labeled with  $n$ .

1. For each fiber obtained vector  $v_k$  is parallel to its main axis

$$\forall k \in \{1, 2, \dots, n\} \quad v_k = (v_{k,1}, v_{k,2}, v_{k,3}) \quad (9.3)$$

2. For each fiber vector  $v_k$  assigned to the fiber, should be provided using spherical coordinates

$$\forall k \in \{1, 2, \dots, n\} \quad v_k = (\varphi_k, \theta_k, r_k) \quad (9.4)$$

3. For each vector parallel to a fiber  $\varphi_k$  a new vector  $\omega_k$  is assigned, whose two first coordinates are angles  $\varphi_k, \theta_k$  and its third coordinate equals 1

$$\forall k \in \{1, 2, \dots, n\} \quad \omega_k = (\omega_{k,1}, \omega_{k,2}, \omega_{k,3}) = (\varphi_k, \theta_k, 1) \quad (9.5)$$

4. Let  $c$  be the number of groups to which each angle parameter is divided. The value of  $c$  should be a divisor of 180

$$(c \in \{1, 2, 3, 4, 5, 6, 9, 10, 12, 15, 18, 20, 30, 36, 45, 60, 90, 180\})$$

and it is set for both  $\varphi$  and  $\theta$ . This gives a total number of  $c^2$  groups of equal width intervals for these angles.

5. Let  $n_{i,j}$  be the number of vectors  $\omega_i$  that belong to the  $i$ -th group in terms of angle  $\varphi$  and in the  $j$ -th group in terms of angle  $\theta_0$

$$\forall i \in \{1, 2, \dots, c\}, \forall j \in \{1, 2, \dots, c\}, n_{i,j} = \sum_{k=1}^n \chi S_{i,j}(\omega_k), \quad (9.6)$$

where  $\chi$  is the characteristic function defined as

$$\chi_{S_{i,j}}(\omega_k) = \begin{cases} 1, & \omega_k \in S_{i,j} \\ 0, & \omega_k \notin S_{i,j} \end{cases}$$

where the set  $S_{i,j}$  is defined as follows

$$\forall i \in \{1, 2, \dots, c\}, \forall j \in \{1, 2, \dots, c\}$$

$$S_{i,j} = \left\{ (\varphi, \theta) : \frac{180}{c} \cdot (i-1) \leq \varphi < \frac{180}{c} \cdot i \quad \wedge \quad \frac{180}{c} \cdot (j-1) \leq \theta < \frac{180}{c} \cdot j \right\}.$$

6. Spherical histogram consists of a sphere, serving as a reference object, and up to  $c^2$  cylinders, whose main axes of symmetry are parallel to vectors that are representatives of each class and whose heights equal appropriate  $n_{i,j}$  values. Two first spherical coordinates of the class representatives should be calculated using the formula

$$\varphi = \frac{180}{c} \cdot \left(i - \frac{1}{2}\right), \theta = \frac{180}{c} \cdot \left(j - \frac{1}{2}\right). \quad (9.7)$$

Spherical histograms enable visual assessment of the typical fiber orientation in a beam. Histograms shown in Fig. 9.7(a) and Fig. 9.7(b) include fiber orientation of the whole beam, but through appropriate narrowing the data range the orientation of fibers in different parts of the beam can be analyzed and compared with each other.

Since the fiber orientation in the beam is one of the most important parameters that determine the beam strength, angle values  $\theta_k$  should be studied, as that are the angles between the beam main axis and a particular  $k$ -th fiber.

First, the mean  $\bar{x}$  and the standard deviation  $\sigma$  should be calculated. Relying on the three sigma rule it can be considered, that the inclination angle of approximately 2/3 of the fibers from the beam main axis will be between  $\bar{x} - \sigma$  and  $\bar{x} + \sigma$ .

Using the Pearson's chi-squared test a distribution can be fitted to the two dimensional histogram of angles  $\theta$ . The null hypothesis states that the analyzed parameter has a particular distribution, whereas the alternative hypothesis claims the opposite. The higher the value of the parameter  $p$ , the better the distribution fits the analyzed data, since  $p$  denotes the probability of a type I error (the propability that rejecting the null hypothesis would be incorrect) (Ponikiewski and Gołaszewski, 2012).

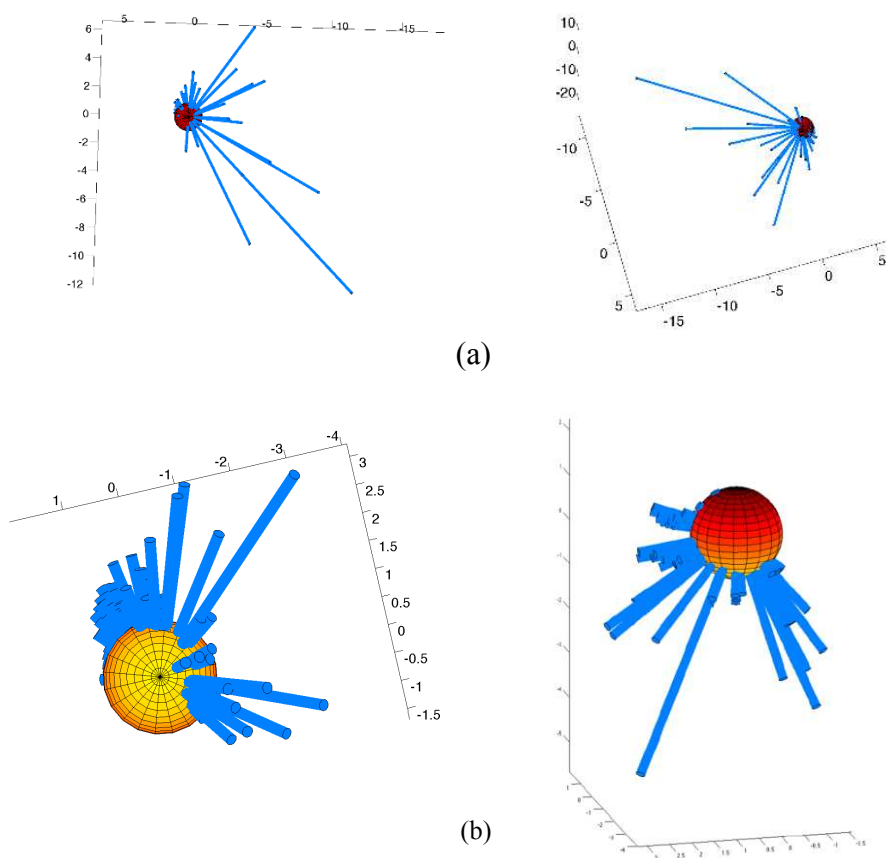


**Fig. 9.7.** Exemplary spherical histograms for (a)  $c = 10$  (2 views), (b)  $c = 30$  (2 views), (Rudzki *et al.*, 2013),

## 9.6. Experimental results and discussion

Five distributions of fibres were fitted to the histograms of  $\theta$  (Fig. 9.8(a)-9(e)) (Rudzki *et al.*, 2013):

- normal,
- exponential,
- gamma,
- lognormal,
- chi-squared.

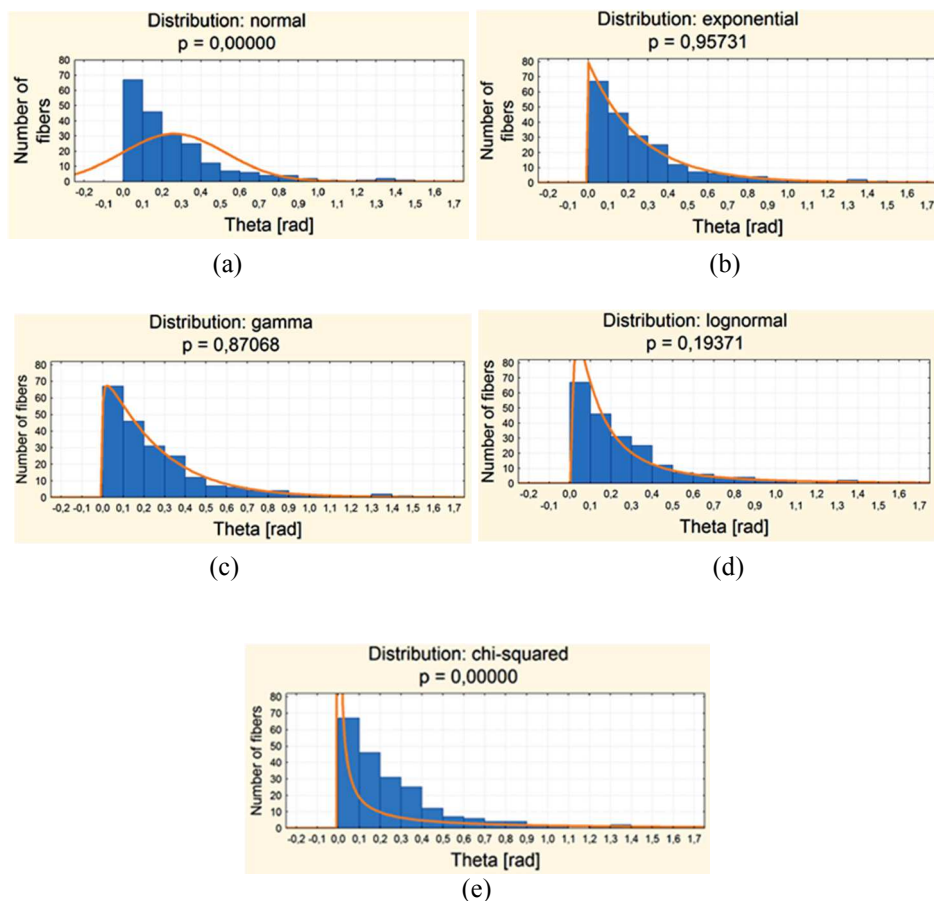
A good fit was obtained for the gamma distribution (Fig. 9.8(c)), however, the best fitted distribution is the exponential one (Fig. 9.8(b)).

Another useful statistical tool is the Welch's t-test, which is an adaptation of Student's t-test intended for use with two samples having possibly unequal variances. It can be used to verify the hypothesis, that the fiber orientation does not depend on their position in the beam (upper/lower part or beam end/center).

The null hypothesis states that the mean angles  $\theta$  are equal for various beam parts and the alternative hypothesis is that they are different.

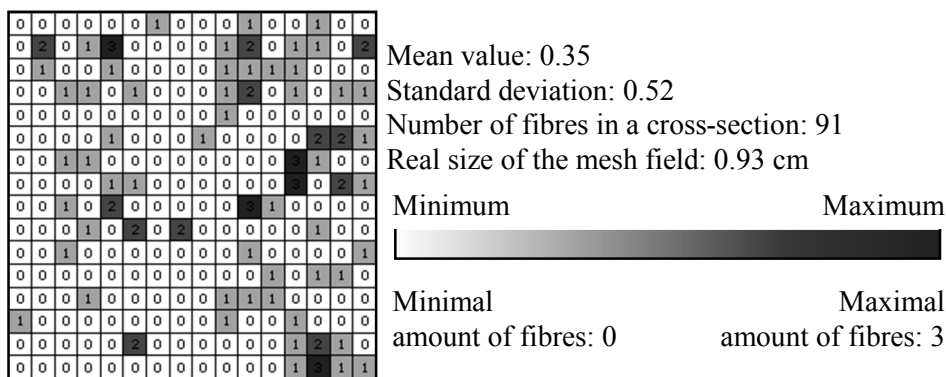
Preliminary examinations resulted in the conclusion that fibers in the upper part of the beam have a greater tendency to form parallel to the beam axis and those in the lower part are characterized by a larger orientation variety. On the other hand according to the test results, the average angle  $\theta$  does not depend on the beam part in terms of its end or center.

Due to the exponential nature of the angle between the fibers and the axis of the beam, the hypothesis that this angle is nearly 0, might be tested using a one-sample t-test. The preliminary studies showed that this angle is significantly different from zero. Therefore it cannot be assumed that the fibers are arranged parallel to the axis of the beam, although the observation of the 3D graphs and further analysis showed that they have this tendency. Thus it should be concluded that the arrangement of fibers in 3D space creates an object that resembles more a cone than a cylinder.



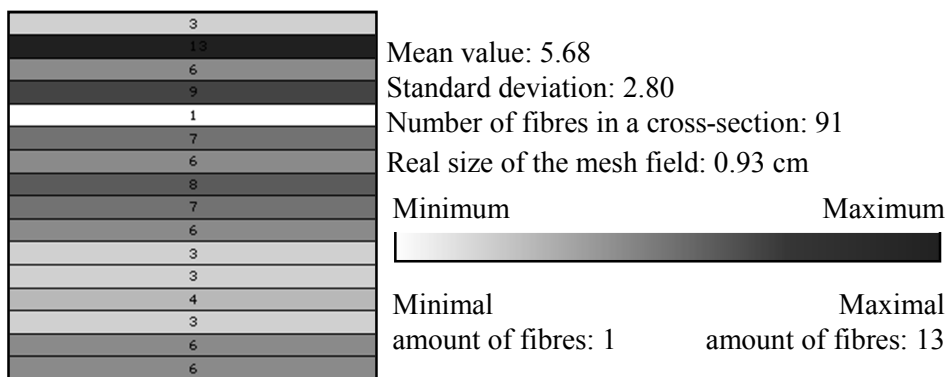
**Fig. 9.8.** Tested distributions: (a) normal, (b) exponential, (c) gamma, (d) log-normal, (e) chi (Rudzki *et al.*, 2013).

The results, presented below are based on investigation of the whole concrete element (Fig. 9.3), consisting of 9 sections. The full report generated by the computer program is very large, so only a local analysis of 1 micro-section is presented here. Fig. 9.9 shows a pictorial presentation of the results of a fibre count in a selected cross-section of concrete C2 divided into 16 x 16 squares. On this basis the real distribution of fibres per unit of area in the sample cross-section was determined.



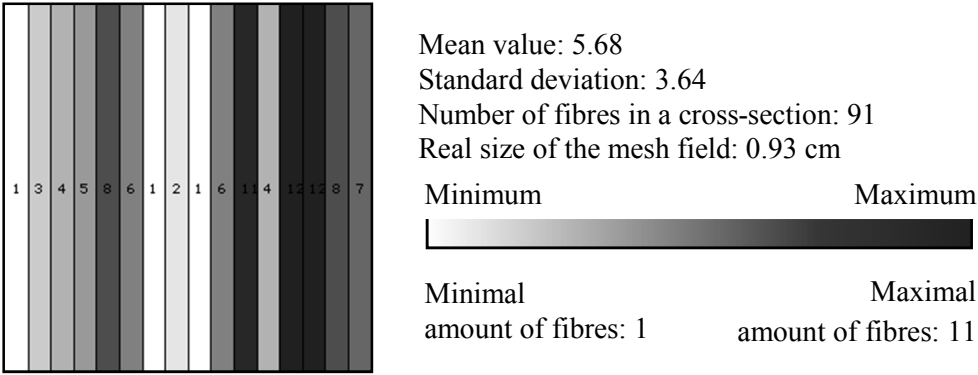
**Fig. 9.9.** Example of a concrete C2 cross-section for the division 16 x 16 and analysis of the number of fibres

Fig. 9.10 is a pictorial presentation of the results of the fibre count in a selected cross-section of concrete C2 with a division mesh 1 x 16 (rows). On this basis the summary distribution of fibres in horizontal cross-sections of the concrete sample, describing their local and global 3-dimensional concentration in a horizontal direction can be determined.



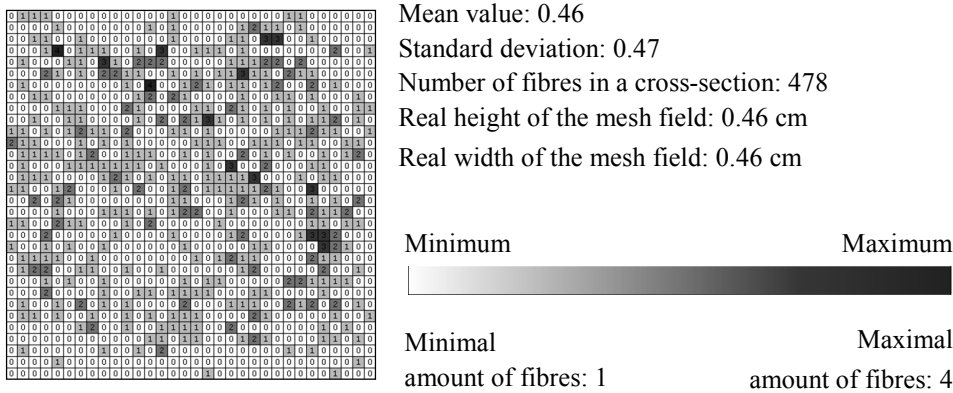
**Fig. 9.10.** Example of a concrete C2 cross-section for the division 16 x 16 and analysis of the number of fibres, data from the rows

Fig. 9.11 is the pictorial presentation of the results of the fibre count in a selected cross-section of concrete C2 with a division mesh 1 x 16 (columns). On this basis the summary distribution of fibres in vertical cross-sections of the concrete sample, describing their local and global 3-dimensional concentration in a vertical direction can be determined.



**Fig. 9.11.** Example of a concrete C2 cross-section for the division 16 x 16 and analysis of the number of fibres, data from the columns

The application of global scale to a substantial extent decreases the transparency of result presentation, because depending on the degree of divisions, the number of fibres in a sampled field fluctuated from 0 to 53. The global results are obtained by generating diagrams illustrating the number of fibres in cross-sections and in the whole concrete structural element. Figures 9.12-9.14 show the results for the selected three of nine sections of the test element made of C3 fibre concrete, mesh 32 x 32. On the basis of deployment of fibres in a sample, one can tell what the general trends of their dispersion are.



**Fig. 9.12.** Cross-section 200 mm of concrete C3 for the division 32 x 32 and analysis of the number of fibres



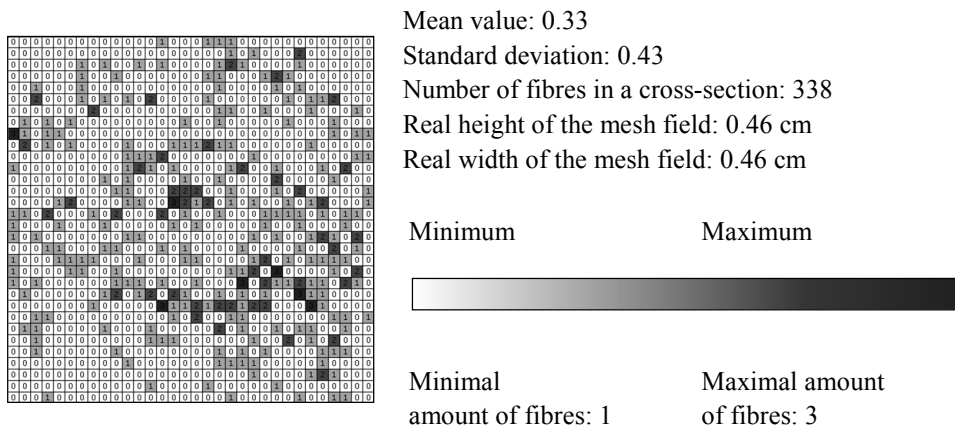


**Fig. 9.13.** Cross-section 400 mm of concrete C3 for the division 32 x 32 and analysis of the number of fibres

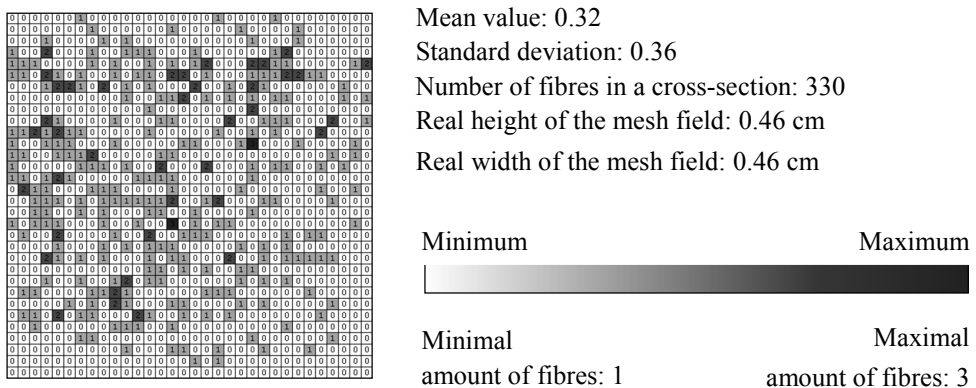


**Fig. 9.14.** Cross-section 500 mm of concrete C3 for the division 32 x 32 and analysis of the number of fibres

The results of the computer tomography studies are presented in Figures 9.15 – 9.17. 2D sections of concrete beams for the sections of C4: 100 mm, 200 mm, 400 mm and 550 mm from the edge of the concrete are shown in Figures 9.12. It should be noted that the characteristic rounding of edges of individual sections of images result from the scanning method, not from the internal structure of the concrete. The selected sections of the concrete in question prove generally to have an even distribution of fibres in the volume of the test concrete. There are no large clumps of fibres in a matrix of concrete. Visually it

could be considered a parallel arrangement of fibers to the direction of flow of the addition to the mixture in the process of formation. There are only a few fibres arranged perpendicularly to the direction of formation.

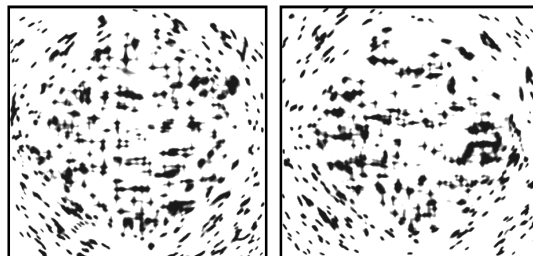


**Fig. 9.15.** 2D sections of concrete beams for the sections of C4: 100 mm, 200 mm from the edge of concrete

Rheological parameters and X-ray 2D sections of SFRHPSCC beams for different kind of fibres and volume are presented in Figures 9.16. In general, increasing fibre content causes linear increase of yield value  $g$  of SFRHPSCC. Nature and range of influence of fibres content on plastic viscosity  $h$  of SFRHPSCC also depends on the geometrical properties of fibres. The connection between orientation of fibres and the direction of the mixture flow during moulding was confirmed by X-ray method. The uniform distribution of fibres in the produced concrete element was proved. The measurement's low quality of rheological parameters by Bingham model approximated were determined. There was no evidence of fibre cluster formation. The most important problem is to determine how the deployment of the dispersed reinforcement is dependent on the placement of the concrete mixture in various structures, taking into account its rheological and mechanical properties, the volume ratio and geometric parameters of the steel fibres in SFRSCC. A 3D cross-section of the concrete beam section C2 for 400-500 mm from the edge of the concrete is shown in Figures 9.17. 3D image confirms the trend of the directional orientation of fibers in a matrix of concrete. The fibres are generally evenly distributed in concrete, with the exception of selected sections of the edge of the concrete. On the basis of computed tomography, uneven distribution of steel fibres in concrete volume samples was proved. Whereas, no high concentrations of fibres in concrete matrix were detected. Also, the parallel distribution of fibres was confirmed, in accordance with the direction of movement of the mixture during casting, especially in the case of SW35 fibres. Only few fibres were perpendicularly oriented to this direction. The radial arrangement of fibres in the vicinity of the corners of bars cross-section is associated with the slower movement of the mixture close to the mould walls.

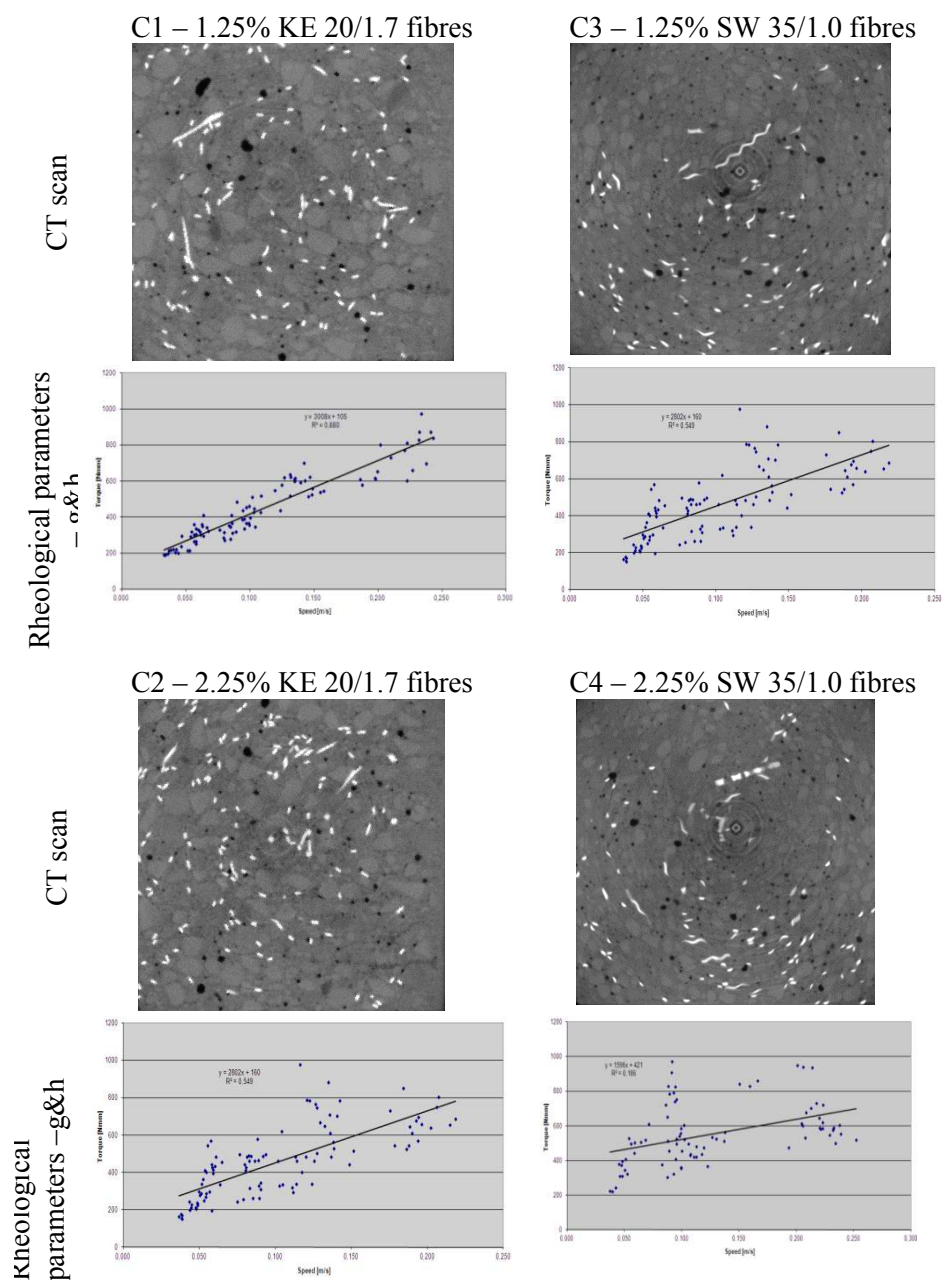


**Fig. 9.16.** Rheological parameters and X-ray 2D sections of SFRHPSCC beams for different kind of fibres and volume

This is due to higher frictional resistance occurring in those areas. The tests have shown that computed tomography gives the possibility of the distribution of steel fibres in the entire volume of concrete examination, and also in small, selected areas. Such analysis allows to obtain two-dimensional (2D) and three dimensional (3D) images of fibres distribution. Obtained results may present the basis for the development of designing methods of self-compacting fibres reinforced concrete, including the form of structural elements. The key problem is to determine changes in distribution of dispersed reinforcement in various structures, depending on used technology of mixture casting and its rheological properties, and also the volume and geometrical forms of steel fibres. Obtained results may also be used for modelling of the properties of selected structural elements.

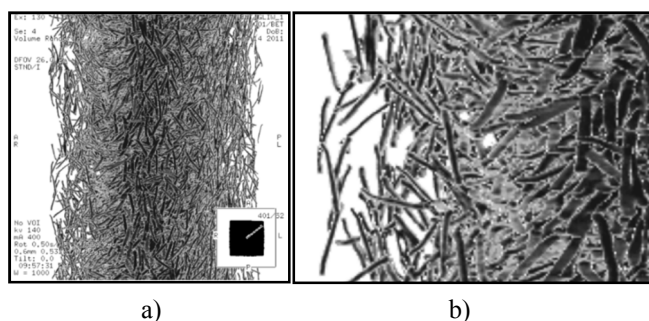


**Fig. 9.17.** X-ray 3D sections of concrete beams C2 for the sections of: a) 400 ÷ 500 mm from the edge of concrete; b) 450 mm from the edge of concrete

## 9.6. Conclusions

On the basis of own studies, using own method and software to analyze the distribution of fibres in concrete, as well as the tomography examinations, the results were obtained within the selected field of research.

The developed computer program allows the analysis of the distribution of individual fibres in samples, both in the global and local systems. It also allows the identification of trends in the distribution of fibres, depending on the direction of concrete mix formation, proximity of the walls of molds and up - down orientation of the form. The computed tomography shows the inner space of concrete with steel fibers in 2D and 3D formats without any limitations.

Both of the applied methods of identifying the deployment of fibre in the concrete SFRHPSCC fibres revealed no tendency for the fibres to stick to the walls of the form, no effects of the wall. It has been observed that there were fewer steel fibres in the immediate proximity of the form walls.

An image analysis method for automatic segmentation and evaluation of steel fibers was presented. Preliminary quantitative analysis showed that the fibers orientation along the beam exhibit an exponential distribution.

Generic statistical models that combine the method of forming, fibers and pores position and orientation with mechanical beam properties are the main subject of future research. As a preliminary step the image processing software allowing automatic fibers and air pores segmentation providing data on position, orientation and shape properties has to be developed.

The number of fibers positioned in most cases parallel to the longitudinal walls of the form leads to the conclusion that such behavior results from the direction of concrete dispersing in the form. The presented method and software is the introduction to research on the relationship between the distribution of fibers in concrete elements and the rheological (low yield value) and strength parameters.

Confirmed was the orientation of fibres consistent with the direction of the formation of a mixture SFRHPSCC. Proved as well was the uniform distribution of fibers in the tested concrete. There was no evidence of fibers too closely placed to each other and the formation of so-called "hedgehogs".

## References

- Brandt, A.M. (2009) 'Cement-based composites. Materials, mechanical properties and performance', *Taylor & Francis, USA & Canada*.
- Ding, Y. *et al.* (2004) 'The investigation on the workability and flexural toughness of fibre cocktail reinforced self-compacting high performance concrete', in: *6th Rilem Symposium on fibre-reinforced concretes (FRC) – BEFIB*, Varenna, Italy 2004.
- Ding, Y. *et al.* (2012) 'Study on residual behaviour and flexural toughness of fibre cocktail reinforced self-compacting high performance concrete after exposure to high temperature', *Construction and Building Materials*, 26 pp. 21–31.
- Ding, Y. *et al.* (2008) *The investigation on the workability of fibre cocktail reinforced self-compacting high performance concrete*, *Construction and Building Materials*, 22, pp. 1462–1470.
- Ibáñez L. (2005) 'Schroeder w., ng l., cates j. *The itk software guide*. Kitware', Available: <http://www.itk.org/itksoftwareguide.pdf>
- Kang, S.-T. and Kim, J.-K. (2011) 'Investigation on the flexural behavior of uhpc considering the effect of fiber orientation distribution', *Construction and Building Materials*, 28, pp. 57–65.
- Kang, S.-T. and Kim, J.-K. (2011) The relation between fiber orientation and

- tensile behavior in an ultra high performance fiber reinforced cementitious composites (UPHPRCC), *Cement and concrete research*, 41, pp. 1001–1014.
- Pająk M. and Ponikiewski, T. (2013) ‘Flexural behavior of self-compacting concrete reinforced with different types of steel fibers’, *Construction and Building Materials*, 47, pp. 397–408.
- Ponikiewski, T. and Gołaszewski, J. (2012) ‘The new approach to the study of random distribution of fibres in high performance self-compacting concrete’, *Cement Wapno Beton*, 79, pp. 165 - 176.
- Ponikiewski, T. and Cygan, G. (2011) ‘Some properties of self-compacting concretes reinforced with steel fibres’, *Cement Wapno Beton*, 78, pp. 203-209.
- Ponikiewski, T. *et al.* (2014) ‘Determination of steel fibres distribution in self-compacting concrete beams using x-ray computed tomography’, *Archives of Civil and Mechanical Engineering*, 15, pp. 558-568.
- Rudzki, M., Bugdol, M. and Ponikiewski, T. (2013) ‘Determination of steel fibers orientation in scc using computed tomography and digital image analysis methods’, *Cement Wapno Beton*, 18, 5, pp. 257-263.
- Sirijaroonchai, K., El-tawil, S. and Parra-montesinos, G. (2009) ‘Behavior of high performance fiber reinforced cement composites under multi-axial compressive loading’, *Cement & concrete composites*, article in press.
- Stroeven, P. and Shah P., S.P. (1978) ‘Use of radiography-image analysis for steel fibre reinforced concrete’, In. “*testing and test methods of fibre reinforced composites*”, R.N. Swamy ed. Construction press, Lancaster, pp. 308-311.
- Tattarsall, G.H. and Banfill, P.F.G. (1983) ‘The rheology of fresh concrete’. *Boston: pitman books limited*. 356 p.
- Tanikella, P.N.D. and Gettu, R. (2008) ‘On the distribution of fibers in self-compacting concrete’, *7th Rilem Symposium on fibre - reinforced concretes (FRC) - Befib*, Chennai, India, pp. 1147-1153.
- Torrijos, M.C. *et al.* (2008) ‘Orientation and distribution of steel fibres in self-compacting concrete’, *7th Rilem symposium on fibre - reinforced concretes (FRC) - Befib 2008*, Chennai, India, pp. 729 - 738.
- Vandewalle, L., Heirman, G. and van Rickstal, F. (2008) ‘Fibre orientation in self-compacting fibre reinforced concrete’, *7th Rilem symposium on fibre - reinforced concretes (FRC) - Befib*, Chennai, India, pp. 719 - 728.
- Yardimci, M.Y., Baradan, B. and Taşdemir, M.A. (2008) ‘Studies on the relation between fiber orientation and flexural performance of sfrscc’, *7th Rilem symposium on fibre - reinforced concretes (FRC) - Befib*, Chennai, India, pp. 711-718.



## 10. Binary alkali-activated materials with brick powder

**Cecílie Mizerová<sup>1</sup>, Pavel Rovnaník<sup>2</sup>**

<sup>1</sup> *Brno University of Technology, Faculty of Civil Engineering, Brno, Czech Republic,  
orcid.org/0000-0001-8080-2721*

<sup>2</sup> *Brno University of Technology, Faculty of Civil Engineering, Brno, Czech Republic,  
orcid.org/0000-0001-8404-6505*

**Abstract:** Waste brick powder represents an easily available supplementary cementitious material that can contribute to the enhanced properties of lime plasters and concretes. Furthermore, the prerequisite properties of the brick powder enable its application in alkali activated materials. In this study, brick powder was used for production of binary alkali activated binders with metakaolin, slag or fly ash. Brick powder based geopolymers were tested for their mechanical properties, porosity and microstructure; flow properties of the fresh geopolymers were evaluated by rheometric measurements. In accordance with the results, brick powder could be a suitable precursor for blended binders with metakaolin and slag. These samples exhibited good mechanical properties and microstructure characteristics. The combination with fly ash was less applicable due to a rapid setting, hardening retarder used in these binders caused significant deterioration of the mechanical properties and massive efflorescence formation.

**Keywords:** alkali-activated, brick powder, binder, metakaolin

### 10.1. Introduction

The continual growth of construction industry is closely linked with growing need of traditional Portland cement that is the second most consumed commodity in the world (Barnes 2014). Unfortunately, its production requires a high volume extraction of natural resources and energy consumption that significantly contribute to emissions of CO<sub>2</sub> and other harmful substances to the atmosphere (Mehta 2001). On the contrary, the technology of alkali-activated binders allows the use of a wide range of secondary or waste products (blast furnace slag, fly ash, silica fume etc.). One of the primary raw material used in geopolymers is metakaolin produced by calcination of kaolinitic clays (2–2.5 times more expensive than cement). The estimated CO<sub>2</sub> savings, comparing alkali-activated materials to Portland cement based on the life-cycle studies, range from 30 to 80 % (Provis 2014) and together with reduced storing capacities needed for unutilized industrial by-products are promising values for



the future. The difference strongly depends on the market conditions and availability of source materials in particular region (Van Deventer, 2010).

Alkali-activated materials result from the reactions of raw materials with a high content of amorphous aluminosilicate phase and the alkaline activator solution. Alkaline activator, in most cases alkaline hydroxide and/or alkaline silicate, ensures the appropriate conditions for the raw materials dissolution and formation of new phases. The first theoretical background of alkaline activation was developed by Glukhovsky in 1959 (Glukhovsky 1959). Afterward, in 1981, prof. Davidovits introduced the term “geopolymer” after studies concerning the alkaline activation of a burnt mixture of kaolinite, limestone, and dolomite resulting in a material with regular polymeric three-dimensional structure (Davidovits 1981). Besides the better environmental performance, engineering properties of alkali-activated binders are comparable or superior to Portland cement in terms of strength, chemical and thermal resistance (Duxson 2007).

Ceramic waste represents a huge amount of industrial waste materials produced. Mostly, it comes from the processing of construction and demolition waste, such material is frequently contaminated by other constituents, e.g. concrete, masonry mortar, etc. Thus, it is primarily used as an inexpensive recycled aggregate for road construction and terrain works. The other source of material, more suitable for use in binder technology, is represented by fine ground brick powder that is recently widely produced during the high-precision plane grinding process of clay blocks (Keppert 2014). Use of waste brick powder does not involve additional costs and environmental impact. In spite of present effort to maximize re-utilization of ceramic waste, the major part is still directed to disposal in landfills (Pachego-Torgal 2010).

Since the ancient times, the finely ground brick powder is used as a pozzolanic admixture to lime plasters to enhance their mechanical performance, heat insulation properties and durability (Baronio 1996). In a similar way, it is nowadays applied in concrete technology. Various studies confirmed higher strength and durability of concrete with brick powder that exhibits lower chloride permeability, reduced autogenous shrinkage and volume changes caused by alkali-silica reaction (Turanli 2003). Use of recycled ceramic aggregate in structural concrete is rather limited due to its higher water absorption and therefore reduced freeze-thaw resistance.

Although the ceramic matrix dominantly consists of the crystalline phase (quartz, cristobalite) and the reactive vitreous content is generally lower, studies focused on the alkaline activation of red ceramic waste already confirmed its reactivity in the geopolymerization process (Robayo 2016). The lower rate of reactions could be increased by a higher specific surface of the material

(additional grinding), tailored alkaline activator or thermal treatment during setting but this is not necessary. When alkali silicate is used for the geopolymerization, mechanical properties show significant improvement (Sun 2013). The application of brick powder in blended alkali-activated materials was predominantly studied in binders with slag; slag–brick powder system allows alkaline activation of brick powder with insufficient reactivity for one-component geopolymers (Rakhimova 2015).

## 10.2. Materials and methods

The alkali-activated materials were composed as a mixture of brick powder with a maximum grain size of 1 mm and one other basic aluminosilicate precursor (metakaolin, ground granulated blast furnace slag or coal fly ash) in different mass ratio. Brick powder content was 0, 25, 50, 75 and 100%. The chemical composition of the aluminosilicate precursors is introduced in Table 10.1. A commercial sodium silicate solution with  $\text{SiO}_2/\text{Na}_2\text{O} = 1.6$  was used as an activator and lower silicate moduli ( $M_s 1.3$ ,  $M_s 1.0$ ) were attained by mixing the water glass with pure solid NaOH (98%). The alkali-activated mortars were prepared using quartz sand with a maximum grain size of 2.5 mm as aggregate.

**Table 10.1.** Chemical composition of aluminosilicate precursors

Material	Brick powder	Metakaolin	Slag	Fly ash
$\text{SiO}_2$ (%)	55.39	55.01	36.72	49.82
$\text{Al}_2\text{O}_3$ (%)	17.07	40.94	8.54	24.67
$\text{Fe}_2\text{O}_3$ (%)	4.49	0.55	0.10	7.50
CaO (%)	13.15	0.55	39.80	3.91
MgO (%)	2.37	0.14	9.93	2.68
$S_{\text{total}}$ (%)	1.96	0.34	1.01	0.91
$\text{Na}_2\text{O}$ (%)	0.69	0.09	-	0.70
$\text{K}_2\text{O}$ (%)	2.79	0.06	-	2.78
MnO (%)	0.06	-	0.24	-
$\text{P}_2\text{O}_5$ (%)	0.24	-	0.03	-
$\text{TiO}_2$ (%)	1.30	-	0.33	-

The raw mix composition presented in Table 10.2 was designed according to the preliminary study when the water content (Fig. 10.1) varied in order to reach the same workability of mortars (EN 1015-3 1999). Fresh brick powder-fly ash blended binders exhibited extremely short setting time, so it was necessary to use a retarding agent (potassium citrate monohydrate) to keep the prolonged workability. This agent was used taking into account its possible adverse effect

on the mechanical properties with workability extended for more than 30 minutes, sufficient for mixing and moulding. The initial setting time of binders with metakaolin or slag was more than 60 minutes.

**Table 10.2.** Mix composition of alkali-activated mortars

Mixture	Aluminosilicate precursor (g)				Sodium silicate (g)	Sand (g)	K-citrate (g)
	BP	MK	S	FA			
MK 0	700	0	-	-	630 (M <sub>s</sub> 1.6, M <sub>s</sub> 1.3)	2100	-
MK 25	525	175					
MK 50	350	350					
MK 75	175	525					
MK 100	0	700					
S 0	700	-	0	-	280 (M <sub>s</sub> 1.6, M <sub>s</sub> 1.3)	2100	-
S 25	525		175				
S 50	350		350				
S 75	175		525				
S 100	0		700				
FA 0	700	-	-	0	490 (M <sub>s</sub> 1.0)	2100	122.5
FA 25	525			175			
FA 50	350			350			
FA 75	175			525			
FA 100	0			700			

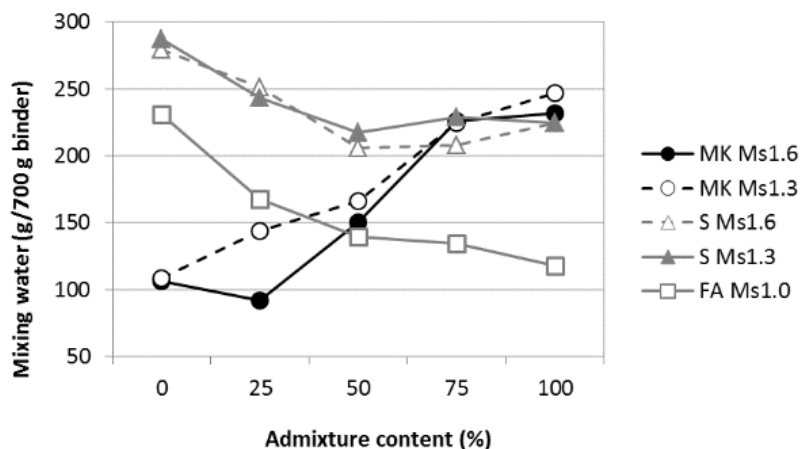


**Fig. 10.1.** Additional mixing water in alkali-activated mortars with various content of metakaolin, slag or fly ash

The mortars were cast into prismatic moulds ( $40 \times 40 \times 160$  mm) and covered with a plastic sealant to avoid moisture loss. After 24 h in the ambient conditions, the specimens were heated at  $40^\circ\text{C}$  for 4 h. After demoulding, the hardened specimens were stored in the laboratory conditions ( $22 \pm 2^\circ\text{C}$ ,  $\phi = 45 \pm 5\%$ ) till the age of 7 or 28 days, respectively.

The mechanical properties (compressive and flexural strength) were tested after 7 and 28 days of curing. The microstructure and porosity of the geopolymers (7 days) were evaluated using Micromeritics Poresizer 9310 and scanning electron microscope (SEM) Tescan MIRA3 XMU.

Alkali-activated pastes for rheology testing were prepared with brick powder of the maximum grain size of 0.125 mm and the water-to-binder ratio remained constant for each binary system to evaluate the influence of both solid precursors and water glass (dosage and viscosity) on the rheological properties of the paste. Mix composition is shown in Table 10.3. The fresh pastes were tested using Discovery HR-1 (TA instruments) hybrid rheometer and TRIOS 4.0.2 software was used for a data evaluation. The measurements were performed in a Peltier Concentric Cylinder system with a DIN rotor at  $25^\circ\text{C}$ . The standard gap for DIN cylinder system (5.917 mm) was adopted. The paste was introduced into the rheometer at the end of the mixing cycle and the measurement followed the procedure listed in Table 10.4. Parameters (yield stress, viscosity, rate index, reliability) were estimated from the decreasing shear branch of the flow curves using Herschel-Bulkley model:

$$\tau = \tau_0 + K\dot{\gamma}^n \quad (10.1)$$

where  $\tau$  is shear stress,  $\tau_0$  is yield stress,  $K$  is coefficient of consistency,  $\dot{\gamma}$  is shear rate and  $n$  is rate index. Investigations were performed at a constant temperature of  $25^\circ\text{C}$ .

**Table 10.3.** Mix composition of alkali-activated pastes for rheology measurements

Mixture	Aluminosilicate precursor (g)				Sodium silicate (g)	K-citrate (g)	Water (ml)
	BP	MK	S	FA			
MK 0	50	0	-	-	42	-	21
MK 25	37.5	12.5					
MK 50	25	25					
MK 75	12.5	37.5					
MK 100	0	50					
S 0	50	-	0	-	20	-	15
S 25	37.5		12.5				
S 50	25		25				
S 75	12.5		37.5				
S 100	0		50				
FA 0	50	-	-	0	35	8.75	14
FA 25	37.5			12.5			
FA 50	25			25			
FA 75	12.5			37.5			
FA 100	0			50			

**Table 10.4.** Procedure of the rheological measurements

Step	Duration	Description
Sample conditioning	60 s	Temperature equilibration (25 °C)
	60 s	Pre-shear, shear rate 100 s <sup>-1</sup>
	60 s	Equilibration
Flow Sweep	600 s	Linear sweep, shear rate 0,1–150 s <sup>-1</sup>

## 10.3. Results and discussion

### 10.3.1. Brick powder–metakaolin geopolymer

Mechanical properties of brick powder–metakaolin geopolymers are presented in Fig. 10.2. Generally, both compressive and flexural strength of the pure brick powder geopolymer (MK 0) were quite low. The strengths of the mixture with silicate modulus of 1.3 were slightly higher to a higher alkaline content, and thus better ability to dissolve aluminosilicate network. The flexural strength of these mixtures decreased with time which can be attributed to the microcrack formation caused by drying shrinkage. A partial replacement of brick powder with metakaolin significantly improved the mechanical performance. Blended binder made from brick powder and metakaolin also exhibited a rather intensive synergistic effect in strength. The best mechanical properties were achieved with metakaolin content of 50% (M<sub>S</sub>1.6) or 75% respectively (M<sub>S</sub>1.3).

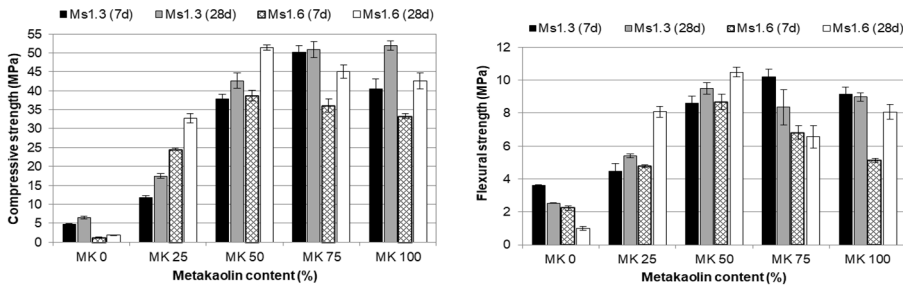


**Fig. 10.2.** Compressive (left) and flexural (right) strength of brick powder–metakaolin geopolymers at the age of 7 and 28 days

Mechanical properties are in good accordance with a pore size distribution of the samples (Fig. 10.3). When the metakaolin content rose above 50%, the binder was characterized by an increased number of gel pores and reduced volume of macropores. Although the total porosity of these samples was slightly higher, it influenced negatively neither compressive nor flexural strength. The porosity of binders with 75% of metakaolin was lower compared to the pure metakaolin geopolymer (in case of both types of water glass), which means that the brick powder in low dosage modifies pore structure and involves in strength enhancement of the material. Water in geopolymers with low Ca content has only a rheological purpose and it is not involved in geopolymerization process. Higher water demand in metakaolin binders was associated with its high specific surface but did not affect mechanical performance.

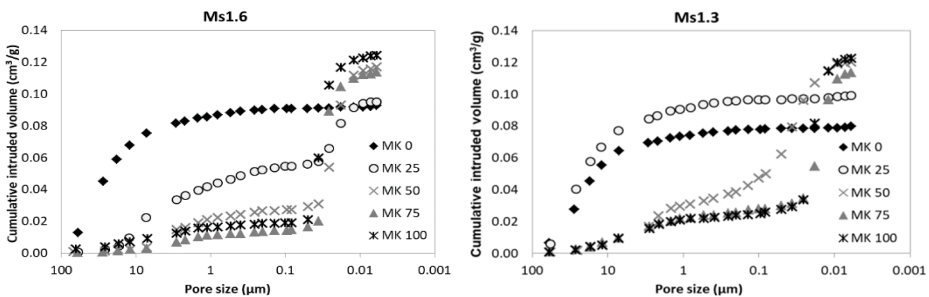


**Fig. 10.3.** Cumulative intruded volume of early brick powder–metakaolin geopolymers

Matrix homogeneity highly depended on the ratio of input materials as can be seen from the first two images of the same magnification (MK 25 and MK 75) in Fig 10.4. The structure of the binder consisted of intact brick particles and residual layered metakaolin particles bound by an aluminosilicate gel (Fig. 10.4, right).

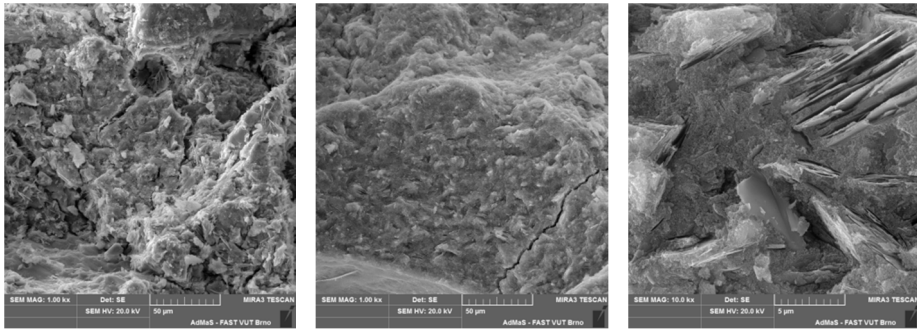


**Fig. 10.4.** SEM images of brick powder–metakaolin geopolymers (scale: MK 25: 50 µm, MK 75: 50 µm, MK 75: 5 µm)

Flow sweep curves recorded for the pastes with different metakaolin/brick powder ratio are shown in Fig. 10.5. With growing metakaolin content, pastes exhibited higher stress, yield stress and consistency coefficient. Pastes MK 0 and MK 25 (with both types of activating solution) were characterized by almost zero yield stress and rate index approaching 1 (Table 10.5) which refers to Newtonian fluids. In this case, the consistency coefficient can be considered a plastic viscosity. Increasing distance between two branches of flow curves for the pastes with increasing metakaolin content is caused by the thixotropic behaviour. Besides the metakaolin/brick powder ratio, all parameters of the fresh pastes with constant water content are also influenced by the silicate modulus (therefore viscosity) of alkaline activator solution. The consistency coefficient of mixtures with water glass of lower silicate modulus ( $M_s1.3$ ) is almost doubled with respect to the mixtures with other type of water glass ( $M_s1.6$ ). The rate index increased with higher metakaolin content indicating a slightly shear-thickening behaviour of metakaolin.

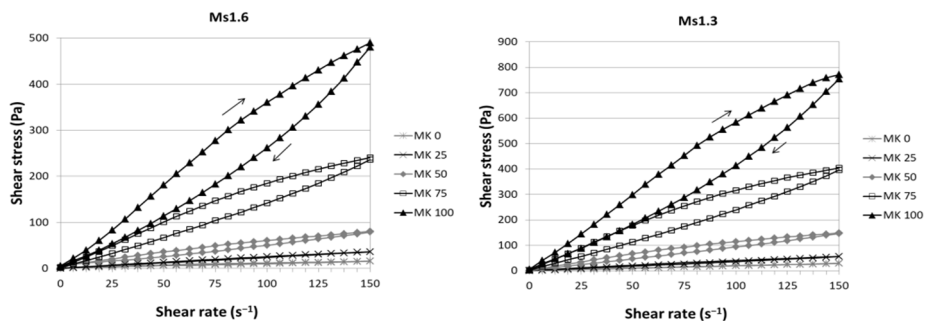


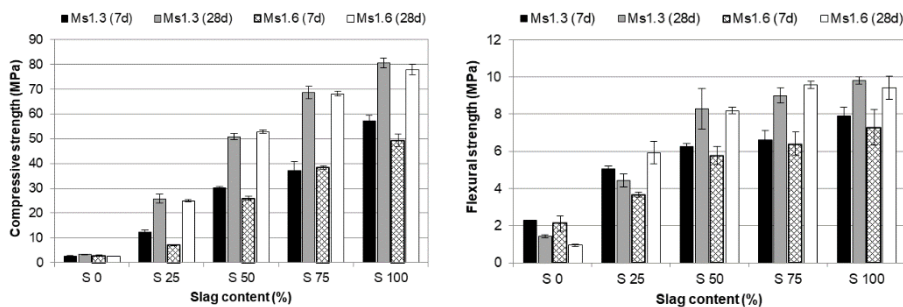
**Fig. 10.5.** Flow sweep curves of brick powder–metakaolin pastes

**Table 10.5.** Yield stress and viscosity of brick powder–metakaolin pastes

Mixture	Yield stress (Pa)		Consistency coefficient (Pa·s)		Rate index (-)	
	M <sub>S</sub> 1.6	M <sub>S</sub> 1.3	M <sub>S</sub> 1.6	M <sub>S</sub> 1.3	M <sub>S</sub> 1.6	M <sub>S</sub> 1.3
MK 0	0.40	0.06	0.10	0.20	0.99	0.99
MK 25	0.24	0.54	0.22	0.29	1.02	1.04
MK 50	5.55	2.13	0.21	0.66	1.16	1.07
MK 75	5.03	9.38	0.54	0.93	1.20	1.20
MK 100	15.55	26.93	0.32	0.53	1.44	1.44

### 10.3.2. Brick powder–slag binder

Alkali-activated brick powder binders with slag exhibited an apparent trend in mechanical strength evolution with a decreasing brick powder/slag ratio depicted in Fig. 10.6. Slag was responsible for high compressive strength (around 80 MPa) but binder with 50% of brick powder also reached a satisfactory value of around 50 MPa. Considerable influence of silicate modulus of the alkaline activator was not observed; the only difference consisted in slower compressive strength gains. Mechanical properties after 28 days of curing were comparable while 7 days strength was slightly higher for M<sub>S</sub>1.3 mixture. The flexural strengths followed a similar trend and were quite comparable with brick powder–metakaolin blends. Porosity changed in accordance with the results mentioned. Total pore volume of brick powder geopolymer was twice as high as the one of alkali-activated slag and the maximum of volume is associated with large capillary pores between 0.5–20  $\mu\text{m}$  (Fig. 10.7). In case of slag-rich binders, the water demand is lower but it is partly consumed during the hydration of Ca-rich slag to form C-A-S-H binding products.

**Fig. 10.6.** Compressive (left) and flexural (right) strength of brick powder–slag geopolymers at the age of 7 and 28 days



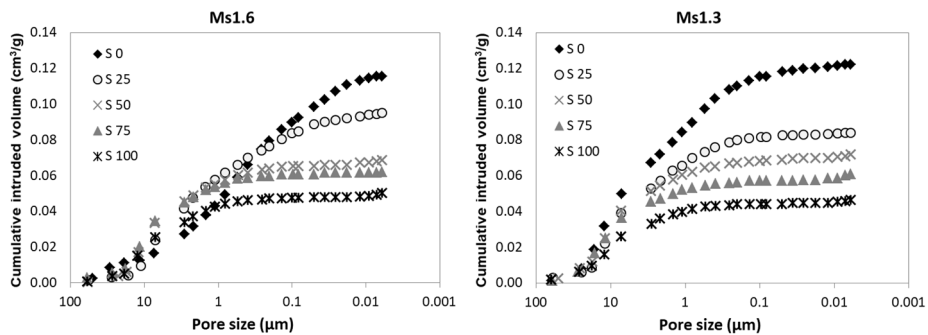


**Fig. 10.7.** Cumulative intruded volume of early brick powder–slag geopolymers

The SEM images in Fig. 10.8 show less homogenous structure with microcracks due to drying during the sample preparation procedure and needle-like crystals indicating the initial carbonation process. Carbonation of some metakaolin-based samples was also observed.

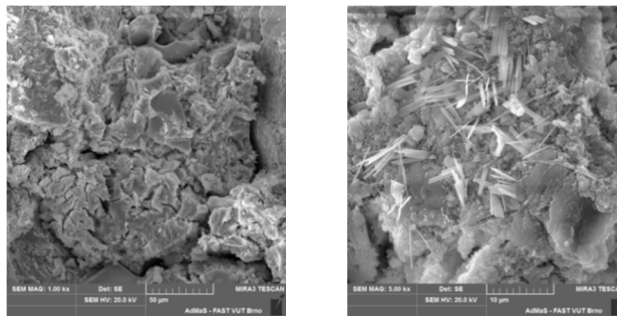


**Fig. 10.8.** SEM images of brick powder–slag geopolymers (scale: S 25: 50  $\mu\text{m}$ , S 25: 10  $\mu\text{m}$ )

Slag addition showed an adverse effect on the rheology of geopolymers (compared to metakaolin) and reduced the shear stress of the geopolymer pastes (Fig. 10.9). All pastes in the  $M_{S1.3}$  series containing slag showed similar yield stress and slightly decreasing consistency coefficient with a higher slag content (Table 10.6). However, mixture S 0 showed the worst workability because its coefficient of consistency is more than five times higher. Since rate index of all mixtures is very close to 1.0, the consistency index can be considered a plastic viscosity of geopolymer pastes. Pastes with activator  $M_{S1.6}$  showed similar trend with even lower viscosity of mixtures having more than 25% of slag. The exception was a pure brick powder mixture (S 0) for which the measurement was not completed due to the accelerated setting time. The maximal stress ascended to more than 1250 Pa and did not decrease during measurement of

decreasing branch of the flow curve. Therefore, it was not possible to assess the rheological parameters.

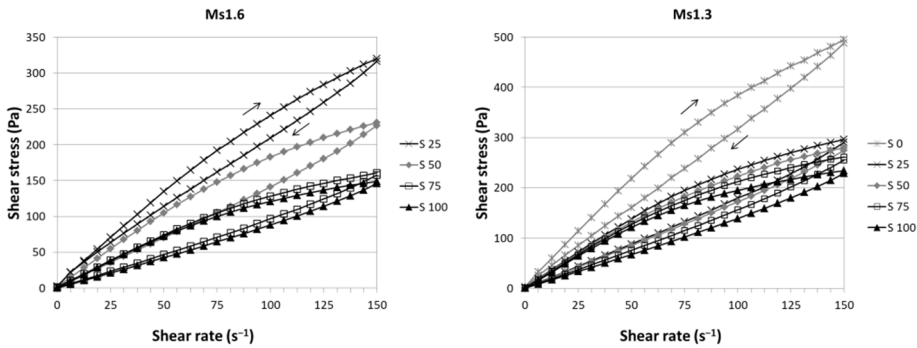


Fig. 10.9. Flow curves of brick powder-slag pastes

Table 10.6. Yield stress and viscosity of brick powder-slag pastes

Mixture	Yield stress (Pa)		Consistency coefficient (Pa·s)		Rate index (-)	
	Ms1.6	Ms1.3	Ms1.6	Ms1.3	Ms1.6	Ms1.3
S 0	-	0.59	-	5.62	-	0.89
S 25	7.43	4.86	2.46	1.02	0.96	1.12
S 50	4.07	s86	0.87	1.10	1.10	1.09
S 75	2.87	4.43	0.48	0.78	1.15	1.15
S 100	2.82	4.11	0.39	0.66	1.17	1.16

### 10.3.3. Brick powder-fly ash binder

While the brick powder-fly ash pastes tested in the preliminary study achieved excellent mechanical properties (more than 60 MPa in compression and 13 MPa in flexure after 7 days), addition of retarding agent to blended mortars caused an extreme drop in both compressive and flexural strength which varied within 7–13 MPa and 3.7–4.7 MPa, respectively (Fig. 10.10). Nevertheless, the combination of precursors did show a considerable synergistic effect. Samples with 50 and 75% of fly ash reached comparable properties but increased brick powder content resulted in lower 7 days strength. Fly ash-based binders usually exhibit good workability and required the lowest water content despite the higher viscosity of water glass with low silicate modulus (Ms1.0). Poor performance of brick powder-fly ash mortars was associated with a higher content of macropores (Fig. 10.11) and lower binding ability of constituent parts

probably affected by the retarding agent. This fact was also evidenced by SEM images in Fig. 10.12 illustrating low degree of particles dissolution and matrix

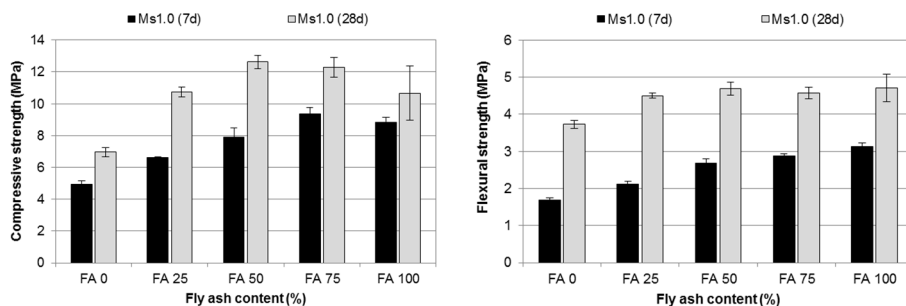


**Fig. 10.10.** Mechanical properties of brick powder–fly ash geopolymers (FA 1.0) after 7 and 28 days of curing

inhomogeneity. Moreover, the excess of alkalis that were not consumed during the geopolymerization process was reflected in a massive efflorescence formation (Fig. 10.12, right).

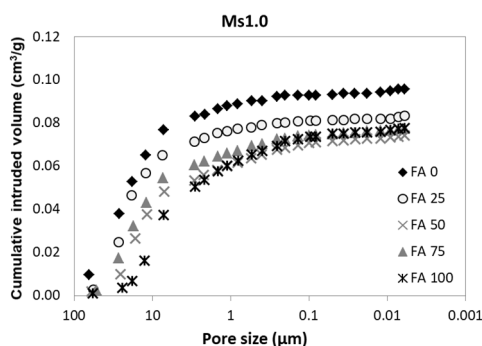


**Fig. 10.11.** Cumulative intruded volume of early brick powder–fly ash geopolymers

Addition of fly ash to the brick powder paste also decreased the stress but the differences were very small (Fig. 10.13). The pastes also showed less thixotropic behaviour compared to mixtures with slag and metakaolin. Yield stress of pure brick powder paste was slightly higher (1.32 Pa) than the one obtained for the pastes containing fly ash (0.66–0.76 Pa). In general, all the values could be considered as zero yield stress typical for Newtonian fluids (Table 10.7). Newtonian behaviour is also supported by the values of rate index which are almost equal to 1.00. Viscosity almost linearly decreased with the

decrease of brick powder/fly ash ratio. This can be explained by mostly spherical fly ash particles which increase the fluidity of the system.

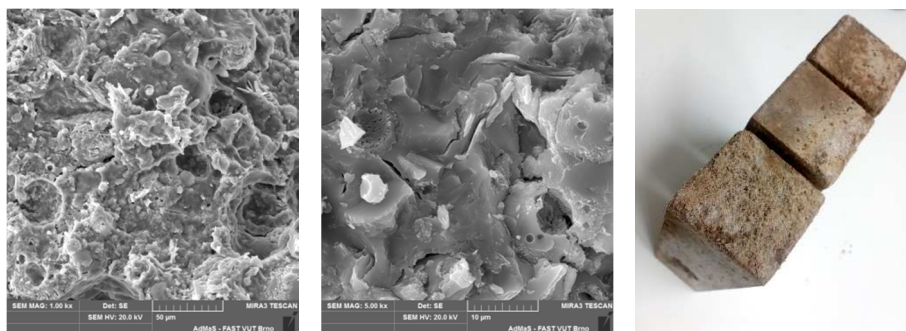


**Fig. 10.12.** SEM images of brick powder–fly ash matrix (scale: FA 50: 50  $\mu\text{m}$ , FA 50: 10  $\mu\text{m}$ ) and photograph of geopolymer sample with efflorescence.

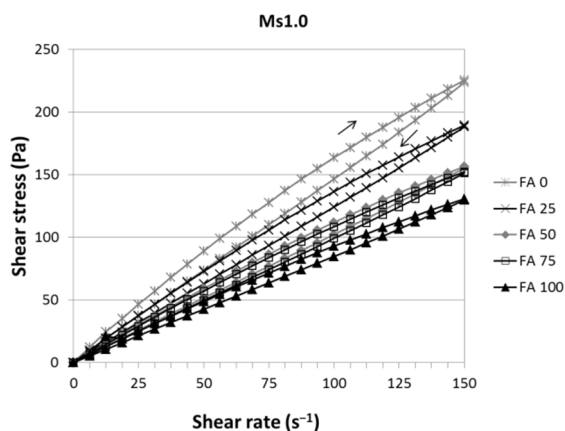


**Fig. 10.13.** Flow curves of brick powder–fly ash pastes

**Table 10.7.** Yield stress and viscosity of brick powder–fly ash pastes

Mixture	Yield stress (Pa)	Consistency index ( $\text{Pa}\cdot\text{s}$ )	Rate index (-)
FA 0	1.32	1.35	1.02
FA 25	0.76	1.21	1.01
FA 50	0.66	0.98	1.01
FA 75	0.75	0.89	1.02
FA 100	0.70	0.75	1.03

## 10.4. Conclusions

This study aimed to analyse the possibility of use of red clay brick powder in a binary alkali-activated binder with metakaolin, slag and fly ash. The best performance in terms of mechanical properties was observed in case of brick powder–metakaolin and brick powder–slag matrix, both of these reached the compressive strength of more than 40 MPa with 50% brick powder content. Brick powder geopolymers blended with slag exhibited lower porosity, and therefore, enhanced mechanical properties. Although the total pore volume of samples with higher metakaolin content was higher, it did not weaken the binder structure because of their small diameter (gel pores). Brick powder–fly ash geopolymers required highly concentrated alkaline activator solution which caused significant shortening in the setting time. The application of potassium citrate as retarding agent resulted in a considerable drop of strength accompanied by the formation of strong efflorescence. Metakaolin was the only precursor that increased yield stress and viscosity of fresh brick powder geopolymer pastes during rheological measurement, fly ash and slag caused their decrease. While the pastes with slag and a high percentage of metakaolin were thixotropic, parameters of all other mixture proved Newtonian fluid-like behaviour.

## Acknowledgement

This outcome has been achieved with the financial support of the Ministry of Education, Youth and Sports of the Czech Republic under the ‘National Sustainability Programme I’ (project No. LO1408 AdMaS UP).

## References

- Barnes, P & Bensted, J, 2014, *Structure and performance of cements*, CRC Press.
- Baronio, G & Binda, L, 1997, Study of the pozzolanicity of some bricks and clays, *Construction and Building Materials*, 11(1), pp. 41-46.
- Davidovits, J, 1994, Properties of geopolymer cements, *First international conference on alkaline cements and concretes*, pp. 131-149.
- Duxson, P, Fernández-Jiménez, A, Provis, JL, Lukey, GC, Palomo, A & van Deventer, JS, 2007, Geopolymer technology: the current state of the art, *Journal of materials science*, 42(9), pp. 2917-2933.
- EN 1015-3 (1999) – Methods of test for mortar for masonry - Part 3: Determination of consistence of fresh mortar (by flow table).
- Gluchovsky, VD, 1959, *Soil Silicates (Gruntosilikaty)*, Budivelnik Publisher,

Kiev.

- Keppert, M, Čáchová, M, Pavlíková, M, Trník, A, Žumár, J & Černý, R, 2014, Waste ceramics as supplementary cementitious material: characterization and utilization, *WIT Trans. Built Env.*, 142, pp. 231-239.
- Mehta, KP, 2001, Reducing the environmental impact of concrete. *Concrete international*, 23.10, pp. 61-66.
- Pachego-Torgal, F & Jalali, S, 2010, Reusing ceramic wastes in concrete, *Construction and Building Materials*, 24.5, pp. 832-838.
- Provis, JL & van Deventer, JSJ, 2014, *Alkali Activated Materials*, Springer.
- Rakhimova, NR & Rakhimov, RZ, 2015, Alkali-activated cements and mortars based on blast furnace slag and red clay brick waste, *Materials & Design*, 85, pp. 324-331.
- Robayo, RA, Mulford, A, Munera, J & de Gutiérrez, RM, 2016, Alternative cements based on alkali-activated red clay brick waste. *Construction and Building Materials*, 128, pp. 163-169.
- Sun, Z, Cui, H, An, H, Tao, D, Xu, Y, Zhai, J & Li, Q, 2013, Synthesis and thermal behavior of geopolymer-type material from waste ceramic, *Construction and Building Materials*, 49, pp. 281-287.
- Turanli, L, Bektas, F & Monteiro, PJM, 2003, Use of ground clay brick as a pozzolanic material to reduce the alkali-silica reaction *Cement and Concrete Research*, 33(10), pp. 1539-1542.
- Van Deventer, JSJ, Provis, L, Duxson, P & Brice, DG, 2010, Chemical research and climate change as drivers in the commercial adoption of alkali activated materials. *Waste and Biomass Valorization*, 1.1, pp. 145-155.



## 11. Numerical analysis of the temperature distribution in an office room

**Maciej Major<sup>1</sup>, Izabela Major<sup>2</sup>, Jarosław Kalinowski<sup>3</sup>, Mariusz Kosiń<sup>4</sup>**

<sup>1</sup> *Czestochowa University of Technology, Faculty of Civil Engineering, Department of Metal Structures and Building Materials, Częstochowa, Poland, [orcid.org/0000-0001-5114-7932](https://orcid.org/0000-0001-5114-7932)*

<sup>2</sup> *Czestochowa University of Technology, Faculty of Civil Engineering, Department of Technical Mechanics and Engineering Graphics, Częstochowa, Poland, [orcid.org/0000-0003-1234-9317](https://orcid.org/0000-0003-1234-9317)*

<sup>3</sup> *Czestochowa University of Technology, Faculty of Civil Engineering, Department of Civil Engineering and Architecture, Częstochowa, Poland, [orcid.org/0000-0001-8922-4788](https://orcid.org/0000-0001-8922-4788)*

<sup>4</sup> *Czestochowa University of Technology, Faculty of Civil Engineering, Department of Construction Organization and Technology, Częstochowa, Poland, [orcid.org/0000-0003-2683-7784](https://orcid.org/0000-0003-2683-7784)*

**Abstract:** The article sets the temperature distribution for the office room and people in it. The analysis was made on the basis of the numerical solution of the state determined in the ANSYS-Fluent.

**Keywords:** numerical analysis, temperature distribution, thermal comfort

### 11.1. Introduction

Maintaining thermal comfort at work is recommended not only to ensure adequate employee performance. Employee is obliged to adjust individual air parameters to the standards defined in the Regulation of the Minister of Labour and Social Policy (Rozporządzenie Ministra Pracy i Polityki Socjalnej w sprawie ogólnych przepisów bezpieczeństwa i higieny pracy). According to this regulation, temperature in office rooms cannot be lower than 18°C. Thermal comfort in rooms is felt individually and subjectively. An ideal was the system that guaranteed the lowest percentage possible of people dissatisfied with indoor conditions. Due to the fact that humans spend most of their time indoors, evaluation of these conditions is critical. Thermal comfort in rooms has been examined by numerous researchers, including those conducted by Ravikumar & Prakash 2009, Stavrakakis et al. 2008, Myhren & Holmberg 2008, Fanger et al. 1974. Many researchers have used numerical analyses, with their studies concerning three-dimensional steady-state numerical analysis in a room heated by two-panel radiators (Sevilgen & Kilic 2011), or numerical evaluation of



thermal comfort in a room (Embaye et al. 2016) also in a cross-ventilated space with top-hung windows (Deng et al. 2017).

The aim of this study is to present parameters of thermal comfort using the ANSYS Fluent software with the example of the selected office room. The paper presents a three-dimensional numerical analysis of temperature distribution conducted for an office room. A real room heated with a steel two-panel heater was analysed. Furthermore, floor heating and thermal carriers were adopted for comparison. People remaining in this room were also taken into consideration. It was demonstrated that with the computation methods used, it is possible to perform analysis of technological and material solutions already at the stage of design and use of the room.

## 11.2. Focus of the analysis

The analysis concerned an office room on the last floor of the building of the Faculty of Civil Engineering, Częstochowa University of Technology in Częstochowa, Poland (Fig. 11.1). Room dimensions are  $5.32 \text{ m} \times 3.78 \text{ m} \times 3 \text{ m}$ , with a cutout for the chimney channel with dimensions of  $0.15 \text{ m} \times 1.6 \text{ m} \times 3 \text{ m}$  (Fig. 11.2). There was a wall unit and three desks in the room (Figs. 11.1a and 11.1b).

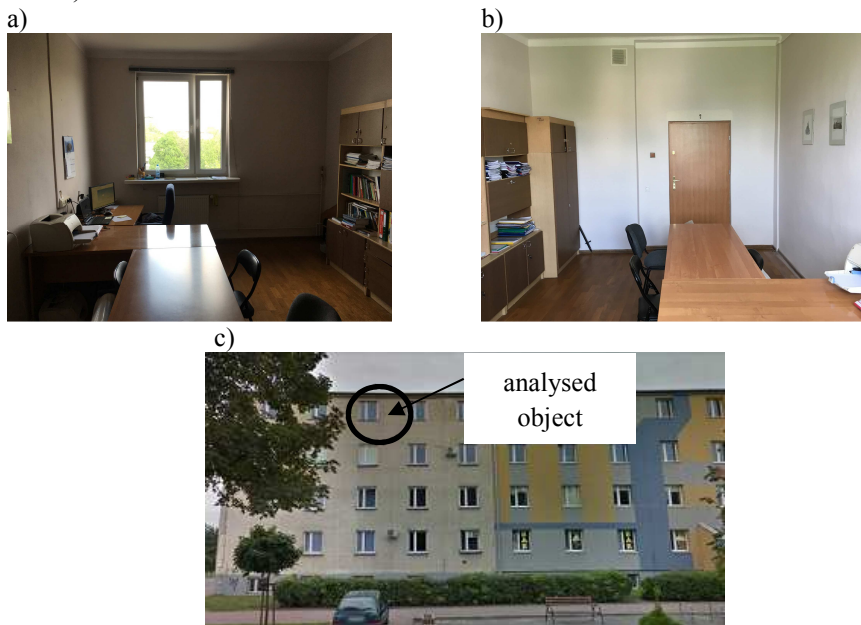


**Fig. 11.1.** Real view of the analysed room: a) view to the window, b) view to the door, c) front façade of the building

The computations took into consideration three cases of heating. Case 1 reflected the real conditions of heating by means of a two-panel steel heater with dimensions of  $0.8 \text{ m} \times 0.6 \text{ m}$ , fed from the university's heating plant. Case 2 assumed the use of floor heating, whose heating field is removed from each wall by  $0.4 \text{ m}$ , with total heating surface of the heating of  $12.2 \text{ m}^2$ . Case 3, the last in the examinations, assumes the use of a two-panel heater with dimensions of  $0.8 \text{ m} \times 0.6 \text{ m}$  (as in the Case 1) and floor heating with surface area of  $12.2 \text{ m}^2$  (installed as in the Case 2).

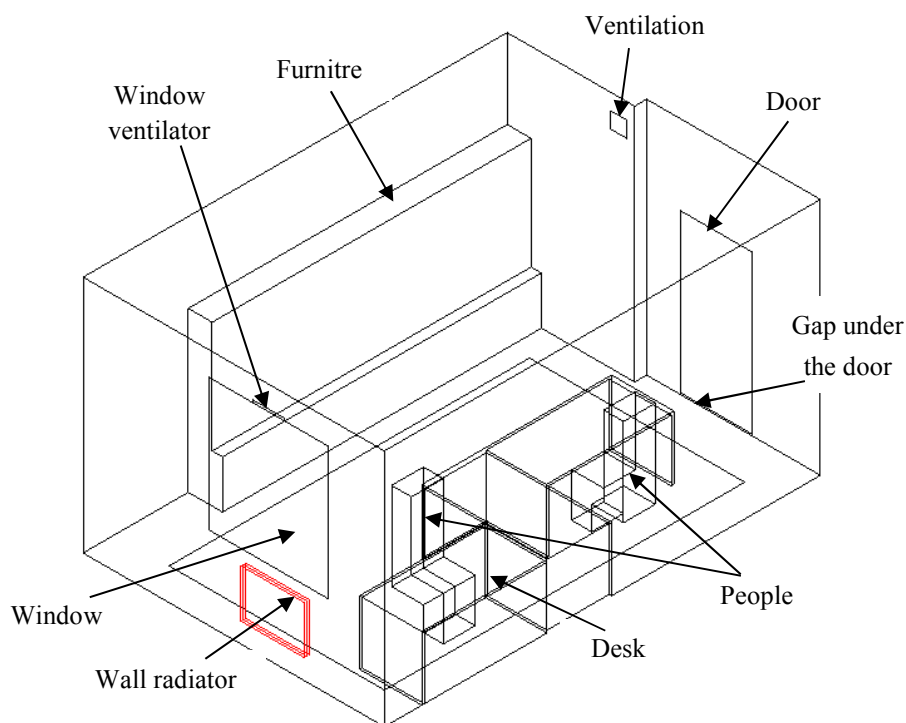


**Fig. 11.2.** Model of the room analysed

### 11.3. Numerical model and case study

ANSYS - Fluent software was used for numerical analysis (comp. Major & Kosiń 2016 or Major & Kosiń 2017). A source of heat adopted for computations was one of the cases (Case 1, Case 2 and Case 3) and heat from two people. Temperature of heating devices was  $70^{\circ}\text{C}$  for the wall heater and  $29^{\circ}\text{C}$  for floor

heating. Due to the clothing, the temperature generated by humans was adopted as  $33.7^{\circ}\text{C}$ .

The external air temperature of  $-20^{\circ}\text{C}$  was adopted for the analysis. The temperature of air flowing from the rooms adjacent to the building was  $20^{\circ}\text{C}$ . Numerical analysis did not take into consideration the heat gains from solar radiation.

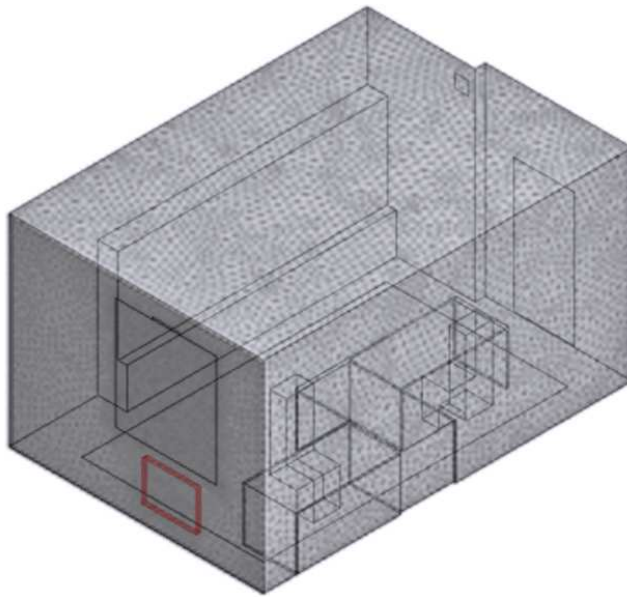


**Fig. 11.3.** The view of the generated net of finite elements

Inflow of air from the outside occurred through the window air inlet, for which entire value of ventilation air flux was  $0.007\text{ kg/s}$ . Furthermore, air outflow was ensured by gravitational ventilation outlet with dimensions of  $0.2\text{ m} \times 0.2\text{ m}$  and a gap under the door ( $0.9\text{ m} \times 0.02\text{ m}$ ) leading to the building corridor.

Due to the shortening of the computation time, a grid with four-wall components was generated (Fig. 11.3). Details of grid generation and solutions were derived from the literature: Ansys Fluent 12 User's Guide 2001 and Major & Kosiń 2016. The computational domain was composed of nearly three million nodes.

## 11.4. Solutions

For the analysed cases (1 to 3), the figures below (11.4a-c and 11.5a-c) present isotherms on the plane parallel to the floor and on the vertical plane. The assumed planes parallel to the floor were placed, respectively, at the floor level (height: 0.00 m), over the desk (height: 1.00 m) and at the level of the head of a sitting person (height: 1.4 m).

Figs. 11.4d and 11.5d illustrate distribution of temperatures in the vertical plane passing through the centre of the window air inlet (compare Fig. 11.2).

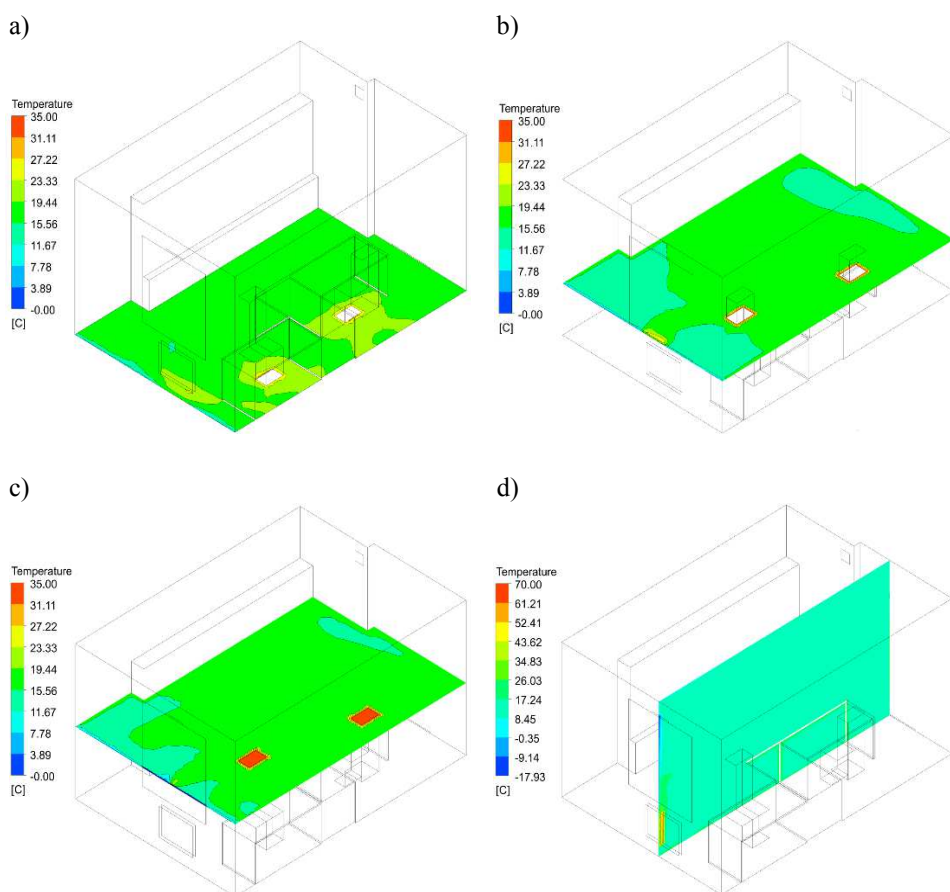


**Fig. 11.4.** Distribution of temperature: Case 1: a) level of floor of 0.00 m, b) level over the desk 1 m, c) level of the head 1.4 m, d) vertical plane passing through the centre of the air inlet

In the Case 1, moving planes show a disturbed distribution of temperature at the side of the wall with the window and wall with the door (Fig. 11.4b, c). The change in the temperature fields occurs also in the area of sitting people (Fig. 11.4a). Fig. 11.4a shows heat radiation from the heater and the effect of low temperature from the window part (Fig. 11.4d).

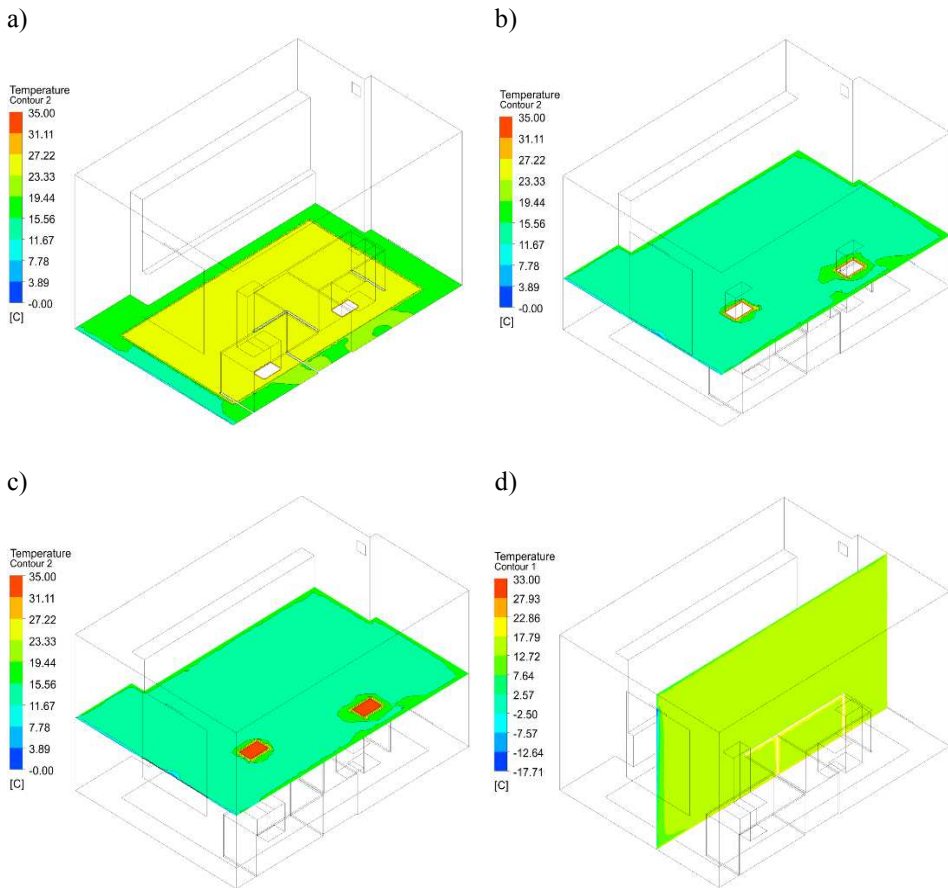


**Fig. 11.5.** Distribution of temperature: Case 2: a) level of floor of 0.00 m, b) level over the desk 1 m, c) level of the head 1.4 m, d) vertical plane passing through the centre of the air inlet.

The isolines at the floor level in the Case 2 show variable fields of temperatures near the external wall and in the area of feet of the people sitting at desks (Fig. 11.5a). In other vertical planes, distribution is not homogeneous, with light

disturbances near people sitting in the room (Fig. 11.5b, 11.5d). The window zone, presented in Fig. 11.5d, contains a band of cooler temperature over the height of the external wall.

For the Case 3, with mixed heating, including heating with a two-panel steel wall heater with the dimensions of  $0.8 \text{ m} \times 0.6 \text{ m}$  and floor heating with the surface area of  $12.2 \text{ m}^2$ , distribution of temperature at the floor level (Fig. 11.6a) differs significantly from the Case 2. The vertical plane shows greater changes in temperatures in the area near the window (Fig. 11.6d).

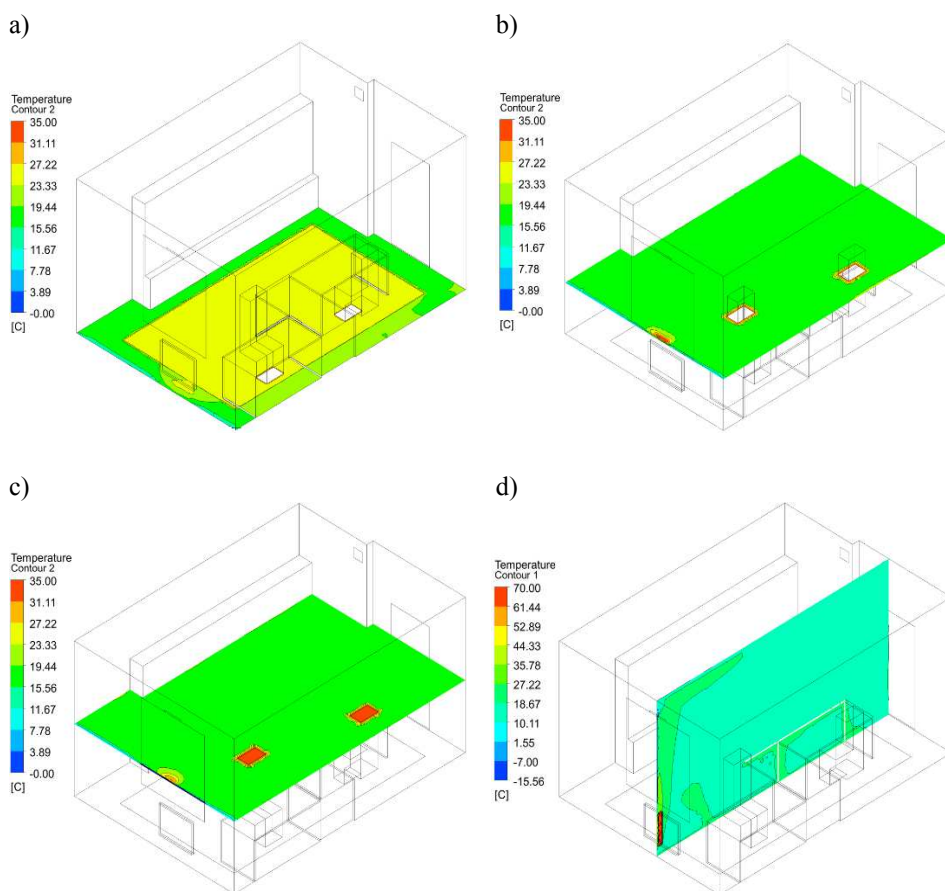


**Fig. 11.6.** Distribution of temperature: Case 3: a) level of floor of 0.00 m, b) level over the desk 1 m, c) level of the head 1.4 m, d) vertical plane passing through the centre of the air inlet.

Other figures (Figs. 11.7 – 11.9) showed isolines of the velocity of air moving in the analysed room. In the first case, the most intensive air stream can be observed in the part of the room located nearest the heater (Fig. 11.7). Different situation is observed for the Case 2 and 3, where substantially greater changes occur in the area near the floor i.e. near the person sitting nearest the window (Figs. 11.7c and 11.7d, 11.8c and 11.8d).

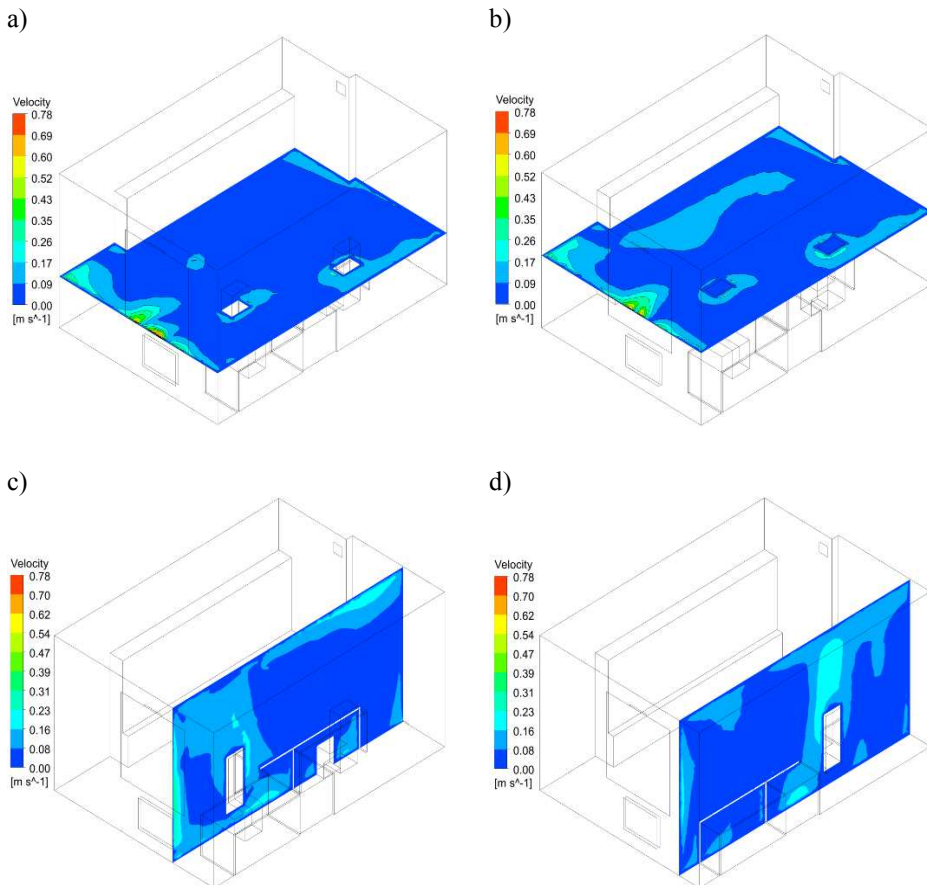


**Fig. 11.7.** Velocity isolines: Case 1: a) horizontal surface over the desk (1m), b) horizontal plane at the height of the head (1.4 m), c) vertical plane passing through the person sitting nearest the window, d) vertical plane passing through the person sitting further from the window



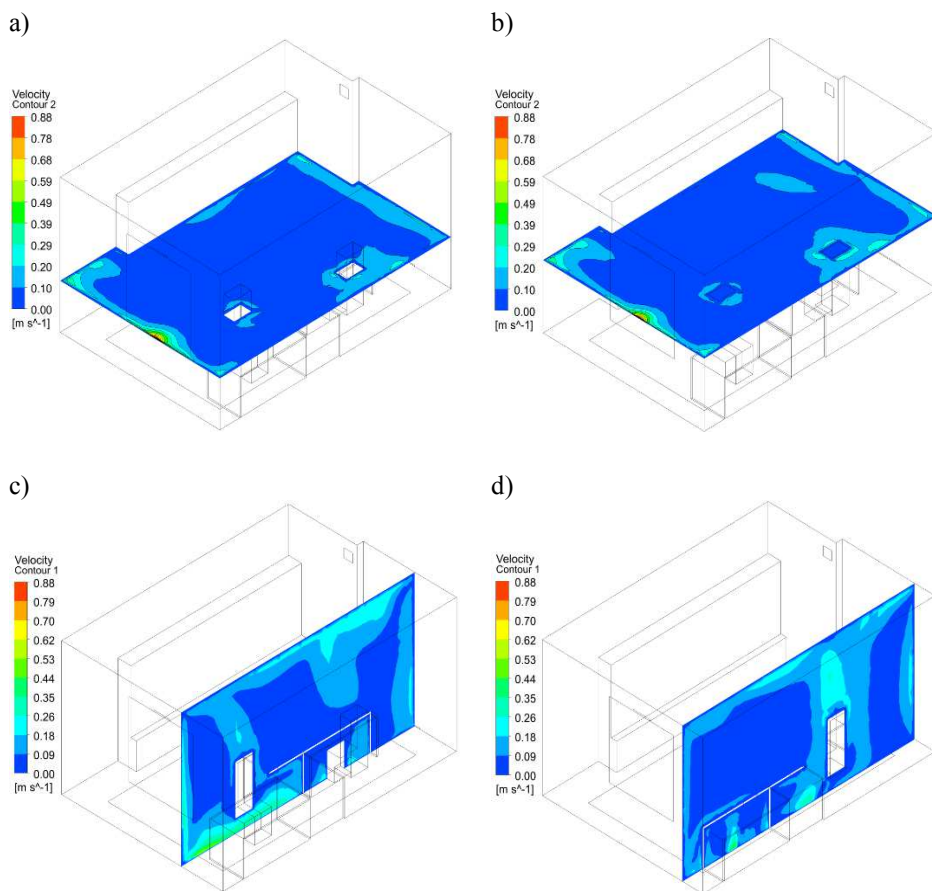


**Fig. 11.8.** Velocity isolines: Case 2: a) horizontal surface over the desk (1m), b) horizontal plane at the height of the head (1.4 m), c) vertical plane passing through the person sitting nearest the window, d) vertical plane passing through the person sitting further from the window



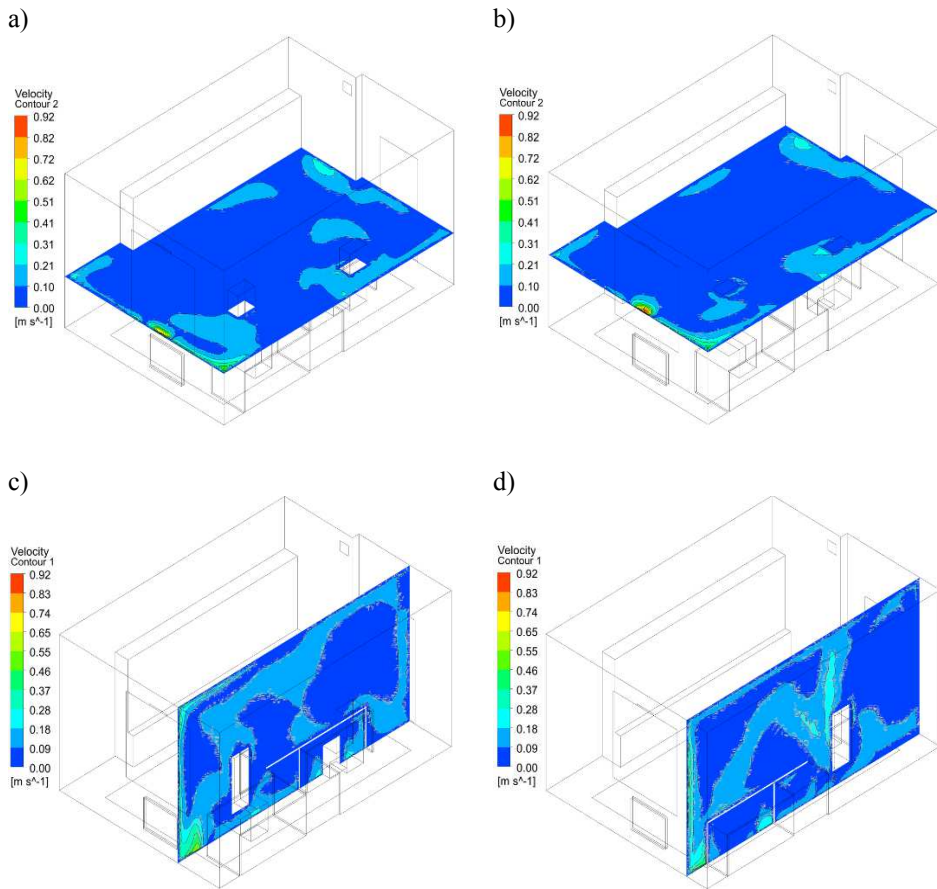


**Fig. 11.9.** Velocity isolines: Case 3: a) horizontal surface over the desk (1m), b) horizontal plane at the height of the head (1.4 m), c) vertical plane passing through the person sitting nearest the window, d) vertical plane passing through the person sitting further from the window

## 11.5. Conclusions

The aim of this study was to model the problems connected with the evaluation of the temperature distribution for various heat carriers by means of numerical methods. The use of numerical software allows for a relatively fast evaluation of the adopted methods of room heating and allows for verification of the adopted solutions. Numerical computations provide both information about the parameters of concern and they allow for a graphical representation of the

distribution of these parameters in the room analysed. Consequently, analysis of technological and construction solutions can be made at the design stage, which has a substantial effect on the functional properties of the building. This allows for an effective designing of solutions and assessment of the thermal comfort in the room where humans are expected to spend time, whereas their individual sensations will determine their work performance. One should strive to ensure that the system that guarantees thermal comfort in a room should meet the expectations of people remaining inside. Since humans spend most of their time indoors, numerical analysis of the thermal comfort is a very important and desired form of evaluation of the expected solutions. This can be performed using 3D software such as ANSYS - Fluent.

## References

- Ansys Fluent 12 User's Guide*, Ansys Inc., Lebanon, NH, USA, 2001.
- Rozporządzenie Ministra Pracy i Polityki Socjalnej w sprawie ogólnych przepisów bezpieczeństwa i higieny pracy*, Dz.U. 1997 nr 129 poz. 844 z późn. zm. (in polish).
- Deng X., Cooper P., Ma Z., Kokogiannakis G., *Numerical analysis of indoor thermal comfort in a cross-ventilated space with top-hung windows*, "Energy Procedia" 2017, Vol. 121, p. 222-229.
- Embaye M., AL-Dadah R.K., Mahmoud S., *Numerical evaluation of indoor thermal comfort and energy saving by operating the heating panel radiator at different flow strategies*, "Energy and Buildings" 2016, Vol. 121, p. 298-308, doi.org/10.1016/j.enbuild.2015.12.042
- Fanger P.O., Östberg O., McK. Nicholl A.G., Breum N.O., Jerking E., *Thermal comfort conditions during day and night*, "European Journal of Applied Physiology" 1974, No 33, p. 255-263.
- Major M., Kosiń M., *Modelowanie rozkładu temperatur w przegrodach zewnętrznych wykonanych z użyciem lekkich konstrukcji stalowych*, „Budownictwo o zoptymalizowanym potencjale energetycznym” 2016, No 2(18), p. 55-60, (in polish).
- Major M., Kosiń M., *Numerical thermal analysis of the vertical external partition made as the frame thin-walled steel structure*, "MATEC Web of Conferences", DYN-WIND'2017, 2017, Vol. 107, p. 1-8.
- Myhren J. Are, Holmberg S., *Flow patterns and thermal comfort in a room with panel, floor and wall heating*, "Energy and Buildings" 2008, Vol. 40(4), p. 524-536.
- Ravikumar P., Prakash D., *Analysis of thermal comfort in an office room by varying the dimensions of the windows on adjacent walls using CFD: a case study based on numerical simulation*, "Building simulation" 2009,

Vol. 2(3), p. 187–196.

Sevilgen G., Kilic M., *Numerical analysis of air flow, heat transfer, moisture transport and thermal comfort in a room heated by two-panel radiators*, “Energy and Buildings” 2011, Vol. 43(1), p. 137-146.

Stavrakakis G. M., Koukou M. K., Vrachopoulos M. Gr., Markatos N.C., *Natural cross-ventilation in buildings: building-scale experiments, numerical simulation and thermal comfort evaluation*, “Energy and Buildings”, 2008, Vol. 40(9), p. 1666–1681.

## 12. Generalized maximum tangential stress criterion in double cantilever beam specimens: choice of the proper critical distance

Lucie Malíková<sup>1</sup>, Hana Šimonová<sup>1</sup>

<sup>1</sup> Brno University of Technology, Faculty of Civil Engineering, Institute of Structural Mechanics, Brno, Czech Republic, [orcid.org/0000-0001-5868-5717](https://orcid.org/0000-0001-5868-5717), [orcid.org/0000-0003-1537-6388](https://orcid.org/0000-0003-1537-6388)

**Abstract:** The papers is focused on generalized maximum tangential stress criterion in double cantilever beam specimens. The conducted research programme allowed to find the critical distance between 0.35 and 0.6 mm which seems to be suitable for the specimens with the defined geometry and made of the material under the study.

**Keywords:** tangential stress, beam, defect, critical distance

### 12.1. Introduction

When a defect/crack is detected in a structure, the fracture mechanics concept is applied in order to estimate the reliability and/or lifetime of the damaged structure. Generally, fracture mechanics (Anderson, 2004) deals with description of cracks behaviour in various kind of materials where different types of fracture can occur; they are usually classified as the brittle, the elastic-plastic or the quasi-brittle case, see e.g. (Bažant and Planas, 1998; Shah *et al.*, 1995). For each kind of fracture specific approaches have been derived and they should not be applied elsewhere because of their limited validity. For example, the linear elastic fracture mechanics approaches cannot predict correct failure response in the case of elastic-plastic or quasi-brittle fracture. Similarly, the strength theory ignoring the stress concentration at cracks/notches/defects tips and also ductile fracture models are not suitable for failures with a rapid and huge energy release (typical for brittle fracture and in some cases for quasi-brittle fracture).

Nevertheless, sometimes the fracture response does not follow any of the theories suggested for the three kinds of fracture; of course, there exist transition zones between the individual types of fracture, see (Veselý *et al.*, 2017). There are always efforts to find some theory that would enable to cover as many fracture kinds as possible.

One of useful tools how to get more precise results when fracture response is described seems to be utilization of the multi-parameter fracture mechanics concept. This theory is based on the assumption that the stress/displacement field near a crack tip can be expressed by means of a power series (Williams, 1957), Williams expansion (WE), i.e. that not only the first (singular) term controls the crack propagation but also the terms of higher orders are significant. This is especially important for materials where the fracture process occurs not only very close to the crack tip but also in a further distance from the crack tip. Typically, the material behaviour in this region is mostly nonlinear and is not sufficiently explored. Moreover, the size/geometry/boundary effect has to be taken into account, see (Ayatollahi and Akbardoost, 2012; Duan *et al.*, 2007; Karihaloo *et al.*, 2006). The influence of the specimen shape on the mode I fracture strength has been demonstrated recently (Chao *et al.*, 2001; Davenport and Smith, 1993; Khan and Al-shayea, 2000; Kumar *et al.*, 2011; Liu and Chao, 2003; Sun and Qian, 2009).

The multi-parameter concept has been applied to several fracture mechanics tasks (such as near-crack-tip stress field approximation, crack propagation assessment, plastic zone extent estimation, etc.) and its significance has been proved ((Šestáková) Malíková, 2013; Šestáková, 2014; Veselý *et al.*, 2014). Subsequent investigations are introduced in this paper.

Particularly, the topic of the presented work is connected to the interest in investigations of the crack path. It has been observed that although the crack is loaded under pure mode I (when it is expected that it will propagate along the direction of the original crack plane), it sometimes kinks (Ayatollahi *et al.*, 2010; Betegon and Hancock, 1991; Du and Hancock, 1991; Larsson and Carlsson, 1973; Rice, 1974). This phenomenon is often explained by means of the constraint effect, i.e. it is connected to the value of  $T$ -stress (second/non-singular term of the Williams expansion). Several fracture criteria including some initial terms of the WE have been proposed and it has been observed that taking into account the  $T$ -stress values can bring more reliable fracture assessment (Aliha *et al.*, 2010; Aliha and Ayatollahi, 2010; Ayatollahi *et al.*, 2015; Ayatollahi and Aliha, 2009; Cotterell, 1966; Pook, 2015; Smith *et al.*, 2001).

In order to show importance of the terms of higher orders of the WE, multi-parameter fracture criteria have been derived and effect of  $T$ -stress studied, particularly a Generalized Maximum Tangential Stress (GMTS) criterion (Ayatollahi *et al.*, 2015; Smith *et al.*, 2001) or Average Strain Energy Density (ASSED) criterion (Lazzarin *et al.*, 2009).

In this work a multi-parameter form of the Maximum Tangential Stress (MTS) criterion is suggested and tested in order to find the initial crack propagation angle. The numerical analyses are based on the experimental observations on PMMA specimens. The basic geometry proceeds from the Compact Tension (CT) specimens and then several more specimens with larger widths (representing Double Cantilever Beam (DCB) specimens) are suggested, modelled and a parametrical study is performed. The choice of the crucial length parameter (critical distance from the crack tip, where the criterion is applied) is discussed thoroughly.

## 12.2. Basic terms and theory

The key idea of this paper is the approximation of the stress/displacement field near the crack tip by means of the Williams power series. This theory can be involved in fracture mechanics tasks and assumes that not only the first singular term is important for the stress state in a cracked specimen. Whereas the classical linear elastic fracture mechanics considers only the stress intensity factor as the single-controlling parameter, WE enables to take into account also the higher-order (non-singular) terms. The theory was derived for a crack in an elastic isotropic homogeneous body subjected to an arbitrary remote loading. Then, the stress tensor and displacement vector components for a crack under I+II mixed mode can be expressed as follows:

$$\sigma_{ij} = \sum_{n=1}^{\infty} A_n \frac{n}{2} r^{\frac{n}{2}-1} f_{I,ij}(\theta, n) + \sum_{m=1}^{\infty} B_m \frac{m}{2} r^{\frac{m}{2}-1} f_{II,ij}(\theta, m) \quad (12.1)$$

and

$$u_i = \sum_{n=0}^{\infty} A_n \frac{n}{2} r^{\frac{n}{2}} g_{I,ij}(\theta, n, E, \nu) + \sum_{m=0}^{\infty} B_m \frac{m}{2} r^{\frac{m}{2}} g_{II,ij}(\theta, m, E, \nu) \quad (12.2)$$

The meaning of the symbols is:

- $i, j$  –  $i, j = \{x, y\}$ ,
- $r, \theta$  – polar coordinates (assuming the origin of the coordinate system at the crack tip and the crack faces lying on the negative  $x$ -axis),
- $f_{I,ij}(\theta, n)$  – known functions corresponding to the stress tensor components and mode I of loading,
- $f_{II,ij}(\theta, m)$  – known functions corresponding to the stress tensor components and mode II of loading,
- $g_{I,ij}(\theta, n, E, \nu)$  – known functions corresponding to the displacement vector components and mode I of loading,
- $g_{II,ij}(\theta, m, E, \nu)$  – known functions corresponding to the displacement vector components and mode II of loading,

- $E, \nu$  – material parameters, i.e. Young's modulus and Poisson's ratio,
- $A_n, B_m$  – coefficients of the higher-order terms; depending on the specimen geometry and boundary conditions.

Both Eq. 12.1 and 12.2 are used in their truncated form in the procedure described in the following sections. First, the approximation of the displacements serves for calculation of the coefficients of the higher-order terms and then the approximation of the stresses is a part of the MTS fracture criterion.

Note, that the well-known stress intensity factor corresponds to the first coefficient of the WE ( $K_I = A_1\sqrt{2\pi}$ ,  $K_{II} = -B_1\sqrt{2\pi}$ ). Second (non-singular) term corresponds to the in-plane  $T$ -stress. Coefficients of the higher orders are not connected to any conventional fracture parameters.

### 12.3. Over-deterministic method

When Eq. 12.1 shall be used for approximation of the crack-tip stress field and application of the multi-parameter MTS criterion, it is necessary to determine the coefficients of the WE. This must be done numerically in the most cases, an over-deterministic method (ODM) is applied in this work, see (Aytollahi and Nejati, 2011) for more details.

The principle of the ODM is relatively simple in comparison to other methods such as hybrid crack element method, boundary collocation method or others that require more extensive and deeper knowledge of the special elements or advanced mathematical procedures (Karihaloo and Xiao, 2001; Knésl, 1994/1995; Su and Fok, 2007; Tong *et al.*, 1997; Xiao *et al.*, 2004).

The ODM procedure based on the formulation of linear least-squares consists in the direct application of Eq. 12.2. Particularly, a finite element (FE) model of the cracked specimen according to the experimental configuration was created to get the nodal solution. Then, the displacements  $u_x, u_y$  of a set of nodes at a selected radial distance from the crack tip were further used as inputs for the ODM application. When the FE solution is known in the set of  $k$  nodes, a system of  $2k$  equations arises. Solution of such a defined system is represented by the coefficients of the individual terms of the WE. Naturally, the crucial idea of the ODM is that the system of equations must be over-determined, i.e. when  $N$  mode I coefficients and  $M$  mode II coefficients shall be calculated, at least  $(N + M)/2 + 1$  nodes with their coordinates and displacements must be taken as inputs for the ODM procedure. Further details on the accuracy, convergence,

mesh sensitivity of the method can be found in (Malíková, 2015; Růžička *et al.*, 2017; Šestáková (Malíková), 2013; Šestáková and Veselý, 2013).

## 12.4. Cracked specimen geometry

As is mentioned in the previous text, several cracked geometries have been chosen and the Compact Tension was the basic one. Additionally, the width of the original specimen was enlarged and several double cantilever beam (DCB) specimen configurations were considered ( $W = 60, 90$  and  $150$  mm), see Fig. 12.1a.

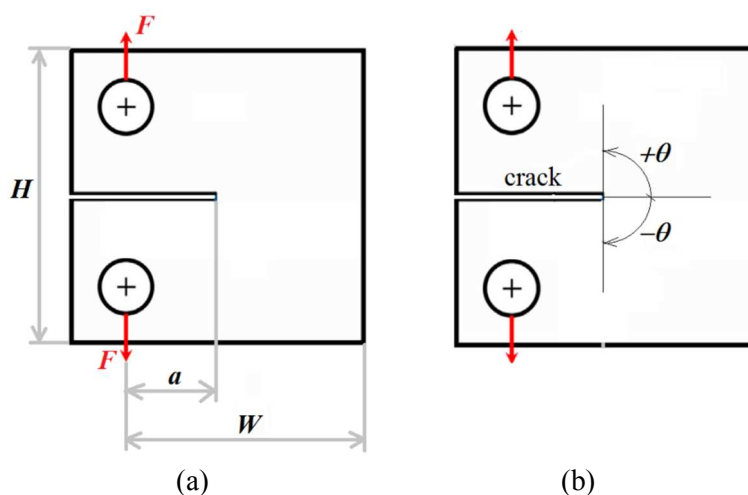


**Fig. 12.1.** (a) Schema of the investigated cracked specimen:  $W = 30$  (CT),  $W = 60, 90$  and  $150$  mm (DCB); (b) region where the tangential stress was investigated

The specimen dimensions were considered as follows: specimen height  $H = 30$  mm, specimen thickness  $B = 10$  mm and specimen width  $W = 30$  (CT),  $W = 60, 90$  and  $150$  mm (DCB). The crack length (following the designation introduced in Fig. 12.1a) was always a half of the width,  $a = W/2$ . The specimen was subjected to tensile loading, the values of the loading force were set up with regard to experimental observations (Ayatollahi *et al.*, 2016). The values of the fracture forces were measured as:  $F = 319, 214, 141$  and  $87$  N (corresponding to the specimen width  $30, 60, 90$  and  $150$  mm).

Based on the specified geometry, the specimen was modelled in a FE code, particularly in ANSYS FE code (Ansys, 2016). The most important properties of the model were: two-dimensional, linear elastic, meshed with quadratic 8-



node PLANE183 elements, refined mesh around the crack tip, plane strain conditions. The square root singularity of the stress at the crack tip was emphasized by means of using shifted mid-side in the first row of elements. The elastic material constants corresponded to the PMMA material teste experimentally, i.e. Young's modulus  $E = 2900$  MPa and Poisson's ratio  $\nu = 0.35$ .

From the FE solution of the problem, the displacement field of the nodes at the distance of 1 mm from the crack tip was taken to apply the ODM. The ODM procedure was programmed in Wolfram Mathematica software (Wolfram Mathematica, 2018). The coefficients of higher-order terms have been obtained as the result.

The tangential stress could be then reconstructed at various distances considering various numbers (between 1 and 10) of initial higher-order terms of the WE, see the range where the tangential stress was investigated in Fig. 12.1b. In order to find the angle of the further crack propagation, the angle where the tangential stress reaches its maximum had to be found. The influence of the selected critical distance as well as number of initial WE terms is discussed in the following section.

## 12.5. Results

In Fig. 12.2 the tangential stress distribution approximated by means of Eq. 12.1. and taking into account 1, 2, 3, 6 and 10 initial terms of the WE. The stress is reconstructed in front of the crack tip according to Fig. 12.1b. Comparison between the specimens with various widths ( $W = 30$  (CT),  $W = 60$ , 90 and 150 mm (DCB)) as well as between the results calculated at various distances from the crack tip ( $r_c = 0.1$ , 1, and 5 mm) can be seen.

The results presented in Fig. 12.2 can be commented with regard to the choice of the proper critical distance in the following way. If the critical distance is chosen very small, the singularity of the first singular term is dominant, and these results differ significantly from the ones obtained by means of the WE assuming more terms. This is more evident for specimens with larger widths.

When the point of view of the angle of the further crack propagation is considered (using the generalized MTS criterion), it can be seen in Fig. 12.2 that when the criterion is applied at a very small distance ( $r_c = 0.1$  mm), the prediction of the propagation angle would be the same independently on the specimen width – i.e. the crack should propagate along its original plane. The same results were observed when the classical one-parameter form of the MTS criterion is assumed ( $NM = 1$  in Fig. 12.2). But the experiments performed on PMMA CT and especially DCB specimens say something else (Ayatollahi *et*

*al.*, 2016): when the specimen width is 60 mm and larger, the crack kinks from its original direction in spite the fact that it is loaded under pure mode I. Thus, the generalized (multi-parameter) MTS criterion instead of the classical one-parameter should be used and furthermore, the critical distance where the criterion is applied must be large enough.

Although there have been published several recommendations how to estimate this parameter  $r_c$  (Seweryn and Lukaszewicz, 2002; Sih and Ho, 1991; Sumsle, 2008), a really universal and reliable instruction does not exist yet. Therefore, several values of the critical distance are applied, tested and based on the comparison between the numerical and experimental results discussed.

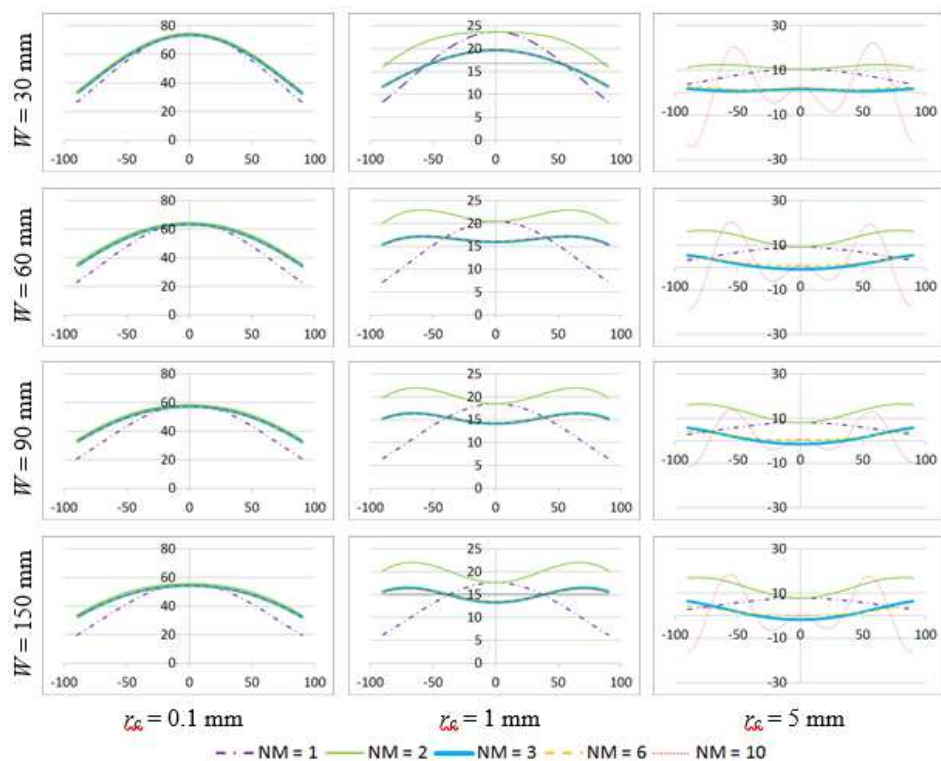


**Fig. 12.2.** Dependence of the tangential stress distribution (vertical axes in [MPa]) ahead of the crack tip on the angle  $\theta$  between  $-90^\circ$  and  $90^\circ$  (horizontal axes) for various critical distances  $r_c = 0.1, 1$  and  $5 \text{ mm}$  approximated via WE assuming 1, 2, 3, 6 and 10 initial higher-order terms. Each row corresponds to the cracked specimen with different width:  $W = 30 \text{ (CT)}$ ,  $W = 60, 90$  and  $150 \text{ (DCB)}$

In Fig. 12.3 the dependence of the initial crack propagation angle determined by means of the generalized (multi-parameter) MTS criterion considering various numbers of the initial terms on the critical distance where the criterion is applied can be seen for cracked specimens with different widths  $W = 30, 60, 90$  and  $150$  mm.

From the results presented in Fig. 12.3 the following conclusions can be highlighted:

- When the crack propagation in the CT specimen is investigated, it is found out that the crack will propagate in its original direction (no kinking occurs) independently on the distance where the generalized MTS criterion is applied as well as on the number of the initial WE terms considered; this fully agrees with the experimental observations (Ayatollahi *et al.*, 2016).

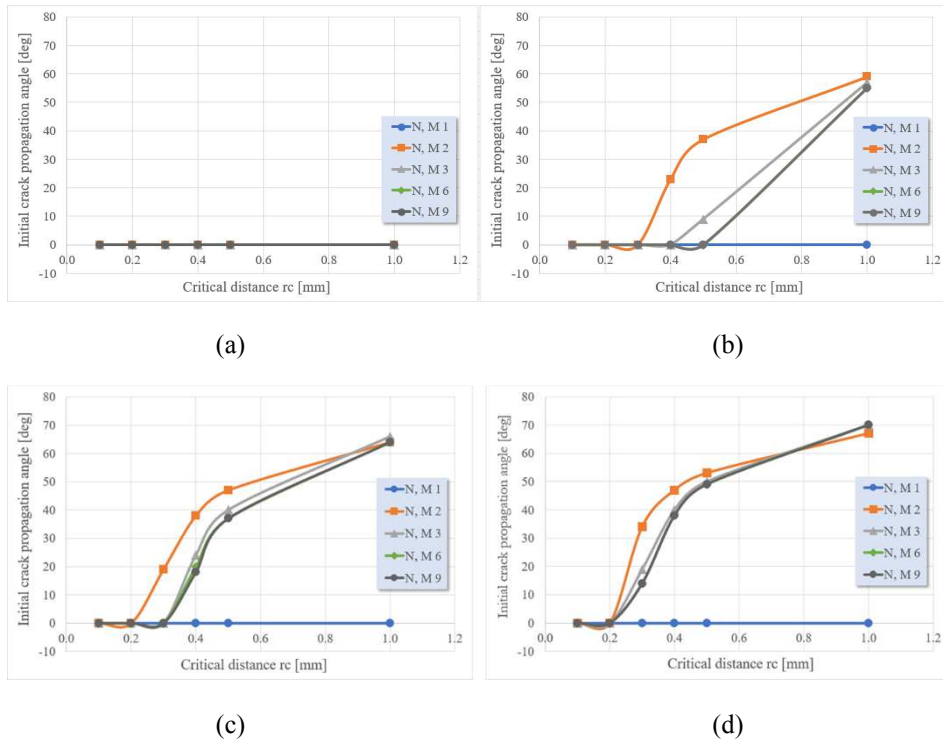


**Fig. 12.3.** How the initial crack propagation angle depends on the critical distance where the generalized (multi-parameter) MTS criterion (considering 1, 2, 3, 6 and 9 initial terms of the WE) is applied: (a) CT specimen,  $W = 30$  mm, (b) DCB specimen,  $W = 60$  mm, (c) DCB specimen,  $W = 90$  mm, (d) DCB specimen,  $W = 150$  mm

- When the initial crack propagation angle in DCB specimens is investigated, various results of the kink angle can be obtained in dependence on the choice of the critical distance and on the number of the WE terms assumed, see the following discussion.
- When the crack propagation in the DCB specimens with larger width (higher geometric constraint) is investigated, it is found out that the classical (one-parameter) MTS criterion is not able to describe the crack deflection; it predicts the straightforward crack propagation for all the DCB configurations considered despite the experimental results.
- Therefore, the multi-parameter (generalized) form of the MTS criterion is to be recommended for this kind of specimens to get better results.
- The initial kink angle calculated by means of the multi-parameter MTS criterion considering 3 and more WE terms does not change significantly when more WE terms are considered.
- When the crack propagation angle is determined from the stress distribution very close to the crack tip, it seems that the crack will propagate straight ahead for all specimen widths, which is inconsistent with the experiments.
- Therefore, rather larger critical distance can be recommended.
- When the experimental values of the initial crack propagation angle are compared to the dependences obtained numerically, the generalized MTS criterion considering initial 3 terms of the WE brings good results for the critical distance of 0.6 mm for 150 mm wide DCB specimens and critical distance of 0.35 mm for 90 mm wide DCB specimens.

## **12.6. Conclusions**

Within this work, the importance of the multi-parameter (generalized) fracture mechanics is emphasized. It is shown that the classical one-parameter fracture mechanics is not able to describe the crack kinking when the crack propagation in the specimens with higher geometric constraint is investigated. It is also proved that the proper choice of the critical distance where the generalized fracture criterion is applied is crucial. All the conclusions are made based on the comparison between the numerical analysis and experimental campaign. It is recommended to consider at least three terms of the WE when the crack propagation in the DCB specimens with larger width shall be investigated. The critical distance between 0.35 and 0.6 mm seems to be suitable for the specimens with the defined geometry and made of the material under the study.

## Acknowledgment

The financial support of the Czech Science Foundation, project No. 18-12289Y, is gratefully acknowledged. This paper has been worked out under the "National Sustainability Programme I" project "AdMaS UP – Advanced Materials, Structures and Technologies" (No. LO1408) supported by the Ministry of Education, Youth and Sports of the Czech Republic and Brno University of Technology.

## References

- Aliha, M.R.M. *et al.* (2010) 'Geometry and size effects on fracture trajectory in a limestone rock under mixed mode loading', *Engineering Fracture Mechanics*, 77, p. 2200.
- Aliha, M.R.M., Ayatollahi, M.R. (2010) 'Geometry effects on fracture behavior of polymethylmethacrylate', *Materials Science and Engineering*, 527, p. 526.
- Anderson, T.L. (2004) *Fracture mechanics: Fundamentals and Applications*, CRC Press, Boca Raton.
- Ansys® Release 17.2. Academic research (2016) Crack analysis guide Mechanical APDL Documentation guide.
- Ayatollahi, M.R., Akbardoost, J. (2012) 'Size effects on fracture toughness of quasi-brittle materials – A new approach', *Engineering Fracture Mechanics*, 92, p. 89.
- Ayatollahi, M.R., Aliha, M.R.M. (2009) 'Mixed-mode fracture in soda-lime glass analyzed by using the generalized MTS criterion', *International Journal of Solids and Structures*, 46, p. 311.
- Ayatollahi, M.R. *et al.* (2010) 'Crack tip plastic zone under Mode I, Mode II and mixed mode (I + II) conditions', *Structural Engineering and Mechanics*, 36, p. 575.
- Ayatollahi, M.R. *et al.* (2015) 'A generalized strain energy density criterion for mixed mode fracture analysis in brittle and quasibrittle materials', *Theoretical and Applied Fracture Mechanics*, 79, p. 70.
- Ayatollahi, M.R. *et al.* (2016) 'Geometry effects on fracture trajectory of PMMA samples under pure mode-I loading', *Engineering Fracture Mechanics*, 163, p. 449.
- Ayatollahi, M.R., Nejati, M. (2011) 'An over-deterministic method for calculation of coefficients of crack tip asymptotic field from finite element analysis', *Fatigue and Fracture of Engineering Materials*, 34(3), p. 159.
- Bazant, Z.P., Planas, J. (1998) *Fracture and size effect in concrete and other quasibrittle materials*, CRC Press, Boca Raton.

- Betegon, C., Hancock, J.W. (1991) 'Two-parameter characterization of elastic-plastic crack-tip fields', *Journal of Applied Mechanics*, 58, p. 104.
- Chao *et al.* (2001) 'Brittle fracture: variation of fracture toughness with constraint and crack curving under mode I conditions', *Experimental Mechanics*, 41, p. 232.
- Cotterell, B. (1966) 'Notes on the paths and stability of cracks', *International Journal of Fracture Mechanics*, 2(3), p. 526.
- Davenport, J.C.W., Smith, D.J. (1993) 'A study of superimposed modes I, II and III on PMMA', *Fatigue and Fracture of Engineering Materials and Structures*, 16, p. 1125.
- Du, Z.Z., Hancock, J.W. (1991) 'The effect of non-singular stresses on crack tip constraint', *Journal of the Mechanics and Physics of Solids*, 39, p. 555.
- Duan, K. *et al.* (2007) 'Size effect on specific fracture energy of concrete', *Engineering Fracture Mechanics*, 74, p. 87.
- Karihaloo, B.L., Xiao, Q.Z. (2001) 'Accurate determination of the coefficients of elastic crack tip asymptotic field by a hybrid crack element with *p*-adaptivity', *Engineering Fracture Mechanics*, 68, p. 1609.
- Karihaloo, B.L. *et al.* (2006) 'Deterministic size effect in the strength of cracked concrete structures', *Cement and Concrete Research*, 36, p. 171.
- Khan, K., Al-Shayea, N.A. (2000) 'Effect of specimen geometry and testing method on mixed Mode I–II fracture toughness of a limestone rock from Saudi Arabia', *Rock Mechanics and Rock Engineering*, 33, p. 179.
- Knésl, Z. (1994/1995) 'Evaluation of the elastic T-stress using a hybrid finite element approach', *International Journal of Fracture*, 70(1), p. R9.
- Kumar, B. *et al.* (2011) 'Significance of K-dominance zone size and nonsingular stress field in brittle fracture', *Engineering Fracture Mechanics*, 78, p. 2042.
- Larsson, S.G., Carlsson, A.J. (1973) 'Influence of non-singular stress and specimen geometry on small-scale yielding at each tip in elastic-plastic materials', *Journal of the Mechanics and Physics of Solids*, 21, p. 263.
- Lazzarin, P. *et al.* (2009) 'Fatigue-relevant stress field parameters of welded lap joints: pointed slit tip compared with keyhole notch', *Fatigue and Fracture of Engineering Materials and Structures*, 32(9), p. 713.
- Liu, S., Chao, Y.J. (2003) 'Variation of fracture toughness with constraint', *International Journal of Fracture*, 124, p. 113.
- Malíková, L. (2015) 'Multi-parameter fracture criteria for the estimation of crack propagation direction applied to a mixed-mode geometry', *Engineering Fracture Mechanics*, 143, p. 32.
- Pook, L.P. (2015) 'The linear elastic analysis of cracked bodies and crack paths', *Theoretical and Applied Fracture Mechanics*, 79, p. 34.
- Rice, J.R. (1974) 'Limitations to the small scale yielding for crack-tip

- plasticity', *Journal of the Mechanics and Physics of Solids*, 22, p. 17.
- Růžička, V. *et al.* (2017) 'Over-deterministic method: The influence of rounding numbers on the accuracy of the values of Williams' expansion terms', *Frattura ed Integrità Strutturale*, 42, p. 128.
- Shah, S.P. *et al.* (1995) *Fracture mechanics of structural concrete: applications of fracture mechanics to concrete, rock, and other quasi-brittle materials*, John Wiley & Sons, Inc., New York.
- Smith, D.J. *et al.* (2001) 'The role of T-stress in brittle fracture for linear elastic materials under mixed-mode loading', *Fatigue and Fracture of Engineering Materials and Structures*, 24, p. 137.
- Seweryn, A., Lukaszewicz, A. (2002) 'Verification of brittle fracture criteria for elements with V-shaped notches', *Engineering Fracture Mechanics*, 69, p. 1487.
- Sih, G.C., Ho, J.W. (1991) 'Sharp notch fracture strength characterized by critical energy density', *Theoretical and Applied Fracture Mechanics*, 16, p. 179.
- Su, R.K.L., Fok, S.L. (2007) 'Determination of coefficients of the crack tip asymptotic field by fractal hybrid finite elements', *Engineering Fracture Mechanics*, 74, p. 1649.
- Sun, C.T., Qian, H. (2009) 'Brittle fracture beyond the stress intensity factor', *Journal of Mechanics of Materials and Structures*, 4, p. 743.
- Susmel, L. (2008) 'The theory of critical distances: a review of its applications in fatigue', *Engineering Fracture Mechanics*, 75, p. 1706.
- (Šestáková) Malíková, L. (2013) 'Crack path investigation using the generalized maximum tangential stress criterion: antisymmetrical four-point bending specimen', *Applied Mechanics and Materials*, 436, p. 108.
- Šestáková, L. (2014) 'Using the multi-parameter fracture mechanics for more accurate description of stress/displacement crack tip fields', *Key Engineering Materials*, 586, p. 237.
- Šestáková (Malíková), L. (2013) 'How to enhance efficiency and accuracy of the over-deterministic method used for determination of the coefficients of the higher-order terms in Williams expansion', *Applied Mechanics and Materials*, 245, p. 120.
- Šestáková, L., Veselý, V. (2013) 'Convergence study on application of the over-deterministic method for determination of near-tip fields in a cracked plate loaded in mixed-mode', *Applied Mechanics and Materials*, 249–250, p. 76.
- Tong, P. *et al.* (1997) 'A hybrid element approach to crack problems in plane elasticity', *International Journal of Numerical Methods in Engineering*, 7, p. 297.
- Veselý, V. *et al.* (2014) 'Multi-parameter crack tip stress state description for estimation of nonlinear zone width in silicate composite specimens in

- component splitting/bending test geometry', *Fatigue & Fracture of Engineering Materials & Structures*, 38 (2), p. 200.
- Veselý, V. *et al.* (2017) 'Quasi-brittle behaviour of composites as a key to generalized understanding of material structure', *Procedia Engineering*, 190, p. 126.
- Williams, M.L. (1957) 'On the stress distribution at the base of stationary crack', *Journal of Applied Mechanics ASME*, 24, p. 109.
- Wolfram Mathematica (2018), <https://www.wolfram.com/mathematica/>
- Xiao, Q.Z. *et al.* (2004) 'Direct determination of SIF and higher order terms of mixed mode cracks by a hybrid crack element', *International Journal of Fracture*, 125, p. 207.





## 13. Comparison of pulse-echo-methods for testing of heat degradation concrete

**Libor Topolář<sup>1</sup>, Richard Dvořák<sup>2</sup>, Michaela Hoduláková<sup>3</sup>, Luboš Pazdera<sup>4</sup>**

<sup>1</sup> *Brno University of Technology, Faculty of Civil Engineering, Brno, Czech Republic, [orcid.org/0000-0001-9437-473X](https://orcid.org/0000-0001-9437-473X)*

<sup>2</sup> *Brno University of Technology, Faculty of Civil Engineering, Brno, Czech Republic, [orcid.org/0000-](https://orcid.org/0000-0000-0000-0000)*

<sup>3</sup> *Brno University of Technology, Faculty of Civil Engineering, Brno, Czech Republic*

<sup>4</sup> *Brno University of Technology, Faculty of Civil Engineering, Brno, Czech Republic, [orcid.org/0000-0002-9416-5644](https://orcid.org/0000-0002-9416-5644)*

**Abstract:** The paper is focused on comparison of pulse-echo-methods for testing of heat degradation concrete. It was proven that the development of physico-mechanical and physico-chemical changes causes an uneven and stochastic increase of concrete heterogeneity and simultaneously a significant reduction of mechanical properties.

**Keywords:** pulse-echo, concrete, degradation

### 13.1. Introduction

The testing technology of composite materials used in the building industry has its specific characteristics when compared to other technical disciplines (engineering, electrical engineering, etc.). Most non-destructive acoustic measurement methods are well developed for homogeneous, especially basic metallic materials (steel, cast iron, etc.), but are not similarly well-developed for non-homogeneous materials. These non-homogeneous materials of course include building composites, either cement-based or alkali-activated (pastes, mortars, and concrete). That is the reason why it is very important to develop non-destructive defectoscopy testing methods. Non-destructive defectoscopy methods (defect imaging) are diagnostic methods that form an integral part of control processes of products, structures, and designs both in research, development, pre-production and manufacturing stages, as well as in real-life applications. Without defectoscopy, it would not be possible to provide error-free operation, reliability, and safety in many areas such as aviation, nuclear power, chemicals, as well as safety of bridges, dams, etc. In general, non-destructive defectoscopy deals with the testing of the structure of metallic and non-metallic materials and internal or surface defects of objects without

compromising their integrity. Material and product defects include incorrect chemical composition, structural defects, deviations from the specified mechanical and physical properties, non-homogeneity (cracks, tears), cavities (bubbles, pores, precipitates), inclusions (slag, non-metallic and metallic inclusions), shape defects, corrosion, wear, etc. (Kreidl, 2006). Non-destructive defectoscopy testing methods are based on different physical principles and utilize specific material properties. Individual procedures vary in demands on technical equipment and personnel qualifications and it is impossible to establish only one generally valid procedure for the detection of defect. The use of a particular method always depends on the given situation. There is no ideal universal defectoscopy method for the control of specific components or materials. The choice of the optimal method or a combination of methods depends on the particular application, material, etc. A combination of several different methods and procedures are therefore commonly used to determine the most accurate information for the given case. This chapter will deal with pulse-echo methods and the method of the maximum length sequence (MLS).

### **13.1.1 Principle of Impact and Pulse-echo methods**

The Impact-echo (IE) method, often referred to as "indirect" acoustic emission, uses an external source of the acoustic signal. The term hammer method is also used and usually employs a mechanical impulse as the signal transmitter– a hammer stroke, or the fall of a steel ball (Fig. 13.1 and Fig. 13.2). This method deals with a response, where we monitor the parameters of the signal that has been transformed by the passage through the material and recorded on the surface of the examined sample (Malhotra and Carino, 2004; Kopec, 2008). The Impact-echo method is based on the analysis of the response of a mechanical impulse that creates harmonic waves in the studied object at its natural frequency and at higher harmonic frequencies. These frequencies primarily depend on the dimensions and material characteristics of the tested object. A transient stress pulse applied to the surface creates elastic waves in the material, which further propagate through the material by spherical wavefronts as longitudinal and transverse waves and is superimposed by reflected waves from the outer surfaces as well as from internal defects (inconsistencies, non-homogeneities, cavities, micro and macro cracks, etc.).

These waves are transformed on the surface of the sample into surface waves, also called Rayleigh's, respectively Lamb waves, which are then recorded and evaluated. The recorded response indicates the existence of structural defects, but does not specify the type of the defect or its shape and size (Kořenská, 2006).

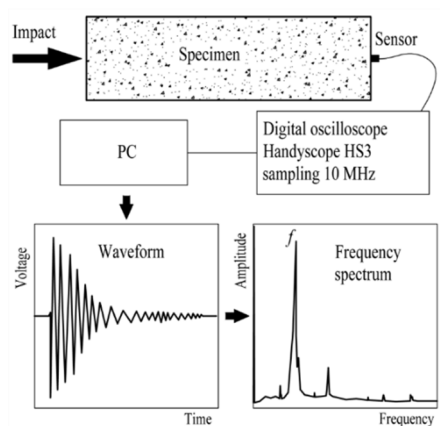


**Fig. 13.1.** Schematic representation of the Impact and Pulse-echo methods

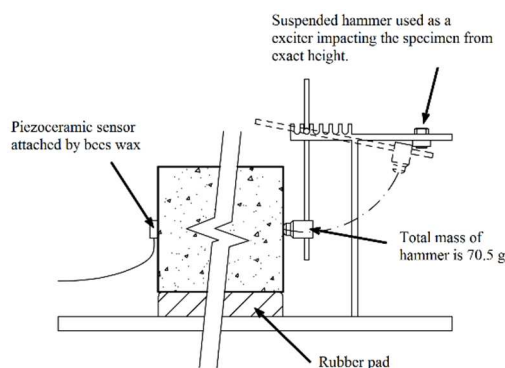


**Fig. 13.2.** The method of signal transmission with a hanging hammer for the Impact-echo method

For impact and pulse-echo methods, the source of the stress impulse applied to the surface of the tested object may be a mechanical impulse or a generated signal. If a mechanical impulse is used for the testing, we talk about the Impact-echo method and if the generate the mechanical wave by a generator, we talk about the Pulse-echo method (Carino, 2001). The generated signal may be in the form of a pulse or a continuous noise or harmonic signal (Malhotra and Carino, 2004; Domain, 2007). The evaluation of the response signals to the transmitted pulse in the tested object can be performed in two basic systems of analysis. In

the first case, the resulting shift in relation to time is evaluated, and in the second case, the signals are converted to the frequency domain and a frequency analysis is performed. The frequency analysis is used more often, where the examined signal is converted from the time domain to the frequency domain with the Fourier Transform, most frequently with the fast Fourier Transform (FFT - Fast Fourier Transform). The Fourier Transform decomposes the signal into many sine waves of different frequencies (Domain, 2007) and thus generates a spectrum of amplitudes depending on the frequency. The individual peaks corresponding to the dominant frequencies indicate the depth of the boundary surfaces of the object or also the depth of the interface on the surface of the cracks and cavities or the depth of the interface between two materials of different acoustic impedances.

### **13.1.2 The principle of the MLS method**

Scientists involved in vibroacoustics have been trying to reduce the noise caused by the transmitted signal in pulse-compression methods. The MLS method was developed for this particular purpose (Fig. 13.3). Instead of transmitting one short impulse in the test sample (whether by a hammer stroke, or a piezoelectric transmitter), it is transmitted by a pseudorandom binary signal (working with only two levels of voltage), which is generated into a continuous chain of the transmitted signal. During recording of the impulse response (IR – “impulse response”), the start and the end of the transmitted signal are not relevant. Due to the nature of the MLS signal, the evaluation algorithm can select any point in the signal, select a sequence of points of the length of the partial transmitted signal and obtain precisely one impulse response. The advantage of this approach is that we can create up to  $2^{16}$  transmitted impulses hidden in one maximum length sequence in a relatively short time interval of a few seconds. By subsequent averaging of each FFT calculated from the partial IR, we obtain a much more accurate impulse response than in the case of the common IE method. This allows a substantial reduction of the quantization noise on the side of the generator, a reduction of the hardware costs, and a reduction of the influence of non-linearities (Lam and Hui, 1982).

MLS can be used in a wider frequency range than in case of the IE method, which works primarily in the low frequency range to 30 kHz. The generation of the transmitted signal can be done by a piezoelectric transmitter or contact speakers with different threshold voltage of the transmitted MLS signal. In this area, we can also speak about a linear and non-linear response of the test specimen (Potchinkov, 2005).

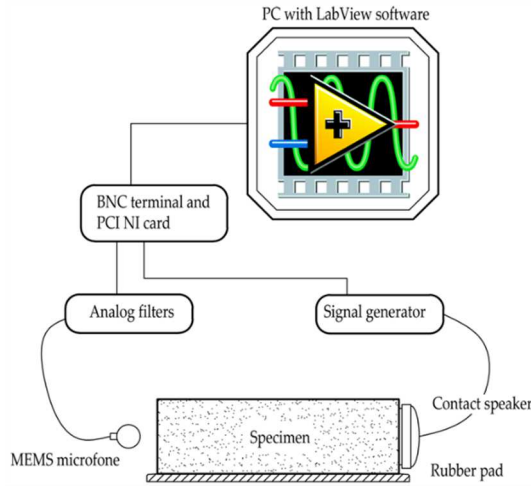


**Fig. 13.3.** Schematic representation of the use of the MLS method

Thanks to the possibility of transmitting the MLS signal with different threshold voltage, it is possible to record the shift of its natural resonance frequency  $f$  at maximum oscillation and the frequency  $f_0$  at minimum oscillation. The proposed method allows both the interpretation of the measured transmitted signal in the frequency domain and the assessment of the parameter  $\alpha$  characterizing the non-linear nature of the tested specimen, which is given by the equation (Carbol, 2016):

$$\alpha = \frac{\Delta f}{f_0} = \frac{f - f_0}{f_0} \quad (13.1)$$

## 13.2. Materials and experimental setup

A total of 30 test specimens with dimensions of  $0.1 \times 0.1 \times 0.4$  m were produced from two mixtures B and C. Each mixture was divided into five temperature sets, one reference set was kept at 20 °C and the remaining sets were divided into individual firing temperatures 400, 600, 800 and 1000 °C. The composition of the mixtures used during the experiments is given in Tab. 13.1. All the samples were kept in a water bath for 28 days. Each test specimen was pre-dried in a laboratory oven at 110 °C for 72 hours. This procedure removed free water from the specimens and consequently spalling of the specimens (Zhao *et al.*, 2014) at temperatures above 400 °C. During firing, the temperature in the oven was set to at an increase of 5 °C/min and the target temperature was then maintained for one hour. The specimens then cooled freely with access to air in the oven to the laboratory temperature.

**Table 13.1.** Mixture design

Compounds	Amount of each compound for 1 m <sup>3</sup> in kg	
	Set B	Set C
Cement CEM I 42.5 R	345	
Mix water	173	176
Superplasticizer Sica Viscocrete 2030	2.5	3.1
Fine aggregate Žabčice 0/4 mm	896	813
Coarse aggregate Olbramovice 4/8 mm	–	1010
Coarse aggregate Olbramovice 8/16 mm	521	–
Coarse aggregate Olbramovice 11/22 mm	391	–

When the signal is transmitted by a mechanical stroke, the hammer is suspended in a horizontal position. To transmit the impulse, it is released and therefore always falls from the same height (Fig. 13.2). In such a situation, it is possible to compare the amplitudes from individual measurements. Tests using the Impact-echo method consist of the first phase of the transmission and recording of the signal using a sensor (DAKEL IDK-09) and oscilloscope (HandyScope HS3), its conversion to a frequency spectrum using FFT and subsequent analysis of the dominant frequencies.

For the pulse-echo method, the pulse generator (Agilent 33220a) was set to the following output values: period 5s; amplitude 10 V<sub>pp</sub>; pulse width 500 μs. These pulse signals were captured after passing through the sample by the piezoelectric sensor (DAKEL IDK 09) and then amplified with a preamplifier (AS3K 433) with a gain of 35 dB and subsequently recorded by the DAKEL XEDO device where they were again amplified if necessary by internal circuits.

The MLS measuring device is automated and consists of the transmission of the pseudo-sequence signal, non-contact recording of the vibration of the test specimen subjected to transmission using a highly sensitive MEMS microphone and vibration decrease and subsequent automatic analysis of the recording. A single test cycle contains three parameters which characterize the linear and nonlinear behaviour of the sample - the resonance frequency  $f$ , the non-guaranteed sound velocity in the material  $v_u$  and the parameter  $\alpha$  characterizing the non-linear character. The use of the pulse compression of the signal is quite unusual in the construction industry. Only recently has the frequency of this issue increased in professional journals. A great potential lies in the mentioned combination of three test methods into one, in high test rate and repeatability of measurements, but also in the theoretical possibility of testing massive elements (Carbol, 2016).

### 13.3. Achieved results in time and frequency domain for each method

#### 13.3.1. Results from the Impact-echo method

Examples of the recorded signals are shown in Fig. 13.4. Several basic characteristic signs of the tested material are distinguishable from the graphs. In both cases applies that the specimens degraded at the temperature of 1000 °C have a lower frequency than non-degraded specimens. In addition, the reference set of the B mixture exhibits a substantially discontinuous decrease of individual oscillations in comparison to the almost continuous attenuation in case of the C mixture.

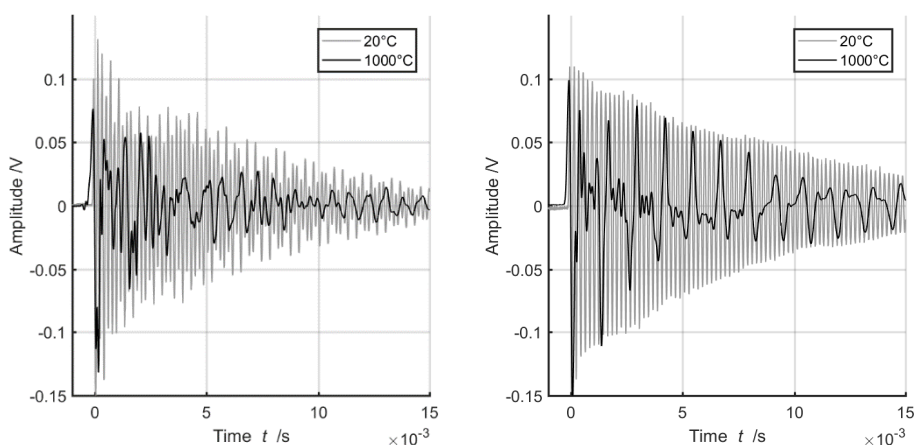


**Fig. 13.4.** An example of a signal from the IE measurement of the test specimens (left – mixture B, right – mixture C)

When comparing the amplitudes, we can observe a more pronounced difference in the course of the amplitude of the degraded sets of both the mixtures. In case of firing to 1000 °C, the signal of the mixture B exhibits some inconsistencies; the signal of the mixture C has a harmonic character.

These differences are noticeable when comparing the FFT of the individual temperature sets from the B mixture shown in Fig 13.5 and the C mixture shown in Fig. 13.6.



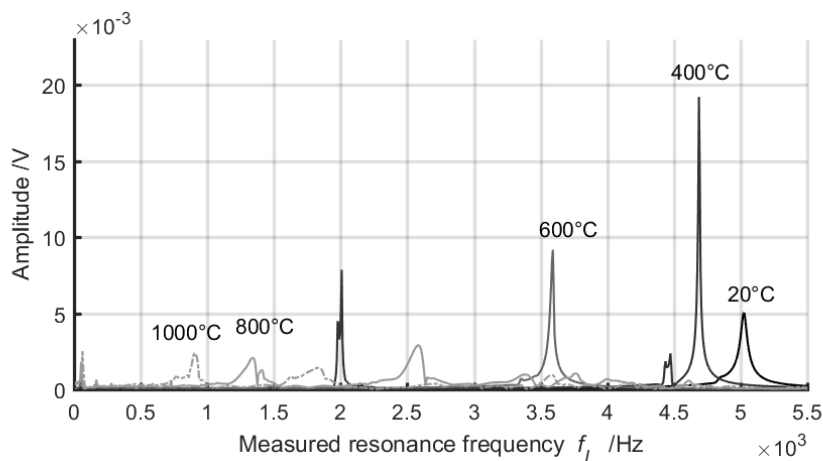


**Fig. 13.5.** Resonance frequency of the mixture B test specimens

These are selected representative frequency spectra from each temperature set and do not include all the conducted measurements. Besides the frequency shift of the resonance frequency between the individual temperatures, which is evident on both graphs, both mixtures have different amplitude of the measured frequencies. The amplitude of the mixture C is up to twice that of the mixture B. From 800 °C, the peaks of the resonance frequencies of mixture B exhibit a slight flattening due to a higher degree of noise as seen in Fig. 13.4 (left).

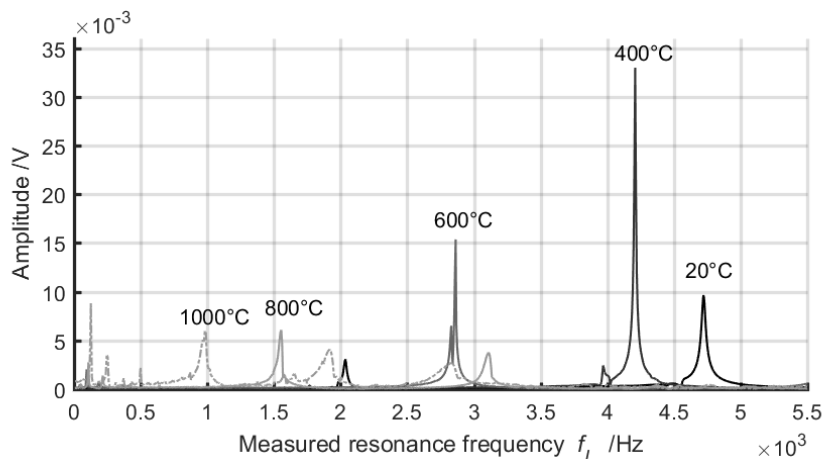


**Fig. 13.6.** Resonance frequency of the mixture C test specimens

Since both mixtures differ only in the amount of the coarse aggregate (Tab 13.1.), we can attribute these differences to the used aggregate and the overall behaviour of the used materials at high temperatures. While the basically fine-grained mixture C has a high response in all temperature sets, the mixture B behaves like a less compact material and dampens the mechanical impulse to a higher degree.

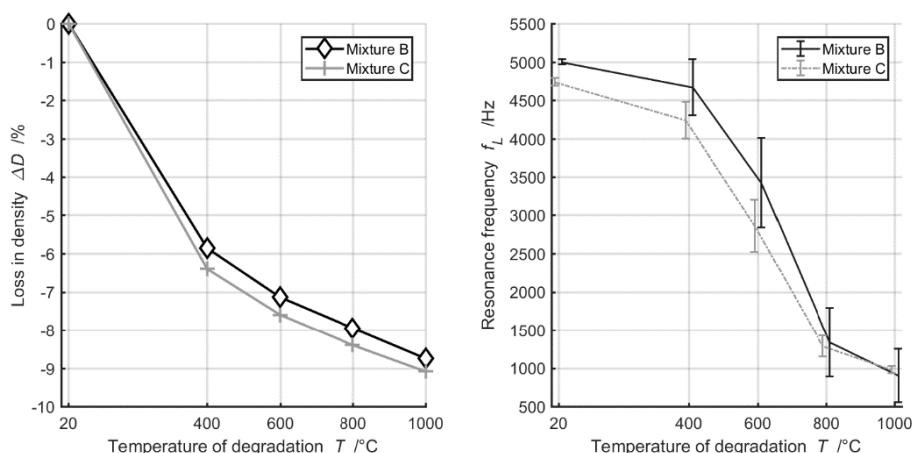


**Fig. 13.7.** Relative density loss of the tested sets (left graph), average resonance frequency of longitudinal waves of mixtures B and C (right graph)

The change in the resonance frequency of the test specimens in the longitudinal direction of testing indicates the most significant change in the residual physical-mechanical properties of the tested mixtures. Both mixtures reach their reference resonance frequencies from 4.7 kHz to 4.9 kHz with little variance of the values, as shown in Fig. 13.7 (right). The change in frequencies for specimens fired to 400 °C is not so significant when compared to other temperatures, but demonstrates the effect of the present physically and chemically bound water. The physically bound water escapes in the form of steam from the plain concrete at around 100 to 180 °C, and at the critical temperature of 374 °C, the chemically bound water can no longer be present (Hager, 2004). The mixture B reaches a reduction of 6% in this case and the mixture C of up to 10%. Since the measured amplitudes of the 400 °C temperature set for both mixtures exhibit the highest measured amplitude of the resonance frequency, it can be concluded that from the point of degradation, the test specimens were not significantly damaged by the elevated temperature, but the decrease in the frequency is caused by the escaping physically and chemically bound water. Fig. 13.7 (left) shows a decrease in the density of the

tested sets in relation to the degradation temperature. As can be seen, the most significant decrease of 6% is between 20 °C and 400 °C, the rest of the stress temperatures influenced the density by only 3%. In the frequency domain, however, this change corresponds to the main decrease in the resonance frequency and the most significant degradation of both mixtures.

Another interesting behaviour of the tested mixtures was demonstrated on the variance of the measured values. Fig. 13.7 (right) shows the probable error of the arithmetic mean of the measured values presented by error bars. The mixture B exhibits relatively high accuracy only for the reference set, the other measurements of the temperature sets are marked by a relatively large error, which is true up to 1000 °C. The variance of the measured values for mixture C, however, decreases with the increasing temperature stress up to the 1000 °C level, where the error in the mean is almost identical to the reference set.

From the point of view of the cementitious matrix, gradual decomposition of portlandite  $\text{Ca(OH)}_2$  and CSH gels occurs between the temperature of 400 °C and 600 °C and is accompanied by general shrinkage of the cementitious matrix and the first significant formation of cracks on the interface of the filler and binder. On the other hand, quartz components of the material, which mostly form the filler, and are mostly composed of  $\beta$ -quartz, feldspar and mica, experience expansion and cracking of the quartz aggregate. From around 780 °C to 920 °C, gradual decomposition of fine-grained and coarse-grained carbonates  $\text{CaCO}_3$ , and  $\text{CO}_2$  occurs and results in their thermal decomposition to  $\text{CaO}$  and  $\text{CO}_2$ , which further contributes to the density loss as well as to the main shift of the resonance frequencies to a lower frequency domain (Bodnárová, 2013).

### 13.3.2. Results from the Pulse-echo method

The graphs in Fig. 13.8. include the records of the signals in the time domain for both sample mixtures and two selected temperatures. The vertical axis represents the actual amplitude (the total gain has been taken into account) of the individual signals and the horizontal axis represents time. The upper graphs show

a comparison between the two sets for reference samples (20 °C). Both graphs demonstrate the typical pulse signal that has passed through the sample without significant inconsistencies or defects. The larger amount of the fine aggregate of the mixture C probably caused the lower recorded amplitude of the signal. The situation is dramatically different in case of the selected firing temperature (600 °C). The recorded signal is highly attenuated and also greatly distorted. A better picture of the signal attenuation in the time domain is given in Fig. 13.9.

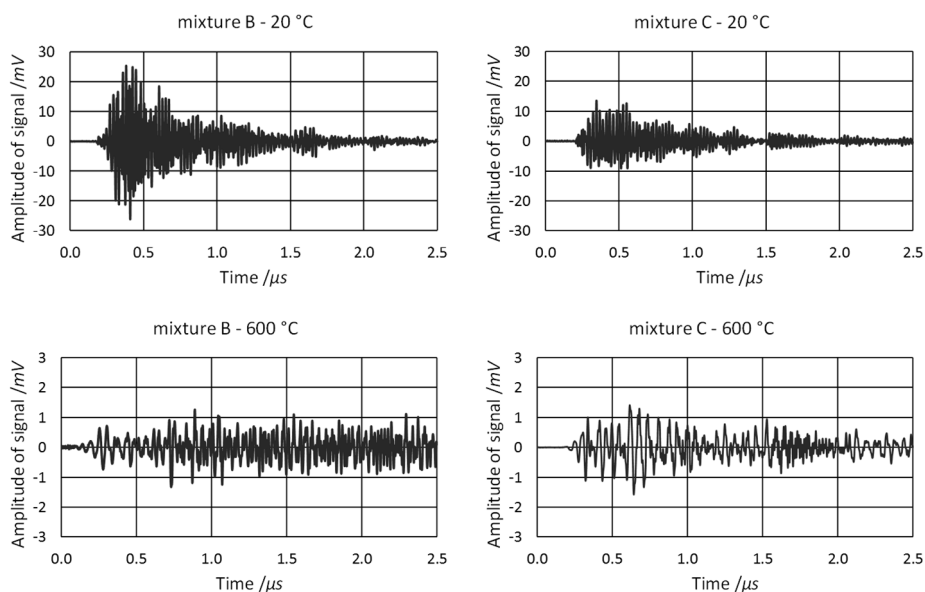


**Fig. 13.8.** Examples of the signal in the time domain from the Pulse-echo method measurements

The graph in Fig. 13.9 shows the decrease in the signal amplitude for individual firing temperatures. The higher amplitude of the degraded samples (200, 400, 600, 800 and 1000 °C) indicates a greater sensitivity of the internal structure, i.e. smaller damage due to elevated temperatures. In this respect, the mixture C samples seem to be better since the amplitude values are higher for all the temperatures, although in case of some temperatures only insignificantly.

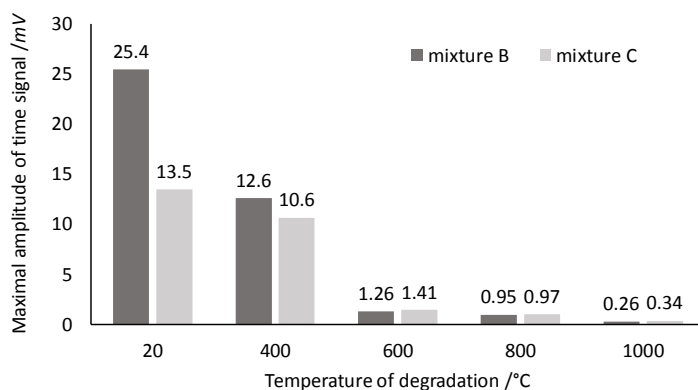


**Fig. 13.9.** Decrease in the signal amplitude in the time domain for mixture B and C

The graphs in Fig. 13.10 present the records of the signal for both mixtures and selected temperatures (reference and 600 °C) in the frequency domain. By comparing individual sets in different temperatures, it is evident that after firing to 600 °C, the dominant frequency shifts towards lower values, i.e. to the left in the frequency spectrum. It can therefore be assumed that lower frequencies indicate higher structural damage of the individual samples. It can also be seen that in addition to the dominant frequency, other significant frequencies occur in the degraded samples, which are not so apparent in the reference samples. The change of the dominant frequencies for both mixtures and all degradation temperatures is summarized in graph (Fig. 13.11).

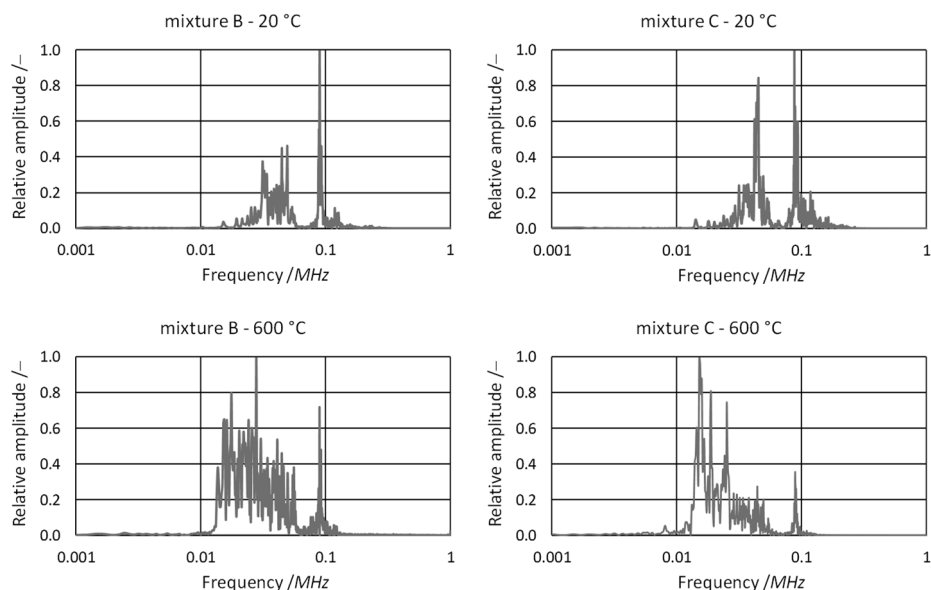


**Fig. 13.10.** Examples of recalculated signals in the frequency domain from the Pulse-echo method measurements

The summary graph shows the shift of the dominant frequency positions to lower values, which again indicates greater damage and structural changes. Compared to the maximum amplitudes from the time domain, there is a slight difference at temperatures of 600 and 800 °C, when the samples first exhibit crystalline changes and consequently the decomposition of Portlandite. This is probably connected to the larger amount of the fine aggregate (cement grains are closer to each other and the change in the Portlandite structure therefore occurs) in samples from the C mixture, which then leads to larger shifts of the dominant frequency positions than in case of the mixture B samples.

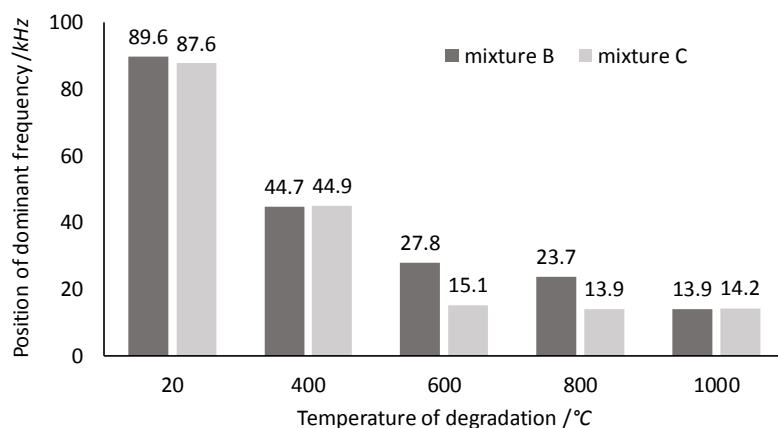


**Fig. 13.11.** A change of the position of the dominant frequencies for mixtures B and C

### 13.3.3. Results from the MLS method

The resulting frequency spectra obtained with the MLS method exhibit significantly greater response on particular resonance and harmonics frequencies (Fig 13.12 to 13.17). All the measured spectra are created using three threshold transmission voltages 8 V, 16 V and 24 V. The sequence length of the maximum length was set to 17 bits with the generating frequency of 100 kHz. The sample response was read with a sampling frequency of 1 MHz. A Sono gel was used as a coupling medium between the speaker and the test specimen, and the response of the specimen was recorded by a sensitive MEMS microphone through air. The LabView software from National Instruments was used to evaluate the measured response (Carbol, 2015). The tested specimens of mixture B and C can therefore be evaluated on a wider frequency spectrum of up to 30 kHz. When compared to IE, the individual peaks are considerably sharper. The created spectra for the reference samples allow clear detection of the first dominant resonance frequency and then its subsequent harmonic frequencies, both for the mixture B in Fig. 13.12. as well as for the mixture C in Fig. 13.15. The measured resonance frequencies match the frequencies obtained using the IE method with maximum differences in single percentages. The measured values of the individual temperature sets of both mixtures are presented in table Tab. 13.2.

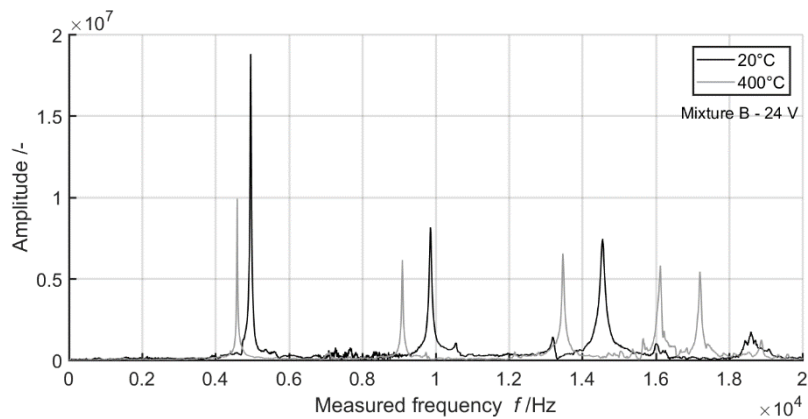


**Fig. 13.12.** The frequency spectrum of the mixture B obtained by MLS testing (20 °C and 400 °C)

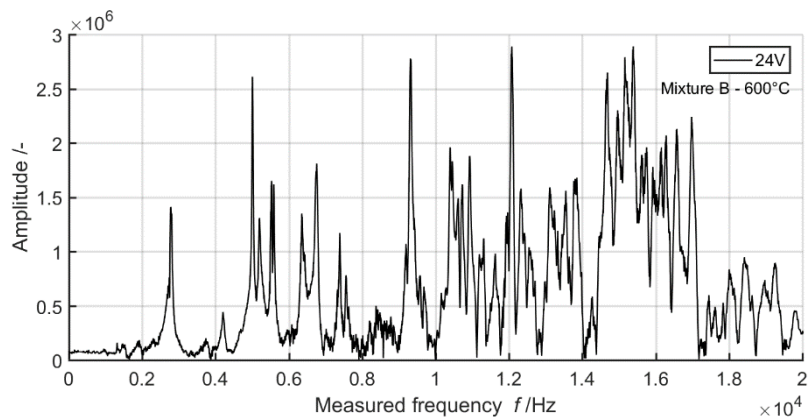


**Fig. 13.13.** The frequency spectrum of the mixture B obtained by MLS testing (600 °C)

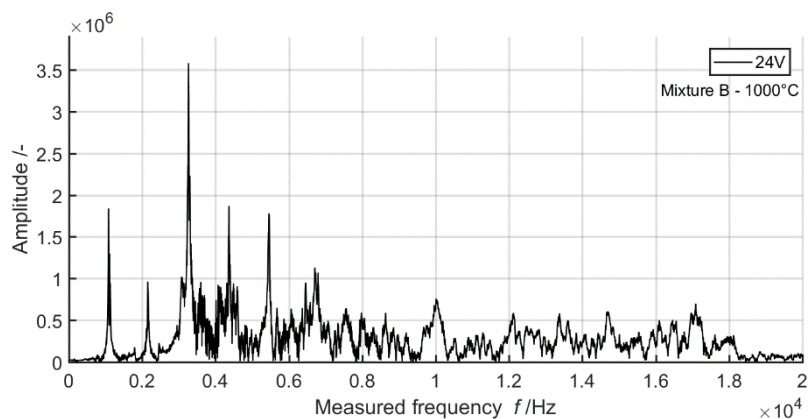


**Fig. 13.14.** The frequency spectrum of the mixture B obtained by MLS testing (1000 °C)

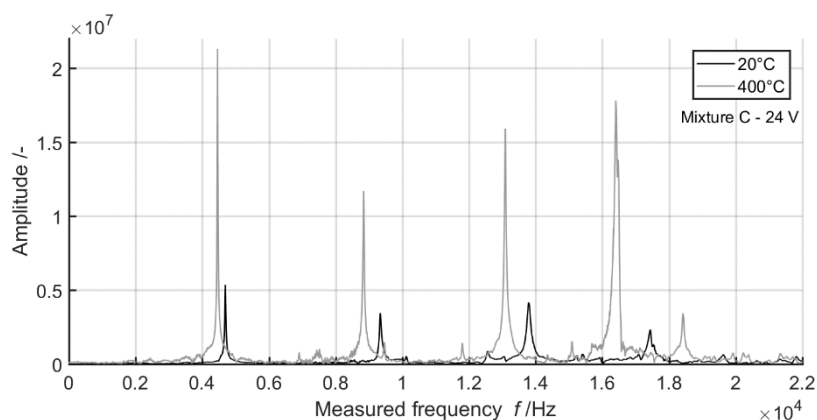


**Fig. 13.15.** The frequency spectrum of the mixture C obtained by MLS testing (20 °C and 400 °C)



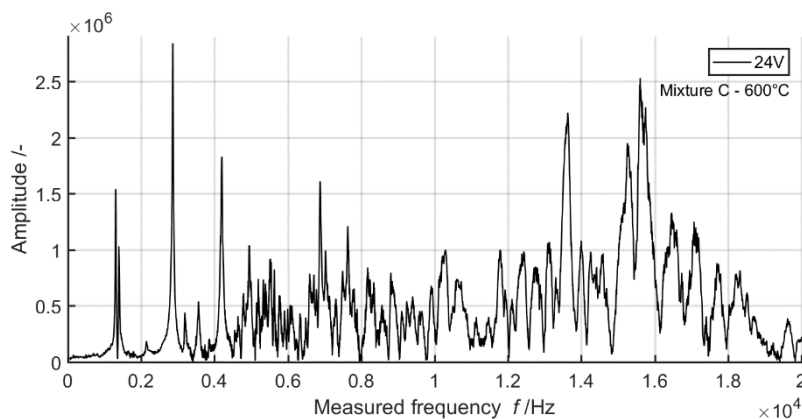


**Fig. 13.16.** The frequency spectrum of the mixture C obtained by MLS testing (600 °C)

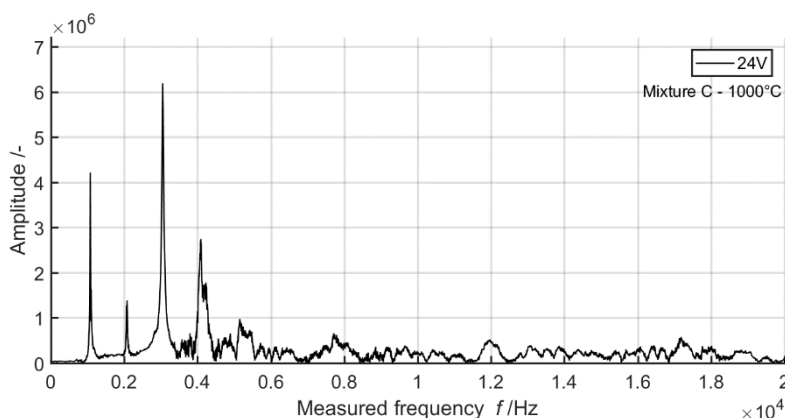


**Fig. 13.17.** The frequency spectrum of the mixture C obtained by MLS testing (1000 °C)

To be more understandable, the graphs Fig. 13.12 to 13.17 were generated only from a part of the frequency spectrum transmitted by the signal with the threshold voltage of 24 V. All three voltages are shown in graphs 13.18, which illustrate the linear and non-linear character of the temperature sets.

With increasing temperature degradation, the rate of the signal noise increases. The way in which the MLS method creates individual frequency spectra allows a higher response on the resonance frequencies of the tested material. MLS testing achieves much more pronounced results especially when compared to the IE method.

Graphs 13.12 and 13.15 compare the change of the frequency spectrum between the set of 20 °C and 400 °C. While firing to 400 °C in case of the mixture B caused a slight shift of the resonance frequency and a decrease in the response of the amplitude, there was an increase in the response amplitude in case of the mixture C. Only mixture C therefore corresponds to the development of the amplitude obtained during IE testing. As has been mentioned above, the IE method, in the initial firing phase of up to 400 °C, is most influenced by the physically and chemically bound water in the tested mixtures. The first dominant resonance frequencies are easily recognisable up to 1000 °C.

In case of the reference sets, we can also observe decreasing amplitude of the harmonic frequencies. The monitoring of the harmonic frequencies of non-linear ultrasonic testing of concrete can determine the presence of an internal defect. Looking at the resonance frequencies and the first three harmonic frequencies, we find a similar development in this case as well (Ongpeng, Oreta and Hirose, 2015).

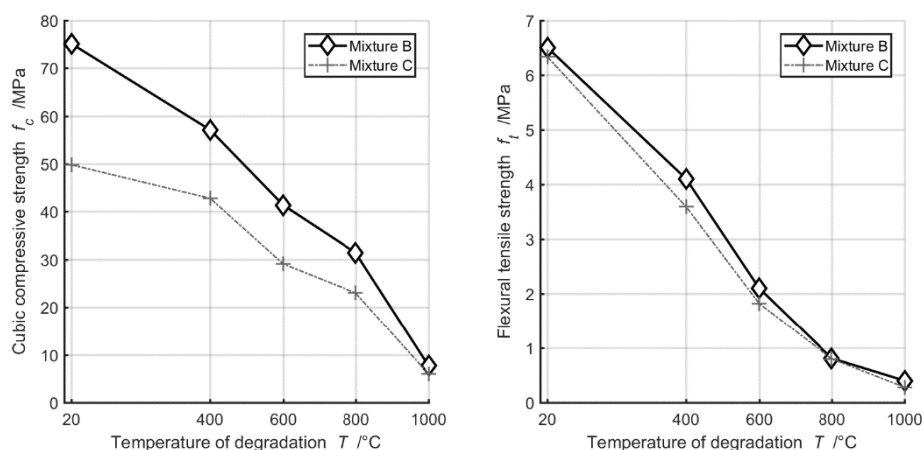


**Fig. 13.18.** Average compressive (left) and tensile strength (right)

In case of mixture B and C for the temperature sets of 20 °C, the first dominant frequency exhibits the highest amplitude and the other harmonic frequencies have decreasing amplitudes. For temperature sets of 600 °C and 1000 °C, the amplitudes change and the first dominant frequency have a lower amplitude than its following harmonic frequencies. Due to the knowledge of the residual physical-mechanical properties, which were described in graphs 13.19 to 13.20, we can state that the changes obtained with non-destructive methods in the

tested material correlate with the destructive tests and in particular with the compressive and tensile strengths.

The strengths of the tested mixtures correspond to the used material composition. The mixture B containing coarse aggregate 8/16 mm and 11/22 mm achieves the highest strengths in both compressive and tensile tests. With gradual degradation, however, its compressive and tensile strengths gradually approach the mixture C until they reach almost the same value at the degradation temperature of 1000 °C. This indicates that the temperature of 1000 °C is the material minimum for both tested mixtures.

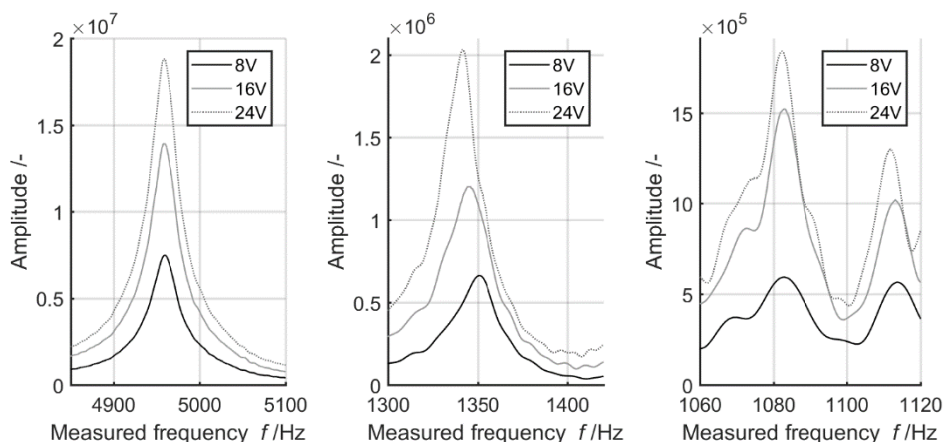


**Fig. 13.19.** Progress of the linear character (left and right) and the non-linear character (centre) of the resonance frequency of the mixture B temperature sets: 20 °C (left), 800 °C (centre), 1000 °C (right)

Looking at the graphs 13.19 to 13.20, we can observe the linear and non-linear character of the tested mixtures. For illustration purposes, we selected the peaks of resonance frequencies of the temperature sets which allow the non-linearity phenomenon to be recognized to the greatest and smallest extent.

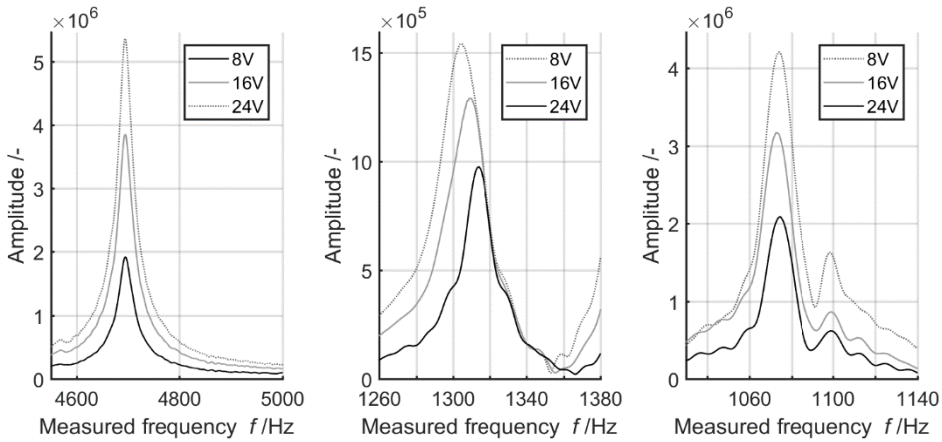


**Fig. 13.20.** Progress of the linear character (left and right) and the non-linear character (centre) of the resonance frequency of the mixture C temperature sets: 20 °C (left), 800 °C (centre), 1000 °C (right)

In practice, almost all materials behave non-linearly, i.e. the stress induced inside the system is non-linearly dependent on strain, and after unloading, it returns to the initial state with persisting plastic deformation. The linearly behaving system, on the other hand, returns to their initial state after unloading without losses of the internal energy – it therefore behaves elastically (Ongpeng, Oreta and Hirose, 2015; LExcellent, 2017). The non-linearity parameter  $\alpha$  was observed in the tested sets and is presented in Tab. 13.2. All the tested sets exhibited the non-linear character, to the lowest extent in case of the B mixture temperature set 20 °C and to the highest extent in case of the temperature set 800 °C of the same mixture. In case of mixture C, non-linearity was manifested to a lesser degree. In the frequency spectrum outside the dominant peaks, skipping of the frequencies between the 8, 16 and 24 V voltage thresholds was also observed. While the graphs 13.19 and 13.20 present gradually increasing amplitudes in the same order as in which the individual signals were chronologically transmitted, other places may show changes in the order. The extent of this phenomenon, however, diminishes in the resonance frequency domain. Overall, the test specimens produced from the mixture C appear to be less usable at high temperatures, but as a substantially more stable material with respect to the measured parameters. This result confirms both the measured values from the evaluation using the Impact-echo method as well as using the MLS method.

**Table 13.2.** Results obtained from MLS measurement of mixture B and C

Mixture	T /°C	$v_L$ /ms <sup>-1</sup>	f /Hz	$f_0$ /Hz	$\alpha \times 10^4$ /–
Mixture B	20	4645	5000	5001	1.50
	400	4089	4671	4671	1.71
	600	2597	3425	3425	30.76
	800	1412	1341	1339	137.00
	1000	975	905	904	99.90
Mixture C	20	4300	4739	4740	2.80
	400	3513	4240	4239	2.36
	600	2429	2863	2863	17.44
	800	1394	1289	1301	33.50
	1000	678	981	978	26.72

### 13.4. Comparison of achieved results and discussions

Tab. 13.3 presents a comparison of the average values of the dominant frequencies ( $f_L$  – impact-echo;  $f_0$  – MLS;  $f_{PE}$  – pulse-echo) of the individual methods including their relative errors. The results in Tab. 13.3 can be interpreted from several points of view:

- In regard to the degree of degradation, it is evident that the lowest relative error values are for specimens that were not degraded. The highest variance of the measured values, on the other hand, was obtained for specimens fired at 600 °C. This development of physico-mechanical and physico-chemical changes causes an uneven and stochastic increase of concrete heterogeneity and simultaneously a significant reduction of mechanical properties. Healthy concrete consists of clearly defined materials and its response to an excited signal is unambiguous. Degraded concrete consists of healthy components, partly degraded or completely degraded components, but also of new phases that are still forming in the material during the firing process.
- Within the ability of the individual methods to provide accurate results, we can describe differences in the accuracy of the measured quantities from the point of view of the application of the test procedure itself. The impact-echo method is dependent on a stroke of a spherical hammer, where the same initial conditions cannot be ensured for each test (the place and force of the impact of a hammer). The MLS method, which employs a sensitive microphone as a receiver and a contact

speaker as an exciter, receives the response of the specimen to an excited signal influenced by the ambient noise (background laboratory acoustic conditions). The lowest relative error values are therefore reached by the pulse-echo method. This result is due to the character of the test assembly with the piezoceramic exciter and the receiver being attached to the surface of the test specimen and the specimen being excited by longitudinal waves at higher frequencies (above 20 kHz). This method is therefore able to ensure the highest homogeneity of the excited signal and therefore the response of the specimen to the excited signal.

From the point of view of the destructive tests (Table 13.4), it can be observed that while mixture B reached the compressive strength of up to 75 MPa and can therefore be considered high performance concrete, the mixture C achieves slightly higher compressive strengths than ordinary concrete but does not exceed 50 MPa. However, the subsequent decreasing trend in the strengths linked to temperature degradation is very similar for both mixtures. The lowest values of mechanical properties were recorded for temperature sets degraded at 1000 °C. At this state, the decomposition of all the key hydraulic components, which ensure internal cohesion and strength of cement composites, has taken place and the material itself had a strong tendency to crumble and cracked.

**Table 13.3.** Results of non-destructive acoustic tests of mixture B and C

Mixture	T /°C	$f_L$ /Hz	$\delta(f_L)$ /%	$f_0$ /Hz	$\delta(f_0)$ /%	$f_{PE}$ /kHz	$\delta(f_0)$ /%
Mixture B	20	5000.25	0.17	5000.50	0.21	89.6	0.32
	400	4624.01	1.39	4670.60	1.70	44.7	0.22
	600	3192.21	5.89	3425.20	3.55	27.8	5.57
	800	1263.49	2.85	1339.20	1.32	23.7	2.52
	1000	744.72	3.19	904.08	3.68	13.9	2.63
Mixture C	20	4958.19	0.43	4740.33	0.37	87.6	0.11
	400	4172.22	2.42	4239.00	1.85	44.9	0.11
	600	2805.22	4.77	2862.80	4.11	15.1	0.37
	800	1365.12	2.68	1301.00	2.37	13.9	0.12
	1000	788.78	2.73	978.00	3.13	14.2	0.23

**Table 13.4.** Results of destructive tests of mixture B and C

Mixture	T /°C	$f_c$ /MPa	$\delta(f_c)$ /%	$f_{ct}$ /MPa	$\delta(f_{ct})$ /%
Mixture B	20	75.10	1.02	6.50	0.27
	400	57.10	1.64	4.10	5.61
	600	41.40	6.59	2.10	11.40
	800	31.40	5.17	0.81	17.43
	1000	7.70	3.90	0.40	12.71
Mixture C	20	49.83	1.15	6.33	0.31
	400	42.78	2.14	3.59	1.87
	600	29.06	6.98	1.82	3.75
	800	22.97	4.58	0.80	7.13
	1000	5.99	1.90	0.28	9.44

If we express the correlation of the employed non-destructive and destructive methods, we will be primarily interested in, mainly from the point of view of the testing practice, the correlation between the non-destructive parameters and flexural strength or compressive strength respectively.

Table 13.5 describes the correlation relationships between destructive and acoustic non-destructive methods. It can be stated that the measured resonance frequencies of the specimens tested by the MLS and the impact-echo methods are in very good correlation - their correlation coefficient reaches the value 0.998.

Both test methods work in lower frequency areas (1 - 20 kHz). At the same time, they are in very good correlation with the development of compressive strength and reach the values 0.960 for impact-echo and 0.948 for MLS.

In contrast, the pulse-echo method reaches lower correlation values with the MLS method, the impact-echo methods and compressive strength. However, it is in good correlation with flexural strength with the value of the correlation coefficient of 0.972. The excitation of the test specimens with higher frequencies (above 20 kHz) therefore correlates more with the flexural strength.

**Table 13.5.** Correlation coefficients of used testing methods

	$f_L$	$f_0$	$f_{PE}$	$f_c$	$f_{ct}$
$f_L$	1.000	0.998	0.852	0.960	0.946
$f_0$	<b>0.998</b>	1.000	0.834	0.948	0.932
$f_{PE}$	0.852	0.834	1.000	0.871	0.972
$f_c$	<b>0.960</b>	<b>0.948</b>	0.871	1.000	0.937
$f_{ct}$	0.946	0.932	<b>0.972</b>	0.937	1.000

### **13.5. Conclusions**

The used non-destructive acoustic methods allowed the tested material to be examined in a wide frequency domain using different methods. The Impact-echo method uses a single mechanical impulse transmitted by the impact of a mechanical hammer to obtain the frequency spectrum of the tested material. The Pulse-echo method using a generated frequency impulse. The MLS method uses a maximum length sequence that creates a frequency spectrum by averaging several dozens of responses of the test specimen to the transmitted signal over a short time interval. Using FFT, the signals were converted from the time domain to the frequency domain.

Thermally degraded concrete specimens of both mixtures exhibited a shift of the resonance frequencies into the lower frequency domain which correlated with the change in the specimens' strength. The difference between the correlation of the pulse-echo method with compressive strength and flexural strength is significant and the method cannot be considered equally suitable to the IE and MLS methods for estimations of compressive strength and flexural strength. Of all the test methods, however, it has the highest correlation with flexural strength, which can be considered a weakness of conventional plain concrete. Flexural strength of concrete of common composition reaches at most 10% of the compressive strength.

From the point of view of quantitative and qualitative evaluation of the degree of damage to the tested material, the employed methods seem to be an appropriate and progressive instrument. Testing using the MLS method can be seen as the next evolutionary step from the Impact and Pulse-echo methods, although it suffers from prototype imperfections in the selected assembly. In case of testing test specimens, it offers a very wide range of test parameters but may only be used for testing of the passage of the transmitted signal in the longitudinal direction. The Impact and Pulse-echo methods have been tested for a long time, are quick and verified even for testing on massive elements with only one accessible side of the construction. The entire MLS method has so far been only tested in the traditional assembly with the transmitter on one side of the test specimen and the receiver on the reverse side. For a wider use of this method, it will be necessary to verify its capabilities in other transmitter – receiver assemblies as well as on more massive elements. However, the MLS method can provide higher resolution and sharpness of the response of the tested material than the Impact and Pulse-echo methods. It is therefore desirable to further develop this method and optimize it for diagnostic practice.

It should also be noted that the concrete used for construction purposes is mainly in the form of reinforced concrete. The interpretation of vibro-acoustic



measurements of temperature-degraded reinforced concrete is, however, a much more demanding discipline, which is not the subject of this chapter.

## Acknowledgement

This work has been supported out under the project GAČR No. 16-02261S supported by Czech Science Foundation.

## References

- Bodnárová, L., Z, J., Hroudová, J. and Válek, J. (2013) Methods for Determination of the Quality of Concretes with Respect to their High Temperature Behaviour. doi: 10.1016/j.proeng.2013.09.040.
- Carbol, L., Martinek, J. and Kusák, I. (2015) Influence of Water Content on Fundamental Frequency of Mortar Sample. doi: <https://doi.org/10.4028/www.scientific.net/AMR.1124.273>.
- Carbol, L. (2016) 'Měření akustických vlastností stavebních materiálů pomocí pseudonáhodné sekvence', Czech Republic, PhD thesis. Brno University of Technology. [in czech]
- Carino, N. (2001) 'The impact-echo method: an overview', in 2001 Structures Congress & Exposition. doi: 10.1061/40558(2001)15.
- Domain, F. (2007) 'Engineering Analysis', Engineering Analysis. doi: 10.1201/9781420049619.
- Lam, F. K. and Hui, M. S. (1982) 'An ultrasonic pulse compression system for non-destructive testing using maximal-length sequences', Ultrasonics, 20(3), pp. 107–112. doi: 10.1016/0041-624X(82)90070-1.
- Lexcellent, C. (2017) Linear and non-linear mechanical behavior of solid materials, Linear and Non-linear Mechanical Behavior of Solid Materials. doi: 10.1007/978-3-319-55609-3.
- Malhotra, V. M. and Carino, N. J. (2004) Handbook on Nondestructive Testing of Concrete, Handbook on Nondestructive Testing of Concrete.
- Ongpeng, J. M. C., Oreta, A. W. C. and Hirose, S. (2015) 'Non-linear ultrasonic test for fiber-reinforced concrete using 3<sup>rd</sup> harmonic generation', in IABSE Conference, Nara 2015: Elegance in Structures - Report.
- Potchinkov, A. (2005) 'Digital signal processing methods of global nonparametric frequency domain audio testing', Signal Processing, 85(6), pp. 1225–1254. doi: 10.1016/j.sigpro.2004.12.007.
- Zhao, J. et al. (2014) 'A meso-level investigation into the explosive spalling mechanism of high-performance concrete under fire exposure', Cement and Concrete Research, 65, pp. 64–75. doi: 10.1016/j.cemconres.2014.07.010.

## 14. Fundamental formulae for the calculation of shear flexible rod structures and some applications

**Mariusz Ruchwa**

*Koszalin University of Technology, Faculty of Civil Engineering Environmental and Geodetic Sciences, Koszalin, Poland, [orcid.org/0000-0003-2260-8423](https://orcid.org/0000-0003-2260-8423)*

**Abstract:** Presented approach concerning analysis of rod structures with shear effects, interacting or not with elastic foundation constitutes consistent and precise solution of the problem. It is characterized by an universal approach in problem description, allowing for analysis of arbitrary particular cases.

**Keywords:** structural analysis, static, Timoshenko beam, elastic foundation

### 14.1. Introduction

At present, due to high requirements concerning the results of numerical analysis of structures, the necessity of taking into account effects of shear on calculated values of displacements and stresses is of growing importance – also for rod structures (Filipkowski and Ruchwa, 1991, Pałkowski, 2009).

For typical problems of structural analysis of rod structures subjected to shear effects the Timoshenko formulation is widely applied, possible to implement into Finite Element Method - FEM (Hughes, 2000, Reddy 2006). Common additional problems concern shear locking and elimination of locking (Belytschko, Liu and Moran, 2000) and also introduction of shear effects for various transversal sections of rods (Cowper, 1966, Filipkowski, 1989). The examples of such analyses of frame structures are available in literature (Filipkowski and Ruchwa, 1991), as well as examples for elements taking into account shear effects for frame-strut bars in mast core (Ruchwa and Matuszkiewicz, 2010).

Although the description of shear effects for basic rod elements is evident (but still used rarely), the entire theoretical description for the rod interacting with foundation is still an interesting problem. Many authors proposed solutions obtained using various computational approaches: Finite Differences Method (Sadecka, 2010), Method of Discrete Singular Convolution - DSC (Akgöz *et al.*, 2016) and Finite Element Method (Frydrýšek, Jančo and Gondek, 2013).

Very valuable are formulations assuming the interaction of the bar with two-parameter elastic foundation without shear effects (Teodoru and Muşat, 2008, Dinev, 2012) and with shear effects (Filipkowski, 1989, 1992, Sienkiewicz and Ruchwa, 1992, Shirima and Giger, 1992).

In this paper the relatively simple and consistent approach taking into account the analytic solution for bars with shear effects, with- or without interaction with two-parameter elastic foundation. This solution was obtained by Filipkowski (Filipkowski, 1989) and developed in following years (Filipkowski and Ruchwa, 1991, Filipkowski and Shirima, 1991, Sienkiewicz and Ruchwa, 1992, Filipkowski, 1992, Shirima and Giger, 1992).

## 14.2. Theoretical background

The considered structure is a beam of monosymmetric cross-section, with shear effects, located on two-parameter elastic foundation. Linear-elastic material model is assumed, as well as small displacement analysis (Fig. 14.1). Details concerning foundation will not be discussed, because necessary information can be found in many studies (Dembicki *et al.*, 1988, El-Garhy and Osman, 2002).

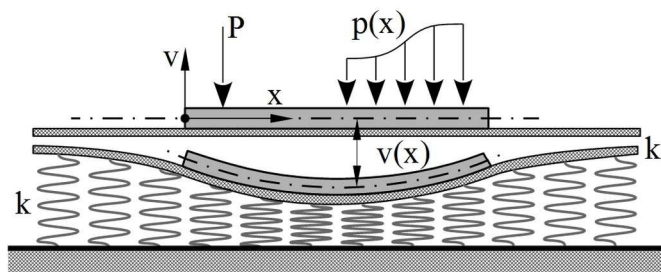


**Fig. 14.1.** Timoshenko beam on two-parameter elastic foundation

Entire potential energy of the beam is defined by a functional:

$$\begin{aligned} \Pi_c(v, \varphi) = & \frac{1}{2} \int_0^L \left( EJ(\varphi')^2 + \kappa GA(v' - \varphi)^2 - p(x)v \right) dx + \\ & + \frac{1}{2} \int_0^L \left( kv^2 + k_1\varphi^2 \right) dx - (Tv + M\varphi) \Big|_0^L \end{aligned} \quad (14.1)$$

where the following parameters are used: vertical displacement of the beam ( $v$ ), flexural angle of rotation ( $\varphi$ ), longitudinal modulus of elasticity ( $E$ ), transversal modulus ( $G$ ), section area ( $A$ ), moment of inertia ( $J$ ), shear coefficient ( $\kappa$ ) of cross-section of the beam, as well as parameters of elastic foundation ( $k$ ,  $k_1$ ), length of the beam ( $L$ ), distributed load ( $p(x)$ ) and loads on beam ends ( $T$ ,  $M$ ).

Due to principle of potential energy minimum the state of static equilibrium is defined by the equation:

$$\delta \Pi_c(v, \varphi) = 0 \quad (14.2)$$

which gives the following differential equation:

$$EJ f'''(x) - (k_1 + \eta k EJ) f''(x) + k(1 + \eta k_1) f(x) = p(x) \quad (14.3)$$

where:

$$\eta = 1/(\kappa GA) \quad (14.4)$$

The geometrical and statical quantities are defined by relations:

$$v(x) = (1 + \eta k_1) f(x) - \eta EJ f''(x) \quad (14.5)$$

$$\varphi(x) = f'(x) \quad (14.6)$$

$$\psi(x) = v' - \varphi = \eta k_1 f'(x) - \eta EJ f'''(x) \quad (14.7)$$

$$T(x) = -EJ f'''(x) + k_1 f'(x) \quad (14.8)$$

$$M(x) = EJ f''(x) \quad (14.9)$$

where:

$$f(x) = D_1 \Phi_1 + D_2 \Phi_2 + D_3 \Phi_3 + D_4 \Phi_4 \quad (14.10)$$

is the solution of homogeneous differential equation, where the constants are defined by relations 14.5 ÷ 14.9, and the final result may be written in a following form:

$$\begin{Bmatrix} v(x) \\ \varphi(x) \\ T(x) \\ M(x) \end{Bmatrix} = \begin{bmatrix} B_{vv} & B_{v\varphi} & B_{vT} & B_{vM} \\ B_{\varphi v} & B_{\varphi\varphi} & B_{\varphi T} & B_{\varphi M} \\ B_{Tv} & B_{T\varphi} & B_{TT} & B_{TM} \\ B_{Mv} & B_{M\varphi} & B_{MT} & B_{MM} \end{bmatrix} \begin{Bmatrix} v_i \\ \varphi_i \\ T_i \\ M_i \end{Bmatrix} \quad (14.11)$$

or

$$\{V(x)\} = [\{B_{\cdot v}\} \quad \{B_{\cdot \varphi}\} \quad \{B_{\cdot T}\} \quad \{B_{\cdot M}\}] \{V_i\} \quad (14.12)$$

and in a brief form

$$\{V(x)\} = [B(x)] \{V_i\} \quad (14.13)$$

where:

$\{V_i\}$  and  $\{V(x)\}$  are the state vectors (initial and resulting),

$[B(x)]$  is the transfer matrix.

If the beam is loaded on its length (Fig. 14.2) it is necessary to consider the additional vector of load  $\{C(x)\}$

$$\{V(x)\} = [B(x)]\{V_i\} + \{C(x)\} \quad (14.14)$$

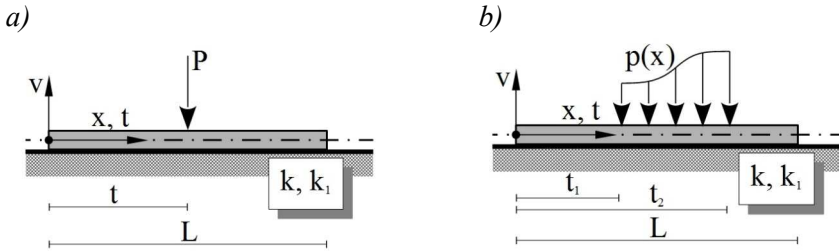


**Fig. 14.2.** Beam load a) concentrated force, b) distributed load.

Applying Macaulay bracket

$$B\langle x-t \rangle = \begin{cases} 0 & , \quad x < t \\ B(x-t), & x \geq t \end{cases} \quad (14.15)$$

for the concentrated force (Fig. 14.2a), relation 14.14 may be written as follows:

$$\{V(x)\} = [B(x)]\{V_i\} + \{B_{,Q}\langle x-t \rangle\} P \quad (14.16)$$

For the distributed load (Fig. 14.2b), his relation has a following form:

$$\{V(x)\} = [B(x)]\{V_i\} + \int_{t_1}^x \{B_{,Q}(x-t)\} p(t) dt \quad (14.17)$$

Generally, for arbitrary load, the equation 14.14 may be applied to describe the kinematic and static entities inside the beam element, included a complex structure, as defined in matrix description of displacement method or Finite Element Method (Pietrzak, Rakowski and Wrzeńskiowski, 1986, Megson, 2014, Kassimali, 2012). Equation 14.14 may be applied also to describe the relations between state vectors in initial and final node of beam element (in its own local coordinates) (Fig. 14.3) taking into account the internode influence load vector as

$$\{V_k\} = [B(L)]\{V_i\} + \{C\} \quad (14.18)$$

where:

$$\{C\} = \{C_v \quad C_\phi \quad C_T \quad C_M\}^T \quad (14.19)$$

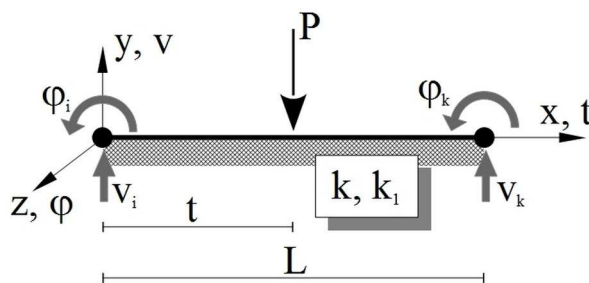


**Fig. 14.3.** Timoshenko beam element on two-parameter foundation with general internode load.

For concentrated force we obtain:

$$\{C\} = \{B_{\cdot T}(L - t)\} P \quad (14.20)$$

and for distributed load:

$$\{C\} = \int_{t_1}^{t_2} \{B_{\cdot T}(L - t)\} p(t) dt \quad (14.21)$$

Relation 14.18 can be rewritten:

$$\begin{Bmatrix} \{\delta_k\} \\ \{f_k\} \end{Bmatrix} = \begin{bmatrix} [B_{ii}] & [B_{ii}] \\ [B_{ii}] & [B_{ii}] \end{bmatrix} \begin{Bmatrix} \{\delta_i\} \\ \{f_i\} \end{Bmatrix} + \begin{Bmatrix} \{C_\delta\} \\ \{C_f\} \end{Bmatrix} \quad (14.22)$$

and leads to the following form:

$$\begin{bmatrix} -[B_{ik}]^{-1}[B_{ii}] & [B_{ik}]^{-1} \\ [B_{ki}] - [B_{kk}][B_{ik}]^{-1}[B_{ii}] & [B_{kk}][B_{ik}]^{-1} \end{bmatrix} \begin{Bmatrix} \{\delta_i\} \\ \{\delta_k\} \end{Bmatrix} = \begin{Bmatrix} \{f_i\} \\ \{f_k\} \end{Bmatrix} + \begin{bmatrix} [B_{ik}]^{-1} & [0] \\ [B_{kk}][B_{ik}]^{-1} & -[1] \end{bmatrix} \begin{Bmatrix} \{C_\delta\} \\ \{C_f\} \end{Bmatrix} \quad (14.23)$$

which is known as equilibrium equation for the element:

$$[k_e]\{\delta_e\} = \{f_e\} + \{f_e^0\} \quad (14.24)$$

used in matrix displacement method and Finite Element Method, where:

$[k_e]$  - stiffness matrix,

$\{\delta_e\}$  - displacement vector,

$\{f_e\}$  - vector of nodal forces,

$\{f_e^0\}$  - vector of resultant internodal loads for the element.

Advantageously is to use the element's stiffness matrix in the following form:

$$[k_e] = \frac{EJ}{L^3} \begin{bmatrix} \gamma & \nu L & -\varepsilon & \delta L \\ \nu L & \alpha L^2 & -\delta L & \beta L^2 \\ -\varepsilon & -\delta L & \gamma & -\nu L \\ \delta L & \beta L^2 & -\nu L & \alpha L^2 \end{bmatrix} \quad (14.25)$$

and the vector of resultant internodal loads as:

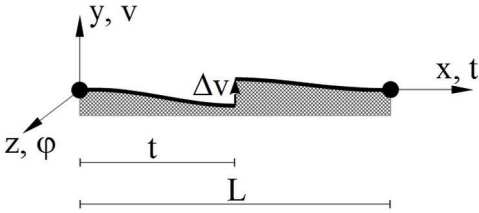
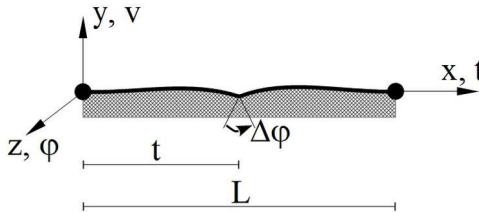
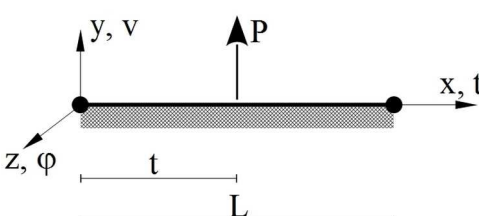
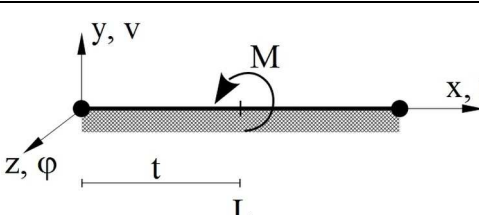
$$\{f_e^0\} = \begin{Bmatrix} T_i^0 \\ M_i^0 \\ T_k^0 \\ M_k^0 \end{Bmatrix} = \frac{EJ}{L^3} \begin{bmatrix} -\varepsilon & \delta L & 0 & 0 \\ -\delta L & \beta L^2 & 0 & 0 \\ \gamma & -\nu L & -L^3/EJ & 0 \\ -\nu L & \alpha L^2 & 0 & -L^3/EJ \end{bmatrix} \begin{Bmatrix} C_v \\ C_\varphi \\ C_T \\ C_M \end{Bmatrix} \quad (14.26)$$

Relations 14.26 and 14.14 show the possibility to consider the arbitrary internodal loads. Examples of concentrated loads are show in Table 1. For similar distributed loads the equations 14.20 and 14.21 should be used.

The obtained equations 14.14 and 14.24 also 14.25 and 14.26 allow to apply the solution introducing the discretization of the structure known from Finite Element Method, and the implementation of above mentioned equations into realization of these methods.

Of course the given description may be in a simple way completed with the state of loads corresponding to bending in perpendicular plane, longitudinal load and torsion. Due to known solutions concerning these problems they will not be considered in this study (Cook, 2002, Megson, 2014, Akgöz *et al.*, 2016).

**Table. 14.1.** Loads and corresponding  $\{C\}$

Load case	$\{C\}$
 <p>Diagram showing a rod segment of length <math>L</math> with a coordinate system <math>(x, t)</math> and <math>(y, v, z, \varphi)</math>. A shear load <math>\Delta v</math> is applied over a segment of length <math>t</math>.</p>	$\{C\} = \{B_{\cdot v}(L - t)\} \Delta v$
 <p>Diagram showing a rod segment of length <math>L</math> with a coordinate system <math>(x, t)</math> and <math>(y, v, z, \varphi)</math>. A torsional load <math>\Delta \varphi</math> is applied over a segment of length <math>t</math>.</p>	$\{C\} = \{B_{\cdot \varphi T}(L - t)\} \Delta \varphi$
 <p>Diagram showing a rod segment of length <math>L</math> with a coordinate system <math>(x, t)</math> and <math>(y, v, z, \varphi)</math>. A point load <math>P</math> is applied at the center of the segment.</p>	$\{C\} = \{B_{\cdot T}(L - t)\} P$
 <p>Diagram showing a rod segment of length <math>L</math> with a coordinate system <math>(x, t)</math> and <math>(y, v, z, \varphi)</math>. A bending moment <math>M</math> is applied at the center of the segment.</p>	$\{C\} = \{B_{\cdot M}(L - t)\} M$



### 14.3. Influence of shear for rods without foundation

Presented relations in this case lead to known equations concerning the Timoshenko beam element. Transfer matrix has a following form:

$$[B(x)] = \begin{bmatrix} 1 & x & \frac{x}{6EJ}(x^2 - 6\mu L^2) & \frac{-x^2}{2EJ} \\ 0 & 1 & \frac{x^2}{2EJ} & \frac{-x}{EJ} \\ 0 & 0 & -1 & 0 \\ 0 & 0 & x & -1 \end{bmatrix} \quad (14.27)$$

where

$$\mu = \eta \frac{EJ}{L^2} = \frac{EJ}{\kappa G A L^2} \quad (14.28)$$

and the coefficients of element stiffness matrix:

$$\begin{aligned} \alpha &= 4 \frac{1+3\mu}{1+12\mu} & \beta &= 2 \frac{1-6\mu}{1+12\mu} \\ \delta = \nu &= 6 \frac{1}{1+12\mu} & \gamma = \varepsilon &= 12 \frac{1}{1+12\mu} \end{aligned} \quad (14.29)$$

For Bernoulli-Euler beam theory the  $\mu = 0$  should be assumed.

Describing the influence of shear, the important factor is the shear stiffness, defined in a literature as one of four possible denominations

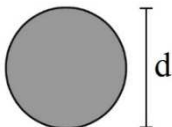
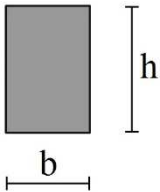
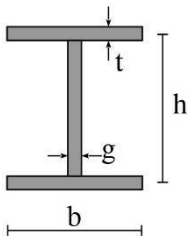
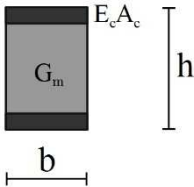

$$\kappa G A = \frac{GA}{k} = GA_z = S_v \quad (14.30)$$

The shear coefficient ( $\kappa$ ) can be calculated from the following relation:

$$\kappa = \frac{J^2}{A \int_A \frac{S^2}{b^2} dA} \quad (14.31)$$

In Table 14.2. the examples of various shear coefficients are given.

**Table. 14.2.** Examples of shear coefficients

Section	Shape	Coefficient
Circle (*)		$\kappa = \frac{6(1+\nu)}{7+6\nu}$
Rectangle (*)		$\kappa = \frac{10(1+\nu)}{12+11\nu}$
Thin-Walled I - Section (*)		$\kappa = 10(1+\nu)(1+3m)^2 / p,$ $m = 2bt / hg,$ $n = b / h,$ $p = 12 + 72m + 150m^2 + 90m^3 +$ $+ \nu(11 + 66m + 135m^2 + 90m^3) +$ $+ 30n^2(m + m^2) +$ $+ 5\nu n^2(8m + 9m^2)$
Sandwich (**)		$\mu = \frac{E_c A_c h}{G_m b}$
Truss (***)		$S_v = EA_k \sin^2 \alpha \cos \alpha$

(\*) – Cowper G.R. (Cowper, 1966),

(\*\*) – Filipkowski J. (Filipkowski, 1989),

(\*\*\*) – Pałkowski Sz. (Pałkowski, 2009).

In order to describe the influence of shear, the adequate numerical analyses have been performed for the cantilever beam loaded with concentrated force (Fig. 14.4). Steel I-section has been assumed, similar to I240, with following characteristics:  $E = 210$  GPa,  $G = 81$  GPa,  $A = 46,111$  cm<sup>2</sup>,  $J = 4253,3$  cm<sup>4</sup>,  $\kappa = 0,4423$  (calculated from equation 14.31) and variable  $L$  (Table 14.3), in relation to assumed  $L/h$ , where  $h = 240$  mm.

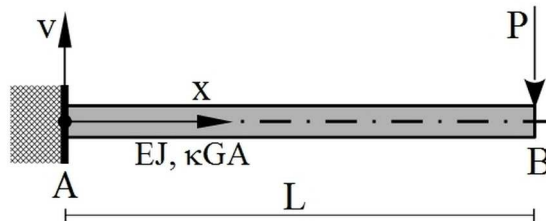


**Fig. 14.4.** Cantilever beam loaded with concentrated force

Calculations of displacement ( $v$ ) in B have been performed according the Timoshenko beam ( $v^T$ ) and Bernoulliego-Eulera ( $v^{BE}$ ) theories, consistent equations 14.27 ÷ 14.31 using MATLAB system, applied also in FEM analyses (Ferreira, 2009).

As reference results, in order to evaluate the consistence of solution the 3D Finite Element Method analysis has been performed ( $v^{FEM}$ ). In discrete numerical model the symmetry of the structure was applied. Three-dimensional brick elements have been applied in discrete FEM model, for each mesh built with hundreds thousands elements. Symmetry of the model and load relative to the vertical plane has been assumed. Static linear analyses were performed using ABAQUS (SIMULIA, 2014) computer code. The examples of obtained FEM results are show in Fig. 14.5.

In Table 14.3. the displacements ( $v^{FEM}$ ,  $v^T$  and  $v^{BE}$ ) and values of relative percentage errors for Timoshenko ( $\delta v_{FEM}^T$ ) oraz Bernoulli-Euler ( $\delta v_{FEM}^{BE}$ ) models (in relations to FEM solution) as well as solution error of Bernoulli-Euler model in relation to Timoshenko ( $\delta v_{E-T}^{BE}$ ) model.

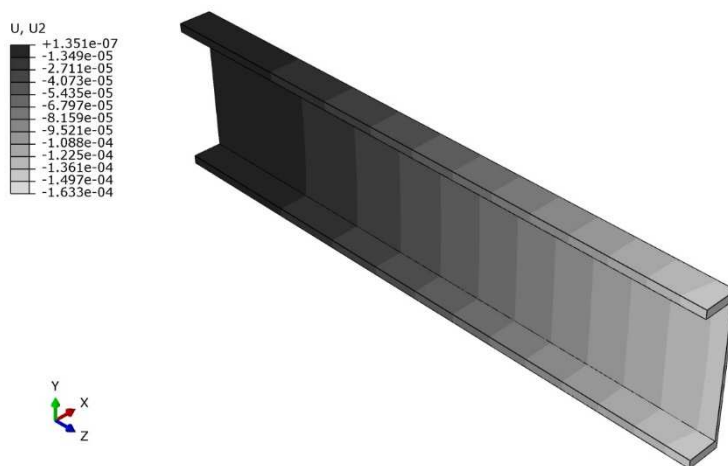


**Fig. 14.5.** Distribution of vertical displacements obtained by FEM analysis, for  $L/h=4$  (values in meters)

**Table. 14.3.** Displacements and relative percentage errors

$L/h$ [-]	$v^{FEM}$ [mm]	$v^T$ [mm]	$v^{BE}$ [mm]	$\delta v^T_{FEM}$ [%]	$\delta v^{BE}_{FEM}$ [%]	$\delta v^{BE}_T$ [%]
12	3,6320	3,6356	3,5660	-0,10	1,82	1,92
10	2,1194	2,1217	2,0636	-0,11	2,63	2,74
8	1,1018	1,1031	1,0566	-0,12	4,10	4,22
6	0,4800	0,4806	0,4457	-0,12	7,14	7,26
5	0,2866	0,2870	0,2580	-0,12	10,01	10,12
4 (*)	0,1551	0,1553	0,1321	-0,14	14,84	14,97
3 (*)	0,0730	0,0732	0,0557	-0,24	23,65	23,83

(\*) – In author's opinion, beam theory can be used for  $L/h$  above 5, results for  $L/h = 3$  and 4 are shown only for demonstrative purposes.

The good consistence between FEM solutions and results for Timoshenko beam can be observed, even for  $L/h < 5$ . Results for Bernoulli-Euler model, for shorter cantilevers have growing error values (to 24%).

Assuming the shear coefficient  $\kappa = 0,4055$ , calculated according Cowper G.R. (Cowper, 1966), see Table 14.3, values  $\delta v_{FEM}^T$  are growing, and in relation to  $L/h$  have the values from -0,28% to -2,41%. If we assume the approximate value of coefficient  $\kappa = 0,4034$  (calculated as relation of the web area to the total section area) the values of  $\delta v_{FEM}^T$  will slightly grow and have the values between -0,29% and -2,55%.

More examples of differences between Timoshenko and Bernoulli-Euler models are available in publication of Filipkowski and Ruchwa (Filipkowski and Ruchwa, 1991).

#### 14.4. Beams on elastic foundation

Looking for solution in the case of the beam interacting with two-parameter elastic foundation, in order to solve the differential equation 14.3 it is necessary to solve the homogeneous equation with auxiliary coefficients:

$$b_1 = (k_1 + \eta k EJ)/EJ \quad b_2 = (1 + \eta k_1)k/EJ \quad b_3 = 4b_2/b_1^2 \quad (14.32)$$

According to the values of parameter  $b_3$ , the equation has two variants (cases) of solution:

- Variant I (a.k.a. *strong foundation*) -  $b_3 \geq 1$  (14.33)

- Variant II (a.k.a. *weak foundation*) -  $b_3 < 1$  (14.34)

If we assume additional parameters, defined with equations

$$\lambda = \sqrt[4]{(1 + \eta k_1)k/EJ} \quad \Lambda = \lambda L \quad (14.35)$$

$$k_2 = \lambda^2 EJ \quad k_d = k_1 + k_2 \quad k_r = k_1 - k_2 \quad (14.36)$$

$$A = 1 + \eta k_d \quad B = 1 + \eta k_r \quad C = 1 + \eta k_1 \quad (14.37)$$

the relations 14.35 ÷ 14.51. will give the exact transfer and stiffness matrices for both variants of solution for Timoshenko beam on two-parameter elastic foundation.

Variant I (strong foundation)

$$a = \sqrt{\frac{1}{2} \left( 1 - \frac{b_1}{2\sqrt{b_2}} \right)} \quad b = \sqrt{\frac{1}{2} \left( 1 + \frac{b_1}{2\sqrt{b_2}} \right)} \quad S = 2ab \quad (14.38)$$

$$\begin{aligned} \phi_1 &= \sin(a\lambda x) \sinh(b\lambda x) & \phi_2 &= \sin(a\lambda x) \cosh(b\lambda x) \\ \phi_3 &= \cos(a\lambda x) \sinh(b\lambda x) & \phi_4 &= \cos(a\lambda x) \cosh(b\lambda x) \end{aligned} \quad (14.39)$$

**Table. 14.5.** Transfer matrix (for strong foundation)

$\{B_{\cdot v}\}$ (14.40)	$\{B_{\cdot \varphi}\}$ (14.41)
$B_{vv} = \frac{a^2 A - b^2 B}{SC} \phi_1 + \phi_4$ $B_{\varphi v} = -\frac{b\lambda}{SC} \phi_2 + \frac{a\lambda}{SC} \phi_3$ $B_{Tv} = -\frac{b\lambda k_r}{SC} \phi_2 + \frac{a\lambda k_d}{SC} \phi_3$ $B_{Mv} = -\frac{k_2}{SC} \phi_1$	$B_{v\varphi} = \frac{b}{S\lambda} \phi_2 + \frac{a}{S\lambda} \phi_3$ $B_{\varphi\varphi} = \frac{a^2 k_d + b^2 k_r}{Sk_2} \phi_1 + \phi_4$ $B_{T\varphi} = \frac{a^2 k_d^2 + b^2 k_r^2}{Sk_2} \phi_1$ $B_{M\varphi} = \frac{bk_r}{S\lambda} \phi_2 + \frac{ak_d}{S\lambda} \phi_3$
$\{B_{\cdot T}\}$ (14.42)	$\{B_{\cdot M}\}$ (14.43)
$B_{vT} = \frac{bB}{S\lambda k_2} \phi_2 - \frac{aA}{S\lambda k_2} \phi_3$ $B_{\varphi T} = \frac{1}{Sk_2} \phi_1$ $B_{TT} = \frac{a^2 k_d + b^2 k_r}{Sk_2} \phi_1 - \phi_4$ $B_{MT} = \frac{b}{S\lambda} \phi_2 + \frac{a}{S\lambda} \phi_3$	$B_{vM} = -\frac{1}{Sk_2} \phi_1$ $B_{\varphi M} = -\frac{bB\lambda}{SCk_2} \phi_2 - \frac{aA\lambda}{SCk_2} \phi_3$ $B_{TM} = -\frac{b\lambda}{SC} \phi_2 + \frac{a\lambda}{SC} \phi_3$ $B_{MM} = \frac{a^2 A - b^2 B}{SC} \phi_1 - \phi_4$

*Warient II (weak foundation)*

$$a = \sqrt{\frac{1}{2} \left( -1 + \frac{b_1}{2\sqrt{b_2}} \right)} \quad b = \sqrt{\frac{1}{2} \left( 1 + \frac{b_1}{2\sqrt{b_2}} \right)} \quad S = 2ab \quad (14.44)$$

$$\begin{aligned} \phi_1 &= \sinh(a\lambda x) \sinh(b\lambda x) & \phi_2 &= \sinh(a\lambda x) \cosh(b\lambda x) \\ \phi_3 &= \cosh(a\lambda x) \sinh(b\lambda x) & \phi_4 &= \cosh(a\lambda x) \cosh(b\lambda x) \end{aligned} \quad (14.45)$$

**Table. 14.6.** Transfer matrix (for weak foundation)

$\{B_{\cdot v}\}$ (14.46)	$\{B_{\cdot \varphi}\}$ (14.47)
$B_{vv} = -\frac{a^2 A + b^2 B}{SC} \phi_1 + \phi_4$ $B_{\varphi v} = -\frac{b\lambda}{SC} \phi_2 + \frac{a\lambda}{SC} \phi_3$ $B_{Tv} = -\frac{b\lambda k_r}{SC} \phi_2 + \frac{a\lambda k_d}{SC} \phi_3$ $B_{Mv} = -\frac{k_2}{SC} \phi_1$	$B_{v\varphi} = \frac{b}{S\lambda} \phi_2 + \frac{a}{S\lambda} \phi_3$ $B_{\varphi\varphi} = \frac{-a^2 k_d + b^2 k_r}{Sk_2} \phi_1 + \phi_4$ $B_{T\varphi} = \frac{-a^2 k_d^2 + b^2 k_r^2}{Sk_2} \phi_1$ $B_{M\varphi} = \frac{bk_r}{S\lambda} \phi_2 + \frac{ak_d}{S\lambda} \phi_3$
$\{B_{\cdot T}\}$ (14.48)	$\{B_{\cdot M}\}$ (14.49)
$B_{vT} = \frac{bB}{S\lambda k_2} \phi_2 - \frac{aA}{S\lambda k_2} \phi_3$ $B_{\varphi T} = \frac{1}{Sk_2} \phi_1$ $B_{TT} = \frac{-a^2 k_d + b^2 k_r}{Sk_2} \phi_1 - \phi_4$ $B_{MT} = \frac{b}{S\lambda} \phi_2 + \frac{a}{S\lambda} \phi_3$	$B_{vM} = -\frac{1}{Sk_2} \phi_1$ $B_{\varphi M} = -\frac{bB\lambda}{SCk_2} \phi_2 - \frac{aA\lambda}{SCk_2} \phi_3$ $B_{TM} = -\frac{b\lambda}{SC} \phi_2 + \frac{a\lambda}{SC} \phi_3$ $B_{MM} = -\frac{a^2 A + b^2 B}{SC} \phi_1 - \phi_4$

**Table. 14.7.** Stiffness matrix for element on elastic foundation

$[\mathbf{k}_e]$ - for strong foundation	(14.50)
$\alpha = \Lambda \frac{a A \sinh(b\Lambda) \cosh(b\Lambda) - b B \sin(a\Lambda) \cos(a\Lambda)}{\Delta} S_C$	
$\beta = -\Lambda \frac{a A \sinh(b\Lambda) \cos(a\Lambda) - b B \sin(a\Lambda) \cosh(b\Lambda)}{\Delta} S_C$	
$\gamma = \Lambda^3 \frac{a A \sinh(b\Lambda) \cosh(b\Lambda) + b B \sin(a\Lambda) \cos(a\Lambda)}{\Delta} S$	
$\delta = \Lambda^2 \frac{\sin(a\Lambda) \sinh(b\Lambda)}{\Delta} S_C$	
$\varepsilon = \Lambda^3 \frac{a A \sinh(b\Lambda) \cos(a\Lambda) + b B \sin(a\Lambda) \cosh(b\Lambda)}{\Delta} S$	
$v = \Lambda^2 \frac{a^2 A \sinh^2(b\Lambda) + b^2 B \sin^2(a\Lambda)}{\Delta}$	
$\Delta = (a A \sinh(b\Lambda))^2 - (b B \sin(a\Lambda))^2$	
$[\mathbf{k}_e]$ - for weak foundation	(14.51)
$\alpha = \Lambda \frac{a A \sinh(b\Lambda) \cosh(b\Lambda) - b B \sinh(a\Lambda) \cosh(a\Lambda)}{\Delta} S_C$	
$\beta = -\Lambda \frac{a A \sinh(b\Lambda) \cosh(a\Lambda) - b B \sinh(a\Lambda) \cosh(b\Lambda)}{\Delta} S_C$	
$\gamma = \Lambda^3 \frac{a A \sinh(b\Lambda) \cosh(b\Lambda) + b B \sinh(a\Lambda) \cosh(a\Lambda)}{\Delta} S$	
$\delta = \Lambda^2 \frac{\sinh(a\Lambda) \sinh(b\Lambda)}{\Delta} S_C$	
$\varepsilon = \Lambda^3 \frac{a A \sinh(b\Lambda) \cosh(a\Lambda) + b B \sinh(a\Lambda) \cosh(b\Lambda)}{\Delta} S$	
$v = \Lambda^2 \frac{a^2 A \sinh^2(b\Lambda) + b^2 B \sinh^2(a\Lambda)}{\Delta}$	
$\Delta = (a A \sinh(b\Lambda))^2 - (b B \sinh(a\Lambda))^2$	



### 14.5. Examples of Timoshenko beam on elastic foundation

In order to show the possibilities of the considered algorithm, an example of a beam with shear effects and located on two-parameter elastic foundation was analyzed (Fig. 14.6).

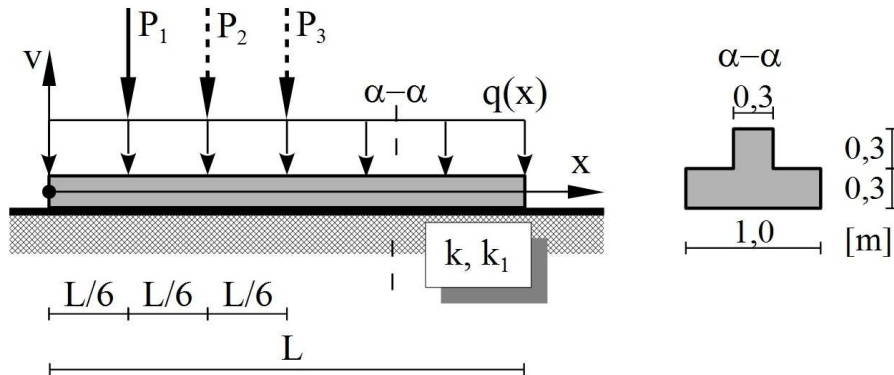


**Fig. 14.6.** An example of a Timoshenko beam on two-parameter elastic foundation.

Assumed characteristics of the beam:

- $E = 33 \text{ GPa}$ ,  $G = 14 \text{ GPa}$  (concrete C30/37),
- $A = 3900 \text{ cm}^2$ ,  $J = 915580 \text{ cm}^4$ ,  $\kappa = 0,7008$  (T-section),
- $L = 3 \text{ m} / 6 \text{ m} / 12 \text{ m}$  ( $L/h = 5 / 10 / 20$ );

characteristics of foundation:

- $k = 80 \text{ MN/m}$
- $k_1 = 20 \text{ MN}$ ;

applied load:

- $q = 10 \text{ kN/m}$  (own weight),
- $P_1 = P_2 = P_3 = 750 \text{ kN}$  (concentrated load).

Various configurations of analyzed example have been assumed: 3 variants of length, 3 variants of concentrated force  $P_i$  localization, two computational models was also assumed: beam with shear effects on two-parameter elastic foundation (T2) and beam without shear effects on Winkler foundation (BE1). All calculations were performed using MATLAB (MathWorks, 2015) code, applying the matrix version of displacements method and described relations. On Figs 14.7 ÷ 14.10 the obtained kinematic and static results are presented.

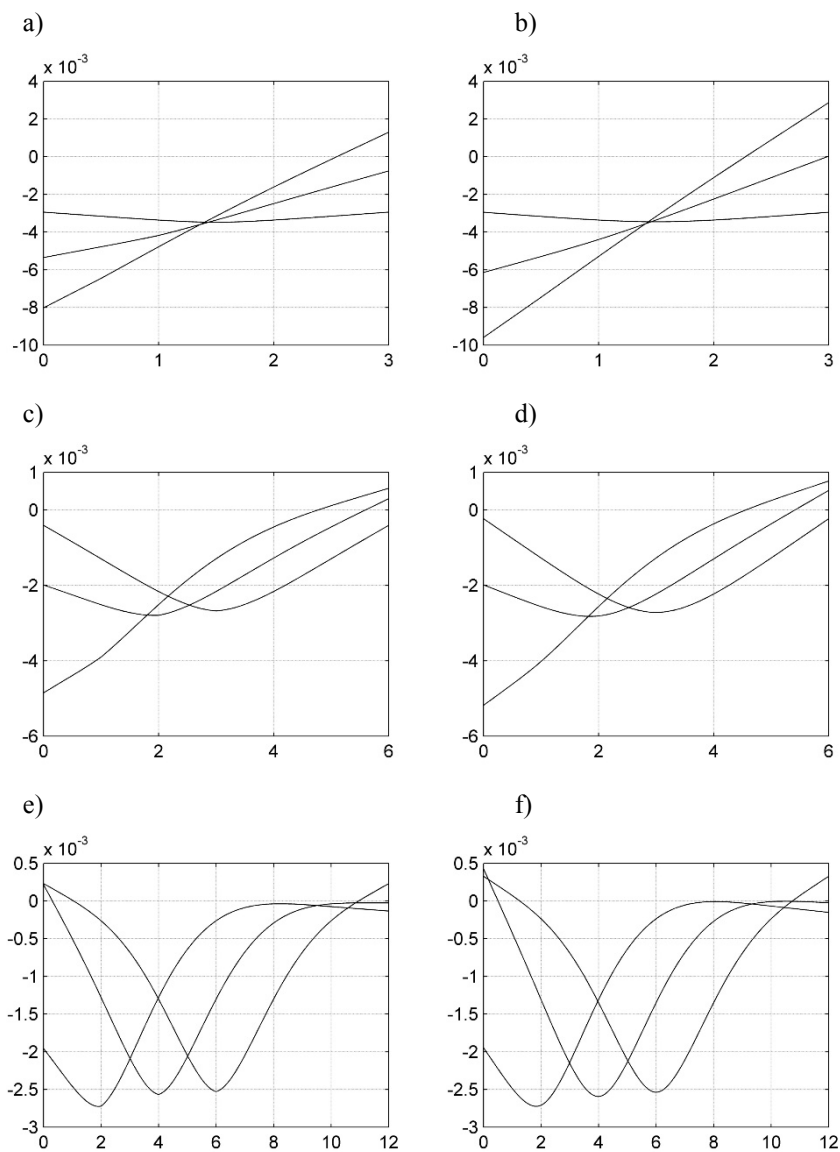


**Fig. 14.7.** Displacement function for the beam for various positions of concentrated load, length of the beam  $L = 3$  m (a, b), 6 m (c, d), 12 m (e, f) computational model of the beam - variant T2 (a, c, e) and variant BE1 (b, d, f).

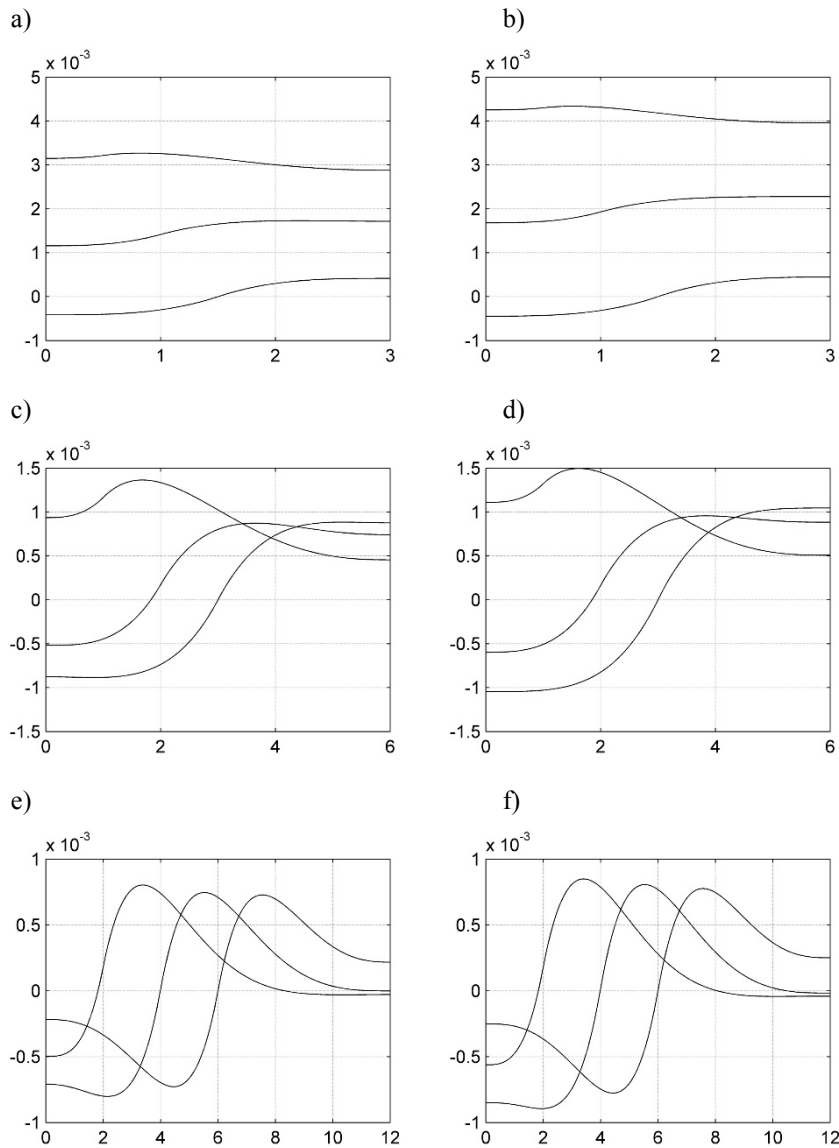


**Fig. 14.8.** Rotation angle for the beam for various positions of concentrated load, length of the beam  $L = 3$  m (a, b), 6 m (c, d), 12 m (e, f) computational model of the beam - variant T2 (a, c, e) and variant BE1 (b, d, f).

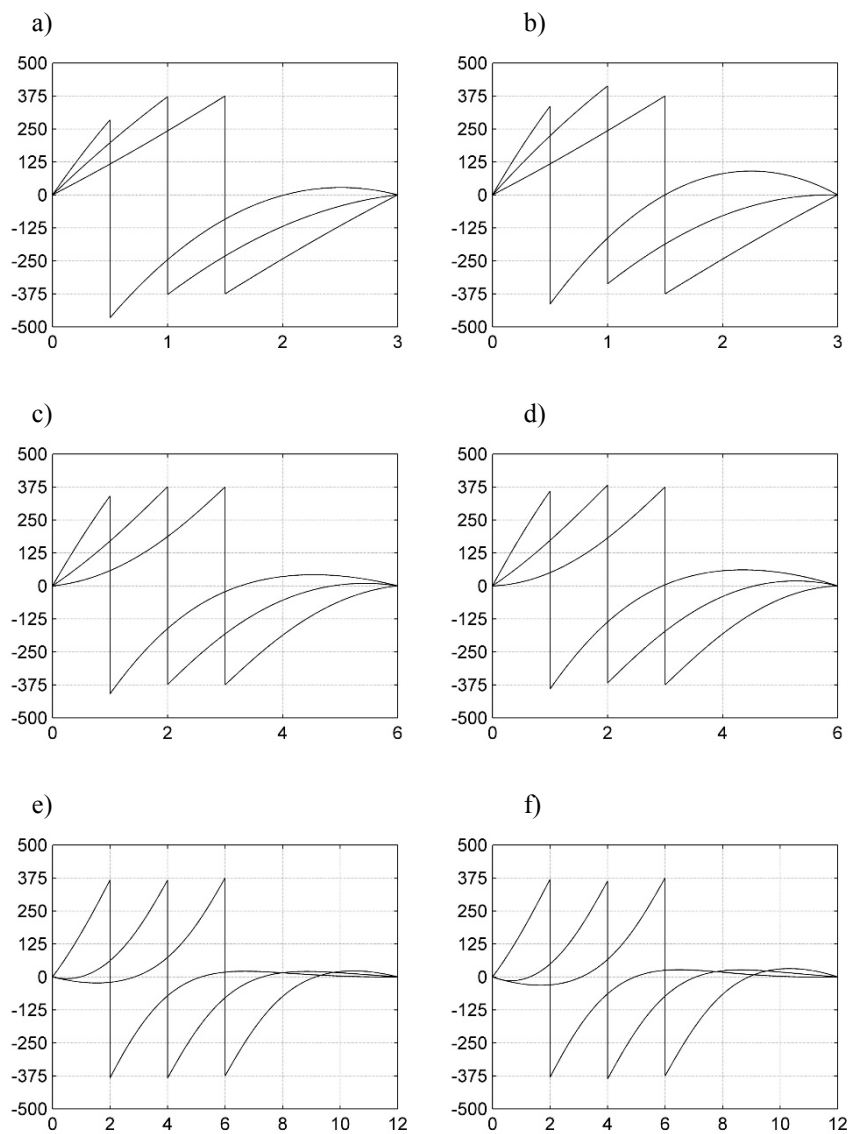


**Fig. 14.9.** Transversal force function for the beam for various positions of concentrated load, length of the beam  $L = 3$  m (a, b), 6 m (c, d), 12 m (e, f) computational model of the beam - variant T2 (a, c, e) and variant BE1 (b, d, f).

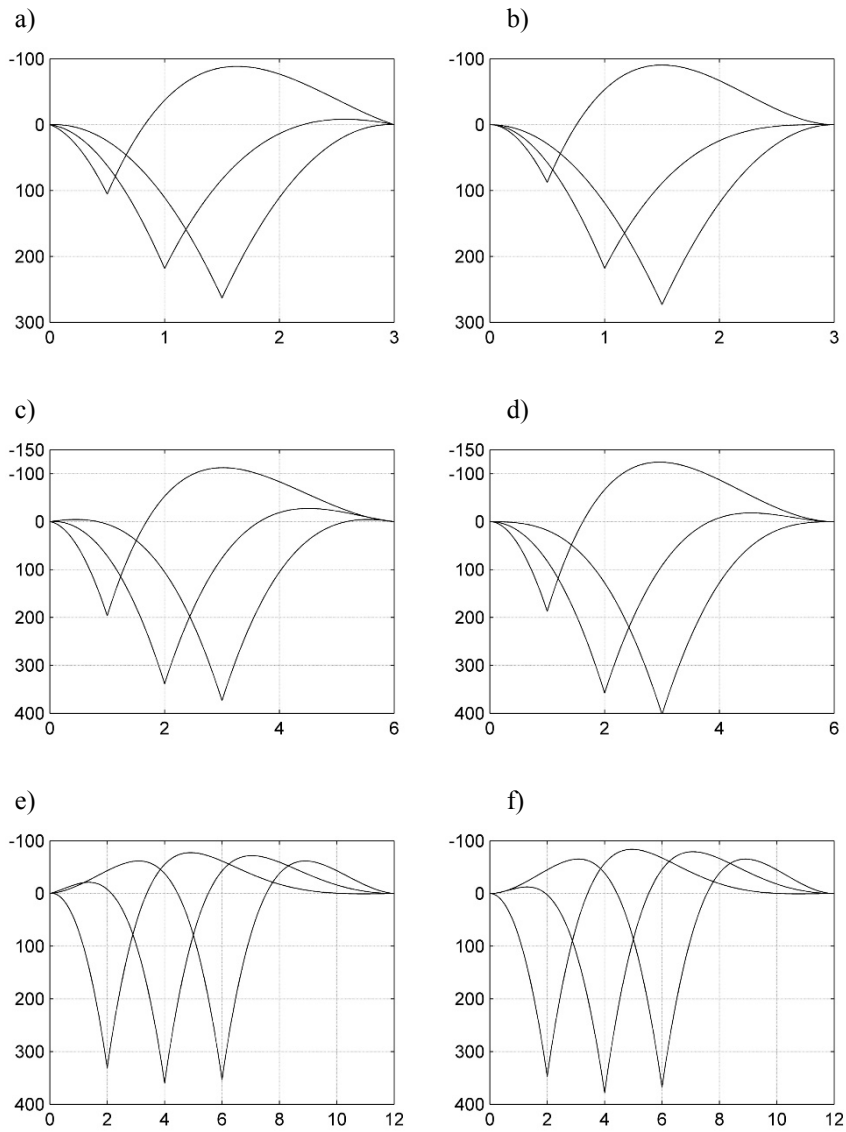


**Fig. 14.10.** Bending moment for the beam for various positions of concentrated load, length of the beam  $L = 3$  m (a, b), 6 m (c, d), 12 m (e, f) computational model of the beam - variant T2 (a, c, e) and variant BE1 (b, d, f).

In Figures 14.7 and 14.8 considerable differences are visible for displacements and rotation angles for beams of 3 m length, loaded with forces  $P_1$  or  $P_2$ . Differences are diminishing when the length grows (6 or 12 m) or we have the symmetric variant of load with force  $P_3$ . The diagrams of internal forces given in Figures 14.9 and 14.10 show the bigger differences for transversal forces than for bending moments. The biggest differences are observed for short beams ( $L = 3$  m,  $L/h = 5$ ) loaded with forces  $P_1$  or  $P_2$ .

## 14.6. Conclusions

Presented approach concerning analysis of rod structures with shear effects, interacting or not with two-parameter elastic foundation constitutes consistent and precise solution of the problem. It is characterized by an universal and simple approach in problem description, allowing for analysis of arbitrary particular cases, concerning various variants of analysis – taking into account or not the shear effects ( $\eta = 0$ ), interaction with two- or one-parameter elastic foundation ( $k_1 = 0$ ) and considering various loads: concentrated or distributed. This approach can be used for rods with consistent sections, three-layer sections or elements with truss sections. The presented equations can be applied in matrix version of displacement method or Finite Element Method.

Due to assumed very often high economics of design solutions, we should not be content with traditional models ignoring shear effects. This will protect against incorrect assessment of the situation.

## Acknowledgments

This study came forth due to suggestion of Professor Jan Filipkowski. I would like to thank him for many years of collaborative work in Division of Structural Mechanics and many interesting discussions.

## References

- Akgöz, B. *et al.* (2016) ‘Static analysis of beams on elastic foundation by the method of discrete singular convolution’, *International Journal of Engineering & Applied Sciences (IJEAS)*, 8, pp. 67-73.
- Belytschko, T., Liu, W.K. and Moran, B. (2000) ‘Nonlinear Finite Elements for Continua and Structures’, John Wiley & Sons.
- Cook, R.D. *et al.* (2002) ‘Concepts and Applications of Finite Element Analysis’, John Wiley & Sons.
- Cowper, G.R. (1966) ‘The shear coefficient in Timoshenko’s beam theory’, *J Appl Mech ASME*, 33, pp. 335-340.

- Dembicki, E. *et al.* (1988) 'Fundamentowanie. Projektowanie i wykonawstwo, t.2.', Arkady, Warszawa.
- Dinev, D. (2012) 'Analytical solution of beam on elastic foundation by singularity functions', *Engineering Mechanics*, 19(6), pp. 381–392.
- El-Garhy, B. and Osman, M.M. (2002) 'Winkler coefficient for beams on elastic foundation', *Engineering Research Journal*, Minufiya University, Egypt, 25(3), pp. 1-18.
- Ferreira, A.J.M. (2009) 'MATLAB Codes for Finite Element Analysis: Solids and Structures', *Solid Mechanics and Its Applications*, 15(7) Springer.
- Filipkowski, J. (1989) 'Prismatic Beam on Two-Parameter Elastic Foundations' [Lecture]. The University of Dar es Salaam, Tanzania.
- Filipkowski, J. (1992) 'O obliczaniu konstrukcji prętowych współpracujących z podłożem gruntowym', *Zastosowanie mechaniki w inżynierii wodnej i lądowej*, IBW PAN, Gdańsk, pp. 57-68.
- Filipkowski, J. and Ruchwa, M. (1991) 'Wpływ odkształceń postaciowych na wielkości statyczne i geometryczne w ustrojach prętowych', In: *XXXVII Konferencja Naukowa KILiW PAN i KN PZITB Łódź - Krynica 1991: Referaty, tom 1. Teoria Konstrukcji*, Łódź: Politechnika Łódzka, pp. 43-48.
- Filipkowski, J. and Shirima, L.M. (1991) 'Timoshenko beam on two-parameter elastic foundation', In: *X Polish Conference Computer Methods in Mechanics*, Świnoujście, Poland, pp. 173-180.
- Frydryšek, K., Jančo, R. and Gondek H. (2013) 'Solutions of Beams, Frames and 3D Structures on Elastic Foundation Using FEM', *International Journal Of Mechanics*, 4(7), pp. 362-369.
- Hughes, T.J.R. (2000) 'The Finite Element Method: Linear Static and Dynamic Finite Element Analysis', Dover Publications.
- Kassimali, A. (2012) 'Matrix Analysis of Structures', Second Edition, CENGAGE Learning.
- MathWorks (2015) 'MATLAB Documentation', The Math Works Inc.
- Megson, T.H.G. (2014) 'Structural and Stress Analysis', Third Edition, Elsevier.
- Pałkowski, Sz. (2009) 'Konstrukcje stalowe. Wybrane zagadnienia obliczania i projektowania', PWN, Warszawa.
- Pietrzak, J., Rakowski, G. and Wrześniowski, K. (1986) 'Macierzowa analiza konstrukcji', Warszawa: PWN.
- Reddy, J.N. (2006) 'An Introduction to the Finite Element Method', McGraw-Hill.
- Ruchwa, M. and Matuszkiewicz, M. (2010) 'Zastosowanie Metody Elementów Skończonych w obliczeniach statycznych konstrukcji cięgnowych', *Biuletyn Wojskowej Akademii Technicznej*, LIX(4), pp. 363-378.

- Sadecka, L. (2010) 'Metoda różnic skończonych i metoda elementów skończonych w zagadnieniach mechaniki konstrukcji i podłoża', *Studia i Monografie*, z.258, Politechnika Opolska.
- Shirima, L.M. and Giger, M.W. (1992) 'Timoshenko beam element resting on two-parameter elastic foundation', *ASCE J. Eng Mech.*, 118(2), pp. 280-295.
- Sienkiewicz, Z. and Ruchwa, M. (1992) 'Analiza statyczna belek Timoshenki na dwuparametrowym podłożu sprężystym', In: *XXXVIII Konferencja Naukowa KILiW PAN i KN PZITB Łódź - Krynica 1992: Referaty, tom 1. Teoria Konstrukcji*, Łódź: Politechnika Łódzka, pp. 103-108.
- SIMULIA (2014) 'Abaqus 6.14 Documentation', Dassault Systèmes Simulia Corp., Providence.
- Teodoru, I.B. and Muşat, V. (2008) 'Beam Elements on Linear Variable Two-Parameter Elastic Foundation', *Bulletin of the Polytechnic Institute of Jassy, Constructions, Architecture Section*. LIV (LVIII), pp. 69-78.







WYDAWNICTWO POLITECHNIKI KOSZALIŃSKIEJ  
[www.wydawnictwo.tu.koszalin.pl](http://www.wydawnictwo.tu.koszalin.pl)



ISSN 0239-7129  
ISBN 978-83-7365-502-7